STRUCTURAL CONTROL STRATEGIES FOR EARTHQUAKE RESPONSE REDUCTION OF BUILDINGS

BY

TAKEHIKO ASAI

DISSERTATION

Submitted in partial fulfillment of the requirements
for the degree of Doctor of Philosophy in Civil Engineering
in the Graduate College of the
University of Illinois at Urbana-Champaign, 2014

Urbana, Illinois

Doctoral Committee:

Professor Bille F. Spencer, Jr., Chair, Director of Research
Professor Larry A. Bergman
Professor Alexander F. Vakakis
Professor Larry A. Fahnestock

Abstract

Destructive seismic events continue to demonstrate the importance of mitigating these hazards to building structures. Structural control has been considered one of the most effective strategies to protect buildings from extreme dynamic events such as earthquakes and strong winds, and has been applied to numerous real buildings in recent years.

Structural control strategies can be divided into four categories: passive, active, semi-active, and hybrid control. Because passive control systems are well understood and require no external power source, they have been accepted widely by the engineering community. However, these passive systems have the limitation of not being able to adapt to structural changes and to varying usage patterns and loading conditions. While active systems are able to adapt various conditions, they require a significant amount of power to generate the necessary large control forces; guaranteeing the availability of such power during seismic events is challenging. Moreover, the stability of active systems is not ensured.

To compensate for the drawbacks of passive and active systems, semi-active control systems have been proposed. Semi-active control devices possess the adaptability to flexible external inputs, do not require large power sources, and do not have the potential to destabilize the structural system. However, semi-active control has been slow to be accepted by engineering practitioners.

The focus of this dissertation is the improvement and the validation of semi-active control strategies, especially with magnetorheological (MR) dampers, for building protection from severe earthquakes. To make semi-active control strategies more practical, further studies on both the numerical and experimental aspects of the problem are conducted.

In the numerical studies, new algorithms for semi-active control are proposed. First, the nature of control forces produced by active control systems is investigated. The relationship between force-displacement hysteresis loops produced by the linear quadratic regulator (LQR) and the linear

quadratic Gaussian (LQG) algorithms is explored. Then, new simple algorithms are proposed, which can produce versatile hysteresis loops. Moreover, the proposed algorithms do not require a model of the target structure to be implemented, which is a significant advantage. The seismic performance of the proposed algorithms on a scaled three-story building model is compared with the LQG-based clipped-optimal semi-active control and LQG active control cases.

In the experimental studies, the effectiveness of semi-active control strategies are shown through real-time hybrid simulation (RTHS) in which a MR damper is tested physically. In this dissertation, two new structural control methods proposed in the literature recently are investigated, i.e., smart outrigger damping systems for high-rise buildings and smart base isolation systems consisting of passive base isolations and semi-active control devices. The accuracy of the RTHS employing the model-based compensator for MDOF structures with a semi-active device is discussed as well.

The research presented in this dissertation contributes the improvement and prevalence of semi-active control strategies in building structures to mitigate seismic damage.

To Father and Mother.

Acknowledgments

I would like to express my sincere thanks to my advisor, Professor Billie F. Spencer, Jr., for his advice, encouragement, and support throughout my time at the University of Illinois at Urbana-Champaign. I learned many things related to academic and professional skills from him. I am honored to have my Ph.D. studies under his supervision. This experience and insight I gained would be one of the most valuable assets for the rest of my life.

I sincerely appreciate the efforts of my committee members, Professor Larry A. Bergman, Professor Alexander Vakakis, and Professor Larry A. Fahnestock. Their comments and suggestions have enriched my dissertation while keeping it grounded and accessible to a wider audience.

I would also like to thank Professor Masayoshi Nakashima and Professor Yoshikazu Araki of Kyoto University for their encouragement to pursue graduate studies at the University of Illinois. I do not forget that they gave me the possibility of studying abroad.

This research was made possible, in part, through the Long Term Fellowship for Study Abroad provided by the Ministry of Education, Culture, Sports, Science and Technology in Japan (MEXT). I am extremely grateful and honored to have received this funding.

I have had the pleasure of interacting with all of the Smart Structure and Technology Laboratory (SSTL) members. I would like to appreciate their support and friendship throughout my research at the University of Illinois. I had a great time to study and work with them. Especially, I would like to thank two of my senior colleagues, Dr. Chia-Ming Chang and Dr. Brian M. Phillips, for their advice and support with my real-time hybrid simulation testing. Also, I am grateful to Fernando Moreu, who shared the joy of running with me.

I would like to thank my friends from Kyoto University. Existence of superior friends has kept stimulating me since the day we met. My sincere desire to catch up with them motivated me to get through some tough times. Without them, I would not be who I am now for sure. I hope our

friendships last forever.

Finally, I thank my parents for instilling in me the importance of hard work, persistence, and dignity. I believe that these precepts last forever in me.

Table of Contents

List of Tables

List of Figures

Chapter 1

Introduction

1.1 Motivation

Severe earthquakes have caused serious damage to buildings all over the world, resulting in tremendous human suffering and great economic loss. Structural control is one of the feasible options to enhance structural performance against such seismic events (Housner et al., 1997). To date, various methods of structural control have been studied by many researchers and engineers, and some of them have been applied successfully to real buildings. However, due to the stability, cost effectiveness, reliability, power requirements, etc., structural control strategies have yet to be fully accepted by the building engineering community.

Structural control systems can be placed into four basic categories: passive, active, semi-active, and hybrid. Passive systems, including base isolation, viscoelastic dampers, and tuned mass dampers, are well understood and are accepted widely by the engineering community as a means for mitigating the effect of strong earthquakes. However, these passive device methods have the limitation of not being able to adapt to structural change and to varying usage patterns and loading conditions. While active systems have the ability to adapt to various operating conditions, they require large power sources to impart forces to the structure, and may fail during seismic events. Another concern of active systems is that the stability of the system is not guaranteed.

Semi-active control devices have received a great deal of attention in recent years as a means to address drawbacks of passive and active systems. They offer the adaptability to structural changes and to various usage patterns and loading conditions, and they do not require large power sources to control devices. In fact, many can operate on battery power, which is critical during seismic events. Moreover, in contrast to active control systems, semi-active control systems do not have the potential to destabilize the structural system (in the bounded input/bounded output sense).

One of the promising devices for semi-active control systems is the magnetorheological (MR) damper (Carlson and Spencer, 1996), which is filled with magnetorheological fluid and controlled by a magnetic field. This magnetic field allows the damping characteristics to be continuously controlled by varying the input amplitude. The advantage of MR dampers is that they contain no moving parts other than the piston, which makes them very reliable. Moreover, MR fluid is not sensitive to impurities such as are commonly encountered during manufacturing and usage, and little particle/carrier fluid separation takes place in modern MR fluid under common flow conditions. So the future of application of MR dampers into civil structures appears to be quite bright. Nonetheless, to make semi-active systems employing MR dampers more implementable, further studies are still needed.

1.2 Semi-active control algorithms

Developing more effective semi-active control algorithms is an important step toward practical use. Although various semi-active control algorithms have been proposed, applying these algorithms in real civil structures needs a relatively accurate model of the structure. However, obtaining accurate parameter values for full-scale structures may not be practical. And the structure may change with time, resulting in the need to continuously update the model. Thus, developing effective simple algorithms which do not require the structural model or a large number of sensors is desirable for practical use.

Moreover, to ensure appropriate seismic performance of structures, the earthquake input energy absorption capability of control devices described by hysteresis loops plays a key role. However, in semi-active control, because only the properties of the devices are controlled, the nature of desired hysteresis loops is difficult to ascertain. For example, MR dampers, for which only input current can be controlled, cannot produce force such that the force and velocity have the same direction. Therefore, semi-active control algorithms which can realize specific hysteresis loops are also desirable in the field of seismic response control.

Thus, proposing model-free algorithms which can realize a variety of control force properties is demanded in the field of semi-active control.

1.3 Experimental verification of semi-active control strategies

Second, experimental verification for semi-actively controlled structures is necessary. However, experimental studies at large scale have been limited. Because creating the mathematical model of a MR damper is challenging due to its highly nonlinear response, physical experiments are vital to verify the effectiveness of semi-active methods employing MR dampers. Although shaking table testing provides a direct approach to evaluate the dynamic structural response of civil structures subjected to earthquake loads, even if large facilities such as the E-Defense table in Japan or the shaking table at the University of California at San Diego are available, tests for large civil structures such as high-rise buildings are impractical due to limitations on the size, payload capacity, and cost.

Hybrid simulation is a powerful, cost-effective method for testing structural systems. Through substructuring, the well-understood components of the structure are modeled numerically, while the components of interest are tested physically. Then, by coupling numerical simulation and experimental testing, the complete response of a structure is obtained. When the rate-dependent behavior of the physical specimen is important (e.g., MR damper), real-time hybrid simulation (RTHS) must be employed. In RTHS, computation, communication, and actuator limitations cause delays and lags which lead to inaccuracies and potential instabilities. The higher modes are affected more by these effects, reducing accuracy of the simulation, potentially leading to instability of the RTHS. Thus, research on RTHS has been limited to simple structures; e.g., SDOF and 2DOF.

To compensate for these time delays and lags, as well as control-structure interaction (CSI) between the actuator and the specimen (Dyke et al., 1995), model-based actuator-control approaches have been proposed (Carrion and Spencer, 2007; Phillips and Spencer, 2012). However, applications of this method to MDOF structures, which include high frequency components, are still limited. To show the effectiveness of the model-based compensator for RTHS, further studies on MDOF structures should be implemented.

One of the structural control methods to show its effectiveness is smart outrigger damping systems employing semi-actively controlled MR dampers. The effectiveness of this method has been verified through numerical simulations (Chang et al., 2013), however experimental validations have not conducted yet.

Smart base isolation systems are another class of structural control systems that need further

experimental validation. They are composed of a base isolation system combined with semi-actively controlled MR dampers. Passive base isolation is one common type of structural control system, increasing the structure's flexibility to mitigate the effect of potentially dangerous seismic ground motions. However, large base displacements resulting from the increased flexibility of the passive isolation system can potentially exceed the allowable limit of structural designs under severe seismic excitations. Smart base isolation systems are a potential alternative means to address the drawbacks of passive and active isolation systems.

1.4 Overview of dissertation

This dissertation focuses on the development and experimental verification of semi-active control strategies for earthquake response reduction of buildings. To show that semi-active control is a structural control strategy comparable to active control or even better in a sense, theoretical and experimental studies are conducted. This section provides a description of the contents of each chapter of this dissertation.

Chapter 2 contains a detailed review of the previous studies related to this dissertation. First of all, various types of structural control strategies, especially outrigger damping and base isolation systems, are reviewed. Second, literature about hysteresis loops produced by structural control forces are introduced. Third, studies on RTHS with a focus on compensators are summarized. The issues and difficulties to overcome are addressed briefly, as well.

Chapter 3 provides technical background necessary for this dissertation that might be unfamiliar to researchers and engineers in civil engineering. The basics of modern control theory focusing on linear quadratic regulator (LQR), Kalman filter, and linear quadratic Gaussian (LQG) control theories are presented. Also, a servo-hydraulic model used in this dissertation is presented. Two types of model-based compensators for the dynamics of the servo-hydraulic system, such as bumpless feedforward and feedforward-feedback compensation, are developed as well.

Chapter 4 builds the MR damper model used for numerical simulation and describes the experimental setup for RTHS. The servo-hydraulic model is created and the two model-based compensators discussed in Chapter 3 are designed for RTHS, as well.

Chapter 5 investigates the nature of the hysteresis loops produced by active control forces. The

behavior of the hysteresis force-displacement loops produced by the LQR full-state feedback and the LQG-based acceleration feedback strategies is considered through numerical simulation studies on scaled one-story and three-story buildings. By comparing the results obtained from these two algorithms, the accuracy of the acceleration feedback is explored as well.

Chapter 6 describes algorithms for semi-active control strategies. First, the LQG-based clipped-optimal control, one of the widely accepted algorithms, is reviewed briefly. Then, new simple algorithms are presented, which do not require a structure model and enable versatile control force properties. Subsequently, hysteresis loops and seismic performance produced by these algorithms are compared through numerical simulation on a scaled three-story building model.

Chapter 7 verifies the effectiveness of the model-based RTHS compensator for a semi-actively controlled MR damper installed in a MDOF structure. For the MDOF structure, a high-rise building model with an outrigger damping system is employed which is analyzed numerically, while the MR damper is tested physically. The effect of the compensation errors in RTHS is examined. Also, seismic performance of the smart outrigger damping system employing MR dampers is explored.

Chapter 8 extends the application of the semi-active control framework into hybrid base isolation systems. The six-story base isolation building model in the Smart Structures Technology Laboratory (SSTL) at the University of Illinois at Urbana-Champaign is employed to verify the effectiveness of the smart base isolation system, in which MR dampers are installed to a passive base isolation system; this is shown through numerical simulation and RTHS. Finally, the seismic performance is discussed by comparing it with the active base isolation case.

Chapter 9 summarizes the research presented in this dissertation and provides recommendations and possible directions for future work on structural control technologies for seismic protection of buildings.

Chapter 2

Literature Review

This chapter provides a literature review of various types of structural control methods focusing on outrigger damping and base isolation systems. A brief review of the behavior of the force-displacement hysteresis loops produced by structural control strategies, as well as RTHS techniques, is also included.

2.1 Structural control

The purpose of the structural control in civil structures is to reduce structural vibration produced by external forces, such as earthquake and wind, by various means such as modifying stiffness, mass, damping, or shape. Structural control systems employed in civil engineering fall into four basic categories, i.e., passive, active, semi-active, and hybrid control. This section describes various structural control methods in each category studied by many researchers to this date, focusing on outrigger damping systems and base isolation systems.

Passive systems employ supplemental devices, which respond to the motion of the structure, to dissipate vibratory energy triggered by strong earthquakes and high winds in the structural system without external power sources. These systems are simple to understand and are accepted by the engineering community as a means for mitigating the effects of severe dynamic loadings. A variety of passive control mechanisms have been suggested by many researchers and engineers, including metallic yield dampers (Whittaker et al., 1991), viscous dampers (Constantinou et al., 1993; Reinhorn et al., 1995), tuned mass damper (Den Hartog, 1956; Villaverde, 1994), and base isolation (Kelly et al., 1987; Kelly, 1997). However, because these passive devices cannot adapt to structural changes and to varying usage patterns and loading conditions, there exist limitations.

Active control systems operate by using external energy supplied by actuators to impart forces

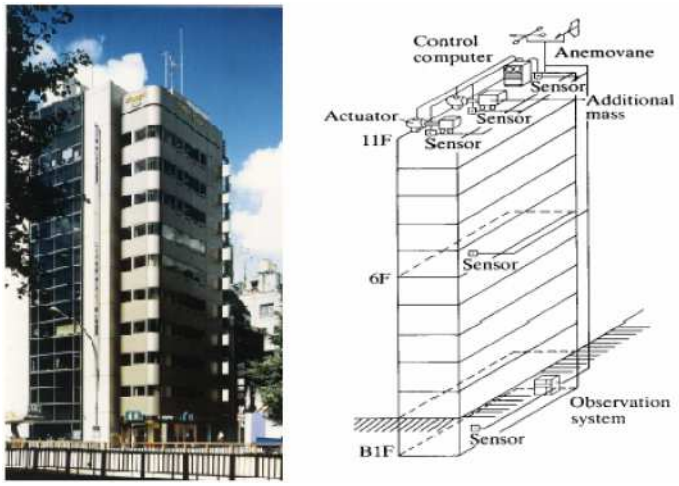

Figure 2.1: Kyobashi Center building with AMD installation

on the structure. The appropriate control action is determined based on measurements of the structural responses. The concept of the strategy in civil structures was first suggested by Yao (1972). Yang (1975) applied modern control theory to control the vibration of civil engineering structures under random loadings. Active control techniques are generally able to achieve higher control performance, as compared to passive control techniques (Soong and Costantinou, 1995).

The first full-scale application of an actively controlled building, the Kyobashi Center building (Figure 2.1), was achieved in 1989 in Japan by the Kajima Corporation (Kobori, 1990, 1996). Subsequently, active control strategies have been applied to many buildings and bridges, particularly in Asia. To date, many studies related to active control methods have been performed, and significant progress has been made toward protecting civil structures from severe environmental loads using these advances including the active bracing system (Reinhorn et al., 1989), the active tuned mass damper/driver (Abdel-Rohman and Leipholz, 1983; Chang and Soong, 1980) and the active aerodynamic appendage mechanism (Soong and Skinner, 1981; Abdel-Rohman, 1984).

Various control algorithms for active systems have been considered. Output feedback strategies using absolute acceleration measurements were developed by Spencer et al. (1994); Suhardjo et al. (1992). Control algorithms which account for the force and stroke limitations of control actuators have been investigated (Tamura et al., 1994). Nonlinear control algorithms have also been considered in an effort to increase the effectiveness of these active systems (Gattulli et al., 1994).

Other types of control algorithms that have been suggested for active control systems include fuzzy control (Chameau et al., 1991; Furuta et al., 1994), neural-based control (Casciati et al., 1993; Shoureshi et al., 1994), and sliding mode control (Yang et al., 1994).

Although many successful experiments and implementations proved the active control technology as a practical technique, some potential risks still exist in their real-time implementation; for example, the external energy injected by the active control devices might destabilize the system if the measurements of structural responses have been perturbed, the control laws are developed from a system model that misrepresents the true behavior of systems, the interaction between the structure and the control devices has been exclusively considered in the development of control laws, and so on. These details involved in the structural implementation of active control techniques continue to be an area of research interest.

Semi-active control devices have received a great deal of attention in recent years because they offer the adaptability of active control devices without requiring the associated large power sources. In fact, many can operate on battery power, which is critical during seismic events when the main power source to the structure may fail. According to presently accepted definitions, a semi-active control device is one that cannot increase the mechanical energy in the controlled system (i.e., including both the structure and the device), but has properties which can be dynamically varied to optimally reduce the responses of a structural system. Therefore, in contrast to active control devices, semi-active control devices do not have the potential to destabilize the structural system (in the bounded input/bounded output sense). Preliminary studies indicate that appropriately implemented semi-active systems perform significantly better than passive devices and have the potential to achieve, or even surpass, the performance of fully active systems, thus allowing for the possibility of effective response reduction during a wide array of dynamic loading conditions.

To date, various semi-active devices have been proposed. Variable-orifice dampers to control the motion of bridges experiencing seismic motion was first discussed by Feng and Shinozuka (1990). Variable damping is achieved by altering the resistance to flow of a conventional hydraulic fluid. Akbay and Aktan (1990, 1991) and Kannan et al. (1995) proposed variable friction devices which consists of a friction shaft which is rigidly connected to the structural bracing. The force at the frictional interface was adjusted to allow controlled slippage. Lou et al. (1994) proposed a semi-

active device based on a passive tuned sloshing damper (TSD), in which the length of the sloshing tank could be altered to change the properties of the device. Haroun et al. (1994) presented a semi-active device based on a tuned liquid column damper (TLCD) with a variable-orifice. Controllable fluids such as electrorheological (ER) fluids and magnetorheological (MR) fluids were discovered in the late 1940s (Winslow, 1947, 1949; Rabinow, 1948). Prior to MR fluid dampers, a number of ER fluid dampers were developed, modeled, and tested for civil engineering applications (Ehrgott and Masri, 1994; Gavin et al., 1994a,b; Gordaninejad et al., 1994; Makris et al., 1995, 1996; McClamroch and Gavin, 1995). The recently developed MR fluids appear to be an attractive alternative to ER fluids for use in controllable fluid dampers (Carlson, 1994; Carlson and Weiss, 1994; Carlson et al., 1996; Spencer et al., 1997; Dyke et al., 1996c).

Because all of these semi-active devices are intrinsically nonlinear, one of the main challenges is to develop control strategies that can optimally reduce structural responses. Various nonlinear control strategies have been developed to take advantage of the particular characteristics of the semi-active devices, including bang-bang control (McClamroch and Gavin, 1995), clipped-optimal control (Patten et al., 1994a,b; Dyke et al., 1996c), bistate control (Patten et al., 1994a,b), fuzzy control methods (Sun and Goto, 1994), and adaptive nonlinear control (Kamagata and Kobori, 1994), pseudo-negative stiffness algorithm (Iemura and Pradono, 2002, 2005), Lyapunov based control (Jansen and Dyke, 2000; Wang and Gordaninejad, 2002), sliding model control (Luo et al., 2000; Moon et al., 2003), backstepping control (Ikhouane et al., 1997; Luo et al., 2006), quantitative feedback theory (Zapateiro et al., 2008), and mixed H_2/H_∞ control (Yang et al., 2003, 2004b; Karimi et al., 2009).

Hybrid control strategies have been investigated by many researchers to exploit their potential to increase the overall reliability and efficiency of the controlled structure (Soong and Reinhorn, 1993). A hybrid control system is typically defined as one which employs a combination of two or more passive, active, or semi-active devices. Because multiple control devices are operating, hybrid control systems can alleviate some of the restrictions and limitations that exist when each system is acting alone. Thus, higher levels of performance may be achievable.

The hybrid mass damper (HMD) is the most common control device employed in full-scale civil engineering applications. The HMD is a combination of a tuned mass damper (TMD) and an active

control actuator. Tanida et al. (1991) developed an arch-shaped HMD that has been employed in a variety of applications, including bridge tower construction, building response reduction and ship roll stabilization. Another class of hybrid control systems which has been investigated by a number of researchers is found in the active or semi-active base isolation system (Inaudy and Kelly, 1990; Spencer et al., 2000), consisting of a passive base isolation system combined with actuators or semi-active devices to supplement the effects of the base isolation system. The details of these systems are discussed in the section 2.1.2.

2.1.1 Outrigger damping system

The number of high-rise buildings in urban areas around the world has dramatically increased in the past two decades, spurred by the development of new materials and technologies. However, this achievement also generates new problems; specifically, how these buildings can be protected from strong winds and severe earthquakes. To protect these tall buildings from such severe loadings, researchers and engineers have considered various passive structural control strategies, such as viscous dampers, viscoelastic dampers, and tuned mass dampers (Kareem et al., 1999; Spencer and Nagarajaiah, 2003). However, interstory drifts of a size that is sufficient to dissipate large amounts of input energy are generally not available in high-rise buildings. To solve this problem, numerous response amplification systems have been proposed, e.g. toggle braces (Constantinou et al., 2001), scissor-jacks (Sigaher and Constantinou, 2003), gear-type systems (Berton and Bolander, 2005), and the mega brace (Taylor, 2003).

Smith and Salim (1981); Charles (2006); Smith and Willford (2007) have proposed outrigger damping systems as an alternative response amplification method. This system employs vertical viscous dampers installed between outrigger walls and perimeter columns in a frame-core-tube structure to enhance structural dynamic performance. Willford et al. (2008) reported on a real-world implementation in a high-rise building in the Philippines. While successful, this approach is a passive system, which is unable to adapt to structural changes, varying usage patterns, and loading conditions. In the outrigger damping system, Wang et al. (2010) and Chang et al. (2013) presented numerical examples of semi-actively controlled outrigger systems employing MR dampers, achieving superior performance over the corresponding passive system.

2.1.2 Base isolation system

A base isolation system falls into passive systems. The concept of seismic base isolation is to isolate the structure and its contents from potentially dangerous ground motion, especially within the frequency range where the building is most affected by inserting low stiffness devices such as lead-rubber bearings, friction-pendulum bearings, or high damping rubber bearings between the structure and ground. The goal is to reduce interstory drifts and absolute accelerations to avoid damage by absorbing earthquake energy with these devices. However, the unacceptable base displacement responses in passive base isolation systems have been reported. Thus, the extra damping devices and controllable devices are encouraged to reduce the base displacements.

To achieve this demand, active base isolation, where a passive isolation system combined with active control devices, such as hydraulic actuators, has been proposed. The combination shares the advantages of the reductions in passive isolation systems, i.e., absolute floor accelerations, interstory drifts, and base shears, as well as the reductions in base displacements from the contributions of the actuators (Inaudy and Kelly, 1990).

Many numerical studies were conducted by applying different control algorithms such as the classic linear quadratic regulation (LQR) control algorithm and the Lyapunov control algorithm (Inaudy and Kelly, 1990; Pu and Kelly, 1991; Loh and Chao, 1996; Yang et al., 1992; Loh and Ma, 1996; Fur et al., 1996). Different active control devices, such as active tuned mass dampers or active vibration absorbers (different from hydraulic actuators), were also considered (Loh and Chao, 1996; Lee-Glauser et al., 1997). Some researchers focused on the numerical analysis of different isolation bearings, such as rubber bearings or sliding bearings (Yang et al., 1995; Feng, 1993).

The effectiveness of active base isolation systems was verified experimentally as well. Yang et al. (1996) employed the sliding mode control algorithm to control a sliding base-isolated, three-story building through shake table testing. Riley et al. (1998) developed a nonlinear controller to experimentally implement a hydraulic actuator for controlling a three-story, base-isolated building. Nishimura and Kojima (1998) considered a building-like structure incorporated with an isolator and an actuator for verification of active base isolation. Although these experiments only considered the in-plane motions of structures under unidirectional excitations, these provided evidence of the applicability and feasibility of active base isolation systems. Chang and Spencer (2012) developed

active isolation strategies for multi-story buildings subjected to bi-directional earthquake loadings and verified the efficacy experimentally.

Smart base isolation is another class of hybrid base isolation system (Spencer et al., 2000; Yoshioka et al., 2002). Smart base isolation is composed of a passive base isolation system combined with control structures with semi-active control devices, e.g., variable orifice dampers (Wongprasert and Symans, 2005); semi-active independently variable dampers (SAIVD) (Nagarajaiah and Narasimhan, 2007), electrorheological dampers (Makris, 1997); and magnetorheological (MR) dampers (Ramallo et al., 1999, 2002; Nagarajaiah and Narasimhan, 2006; Narasimhan et al., 2008; Wang and Dyke, 2013). This combination shares the advantages of semi-active control such as adaptivity to excitations, low-power requirements, and stability, while still performing comparably to actively controlled isolation systems.

Many numerical studies of smart base isolation systems employing MR dampers have been investigated. Ramallo et al. (2002) studied an isolated building with laminated rubber bearings. The results demonstrated acceptable control performance in the reductions of the accelerations and displacements. Nagarajaiah and Narasimhan (2006) shows the effectiveness of a three-dimensional smart base-isolated building with linear and frictional isolation system. Narasimhan et al. (2008) considered the nonlinearities in lead-rubber-bearing (LRB). Chang et al. (2008) applied a scheduled control strategy to a nonlinear control problem of a smart base-isolated building. Wang and Dyke (2013) presented the advantages of applying a modal linear quadratic Gaussian (LQG) approach for base isolation systems. These numerical studies have demonstrated the applicability of smart base isolation systems employing MR dampers.

To show the efficacy of smart base isolation systems employing MR dampers, some experimental studies using a shaking table have been conducted. Yoshioka et al. (2002) verified a smart base isolation system employing laminated rubber bearings of a single-story small-scale building. Sahasrabudhe and Nagarajaiah (2005) applied the Lyapunov-based control algorithm to a scaled two-story smart base isolation system. Lin et al. (2007) employed fuzzy logic control by applying smart base isolation with four high damping rubber bearings and a 300 kN MR damper. Moreover, Shook et al. (2007) considered a single-story building installed with bi-directional sliding bearings and planar MR dampers (e.g., MR dampers were placed in two directions) under bi-directional

excitations. In these studies, most structures are scaled and may misrepresent the performance of controlled structures.

These results proved that the combination of this smart base isolation system can effectively reduce the base displacements as well as interstory drifts. These numerical studies have demonstrated the applicability of semi-active base isolation systems, although a simulation might not sufficiently represent the true control performance in a practical implementation. Therefore, the experimental studies of these systems are needed. Also, since most numerical studies were investigated under unidirectional excitations, the efficacy of multi-axial semi-active base isolation should be shown.

2.2 Hysteresis loops produced by structural control force

In the field of earthquake engineering, energy absorbing-devices are added to structures to dissipate input energy effectively. The input energy absorption capability of these devices plays a key role in mitigating earthquake damage. Therefore, 1) elucidating the relationship between the property of control forces and the structural responses and 2) developing structural control devices and appropriate algorithms for them which enable intended control forces are desirable.

The effectiveness of negative stiffness was found in skyhook control proposed by Karnopp et al. (1974). In the ideal condition of the skyhook system, a structure is connected to a virtual fixed point in the sky through a dashpot. In practical use, the skyhook damper is realized by active or semi-active controllers.

The negative stiffness produced by active control force using linear quadratic regulator (LQR) was investigated by Iemura and Pradono (2005) on a cable-stayed bridge model. They showed that the LQR control algorithm produced hysteresis loops with negative stiffness and reduced the displacements and base shear to earthquake excitations.

Iemura and Pradono (2009) showed that the semi-actively controlled skyhook damper produces a damping force proportional to the absolute velocity of the mass, and negative stiffness appears in the hysteresis loops. Iemura and Pradono (2002, 2005) proposed an algorithm for semi-actively controlled viscous dampers to produce negative stiffness and showed the seismic performance on a cable-stayed bridge. The possibility of producing negative stiffness by MR dampers were shown in Iemura et al. (2006); Weber and Boston (2011); Wu et al. (2013) as well.

Recently, passive methods to produce negative stiffness damping have been reported as well. Negative stiffness friction damper is proposed by Iemura and Pradono (2009); Iemura et al. (2008, 2010), which is quite similar to an ordinary friction pendulum support, but the inverted curve is introduced. Since the vertical weight induced on the unstable convex slide plate accelerates the horizontal deformation due to the gravitational effect, the force is negatively proportional to the deformation. The dynamic behavior of the proposed negative stiffness damper was assessed by using the large-scale shaking table at the Disaster Prevention Research Institute (DPRI) of Kyoto University, Japan. An adaptive negative stiffness device is proposed and developed by Nagarajaiah et al. (2010). In this device, adaptive negative stiffness behavior is realized by possessing predesigned variations of stiffness as a function of structural displacement amplitude. The effectiveness of the proposed mechanism in elastic and inelastic structural systems was demonstrated through simulation for periodic and random input ground motions. Viti et al. (2006) produced negative stiffness passively through a new retrofitting procedure which weakened the strength of the structure and added supplemental damping devices. The proposed method reduced both accelerations and ductility demand on a five-story hospital building.

2.3 Semi-active control algorithms

Semi-active control has been proposed as an alternative method for active control (Housner et al., 1997). Like active control, semi-active control offers the adaptability to structural changes and to various usage patterns and loading conditions. Moreover, semi-active control devices such as the variable-orifice damper, variable-friction damper, electrorheological (ER) damper, and magnetorheological (MR) damper require little power, because the energy is used to modify only the device's properties (e.g., stiffness and damping). The effectiveness of semi-active control has been shown through numerous numerical simulations and experiments (Dyke et al., 1996d,c; Spencer et al., 1997; McClamroch et al., 1994; McClamroch and Gavin, 1995; Leitmann, 1994; Jansen and Dyke, 2000; Wang and Gordaninejad, 2002; Luo et al., 2000, 2003; Moon et al., 2003; Ikhouane et al., 1997; Zapateiro et al., 2009; Luo et al., 2004; Zapateiro et al., 2008).

Various algorithms have been proposed for semi-active control devices to mitigate seismic damage; e.g., linear quadratic Gaussian (LQG)-based clipped-optimal control (Dyke et al., 1996d,c;

Figure 2.2: E-Defense, Miki, Hyogo, Japan

Spencer et al., 1997), bang-bang control McClamroch et al. (1994); McClamroch and Gavin (1995), control based on Lyapunov stability theory (Leitmann, 1994; Jansen and Dyke, 2000; Wang and Gordaninejad, 2002), sliding mode control (Luo et al., 2000, 2003; Moon et al., 2003), backstepping control (Ikhouane et al., 1997; Zapateiro et al., 2009), and quantitative feedback theory (QFT) (Luo et al., 2004; Zapateiro et al., 2008). To apply these algorithms for real civil structures, a relatively accurate model is needed. However, obtaining accurate parameter values for full-scale structures may not be practical. Moreover, the structure may change with time, resulting in the need to continuously update the model. Thus, developing effective simple algorithms which do not require the structural model or a large number of sensors is desirable for practical use.

2.4 Real-time hybrid simulation

Shaking table testing provides a direct approach to evaluate the dynamic structural response of civil structures subjected to earthquake loads. However, shaking table studies at large scale have been limited so far. This is because, even if large facilities such as the E-Defense table in Japan (Figure 2.2) or the shaking table at the University of California at San Diego are available, tests for large civil structures such as high-rise buildings are impractical due to limitations on the size, payload capacity, and cost.

As an alternative method, hybrid simulation was first proposed by Hakuno et al. (1969) to

test a single degree of freedom model subjected to seismic loads. The equations of motion were solved using an analog computer while an electromagnetic actuator was used to excites the physical specimen in real-time. Hardware limitations also compromised the accuracy of the experiment by adding a phase lag that was recognized but uncompensated. Hybrid simulation was established in its current recognizable form through the introduction of discrete time systems and digital controllers (Takanashi et al., 1974, 1975). Employing a digital controller to solve the equations of motion, the real-time loading constraint could be relaxed to a ramp and hold procedure over an extended time scale. Typical quasi-static testing equipment could be used while numerical integration could be performed at a slower rate appropriate for the computers.

As rate-dependent structural control devices such as base isolation bearings and fluid dampers have been developed, the demand of expanding hybrid simulation to include a more rigorously verified real-time framework has been increased. The first modern real-time hybrid simulation using digital computers was conducted by Nakashima et al. (1992) on a SDOF system. In this study, a digital servo-mechanism between the computer performing the numerical integration and the servo-controller was introduced to seek accurate velocity control. This digital servomechanism operated as a ramp generator between numerical integration time steps and also included a feedback loop to improve the displacement performance at substeps of the numerical integration.

Horiuchi et al. (1996) studied the effect of time delay on RTHS in detail and proposed the polynomial extrapolation delay compensation scheme. In this study, a super real-time controller (Umekita et al., 1995) using parallel computing and a special programming language was employed to calculate the equations motions within the required time step. Separating the tasks of signal generation and response analysis was proposed by Nakashima and Masaoka (1999), allowing RTHS to be performed on commercially available processors. Many studies have been reported to enhance the performance of RTHS since these pioneering studies.

Carrion and Spencer (2007) presented another approach for time delay/lag compensation using model-based response prediction. Verification experiments showed that model-based compensation allowed testing systems with natural frequencies as high as 13 Hz for linear response and 15 Hz for inelastic response. Experimental results using a structure with the MR damper verified that the approach and testing system presented were capable of testing rate-dependent devices. Phillips and

Spencer (2012) improved the model-based actuator control by combining a feedback controller with a feedforward controller. The effectiveness of the proposed method was shown on a single-actuator system and multi-actuator system.

2.5 Summary

The references on the development of various types of structural control strategies to reduce damage on buildings from earthquakes are provided in this chapter. This chapter reviews the literature on hysteresis loops produced by control forces and RTHS method to verify the efficacies of these methods as well. Huge efforts have been made by many researchers and engineers to improve structural control technologies in buildings. However, further development is still required to realize their full potential.

Chapter 3

Background

Some background in modern control theory is provided in this chapter to lay the groundwork for subsequent active and semi-active controller designs. A linearized model of the servo-hydraulic actuator system, time delays and lags of real-time hybrid simulation (RTHS), and model-based compensations for RTHS are also described in this chapter.

3.1 Modern control theory

Whereas classical control theory focuses on frequency domain analysis employing transfer function approaches, modern control theory is based on time domain analysis expressed by first-order differential equations utilizing state space representation. This section presents necessary basic knowledge on liner time-invariant system (LTI) to understand this dissertation.

3.1.1 LTI state space model

If the dynamic systems are LTI, the state-space model can be written as

$$\dot{\mathbf{x}} = \mathbf{A}\mathbf{x} + \mathbf{B}\mathbf{u} \tag{3.1}$$

$$\mathbf{y} = \mathbf{C}\mathbf{x} + \mathbf{D}\mathbf{u} \tag{3.2}$$

where $\mathbf{x}$ is the state space vector in $\mathbb{R}^n$, $\mathbf{y}$ and $\mathbf{u}$ are the output and input of the system evolving in $\mathbb{R}^p$ and $\mathbb{R}^m$, respectively, and $\mathbf{A}$, $\mathbf{B}$, $\mathbf{C}$, $\mathbf{D}$ are matrices of appropriate dimensions. The block diagram of Eqs. (3.1) and (3.2) is shown in Figure 3.1. If both the input and the output are scalar, then the system is referred as single input-single output (SISO); if either a control or output are of dimension higher than one, then the system is multi input-multi output (MIMO).

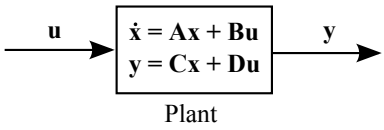

Figure 3.1: LTI system

Assume that an initial condition $\mathbf{x}_0$ is given at $t = 0$. Taking Laplace transforms in Eqs. (3.1) and (3.2) gives the transformed equations:

$$s\mathbf{X} - \mathbf{x}_0 = \mathbf{A}\mathbf{X}(s) + \mathbf{B}\mathbf{U}(s) \tag{3.3}$$

$$\mathbf{Y}(s) = \mathbf{C}\mathbf{X}(s) + \mathbf{D}\mathbf{U}(s) \tag{3.4}$$

Solving for $\mathbf{X}(s)$ gives

$$\mathbf{X}(s) = \mathbf{\Phi}(s)\mathbf{x}_0 + \mathbf{\Phi}(s)\mathbf{B}\mathbf{U}(s) \tag{3.5}$$

where

$$\mathbf{\Phi}(s) = [s\mathbf{I} - \mathbf{A}]^{-1}. \tag{3.6}$$

This is converted into the time domain by taking inverse Laplace transforms. Define

$$\boldsymbol{\phi}(t) = \mathcal{L}^{-1}\{\mathbf{\Phi}(s)\} = \mathcal{L}^{-1}\{[s\mathbf{I} - \mathbf{A}]^{-1}\} \tag{3.7}$$

where the inverse Laplace transform of $\mathbf{\Phi}(s)$ is calculated term by term. Using convolution, Eq. (3.5) can be inverted to give

$$\mathbf{x}(t) = \boldsymbol{\phi}(t)\mathbf{x}_0 + \int_0^t \boldsymbol{\phi}(t-\tau)\mathbf{B}\mathbf{u}(\tau)d\tau \tag{3.8}$$

As for the output, assuming for simplicity that $\mathbf{x}_0 = 0$ and substituting Eq. (3.5) into Eq. (3.4) gives

$$\mathbf{Y}(s) = \mathbf{C}\mathbf{\Phi}(s)\mathbf{B}\mathbf{U}(s) + \mathbf{D}\mathbf{U}(s) \tag{3.9}$$

Therefore the transfer function is a $p \times m$ matrix-valued function of s which takes the form

$$\mathbf{G}(s) = \mathbf{C}\mathbf{\Phi}(s)\mathbf{B} + \mathbf{D} \tag{3.10}$$

Taking the inverse Laplace transform of the transfer function yields the impulse response

$$\mathbf{g}(t) = \mathcal{L}^{-1}\{\mathbf{G}(s)\} = \mathbf{C}\boldsymbol{\phi}(t)\mathbf{B} + \mathbf{D}\delta(t) \tag{3.11}$$

where $\delta(t)$ is Dirac delta function defined as

$$\delta(t) = \begin{cases} +\infty & t = 0 \\ 0 & t \neq 0 \end{cases} \tag{3.12}$$

$$\int_{-\infty}^{\infty} \delta(t)dt = 1 \tag{3.13}$$

Thus, the output is given for zero initial conditions by

$$\mathbf{y}(t) = \mathbf{g} * \mathbf{u}(t) = \int_0^t \mathbf{g}(t-\tau)\mathbf{u}(\tau)d\tau = \int_0^t \mathbf{C}\boldsymbol{\phi}(t-\tau)\mathbf{B}\mathbf{u}(\tau)d\tau + \mathbf{D}\mathbf{u}(t) \tag{3.14}$$

where $*$ represents convolution integral.

3.1.2 State feedback

Assuming that all of the states are available, the simplest controller is given by the state feedback control law

$$\mathbf{u} = -\mathbf{K}\mathbf{x} \tag{3.15}$$

where $\mathbf{K}$ is a $n \times m$ matrix. Substituting this input $\mathbf{u}$ into Eq. (3.1) gives rise to the closed-loop system written as

$$\dot{\mathbf{x}} = \mathbf{A}\mathbf{x} - \mathbf{B}\mathbf{K}\mathbf{x} = (\mathbf{A} - \mathbf{B}\mathbf{K})\mathbf{x} \tag{3.16}$$

The block diagram of this closed-loop system is shown in Figure 3.2.

To determine whether or not $\mathbf{x}(t) \to \mathbf{0}$ as $t \to \infty$ from any initial condition, the eigenvalues of

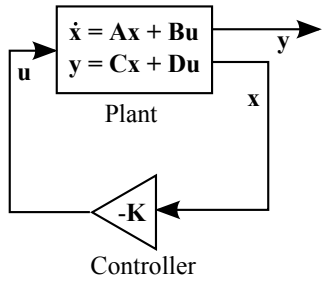

Figure 3.2: State feedback

the closed-loop matrix $(\mathbf{A} - \mathbf{BK})$ must be considered. If and only if $(\mathbf{A}, \mathbf{B})$ is a controllable pair, the eigenvalues of $(\mathbf{A} - \mathbf{BK})$ can be placed arbitrarily, respecting complex conjugate constraints.

3.1.3 Observers

The state feedback approach can be generalized to the situation where only partial measurements of the state are available. In this case, the state, $\mathbf{x}$, should be estimated from the input-output measurements online.

To mimic the behavior of the system given by Eq. (3.1), the estimated system given as

$$\dot{\hat{\mathbf{x}}} = \mathbf{A}\hat{\mathbf{x}} + \mathbf{Bu} \tag{3.17}$$

should be considered, where $\hat{\mathbf{x}}$ is the estimated state for the state $\mathbf{x}$. Defining the error between the real state and the estimated state as

$$\mathbf{e} = \mathbf{x} - \hat{\mathbf{x}} \tag{3.18}$$

from Eqs. (3.1) and (3.17), the error equation is given by

$$\begin{aligned} \dot{\mathbf{e}} &= \dot{\mathbf{x}} - \dot{\hat{\mathbf{x}}} \\ &= \mathbf{Ax} + \mathbf{Bu} - \mathbf{A}\hat{\mathbf{x}} - \mathbf{Bu} \\ &= \mathbf{Ae} \end{aligned} \tag{3.19}$$

Thus

$$\mathbf{e} = e^{\mathbf{A}t}\mathbf{e}(0) \tag{3.20}$$

However, if the open-loop system is unstable, the error will not converge to zero and may diverge to infinity for some initial conditions.

Hence, to control the error, the observer considered is defined as

$$\dot{\hat{\mathbf{x}}} = \mathbf{A}\hat{\mathbf{x}} + \mathbf{B}\mathbf{u} + \mathbf{L}(\mathbf{y} - \hat{\mathbf{y}}), \tag{3.21}$$

where

$$\hat{\mathbf{y}} = \mathbf{C}\hat{\mathbf{x}} + \mathbf{D}\mathbf{u} \tag{3.22}$$

For any fixed $n \times p$ matrix $\mathbf{L}$, from Eqs. (3.1) and (3.21), the error will be

$$\begin{aligned} \dot{\mathbf{e}} &= \dot{\mathbf{x}} - \dot{\hat{\mathbf{x}}} \\ &= \mathbf{A}\mathbf{x} + \mathbf{B}\mathbf{u} - \mathbf{A}\hat{\mathbf{x}} - \mathbf{B}\mathbf{u} - \mathbf{L}(\mathbf{C}\mathbf{x} - \mathbf{C}\hat{\mathbf{x}}) \\ &= (\mathbf{A} - \mathbf{L}\mathbf{C})\mathbf{e} \end{aligned} \tag{3.23}$$

Thus

$$\mathbf{e} = e^{(\mathbf{A}-\mathbf{L}\mathbf{C})t}\mathbf{e}(0) \tag{3.24}$$

To ensure that $\mathbf{e} \to \mathbf{0}$ as $t \to \infty$, the eigenvalues of the matrix $(\mathbf{A} - \mathbf{L}\mathbf{C})$ must be computed. Since

$$\text{eig}(\mathbf{A} - \mathbf{L}\mathbf{C}) = \text{eig}(\mathbf{A}^* - \mathbf{C}^*\mathbf{L}^*) \tag{3.25}$$

the eigenvalues of $(\mathbf{A} - \mathbf{L}\mathbf{C})$ can be placed arbitrarily, provided that the matrix pair $(\mathbf{A}^*, \mathbf{C}^*)$ is controllable. Based on duality, this is simply observability of the pair $(\mathbf{A}, \mathbf{C})$. Thus, the observer poles can be placed arbitrarily if and only if $(\mathbf{A}, \mathbf{C})$ is observable.

The state space form of the observer is given by

$$\dot{\hat{\mathbf{x}}} = \mathbf{A}_\text{O}\hat{\mathbf{x}} + \mathbf{B}_\text{O}\begin{bmatrix} u \\ y \end{bmatrix} \tag{3.26}$$

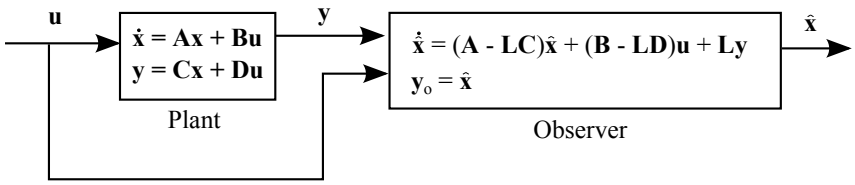

Figure 3.3: Observer

$$\mathbf{y}_{\mathrm{O}} = \mathbf{C}_{\mathrm{O}}\hat{\mathbf{x}} + \mathbf{D}_{\mathrm{O}} \begin{bmatrix} u \\ y \end{bmatrix} \tag{3.27}$$

where

$$\mathbf{A}_{\mathrm{O}} = (\mathbf{A} - \mathbf{LC}) \tag{3.28}$$

$$\mathbf{B}_{\mathrm{O}} = \begin{bmatrix} \mathbf{B} - \mathbf{LD} & \mathbf{L} \end{bmatrix} \tag{3.29}$$

$$\mathbf{C}_{\mathrm{O}} = \mathbf{I} \tag{3.30}$$

$$\mathbf{D}_{\mathrm{O}} = \mathbf{0} \tag{3.31}$$

The block diagram of the observer is depicted in Figure 3.3.

3.1.4 Linear quadratic regulator (LQR)

One of the effective and widely used methods for determining the state feedback gain matrix $\mathbf{K}$ in Eq. (3.15) is LQR algorithm, which minimizes a defined cost function. For a continuous time linear system described by Eq. (3.1), assuming that $\mathbf{x}(t) \to \mathbf{0}$ as $t \to \infty$, the cost function is defined as

$$J(\mathbf{u}) = \int_0^\infty (\mathbf{x}^T\mathbf{Q}\mathbf{x} + \mathbf{u}^T\mathbf{R}\mathbf{u})dt \tag{3.32}$$

where $\mathbf{Q}$ is positive semidefinite ($\mathbf{Q} \succeq 0$) and $\mathbf{R}$ is strictly positive definite ($\mathbf{R} \succ 0$). This is called the *infinite-horizon problem.*

The optimal cost $J_{\min}$ which is the minimum value of J will be

$$J_{\min}(\mathbf{x}_0) = \mathbf{x}_0^T\mathbf{P}_{\mathrm{LQR}}\mathbf{x}_0 \tag{3.33}$$

and the feedback control law $\mathbf{u}$ that minimizes the value of J is given by

$$\mathbf{u} = -\mathbf{K}_{\mathrm{LQR}}\mathbf{x} \tag{3.34}$$

where $\mathbf{K}_{\mathrm{LQR}}$ is given by

$$\mathbf{K}_{\mathrm{LQR}} = \mathbf{R}^{-1}\mathbf{B}^T\mathbf{P}_{\mathrm{LQR}} \tag{3.35}$$

and $\mathbf{P}$ is found by solving the continuous time algebraic Riccati equation (ARE) (Liberzon, 2012)

$$\mathbf{A}^T\mathbf{P}_{\mathrm{LQR}} + \mathbf{P}_{\mathrm{LQR}}\mathbf{A} - \mathbf{P}_{\mathrm{LQR}}\mathbf{B}\mathbf{R}^{-1}\mathbf{B}^T\mathbf{P}_{\mathrm{LQR}} + \mathbf{Q} = \mathbf{0} \tag{3.36}$$

3.1.5 Kalman filter

The Kalman filter (Kalman, 1960), also known as linear quadratic estimation (LQE), is an algorithm to design an optimal observer by measuring the available data. The observer designed by the Kalman filter minimizes the spread of the estimate-error probability density in the process. The Kalman filter was first introduced for discrete time processes by Kalman (1960), and later extended for the continuous time version by Kalman and Bucy (1961), which is called the *Kalman-Bucy filter*. In this subsection, the derivation of the Kalman-Bucy filter for the time-invariant system case is presented.

Consider the linear time-invariant dynamic system expressed as

$$\dot{\mathbf{x}} = \mathbf{A}\mathbf{x} + \mathbf{B}\mathbf{u} + \mathbf{E}\mathbf{w} \tag{3.37}$$

$$\mathbf{y} = \mathbf{C}\mathbf{x} + \mathbf{D}\mathbf{u} + \mathbf{v} \tag{3.38}$$

Suppose that the expected values of the initial state and covariance are

$$E[\mathbf{x}(0)] = \hat{\mathbf{x}}_0 \tag{3.39}$$

$$E\{[\mathbf{x}(0) - \hat{\mathbf{x}}_0][\mathbf{x}(0) - \hat{\mathbf{x}}_0]^T\} = \mathbf{P}_{\mathrm{Kal},0} \tag{3.40}$$

The disturbance input, $\mathbf{w}$, is a white, zero-mean Gaussian random process such that

$$E[\mathbf{w}(t)] = \mathbf{0} \tag{3.41}$$

$$E[\mathbf{w}(t)\mathbf{w}^T(t)] = \mathbf{W}(t)\delta(t-\tau) \tag{3.42}$$

which is specified by its spectral density matrix $\mathbf{W}(t)$, and the measurement error, $\mathbf{v}$, is a white, zero-mean Gaussian random process such that

$$E[\mathbf{v}(t)] = \mathbf{0} \tag{3.43}$$

$$E[\mathbf{v}(t)\mathbf{v}^T(t)] = \mathbf{V}(t)\delta(t-\tau) \tag{3.44}$$

with the measurement uncertainty expressed by its spectral density matrix $\mathbf{V}(t)$. It is assumed that the disturbance input and measurement are uncorrelated.

In the Kalman-Busy filter, the optimal values of $\hat{\mathbf{x}}(t)$ and the covariance matrix, $\mathbf{P}_{\text{Kal}}$, can be computed as follows. First, the covariance estimate, $\mathbf{P}_{\text{Kal}}$, can be calculated by solving the following ARE:

$$\mathbf{A}\mathbf{P}_{\text{Kal}} + \mathbf{P}_{\text{Kal}}\mathbf{A}^T + \mathbf{E}\mathbf{W}\mathbf{E}^T - \mathbf{P}_{\text{Kal}}\mathbf{C}^T\mathbf{V}^{-1}\mathbf{C}\mathbf{P}_{\text{Kal}} = \mathbf{0} \tag{3.45}$$

The optimal filter gain equation is given using the obtained $\mathbf{P}_{\text{Kal}}$ by

$$\mathbf{L}_{\text{Kal}} = \mathbf{P}_{\text{Kal}}\mathbf{C}^T\mathbf{V}^{-1} \tag{3.46}$$

Then, the state estimate is found by integrating

$$\dot{\hat{\mathbf{x}}} = \mathbf{A}\hat{\mathbf{x}} + \mathbf{B}\mathbf{u} + \mathbf{L}_{\text{Kal}}(\mathbf{y} - \mathbf{C}\hat{\mathbf{x}} - \mathbf{D}\mathbf{u}) \tag{3.47}$$

$$\hat{\mathbf{x}}(0) = \mathbf{x}_0 \tag{3.48}$$

Note that the Kalman-Bucy filter problem is the mathematical dual of the LQR problem.

3.1.6 Linear quadratic Gaussian (LQG)

To implement the LQR control, the full state information must be available. So, for the case of the absence of the complete state data or the presence of uncertainties, the LQG controller can be employed instead.

The LQG controller is simply the combination of the Kalman filter with the LQR controller. Consider the linear time-invariant dynamic system given by Eqs. (3.37) and (3.38). Given this system, the cost function of the LQG problem is defined as

$$J(\mathbf{u}) = \lim_{\tau \to \infty} \mathrm{E}\left[\int_0^{\tau} (\mathbf{x}^T \mathbf{Q} \mathbf{x} + \mathbf{u}^T \mathbf{R} \mathbf{u}) dt\right] \tag{3.49}$$

where $\mathbf{Q}$ is positive semidefinite ($\mathbf{Q} \succeq 0$), and $\mathbf{R}$ is positive definite ($\mathbf{R} \succ 0$) as in the case of the LQR. The objective is to find the control input $\mathbf{u}(t)$ which depends on the past measurements $\mathbf{y}(t'), 0 \leq t' < t$.

The LQG controller that solves the LQG control problem is formulated by the following equations:

$$\dot{\hat{\mathbf{x}}} = \mathbf{A}\hat{\mathbf{x}} + \mathbf{B}\mathbf{u} + \mathbf{L}_{\mathrm{LQG}}(\mathbf{y} - \mathbf{C}\hat{\mathbf{x}} - \mathbf{D}\mathbf{u}) \tag{3.50}$$

$$\mathbf{u} = -\mathbf{K}_{\mathrm{LQG}}\hat{\mathbf{x}} \tag{3.51}$$

Because the LQG controller can separate into the Kalman filter and the LQR problems, the matrix gains $\mathbf{L}_{\mathrm{LQG}}$ and $\mathbf{K}_{\mathrm{LQG}}$ can be designed independently by solving the AREs given by Eqs. (3.36) and (3.45), respectively (Stengel, 1986). Hence, by Eqs. (3.35) and (3.46), each gain is given as

$$\mathbf{L}_{\mathrm{LQG}} = \mathbf{L}_{\mathrm{Kal}} = \mathbf{R}^{-1}\mathbf{B}^T\mathbf{P}_{\mathrm{LQR}} \tag{3.52}$$

$$\mathbf{K}_{\mathrm{LQG}} = \mathbf{K}_{\mathrm{LQR}} = \mathbf{P}_{\mathrm{Kal}}\mathbf{C}^T\mathbf{V}^{-1} \tag{3.53}$$

Therefore the state-space form of the LQG controller can be expressed as

$$\dot{\hat{\mathbf{x}}} = \mathbf{A}_{\mathrm{LQG}}\hat{\mathbf{x}} + \mathbf{B}_{\mathrm{LQG}}\mathbf{y} \tag{3.54}$$

$$\mathbf{y}_{\mathrm{LQG}} = \mathbf{C}_{\mathrm{LQG}}\hat{\mathbf{x}} + \mathbf{D}_{\mathrm{LQG}}\mathbf{y} \tag{3.55}$$

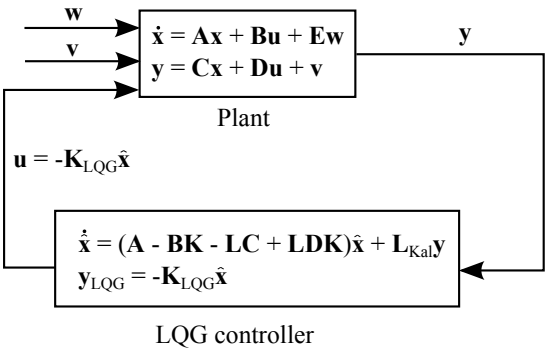

Figure 3.4: LQG controller

where

$$\mathbf{A}_{\mathrm{LQG}} = \mathbf{A} - \mathbf{B}\mathbf{K}_{\mathrm{LQR}} - \mathbf{L}_{\mathrm{Kal}}\mathbf{C} + \mathbf{L}_{\mathrm{Kal}}\mathbf{D}\mathbf{K}_{\mathrm{LQR}} \tag{3.56}$$

$$\mathbf{B}_{\mathrm{LQG}} = \mathbf{L}_{\mathrm{Kal}} \tag{3.57}$$

$$\mathbf{C}_{\mathrm{LQG}} = -\mathbf{K}_{\mathrm{LQR}} \tag{3.58}$$

$$\mathbf{D}_{\mathrm{LQG}} = \mathbf{0} \tag{3.59}$$

The block diagram of the LQG controller is depicted in Figure 3.4.

3.2 Servo-hydraulic system model

This section presents a model of a servo-hydraulic system.The servo-hydraulic system is an assemblage of mechanical and electrical components used to excite a specimen, typically to a prescribed displacement as shown in Figure 3.5. Individual component models can be assembled to create a dynamic model for the complete servo-hydraulic system. Components with nonlinear behavior will be represented by linear models with respect to an operating point such that the complete system model is also linear. The resulting linear model allows use of techniques such as Laplace transforms and frequency domain methods to understand the system behavior.

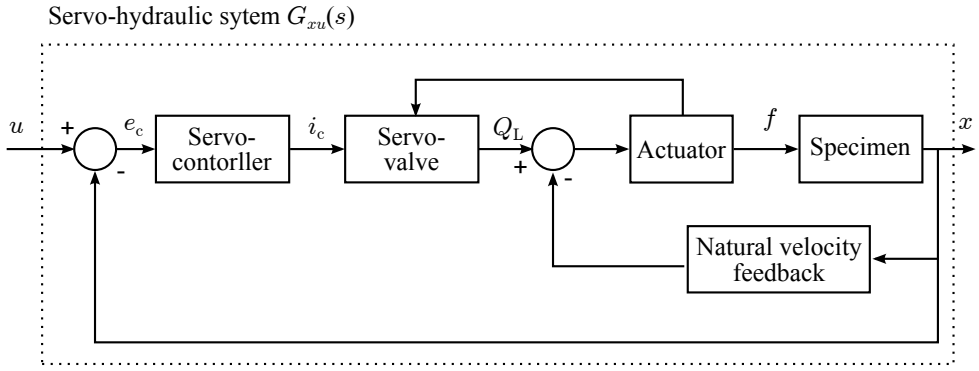

Figure 3.5: Block diagram model of the servo-hydraulic system

3.2.1 Valve flow

The flow characteristics of the servo-valve are given by (Merritt, 1967)

$$Q_{\mathrm{L}} = C_{\mathrm{d}} w x_{\mathrm{v}} \sqrt{\frac{1}{\rho}\left(P_{\mathrm{s}} - \frac{x_{\mathrm{v}}}{|x_{\mathrm{v}}|} p_{\mathrm{L}}\right)} \tag{3.60}$$

where p_{L} is the pressure drop across the load, Q_{L} is the controlled flow through the load, x_{v} is the valve displacement from the neutral position, P_{s} is the system supply pressure, w is the opening ore area gradient of the valve orifices, C_{d} is the coefficient of discharge of the valve orifices, and ρ is the fluid density. The nonlinear flow equation can be linearized with respect to an operating point (i.e., $Q_{\mathrm{L}} = p_{\mathrm{L}} = x_{\mathrm{v}} = 0$) as :

$$Q_{\mathrm{L}} = K'_{\mathrm{q}} x_{\mathrm{v}} - K'_{\mathrm{c}} p_{\mathrm{L}} \tag{3.61}$$

where K'_{q} is the valve flow gain, K'_{c} is the valve flow-pressure gain.

3.2.2 Actuator

The fundamental equations that govern the behavior of a hydraulic actuator are the continuity equation and the equilibrium or force balance. The continuity equation is given by the following relationship (Merritt, 1967)

$$Q_{\mathrm{L}} = A_{\mathrm{act}} \dot{x} + C_1 p_{\mathrm{L}} + \frac{V_{\mathrm{t}}}{4\beta_{\mathrm{e}}} \dot{p}_{\mathrm{L}} \tag{3.62}$$

where C_1 is the total leakage coefficient of the actuator piston, V_t is the total volume of fluid under compression in both actuator chambers, β_e is the effective bulk models of the system, and A_{act} is the area of the actuator piston. Laplace transform of Eq. (3.62) can be written as

$$\frac{p_L(s)}{Q_L - A_{act}x(s)s} = \frac{1}{C_1 + \dfrac{V_t}{4\beta_e}s} \tag{3.63}$$

The force generated by the actuator piston, f, is given by

$$f = A_{act}p_L \tag{3.64}$$

3.2.3 Specimen

The specimen is excited by the actuator. The equation of motion of the specimen (SDOF) is given by

$$m_E\ddot{x} + c_E\dot{x} + k_Ex + F_s = f \tag{3.65}$$

where m_E, c_E, and k_E represent the mass, damping, and stiffness values of the specimen and attachments (which may include the piston rod, load cell, clevis, etc.). F_s represents the force on the piston due to seal friction, x represents the displacement of the specimen, and a dot indicates differentiation with respect to time. Low-friction seals are used in modern actuators; therefore, the frictions force can be viewed as negligible. Thus, the equation of motion can be rewritten as the following transfer function

$$G_{xf}(s) = \frac{1}{m_Es^2 + c_Es + k_E} \tag{3.66}$$

3.2.4 Servo-controller

Some type of control is needed to stabilize the system (Dyke et al., 1995), because hydraulic actuators are inherently unstable. With displacement feedback, the error signal e_c is defined by the difference between the command u and measured displacement x as

$$e_c = u - x \tag{3.67}$$

To eliminate the error, servo-controllers often use the *Proportional-Integral-Derivative* (PID) control given by

$$i_{\mathrm{c}} = K_{\mathrm{prop}} e_{\mathrm{c}} + K_{\mathrm{int}} \int e_{\mathrm{c}} dt + K_{\mathrm{der}} \frac{de_{\mathrm{c}}}{dt} \tag{3.68}$$

where i_{c} is the electrical command signal to the servo-valve, and K_{prop}, K_{int}, and K_{dere} are proportional, integral, and derivative gains, respectively. For real-time applications, proportional gain alone is generally adequate, avoiding the lag introduced by integral control and sensitivity to noise of derivative control. Thus, the resulting control law is given by

$$i_{\mathrm{c}} = K_{\mathrm{prop}} e_{\mathrm{c}} \tag{3.69}$$

3.2.5 Servo-valve

The servo-valve provides an interface between the electrical and mechanical components of the system. The servo-valve receives an electrical signal from the servo-controller which moves the position of the valve spool, controlling the flow of oil into the actuator.

For low frequencies, the servo-valve dynamics have been approximated by a constant (Merritt, 1967; Dyke et al., 1995; Zhao et al., 2006), as given by

$$x_{\mathrm{v}} = k_{\mathrm{v}} i_{\mathrm{c}} \tag{3.70}$$

where k_{v} is the valve gain. In the Laplace domain, Eq. (3.70) can be written as

$$G_{\mathrm{v}} = \frac{x_{\mathrm{v}}(s)}{i_{\mathrm{c}}(s)} = k_{\mathrm{v}} \tag{3.71}$$

If a constant gain is inadequate over the frequency range of interest, a first-order model including a time lag may be used. This transfer function is expressed as

$$G_{\mathrm{v}} = \frac{k_{\mathrm{v}}}{s + \tau_{\mathrm{v}}} \tag{3.72}$$

where τ_{v} is the servo-valve time constant.

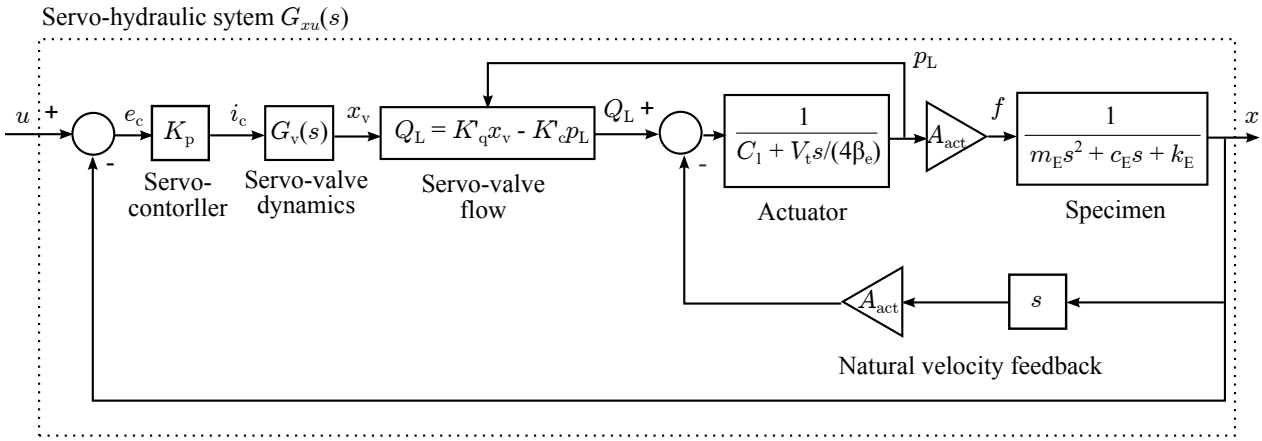

Figure 3.6: Block diagram model of the servo-hydraulic system

3.2.6 Combined model

The servo-hydraulic model can be obtained by combining the mathematical models of the controller, servo-valve, actuator, and specimen derived in 3.2.1 through 3.2.5. The block diagram of the combined model is shown in Figure 3.6.

The transfer function, $G_{xu}(s)$, from the command displacement (input), u, to the measured displacement (output), x, is obtained, in the case of constant servo-valve dynamics (Eq. (3.71)), as

$$G_{xu}(s) = \frac{K_p \dfrac{K_q A_{act}}{K_c}}{D_3 s^3 + D_2 s^2 + D_1 s + D_0} \tag{3.73}$$

where

$$K_q = K'_q k_v \tag{3.74}$$

is the servo-valve gain,

$$K_c = K'_c C_l \tag{3.75}$$

is the total flow-pressure coefficient, and

$$D_3 = \frac{V_t}{4\beta_e K_c} m_E \tag{3.76}$$

$$D_2 = m_{\mathrm{E}} + \frac{V_{\mathrm{t}}}{4\beta_{\mathrm{e}}K_{\mathrm{c}}}c_{\mathrm{E}} \tag{3.77}$$

$$D_1 = c_{\mathrm{E}} + \frac{V_{\mathrm{t}}}{4\beta_{\mathrm{e}}K_{\mathrm{c}}}k_{\mathrm{E}} + \frac{A_{\mathrm{act}}^2}{K_{\mathrm{c}}} \tag{3.78}$$

$$D_0 = k_{\mathrm{E}} + K_{\mathrm{p}}\frac{K_{\mathrm{q}}A_{\mathrm{act}}}{K_{\mathrm{c}}} \tag{3.79}$$

The transfer function given by Eq. (3.73) has three poles and no zeros.

In the case where a first-order model for the servo-valve dynamics (Eq. (3.72)) is used, the transfer function can be expressed as

$$G_{xu}(s) = \frac{K_{\mathrm{p}}\dfrac{K_{\mathrm{q}}A_{\mathrm{act}}}{K_{\mathrm{c}}}}{D_4s^4 + D_3s^3 + D_2s^2 + D_1s + D_0} \tag{3.80}$$

where

$$D_4 = \frac{V_{\mathrm{t}}}{4\beta_{\mathrm{e}}K_{\mathrm{c}}}m_{\mathrm{E}}\tau_{\mathrm{v}} \tag{3.81}$$

$$D_3 = \frac{V_{\mathrm{t}}}{4\beta_{\mathrm{e}}K_{\mathrm{c}}}m_{\mathrm{E}} + m_{\mathrm{E}}\tau_{\mathrm{v}} + \frac{V_{\mathrm{t}}}{4\beta_{\mathrm{e}}K_{\mathrm{c}}}c_{\mathrm{E}}\tau_{\mathrm{v}} \tag{3.82}$$

$$D_2 = m_{\mathrm{E}} + \frac{V_{\mathrm{t}}}{4\beta_{\mathrm{e}}K_{\mathrm{c}}}c_{\mathrm{E}} + \frac{A_{\mathrm{act}}^2}{K_{\mathrm{c}}}\tau_{\mathrm{v}} + c_{\mathrm{E}}\tau_{\mathrm{v}} + \frac{V_{\mathrm{t}}}{4\beta_{\mathrm{e}}K_{\mathrm{c}}}k_{\mathrm{E}}\tau_{\mathrm{v}} \tag{3.83}$$

$$D_1 = c_{\mathrm{E}} + \frac{V_{\mathrm{t}}}{4\beta_{\mathrm{e}}K_{\mathrm{c}}}k_{\mathrm{E}} + \frac{A_{\mathrm{act}}^2}{K_{\mathrm{c}}} + k_{\mathrm{E}}\tau_{\mathrm{v}} \tag{3.84}$$

$$D_0 = k_{\mathrm{E}} + K_{\mathrm{P}}\frac{K_{\mathrm{q}}A_{\mathrm{act}}}{K_{\mathrm{c}}} \tag{3.85}$$

The transfer function given by Eq. (3.80) has four poles and no zeros.

3.3 Real-time hybrid simulation

RTHS is a variation of the hybrid simulation test method in which the imposed displacement and response analysis are conducted in real time. This is very powerful strategy when the test specimen includes rate-dependent components. However, since RTHS is conducted in real time, the dynamics

of the experimental system and specimen affects the results.

3.3.1 Types of delays

In RTHS, there are inevitable experimental errors due to time delays and time lags. These are an intrinsic part of experimental testing and mitigation of their effects is an essential part of RTHS. Time delays and time lags are defined as follows.

Time delay

Time delays are generally caused by the communication of data, A/D and D/A data conversion, and computation time. The transfer function for a pure time delay τ is given by $\exp(-\tau s)$. So time delays have linear phases and constant magnitudes. These delays can be reduced by using faster hardware, smaller numerical integration time steps, and more efficient software.

Time lag

Time lags are a result of the physical dynamics and limitations of the servo-hydraulic actuators, i.e., control-structure-interaction (CSI). Therefore, time lags vary with both the frequency of excitation and specimen conditions (Dyke et al., 1995). Thus, assuming a single time delay is not adequate over a wide frequency range to compensate the errors caused by time lags.

3.3.2 Experimental errors

The most significant experimental error in RTHS is poor phase tracking of the desired displacement. For a simple illustration, let the total time delays and time lags be approximated as s single time delay T_{d}. As shown in Figure 3.7(a), the measured displacement, x, is delayed from the desired displacement, d, by T_{d}. Because of this delay, the force measured and fed back from the experiment does not correspond to the desired displacement (it is measured before the actuator has reached its target position), however, the algorithm assumes that the measured force corresponds to the desired displacement. If the specimen is linear-elastic, the resulting response, as seen by the algorithm, is a counter-clockwise hysteresis loop, instead of the straight line corresponding to the linear behavior, as shown schematically in Figure 3.7(b). This counterclockwise loop leads to additional energy into

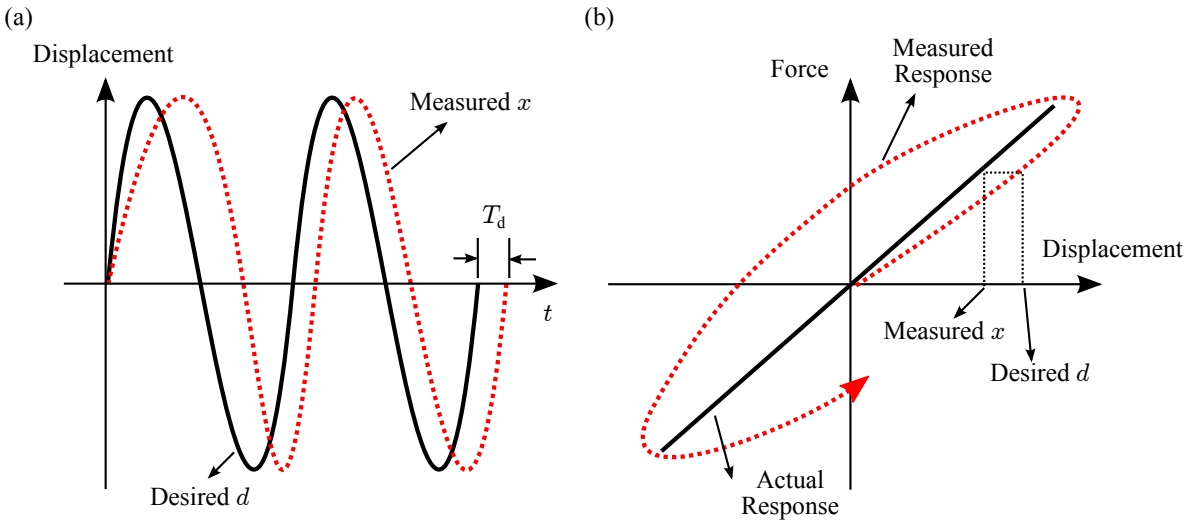

Figure 3.7: Effects of time delay/lag; (a) Displacement history, (b) Force-deformation curve

the structure. Horiuchi et al. (1996) demonstrated that for a SDOF system, the increase in the total system energy caused by the time delay/lag is equivalent to introducing negative damping into the system. This equivalent damping is given by

$$c_{\text{eq}} = -kT_{\text{d}} \tag{3.86}$$

where k is the stiffness of the system. This artificial negative damping becomes large when either the stiffness of the system or the time delay/lag is large. When this negative damping exceeds the structural damping, the system becomes unstable. Instability almost invariably occurs in practice due to the low levels of damping associated with structural frames and the large time delays/lags associated with large hydraulic actuators (Darby et al., 2001). Therefore, introducing compensation for time delays/lags is essential in RTHS.

The effects of the time delays/lags have been traditionally treated together by determining a total delay that includes all of these effects. However, because the time lags vary with frequency, this approximation is valid only over the limited frequency range used for the approximation. If the conditions change significantly during the test (e.g., natural frequency of the test structure due to changes in specimen stiffness), this method is not satisfactory because the system might become unstable (Blakeborough et al., 2001). Additionally, when the response of the test structure includes

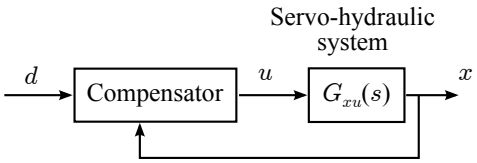

Figure 3.8: Compensation for actuator dynamics

significant contributions at different frequencies (e.g., MDOF), approximating the time lag with a single time delay may cause critical problems. While, the model-based compensators proposed in Carrion and Spencer (2007); Phillips and Spencer (2012) considers the effects of time lags for the wide frequency range. The details of the model-based approach is described in the next section.

3.4 Model-based compensators for RTHS

To compensate time delays and lags caused by RTHS, a model-based actuator controller is designed. To achieve accurate displacements being imposed to specimens, RTHS needs an additional control scheme for compensating the inherent dynamics. As mentioned in Carrion and Spencer (2007); Phillips and Spencer (2012), a model-based approach performs well for RTHS by extending the applicable frequency range, eliminating the lag in the loop, and enabling small damping used in the test structure. In the model-based approach, the servo-hydraulic system is modeled by linearization over the actuator with the specimen as described in Section 3.2. Through a system identification technique, this model is refined to be capable of capturing the command-to-displacement relationship. Based on this identified model, a model-based controller is designed to compensate the unexpected dynamics in RTHS. A scheme of the compensated system is shown in Figure 3.8, in which the desired displacement, d, goes through the compensator, then the command displacement, u, is obtained such that the measured displacement of the specimen, x, becomes the same as the desired displacement, d.

3.4.1 Feedforward compensator employing backward difference method

The feedforward controller is designed to cancel the modeled dynamic of the servo-hydraulic system. Placed in series with the servo-hydraulic system, the inverse of the servo-hydraulic system model

will serve as the feedforward controller, which is expressed as

$$G_{\mathrm{FF}}(s) = \frac{1}{G_{xu}}(s) \tag{3.87}$$

Three-pole model

For the case that the three-pole model for the servo-hydraulic system, which is given by Eq. (3.73), is used, from Eq. (3.87), the feedforward controller can be written as

$$G_{\mathrm{FF}}(s) = a_0 + a_1 s + a_2 s^2 + a_3 s^3 \tag{3.88}$$

where the coefficients a_0 through a_3 can be determined by expanding Eq. (3.87). Since the output of the feedforward controller is expressed as

$$U_{\mathrm{FF}}(s) = G_{\mathrm{FF}}(s) D(s) \tag{3.89}$$

in the Laplace domain, the time domain expression is given by

$$u_{\mathrm{FF}}(t) = a_0 d(t) + a_1 d^{(1)}(t) + a_2 d^{(1)}(t) + a_3 d^{(3)}(t) \tag{3.90}$$

where $d^{(n)}$ represents the n^{th} derivative of d with respect to time. In discrete time, Eq. (3.90) can be written as

$$u_{\mathrm{FF},i} = a_0 d_i + a_1 d_i^{(1)} + a_2 d_i^{(2)} + a_3 d_i^{(3)} \tag{3.91}$$

Thus, the feedforward controller for the three-pole model servo-hydraulic system requires the calculation of displacement, velocity, acceleration, and jerk (derivative of the acceleration) at time step i; however, most numerical integration schemes are only explicit in displacement. In this dissertation, backward difference method is used to calculate the necessary higher-order derivatives. Note that this method is proposed simply to estimate the higher-order derivatives at the required time step and can be selected independently from the numerical integration scheme.

The derivatives up to the fourth order calculated using the BDM are given by

$$d_i^{(1)} = \frac{1}{2\Delta t}\left(3d_i - 4d_{i-1} + d_{i-2}\right) \tag{3.92}$$

$$d_i^{(2)} = \frac{1}{\Delta t^2}\left(2d_i - 5d_{i-1} + 4d_{i-2} - d_{i-3}\right) \tag{3.93}$$

$$d_i^{(3)} = \frac{1}{2\Delta t^3}\left(5d_i - 18d_{i-1} + 24d_{i-2} - 14d_{i-3} + 3d_{i-4}\right) \tag{3.94}$$

where the derivatives are second order accurate. Substituting Eqs. (3.92) through (3.94) into Eq. (3.4.1) yields

$$u_{\mathrm{FF},i} = b_0 d_i + b_1 d_{i-1} + b_2 d_{i-2} + b_3 d_{i-3} + b_4 d_{i-4} \tag{3.95}$$

where

$$b_0 = a_0 + \frac{3a_1}{2\Delta t} + \frac{2a_2}{\Delta t^2} + \frac{5a_3}{2\Delta t^3} \tag{3.96}$$

$$b_1 = \frac{-2a_1}{\Delta t} + \frac{-5a_2}{\Delta t^2} + \frac{-9a_3}{\Delta t^3} \tag{3.97}$$

$$b_2 = \frac{a_1}{2\Delta t} + \frac{4a_2}{\Delta t^2} + \frac{12a_3}{\Delta t^3} \tag{3.98}$$

$$b_3 = \frac{-a_2}{\Delta t^2} + \frac{-7a_3}{\Delta t^3} \tag{3.99}$$

$$b_4 = \frac{3a_3}{2\Delta t^3} \tag{3.100}$$

Since the transfer function of the feedforward controller in discrete time is defined as

$$G_{\mathrm{FF}}(z) = \frac{U_{\mathrm{FF}}(z)}{D(z)}, \tag{3.101}$$

the transfer function of the feedforward compensator is expressed as

$$G_{\mathrm{FF}}(z) = b_0 + b_1 z^{-1} + b_2 z^{-2} + b_3 z^{-3} + b_4 z^{-4} \tag{3.102}$$

Four-pole model

In a similar way, the feedforward controller employing BDM for the four-pole model servo-hydraulic system is derived. The feedforward controller in s-domain is given as

$$G_{\mathrm{FF}}(s) = a_0 + a_1 s + a_2 s^2 + a_3 s^3 + a_4 s^4 \tag{3.103}$$

where the coefficients a_0 through a_4 can be determined by expanding Eq. (3.87). By Eq. (3.89), the output of the feedforward controller is given in continuous time by

$$u_{\mathrm{FF}}(t) = a_0 d(t) + a_1 d^{(1)}(t) + a_2 d^{(1)}(t) + a_3 d^{(3)}(t) + a_4 d^{(4)}(t) \tag{3.104}$$

and, in discrete time, by

$$u_{\mathrm{FF},i} = a_0 d_i + a_1 d_i^{(1)} + a_2 d_i^{(2)} + a_3 d_i^{(3)} + a_4 d_i^{(4)} \tag{3.105}$$

Therefore, when the four-pole model is used, jounce (derivative of the jerk) must be calculated in addition to displacement, velocity, acceleration, and jerk at time step i. The jounce obtained from BDM is given by

$$d_i^{(4)} = \frac{1}{\Delta t^4}\left(3d_i - 14d_{i-1} + 26d_{i-2} - 24d_{i-3} + 11d_{i-4} - 2d_{i-5}\right) \tag{3.106}$$

Substituting Eqs. (3.92), (3.93), (3.94), and (3.106) into gives

$$u_{\mathrm{FF},i} = b_0 d_i + b_1 d_{i-1} + b_2 d_{i-2} + b_3 d_{i-3} + b_4 d_{i-4} + b_5 d_{i-5} \tag{3.107}$$

where

$$b_0 = a_0 + \frac{3a_1}{2\Delta t} + \frac{2a_2}{\Delta t^2} + \frac{5a_3}{2\Delta t^3} + \frac{3a_4}{\Delta t^4} \tag{3.108}$$

$$b_1 = \frac{-2a_1}{\Delta t} + \frac{-5a_2}{\Delta t^2} + \frac{-9a_3}{\Delta t^3} + \frac{-14a_4}{\Delta t^4} \tag{3.109}$$

$$b_2 = \frac{a_1}{2\Delta t} + \frac{4a_2}{\Delta t^2} + \frac{12a_3}{\Delta t^3} + \frac{26a_4}{\Delta t^4} \tag{3.110}$$

$$b_3 = \frac{-a_2}{\Delta t^2} + \frac{-7a_3}{\Delta t^3} + \frac{-24a_4}{\Delta t^4} \tag{3.111}$$

$$b_4 = \frac{3a_3}{2\Delta t^3} + \frac{11a_4}{\Delta t^4} \tag{3.112}$$

$$b_5 = \frac{-2a_4}{\Delta t^4} \tag{3.113}$$

Hence, the feedforward controller employing BDM for the four-pole model is given as

$$G_{\mathrm{FF}}(z) = b_0 + b_1 z^{-1} + b_2 z^{-2} + b_3 z^{-3} + b_4 z^{-4} + b_5 z^{-5} \tag{3.114}$$

3.4.2 Bumpless feedforward compensator

A bumpless transfer algorithm was developed by Carrion and Spencer (2007) to provide a smooth transition between $G_{\mathrm{FF},0}(s)$ and $G_{\mathrm{FF},i_{\max}}(s)$ when the current varies during the experiments. Figure 3.9 shows a schematic block diagram of the modified feedforward term, $G_{\mathrm{FF}}(s)$. Through the feedforward controller, the command displacement, u, is obtained from the desired displacement, d, taking into account changing model dynamics. The feedforward controller is given by the following equations in the Laplace domain:

$$U(s) = U_{\mathrm{a}}(s) + U_{\mathrm{b}}(s)W(s) \tag{3.115}$$

where

$$U_{\mathrm{a}}(s) = G_{\mathrm{FF,a}}(s)D(s) \tag{3.116}$$

$$U_{\mathrm{b}}(s) = G_{\mathrm{FF,b}}(s)D(s) \tag{3.117}$$

$$W(s) = G_t(s)I_{\mathrm{d}}(s) \tag{3.118}$$

and the two transfer functions, $G_{\mathrm{FF,a}}(s)$ and $G_{\mathrm{FF,b}}(s)$, are given by

$$G_{\mathrm{FF},a}(s) = G_{\mathrm{FF},0}(s) \tag{3.119}$$

$$G_{\mathrm{FF,b}}(s) = G_{\mathrm{FF},i_{\max}}(s) - G_{\mathrm{FF},0}(s) \tag{3.120}$$

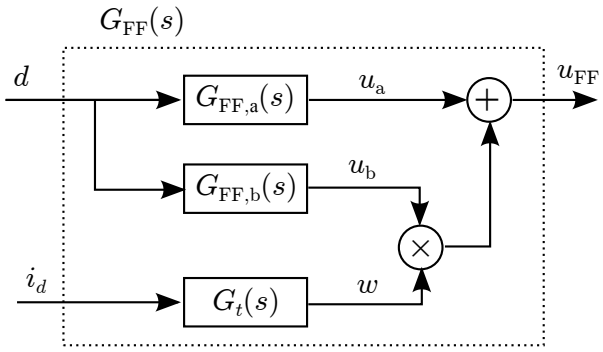

Figure 3.9: Block diagram of bumpless feedforward controller

The transfer function, $G_t(s)$, is used to model the dynamics of the actuator associated with the change in the current of the MR damper. This transfer function provides a smooth transition between the two transfer functions, $G_{\mathrm{FF,a}}(s)$, $G_{\mathrm{FF,b}}(s)$, and is given by

$$G_t(s) = \frac{1}{\frac{\dot{i}_{\max}}{\tau_t s + 1}} \tag{3.121}$$

where τ_t is the time constant of the transfer filter. As the time constant becomes small, the transition becomes faster, approaching a simple switching algorithm, while for large values of the time constant, the transition is slower and smoother.

3.4.3 Feedforward-feedback compensator

The model-based compensation approach employing a feedforward and feedback link in RTHS is shown in Figure 3.10. In this approach, the feedback controller is added to complement the feedforward controller, providing robustness in the presence of changing specimen conditions, modeling errors, and disturbances. For the proposed model-based feedback controller, LQG control is applied to bring the deviation states to zero and thus reduce the tracking error. The derivations of both controllers are given in Phillips and Spencer (2012).

To design the feedback controller, the transfer function $G_{xu}(s)$ given in Eqs. (3.73) and (3.80) is expressed in state-space form:

$$\dot{\mathbf{z}}_{\mathrm{s}} = \mathbf{A}_{\mathrm{s}}\mathbf{z}_{\mathrm{s}} + \mathbf{B}_{\mathrm{s}}u \tag{3.122}$$

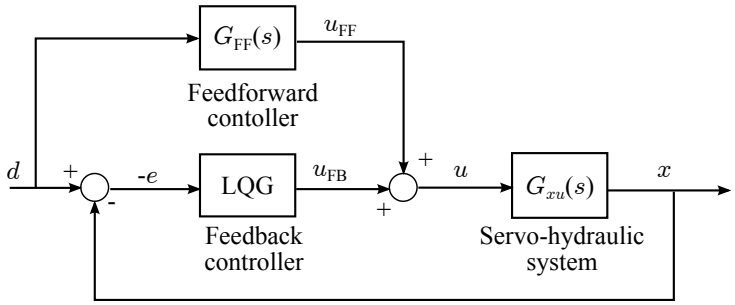

Figure 3.10: Block diagram of feedforward and feedback links

$$x = \mathbf{C}_{\mathrm{s}}\mathbf{z}_{\mathrm{s}} \tag{3.123}$$

where $\mathbf{z}_{\mathrm{s}}$ is the state vector. The tracking error between the desired displacement d and measured displacement x is given by

$$e = d - x \tag{3.124}$$

The command, u, should be chosen such that the tracking error is minimized. If perfect tracking, i.e., $x = d$, is achieved by only the feedforward controller, u_{FF}, the ideal system is described as

$$\dot{\mathbf{z}} = \mathbf{A}_{\mathrm{s}}\mathbf{z}_{\mathrm{i}} + \mathbf{B}_{\mathrm{s}}u_{\mathrm{FF}} \tag{3.125}$$

$$d = \mathbf{C}_{\mathrm{s}}\mathbf{z}_{\mathrm{i}} \tag{3.126}$$

where $\mathbf{z}_{\mathrm{i}}$ is an ideal state. Deviations of the state from the ideal system with respect to the original system is defined as

$$\mathbf{z}_{\mathrm{d}} = \mathbf{z}_{\mathrm{s}} - \mathbf{z}_{\mathrm{i}} \tag{3.127}$$

and assume that deviation of the control is provided by a feedback controller, i.e.,

$$u_{\mathrm{FB}} = u - u_{\mathrm{FF}} \tag{3.128}$$

Then, considering disturbance to the system, w_{f}, and the measurement noise, v_{f}, the state-space representation of the deviation system is

$$\dot{\mathbf{z}}_{\mathrm{d}} = \mathbf{A}_{\mathrm{s}}\mathbf{z}_{\mathrm{d}} + \mathbf{B}_{\mathrm{s}}u_{\mathrm{FB}} + \mathbf{E}_{\mathrm{s}}w_{\mathrm{f}} \tag{3.129}$$

$$-e = \mathbf{C}_\mathrm{s}\mathbf{z}_\mathrm{d} + v_\mathrm{f} \tag{3.130}$$

where $\mathbf{E}_\mathrm{s}$ is a matrix that describes how the disturbance enters the system.

To improve the LQG controller's performance and robustness in the frequency range of interest, the disturbance, w_f, is assumed to be Gaussian white-noise, w, passed through a second-order shaping filter, i.e.,

$$\dot{\mathbf{z}}_\mathrm{f} = \mathbf{A}_\mathrm{f}\mathbf{z}_\mathrm{f} + \mathbf{E}_\mathrm{f}w \tag{3.131}$$

$$w_\mathrm{f} = \mathbf{C}_\mathrm{f}\mathbf{z}_\mathrm{f} \tag{3.132}$$

where

$$\mathbf{A}_f = \begin{bmatrix} 0 & 1 \\ -\omega_\mathrm{f}^2 & -2\eta_\mathrm{f}\omega_\mathrm{f} \end{bmatrix} \tag{3.133}$$

$$\mathbf{E}_f = \begin{bmatrix} 0 \\ 1 \end{bmatrix} \tag{3.134}$$

$$\mathbf{C}_f = \begin{bmatrix} \omega_\mathrm{f}^2 & 2\xi_\mathrm{f}\eta_\mathrm{f}\omega_\mathrm{f} \end{bmatrix} \tag{3.135}$$

and $\mathbf{z}_\mathrm{f}$ is the state vector the shaping filter, $\dot{\mathbf{z}}_\mathrm{f}$ is its time derivative, and the parameters ξ_f, ω_f, and η_f control the peak, bandwidth, and roll-off of the disturbance, respectively. The deviation system can be rewritten as an augmented system that includes the dynamics of the shaping filter. Defining the state

$$\mathbf{z}_\mathrm{FB} = \begin{bmatrix} \mathbf{z}_\mathrm{f}^T \\ \mathbf{z}_\mathrm{d}^T \end{bmatrix}, \tag{3.136}$$

this augmented system is given by

$$\dot{\mathbf{z}}_\mathrm{FB} = \mathbf{A}_\mathrm{FB}\mathbf{z}_\mathrm{FB} + \mathbf{B}_\mathrm{FB}u_\mathrm{FB} + \mathbf{E}_\mathrm{FB}w \tag{3.137}$$

$$-e = \mathbf{C}_\mathrm{FB}\mathbf{z}_\mathrm{FB} + v_\mathrm{f} \tag{3.138}$$

where

$$\mathbf{A}_{\mathrm{FB}} = \begin{bmatrix} \mathbf{A}_{\mathrm{f}} & \mathbf{0} \\ \mathbf{E}_{\mathrm{s}}\mathbf{C}_{\mathrm{f}} & \mathbf{A}_{\mathrm{s}} \end{bmatrix} \tag{3.139}$$

$$\mathbf{B}_{\mathrm{FB}} = \begin{bmatrix} \mathbf{0} \\ \mathbf{B}_{\mathrm{s}} \end{bmatrix} \tag{3.140}$$

$$\mathbf{E}_{\mathrm{FB}} = \begin{bmatrix} \mathbf{E}_{\mathrm{f}} \\ \mathbf{0} \end{bmatrix} \tag{3.141}$$

$$\mathbf{C}_{\mathrm{FB}} = \begin{bmatrix} \mathbf{0} & \mathbf{C}_{\mathrm{s}} \end{bmatrix} \tag{3.142}$$

and the measurement noise vector, v_{f}, is assumed to be comprised of independent Gaussian white noises.

The control u_{FB} can be obtained using LQR design assuming full state feedback and output weighting as follows

$$J_{\mathrm{FB}} = \int_0^\infty \{Q_{\mathrm{FB}}(-e)^2 + R_{\mathrm{FB}}(u_{\mathrm{FB}})^2\}dt \tag{3.143}$$

$$u_{\mathrm{FB}} = -\mathbf{K}_{\mathrm{FB}}\mathbf{z}_{\mathrm{FB}} \tag{3.144}$$

where $\mathbf{K}_{\mathrm{FB}}$ is the optimal state feedback gain matrix, J_{FB} is the cost function minimized by LQR design, Q_{FB} is the weighting matrix on the system outputs, and R_{FB} is the weighting matrix on the system inputs.

The augmented system states $\mathbf{z}_{\mathrm{a}}$ can be estimated using a Kalman filter

$$\dot{\hat{\mathbf{z}}}_{\mathrm{FB}} = \mathbf{A}_{\mathrm{FB}}\hat{\mathbf{z}}_{\mathrm{FB}} + \mathbf{B}_{\mathrm{FB}}u_{\mathrm{FB}} + \mathbf{L}_{\mathrm{FB}}(-e - \mathbf{C}_{\mathrm{FB}}\hat{\mathbf{z}}_{\mathrm{FB}}) \tag{3.145}$$

where $\hat{\mathbf{z}}_{\mathrm{FB}}$ represents the estimated states and $\mathbf{L}_{\mathrm{FB}}$ is the optimal observer gain matrix.

The control law in Eq. (3.144) is then written in terms of the estimated states and included in the estimator

$$\dot{\hat{\mathbf{z}}}_{\mathrm{FB}} = (\mathbf{A}_{\mathrm{FB}} - \mathbf{L}_{\mathrm{FB}}\mathbf{C}_{\mathrm{FB}} - \mathbf{B}_{\mathrm{FB}}\mathbf{K}_{\mathrm{FB}})\hat{\mathbf{z}}_{\mathrm{FB}} + \mathbf{L}_{\mathrm{FB}}(-e) \tag{3.146}$$

$$u_{\mathrm{FB}} = -\mathbf{K}_{\mathrm{FB}}\hat{\mathbf{z}}_{\mathrm{FB}} \tag{3.147}$$

3.5 Summary

This chapter provided the background on modern control theory that is essential to the development of the proposed research. In addition, the servo-hydraulic system model, the effects of time delays/lags in RTHS, and the model-based compensators for RTHS used in this dissertation were described.

Chapter 4

Modeling and Experimental Setup

This chapter provides a model of the MR damper used throughout this dissertation. Based on the background presented in Chapter 3, a model of the servo-hydraulic system and compensators for the system are designed for RTHS as well in this chapter.

4.1 MR damper modeling

The MR damper employed in this study is an RD-1005 MR fluid damper manufactured by the Lord Corporation (Cary, NC, USA) and shown in Figure 4.1. The damper is 8.5 inch long in its extended position, and the main cylinder is 1.5 inch in diameter. The damper has a stroke of ± 1.0 inch and can generate forces up to about 500 lbf. The main cylinder of the damper accommodates the piston, the electromagnet, an accumulator, and 50 ml of MR fluid. The magnetic field produced in the device is generated by a small electromagnet in the piston head (Spencer et al., 1997). Input current commands are supplied to the damper using an RD-1002 Wonderbox from the Lord Corporation, which uses a modulated pulse-width amplifier to generate a current in the MR damper circuit that is proportional to the applied voltage. The maximum input current of the system $i_{\max}$ is 2.0 A. By selecting the input current, the characteristics of the damper may be changed in real-time to vary the forces exerted by the damper. The power required by the MR damper is very small (less than 10 watts), and the system, damper and the current driver, has a response time of typically less than 10 msec (Spencer et al., 1997).

In this dissertation, the MR damper is modeled by the phenomenological model (Spencer et al., 1997) as shown in Figure 4.2 in which the damper force is a function of the damper displacement

(a)

(b)

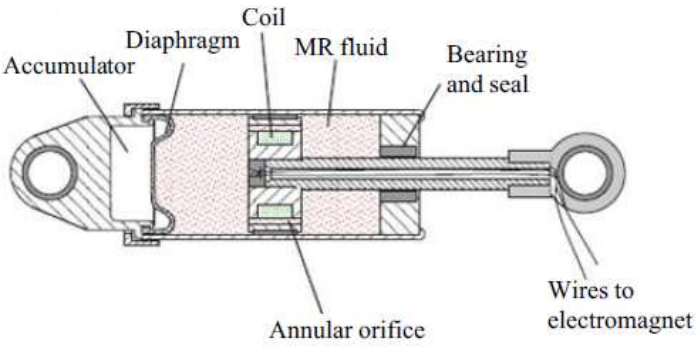

Figure 4.1: Small-scale MR damper

and velocity. The MR damper force f_{MR} is given by

$$f_{\mathrm{MR}} = \alpha z + c_0(\dot{x} - \dot{y}) + k_0(x - y) + k_1 x \tag{4.1}$$

where x is the displacement of the MR damper, y is an internal displacement as illustrated in Figure 4.2, and z is an evolutionary variable (Wen, 1976) governed by

$$\dot{z} = -\gamma|\dot{x} - \dot{y}|z|z|^{n-1} - \beta(\dot{x} - \dot{y})|z|^n + A(\dot{x} - \dot{y}). \tag{4.2}$$

And k_0, k_1, c_0, c_1, α, β, γ, A, and n are parameters for the MR damper model. Since MR dampers are driven by currents, α, c_0, c_1, β and γ are current dependent variables given by

$$\alpha = \alpha_a + (\alpha_b - \alpha_a)\tanh(\alpha_c i_c) \tag{4.3}$$

$$c_0 = c_{0a} + (c_{0b} - c_{0a})\tanh(c_{0c} i_c) \tag{4.4}$$

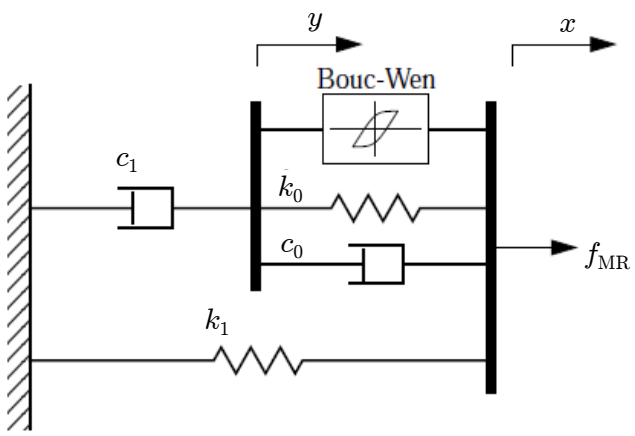

Figure 4.2: Mechanical model of the MR damper

$$c_1 = c_{1a} + (c_{1b} - c_{1a}) \tanh(c_{1c} i_c) \tag{4.5}$$

$$\beta = \beta_a + (\beta_b - \beta_a) \tanh(\beta_c i_c) \tag{4.6}$$

$$\gamma = \gamma_a + (\gamma_b - \gamma_a) \tanh(\gamma_c i_c) \tag{4.7}$$

where i_c is the input current to the MR damper model after a first order filter which is designed to account for the time that the MR fluid takes to reach rheological equilibrium (Carrion and Spencer, 2007):

$$\dot{i}_c = -\eta(i_c - i_d) \tag{4.8}$$

where i_d is the desired current applied to the current driver and η is a parameter obtained experimentally.

To obtain the parameters of the MR damper, the damper is experimentally subjected to a 1 Hz sine wave with 1.02 cm (0.4 in) amplitude and constant current of 0 A, 0.5 A, 1.0 A, 1.5 A, and 2.0 A. Then, the parameters are fit using nonlinear least squares parameter estimation to match the experimental response of the damper. To decide the parameters, importance are placed especially on 0 A and 2.0 A cases because 0 A (passive-off) and 2.0 A (passive-on) modes are used mainly in this dissertation. Table 4.1 provides the parameters obtained from MATLAB (MATLAB, 2013) optimization toolbox. The comparisons between the experimental data and analytical data by the created model are shown in Figures 4.3 through 4.7 for each input current.

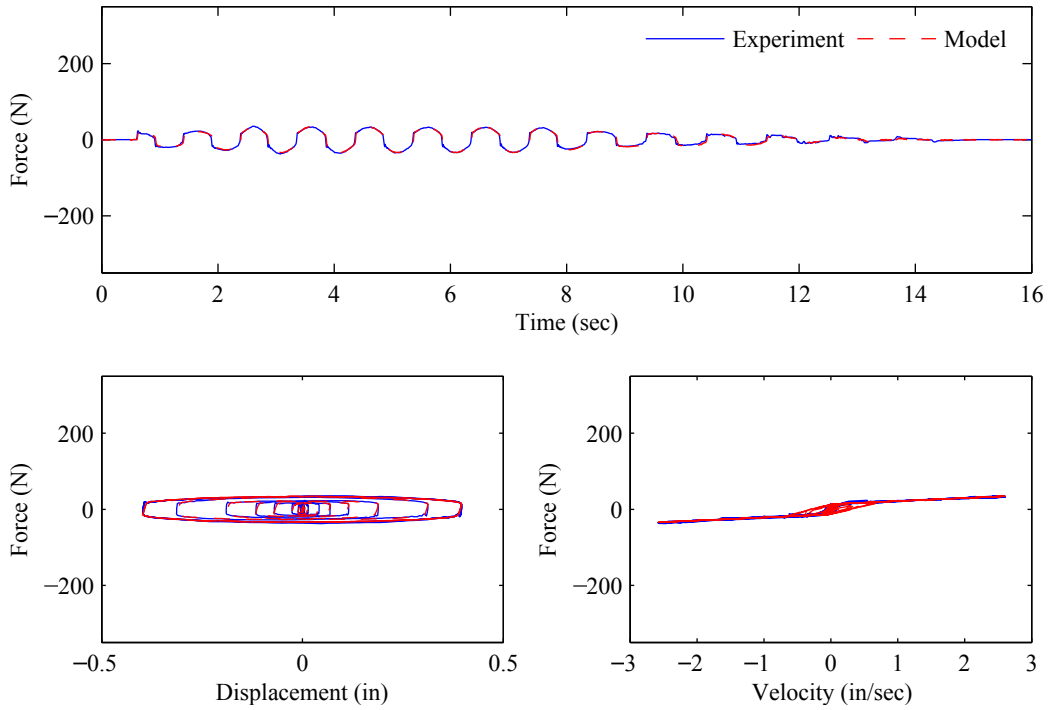

Figure 4.3: MR damper force with 0 A to 0.4 in, 1.0 Hz sine wave

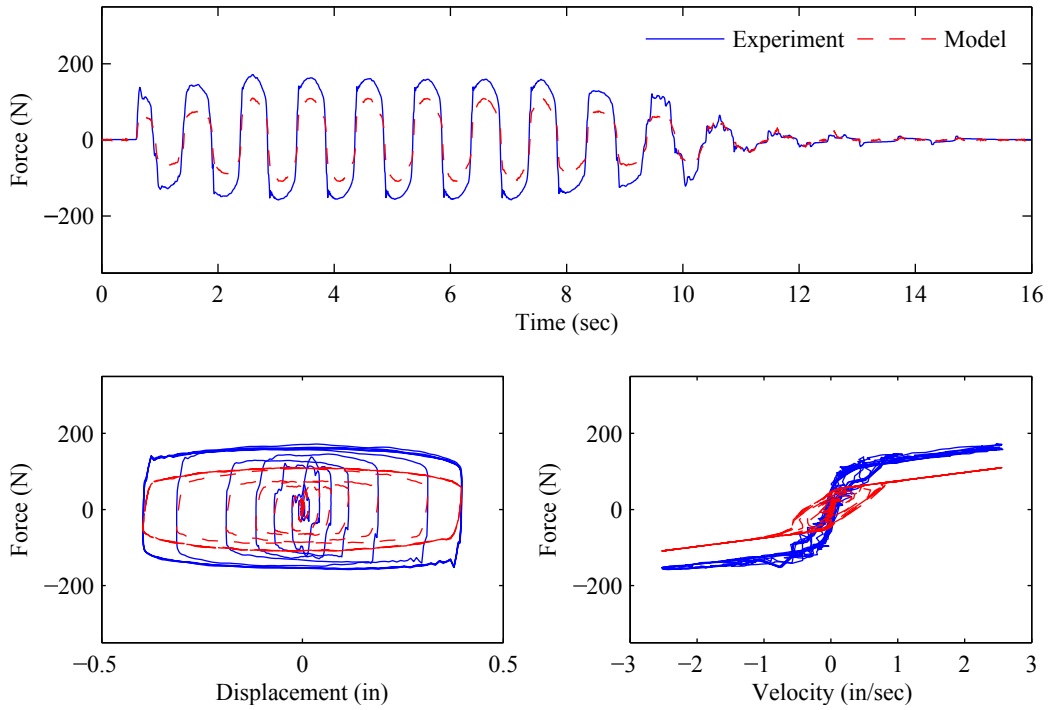

Figure 4.4: MR damper force with 0.5 A to 0.4 in, 1.0 Hz sine wave

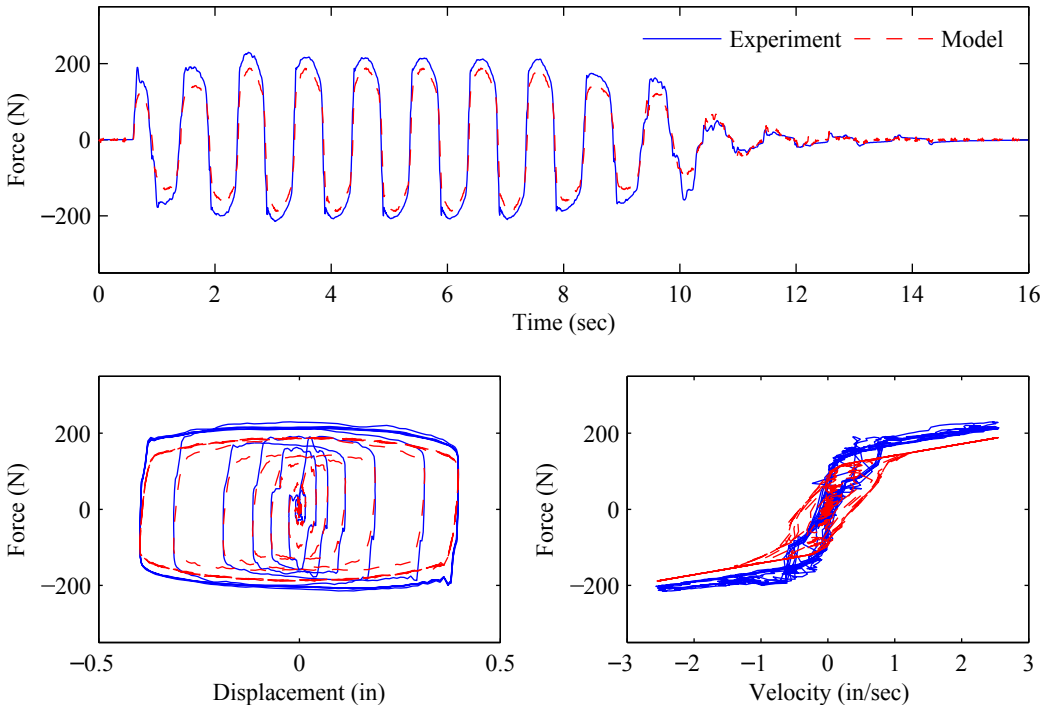

Figure 4.5: MR damper force with 1.0 A to 0.4 in, 1.0 Hz sine waver

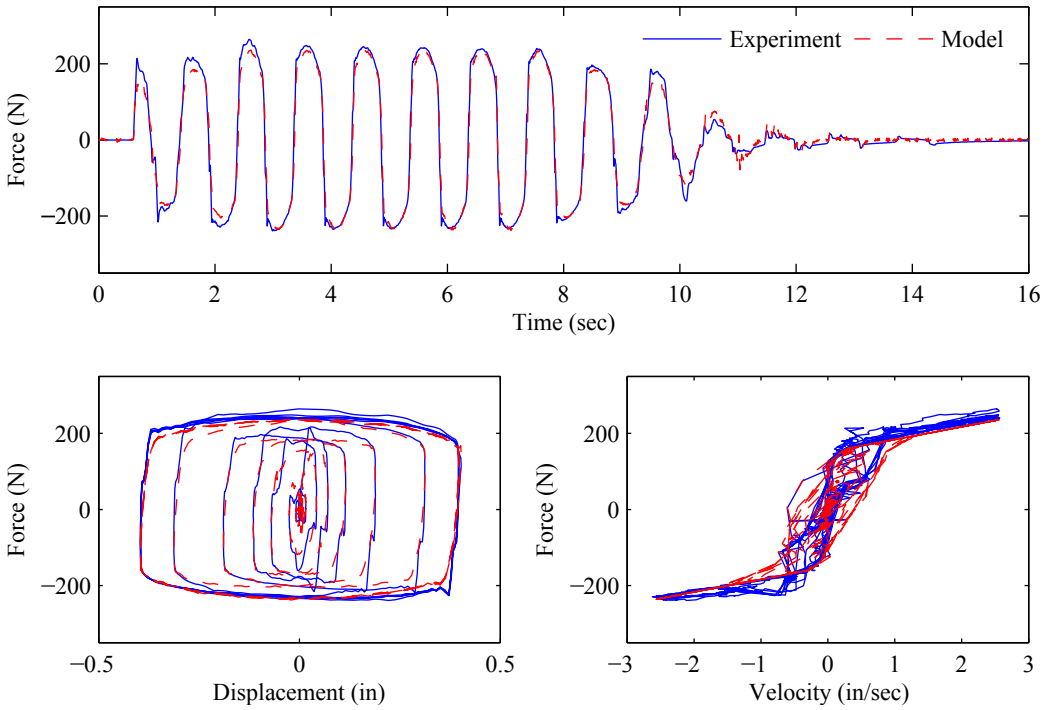

Figure 4.6: MR damper force with 1.5 A to 0.4 in, 1.0 Hz sine wave

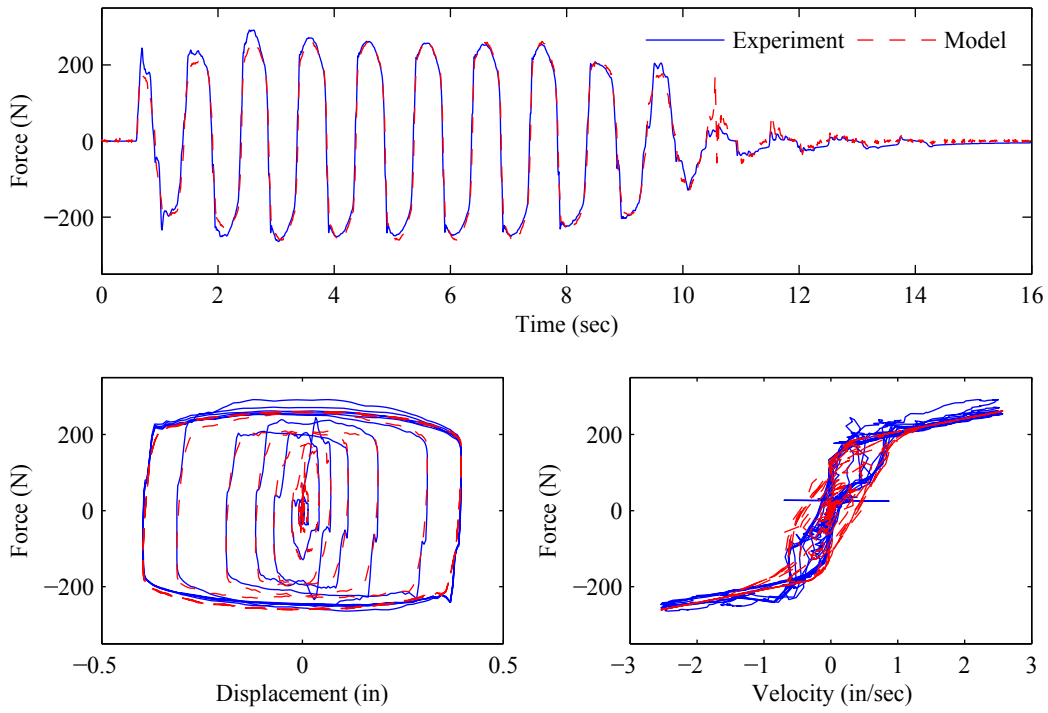

Figure 4.7: MR damper force with 2.0 A to 0.4 in, 1.0 Hz sine wave

4.2 RTHS setup

RTHS consists of a computational model and physical specimen (the MR damper in this dissertation) in a loop, with an appropriate loading unit and testing equipment. A schematic configuration for RTHS in this study is shown in Figure 4.8(a). Testing hardware in the RTHS includes a digital signal processor (DSP) running numerical integration for the structure and generating the command signals, a small-scale MR damper that is driven by a servo-hydraulic actuator, which is controlled by a servo-controller, and Analog-to-Digital (A/D) and Digital-to- Analog (D/A) converters for signal processing. Sensors include a linear variable displacement transducer (LVDT) for displacement measurements and a load cell for measuring the MR damper force.

In Figure 4.8(a), u is the commanded displacement, f_{MR} is the MR damper force measured by the load cell, x is the displacement measured by the LVDT and i is the control current sent to the hydraulic actuator. A detailed description of this RTHS implementation can be found in Carrion and Spencer (2007). Figure 4.8(b) shows a photograph of the experimental setup for RTHS. The experiments are conducted at the Smart Structures Technology Laboratory (SSTL), University of

Table 4.1: Parameters for the MR damper model

c_{0a}	8.129 lbf·sec/in	c_{0b}	37.082 lbf·sec/in	c_{0c}	1.192 /A
k_0	0.012 lbf/in	k_1	0.007 lbf/in	x_0	0 in
c_{1a}	406.314 lbf·sec/in	c_{1b}	786.564 lbf·sec/in	c_{1c}	0.315 /A
α_a	18.361 lbf/in	α_b	100.617 lbf/in	α_c	0.551 /A
γ_a, β_a	145.710 /in^2	γ_b, β_b	17.600 /in^2	γ_c, β_c	2.120 /A
A	167.073	n	2	η	50 /sec

Illinois at Urbana-Champaign (`http://sstl.cee.illinois.edu/`).

4.3 Servo-hydraulic system modeling

As developed in Section 3.2, the entire physical system can be modeled by a transfer function $G_{xu}(s)$, whose input u is the commanded displacement and output x is the piston displacement which is measured by the LVDT. Due to the feedback interaction, the transfer function $G_{xu}(s)$ depends on input current of the MR damper. Because the input current to the MR damper can change during the RTHS, the servo-hydraulic dynamics must be investigated at multiple current levels. To obtain the transfer functions for the 0 A case ($G_{xu,0\mathrm{A}}(s)$) and 2.0 A case ($G_{xu,2\mathrm{A}}(s)$), system identifications are performed with band limited white noise (BLWN) of frequency range of 0 to 50 Hz using the software MFDID developed by Kim et al. (2005). Frequency responses obtained in the experiments are shown in Fgiure 4.9. In this dissertation, a four poles and no zeros model given by Eq. (3.80) is used for each case. These transfer functions are obtained as

$$G_{xu,0\mathrm{A}}(s) = \frac{4.162 \times 10^9}{s^4 + 5.673 \times 10^2 s^3 + 2.784 \times 10^5 s^2 + 5.625 s \times 10^7 s + 4.151 \times 10^9} \tag{4.9}$$

$$G_{xu,2\mathrm{A}}(s) = \frac{3.281 \times 10^9}{s^4 + 5.371 \times 10^2 s^3 + 2.642 \times 10^5 s^2 + 4.602 s \times 10^7 s + 3.259 \times 10^9} \tag{4.10}$$

These transfer functions are compared with experimental results in Figures 4.10 and 4.11. As can be seen, both cases show a good agreement between the experimental data and proposed model. These two transfer functions are used to design the bumpless feedforward controller in the next section.

The results are also averaged to create a third transfer function appropriate for when the MR

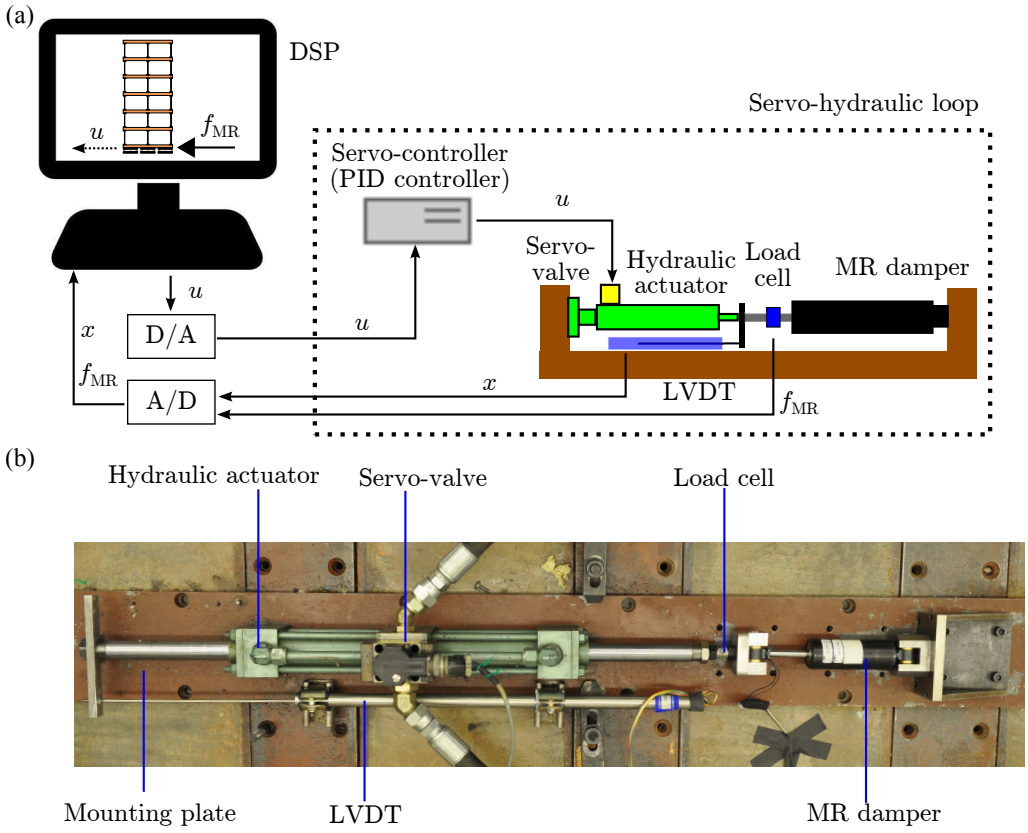

Figure 4.8: Real-time hybrid simulation; (a) Schematic diagram of the RTHS loop, (b) Photograph of the experimental setup

damper conditions are unknown or changing, which is given by

$$G_{xu,\text{avg}}(s) = \frac{3.689 \times 10^9}{s^4 + 5.420 \times 10^2 s^3 + 2.712 \times 10^5 s^2 + 5.080 s \times 10^7 s + 3.670 \times 10^9} \tag{4.11}$$

The comparison with the experimental results can be found in Figure 4.12. This transfer function is used to design the feedforward-feedback compensator in the next section.

4.4 Model-based compensator design for RTHS

In this section, two model-based compensators, i.e., bumpless feedforward and feedforward-feedback compensators, are designed based on the methods presented in Section 3.4. The transfer functions of the servo-hydraulic system obtained in Section 4.3 are applied. To design the feedforward controllers for both compensators, the BDM, whose accuracy has been proven in Phillips and

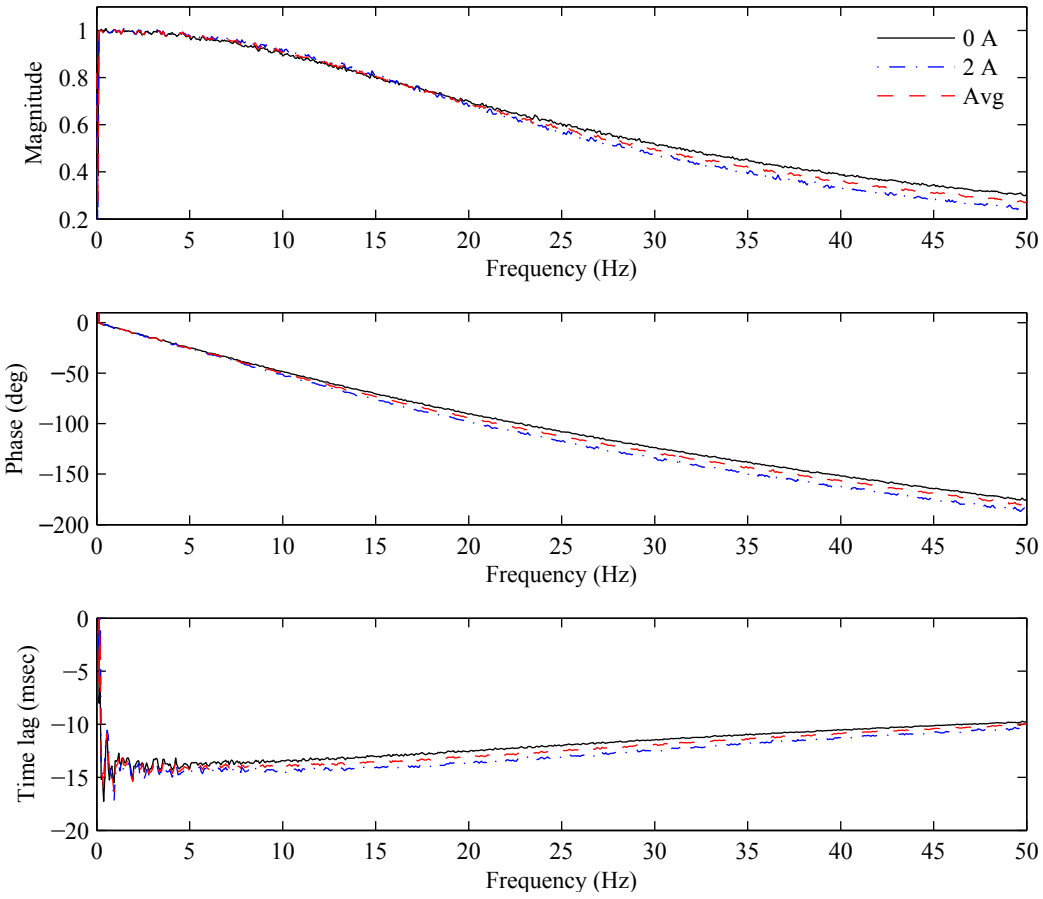

Figure 4.9: Frequency response from the experiments

Spencer (2012), is used. The sampling time Δt used in this research is 5.0×10^{-4} sec.

4.4.1 Bumpless feedforward compensator

The bumpless feedforward compensator is designed here. By using the BDM introduced in Subsection 3.4.1, $G_{\mathrm{FF,0A}}$ and $G_{\mathrm{FF,2A}}$ in discrete time are calculated from Eqs. (4.9) and (4.10), respectively, as

$$G_{\mathrm{FF,0A}}(z) = \sum_{k=0}^{5} b_{k,\mathrm{0A}} z^{-k} \tag{4.12}$$

where

$$\begin{aligned} b_{0,\mathrm{0A}} &= 1.484 \times 10^4, \quad & b_{1,\mathrm{0A}} &= -6.503 \times 10^4, \quad & b_{2,\mathrm{0A}} &= 1.141 \times 10^5, \\ b_{3,\mathrm{0A}} &= -1.002 \times 10^5, \quad & b_{4,\mathrm{0A}} &= 4.393 \times 10^4, \quad & b_{5,\mathrm{0A}} &= -7.689 \times 10^3. \end{aligned} \tag{4.13}$$

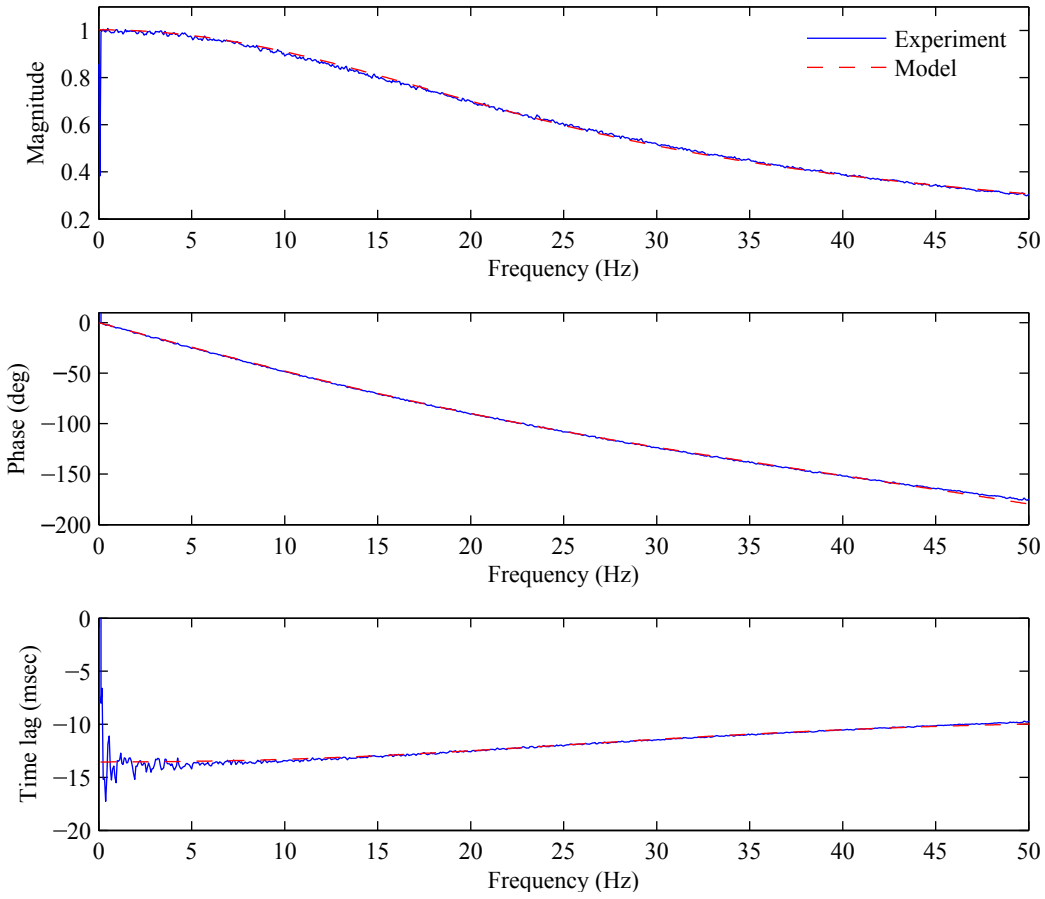

Figure 4.10: Comparison between the experimental data and obtained model for 0 A case

and

$$G_{\mathrm{FF,2A}}(z) = \sum_{k=0}^{5} b_{k,\mathrm{2A}} z^{-k} \tag{4.14}$$

where

$$\begin{aligned} b_{0,\mathrm{2A}} &= 3.756 \times 10^3, \quad & b_{1,\mathrm{2A}} &= -1.670 \times 10^4, \quad & b_{2,\mathrm{2A}} &= 2.969 \times 10^4, \\ b_{3,\mathrm{2A}} &= -2.637 \times 10^4, \quad & b_{4,\mathrm{2A}} &= 1.169 \times 10^4, \quad & b_{5,\mathrm{2A}} &= -2.065 \times 10^3. \end{aligned} \tag{4.15}$$

Also, in this dissertation, τ_t Eq. (3.121) is taken as 0.0048 sec (Carrion and Spencer, 2007). This bumpless feedforward compensator compensator is employed for the RTHS in Chapter 7.

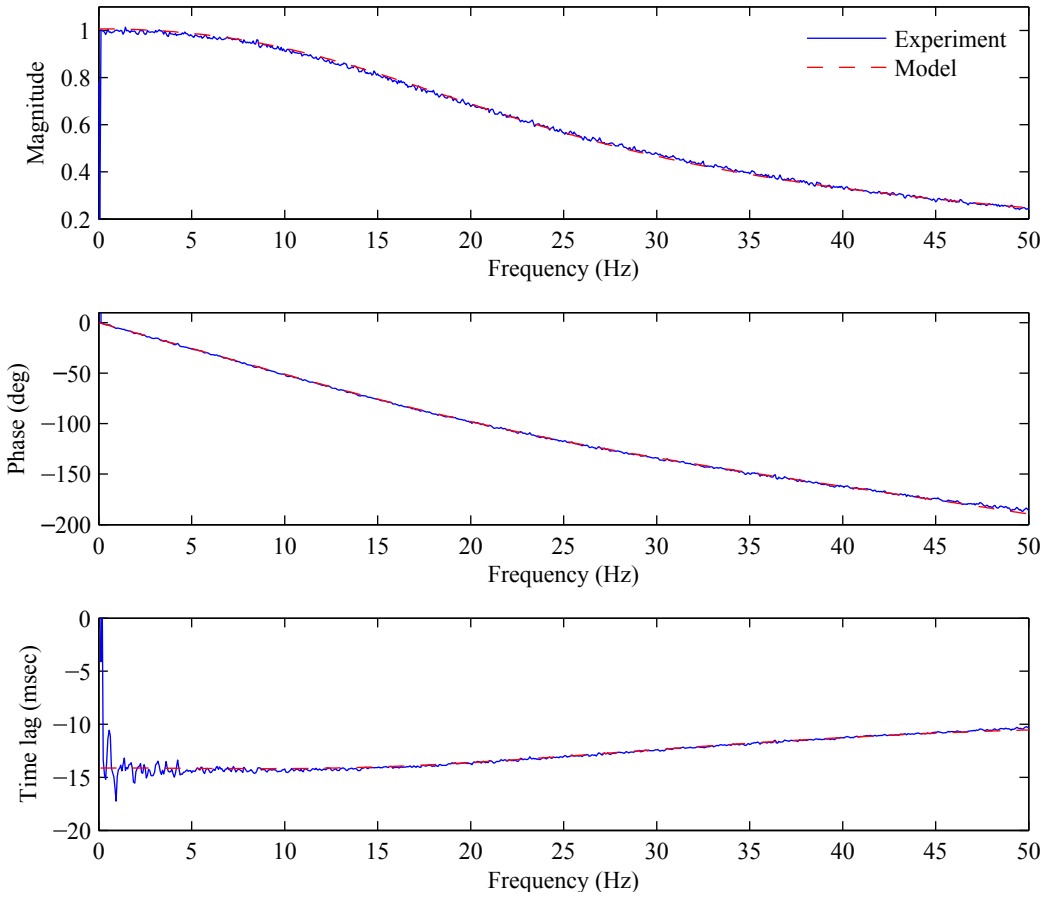

Figure 4.11: Comparison between the experimental data and obtained model for 2.0 A case

4.4.2 Feedforward-feedback compensator

In the feedforward-feedback compensator, the feedforward controller G_{FF} is designed based on the $G_{xu,\mathrm{avg}}(s)$ given by Eq. (4.11). Employing the BDM yields

$$G_{\mathrm{FF}}(z) = \sum_{k=0}^{5} b_k z^{-k} \tag{4.16}$$

where

$$\begin{aligned} b_0 &= 1.658 \times 10^4, \quad & b_1 &= -7.282 \times 10^4, \quad & b_2 &= 1.281 \times 10^5, \\ b_3 &= -1.126 \times 10^5, \quad & b_4 &= 4.947 \times 10^4, \quad & b_5 &= -8.675 \times 10^3. \end{aligned} \tag{4.17}$$

To design the feedback controller, the transfer function given by Eq. (4.11) is transformed into

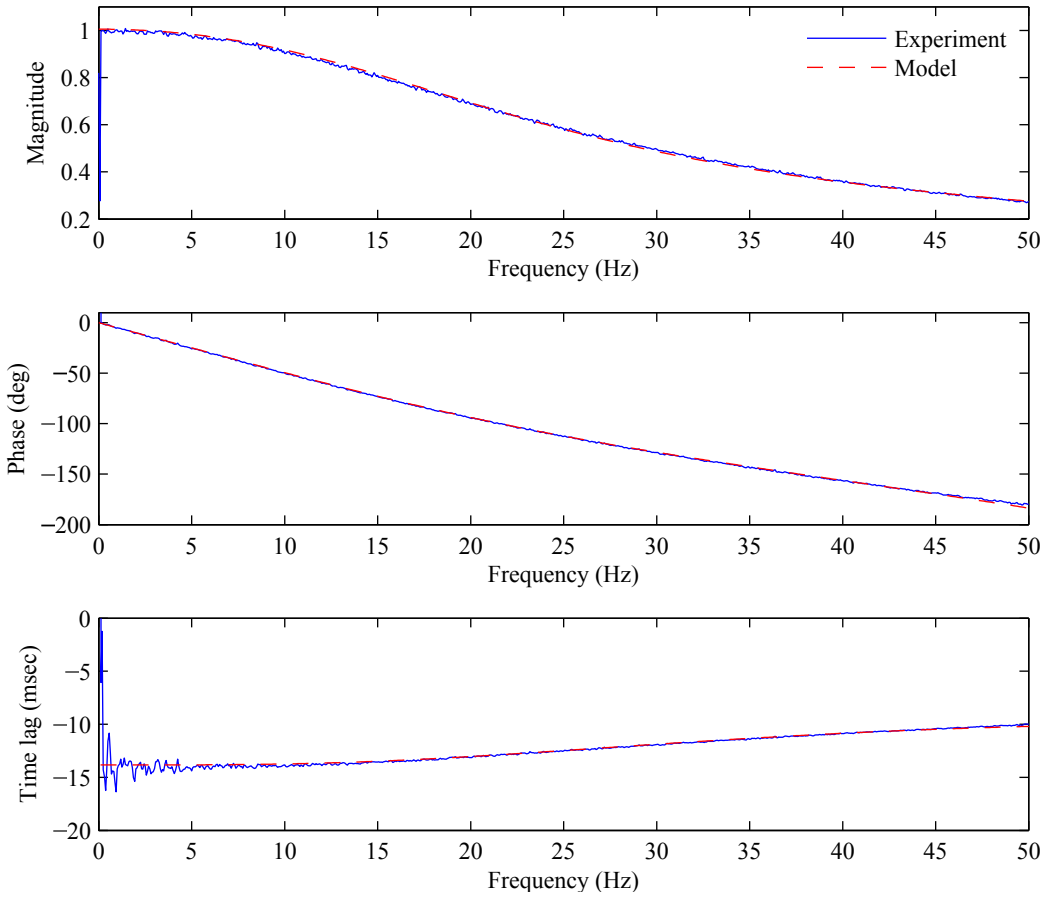

Figure 4.12: Comparison between the experimental data and obtained model for averaged case

a state-space form expressed as Eqs. (3.122) and (3.123). The parameters for the shaping filter given by Eqs. (3.131) and (3.132) are determined by trial and error as

$$\xi_{\mathrm{f}} = 0.7, \qquad \omega_{\mathrm{f}} = 20 \times 2\pi, \qquad \eta_{\mathrm{f}} = 0. \tag{4.18}$$

Then, the parameters for the state-space form of the LQG feedback controller, $\mathbf{A}_{\mathrm{FB}}$, $\mathbf{B}_{\mathrm{FB}}$, $\mathbf{C}_{\mathrm{FB}}$,

and D_{FB}, are calculated, in discrete time, as

$$\mathbf{A}_{\mathrm{FB}} = \begin{bmatrix} 0.881 & 1 & 0 & 0 & 0 & 0 \\ -0.006 & 0.881 & 0.129 & 0.190 & -0.166 & -0.117 \\ 0 & 0 & 0.934 & 1 & 0 & 0 \\ 0 & 0 & -0.004 & 0.934 & -0.038 & -0.027 \\ 0 & 0 & 0 & 0 & 0.921 & 1 \\ 0 & 0 & 0 & 0 & -0.036 & 0.921 \end{bmatrix}, \quad \mathbf{B}_{\mathrm{FB}} = \begin{bmatrix} 0 \\ 0.250 \\ 0 \\ 0.057 \\ 0 \\ 0.051 \end{bmatrix}, \tag{4.19}$$

$$\mathbf{C}_{\mathrm{FB}} = \begin{bmatrix} 0.023 & -0.484 & 0 & 0 & 0 & 0 \end{bmatrix}, \quad D_{\mathrm{FB}} = 0.$$

respectively. This feedback-feedforward compensator is employed for the RTHS in Chapter 8.

4.5 Summary

This chapter provided the MR damper model used for numerical simulations in this dissertation. The experimental setup for RTHS was presented and the servo-hydraulic system was identified. Also, the compensators based on the servo-hydraulic system were designed and their effectiveness was shown here. These compensators will be used for the RTHS verification studies later in this dissertation.

Chapter 5

Hysteresis Loops Produced by Active Control Forces

Active control methods have been applied to numerous civil structures in recent years. A significant amount of the research on active control methods has been based on full-state feedback using the linear quadratic regulator (LQR) control algorithm; because measurement of the full state (i.e., the displacements and velocities of all DOFs) is difficult, such algorithms are impractical in full-scale implementations. Output feedback strategies based on measured acceleration at a limited number of points have been proposed and validated. However, a thorough understanding of the dissipative nature of the associated control forces and the way in which these forces protect the structure have been elusive. Also, to unravel the relationship between the properties of active control forces and the responses will be helpful in designing and developing semi-active controllers.

This chapter considers the hysteric behavior of the control forces produced by the widely employed linear quadratic Gaussian (LQG)-based acceleration feedback control strategies. Numerical simulation studies on one-story and three-story buildings with active bracing are carried out.

5.1 Active control in acceleration feedback: Problem formulation

Consider a structural system, excited by a one-dimensional earthquake loading, with an equation of motion given by

$$\mathbf{M}_s\ddot{\mathbf{x}} + \mathbf{C}_s\dot{\mathbf{x}} + \mathbf{K}_s\mathbf{x} = \mathbf{G}_s\mathbf{f} - \mathbf{M}_s\mathbf{L}_s\ddot{x}_g \tag{5.1}$$

where $\mathbf{f}$ is the vector of control forces, $\ddot{x}_g$ is the ground acceleration, $\mathbf{M}_s$, $\mathbf{C}_s$, and $\mathbf{K}_s$ are the mass, linear damping and stiffness matrices of the structure, respectively, and $\mathbf{G}_s$ and $\mathbf{L}_s$ are the influence coefficient vectors of the control force and structural mass, respectively. $\mathbf{x}$ is the displacement vector, which is composed of the displacement of each floor relative to the ground. An over dot represents the time derivative.

A state-space representation of the equation of motion can be written as

$$\dot{\mathbf{z}} = \mathbf{A}\mathbf{z} + \mathbf{B}\mathbf{f} + \mathbf{E}\ddot{x}_g \tag{5.2}$$

$$\mathbf{y}_{\mathrm{m}} = \mathbf{C}_{\mathrm{m}}\mathbf{z} + \mathbf{D}_{\mathrm{m}}\mathbf{f} + \mathbf{F}_{\mathrm{m}}\ddot{x}_g + \mathbf{v} \tag{5.3}$$

$$\mathbf{y}_{\mathrm{e}} = \mathbf{C}_{\mathrm{e}}\mathbf{z} + \mathbf{D}_{\mathrm{e}}\mathbf{f} + \mathbf{F}_{\mathrm{e}}\ddot{x}_g \tag{5.4}$$

where $\mathbf{z}$ is the state variable of the story displacements and velocities relative to the base, that is,

$$\mathbf{z} = \begin{bmatrix} \mathbf{x}^T & \dot{\mathbf{x}}^T \end{bmatrix}^T \tag{5.5}$$

$\mathbf{y}_{\mathrm{m}}$ is the vector corresponding to the measured outputs including absolute accelerations, $\mathbf{v}$ is an observation noise vector, $\mathbf{y}_{\mathrm{e}}$ is the vector corresponding to the regulated outputs that are used for evaluation of the system. The matrices $\mathbf{A}$, $\mathbf{B}$, and $\mathbf{E}$ are given as

$$\mathbf{A} = \begin{bmatrix} \mathbf{0} & \mathbf{I} \\ -\mathbf{M}_{\mathrm{s}}^{-1}\mathbf{K}_{\mathrm{s}} & -\mathbf{M}_{\mathrm{s}}^{-1}\mathbf{C}_{\mathrm{s}} \end{bmatrix} \tag{5.6}$$

$$\mathbf{B} = \begin{bmatrix} \mathbf{0} \\ \mathbf{M}_{\mathrm{s}}^{-1}\mathbf{G}_{\mathrm{s}} \end{bmatrix} \tag{5.7}$$

$$\mathbf{E} = \begin{bmatrix} \mathbf{0} \\ -\mathbf{L}_{\mathrm{s}} \end{bmatrix} \tag{5.8}$$

And $\mathbf{C}_{\mathrm{m}}$, $\mathbf{C}_{\mathrm{e}}$, $\mathbf{D}_{\mathrm{m}}$, $\mathbf{D}_{\mathrm{e}}$, $\mathbf{F}_{\mathrm{m}}$, and $\mathbf{F}_{\mathrm{e}}$ are appropriately chosen matrices corresponding to the associated output vectors. Acceleration feedback control strategies for the structure described in Eqs. (5.2), (5.3), and (5.4) can be derived based on LQG methods. For the control design, the absolute acceleration of the ground, $\ddot{x}_g$, is taken to be a stationary filtered white noise, and an infinite horizon performance index is chosen that weights the regulated output vector, $\mathbf{y}_{\mathrm{e}}$; that is,

$$J = \lim_{\tau\to\infty} \frac{1}{\tau} \mathrm{E}\left[\int_0^\infty \left\{ (\mathbf{C}_{\mathrm{e}}\mathbf{z} + \mathbf{D}_{\mathrm{e}}\mathbf{f})^T \mathbf{Q} (\mathbf{C}_{\mathrm{e}}\mathbf{z} + \mathbf{D}_{\mathrm{e}}\mathbf{f}) + \mathbf{f}^T\mathbf{R}\mathbf{f} \right\} dt \right] \tag{5.9}$$

where $\mathbf{Q}$ and $\mathbf{R}$ are called weighting matrices. Further, the observation noise is assumed to be an identically distributed, statistically independent Gaussian white noise process. The separation principle is invoked to allow the control and estimation problems to be considered independently. The resulting controller is of the form (Stengel, 1994; Skelton, 1988)

$$\mathbf{f} = -\mathbf{K}\hat{\mathbf{z}} \tag{5.10}$$

where $\hat{\mathbf{z}}$ is the estimated state vector obtained from the Kalman filter, and $\mathbf{K}$ is the full state feedback gain matrix for the deterministic regulator problem given by

$$\mathbf{K} = \tilde{\mathbf{R}}^{-1}(\tilde{\mathbf{N}} + \mathbf{B}^T\mathbf{P}) \tag{5.11}$$

$\mathbf{P}$ is the solution of the algebraic Riccati equation given by

$$\mathbf{P}\tilde{\mathbf{A}} + \tilde{\mathbf{A}}\mathbf{P} - \mathbf{P}\mathbf{B}\mathbf{R}^{-1}\mathbf{B}^T\mathbf{P} + \tilde{\mathbf{Q}} = \mathbf{0} \tag{5.12}$$

and

$$\tilde{\mathbf{Q}} = \mathbf{C}_{\mathrm{e}}^T\mathbf{Q}\mathbf{C}_{\mathrm{e}} - \tilde{\mathbf{N}}\tilde{\mathbf{R}}^{-1}\tilde{\mathbf{N}}^T \tag{5.13}$$

$$\tilde{\mathbf{R}} = \mathbf{R} + {\mathbf{D}_{\mathrm{e}}}^T\mathbf{Q}\mathbf{D}_{\mathrm{e}} \tag{5.14}$$

$$\tilde{\mathbf{A}} = \mathbf{A} - \mathbf{B}\tilde{\mathbf{R}}^{-1}\tilde{\mathbf{N}}^T \tag{5.15}$$

The Kalman filter optimal estimator is given by

$$\dot{\hat{\mathbf{z}}} = \mathbf{A}\hat{\mathbf{z}} + \mathbf{B}\mathbf{f} + \mathbf{L}(\mathbf{y}_{\mathrm{m}} - \mathbf{C}_{\mathrm{m}}\hat{\mathbf{z}} - \mathbf{D}_{\mathrm{m}}\mathbf{f} - \mathbf{F}_{\mathrm{m}}\ddot{x}_g) \tag{5.16}$$

$$\mathbf{L} = (\mathbf{S}\mathbf{C}_{\mathrm{m}} + W\mathbf{E}\mathbf{F}_{\mathrm{m}}^T)\underset{\sim}{\mathbf{R}}^{-1} \tag{5.17}$$

where $\mathbf{S}$ is the solution of the algebraic Ricatti equation given by

$$\mathbf{S}\underset{\sim}{\mathbf{A}} + \underset{\sim}{\mathbf{A}}^T\mathbf{S} - \mathbf{S}\underset{\sim}{\mathbf{G}}\mathbf{S} + \underset{\sim}{\mathbf{H}} = \mathbf{0} \tag{5.18}$$

and

$$\underset{\sim}{\mathbf{A}} = \mathbf{A}^T - \mathbf{C}_\mathrm{m}\underset{\sim}{\mathbf{R}}^{-1}(W\mathbf{F}_\mathrm{m}\mathbf{E}) \tag{5.19}$$

$$\underset{\sim}{\mathbf{G}} = \mathbf{C}_\mathrm{m}^T\underset{\sim}{\mathbf{R}}^{-1}\mathbf{C}_\mathrm{m} \tag{5.20}$$

$$\underset{\sim}{\mathbf{H}} = W\mathbf{E}\mathbf{E}^T - W^2\mathbf{E}\mathbf{F}_\mathrm{m}\underset{\sim}{\mathbf{R}}^{-1}\mathbf{F}_\mathrm{m}\mathbf{E}^T \tag{5.21}$$

$$\underset{\sim}{\mathbf{R}} = \mathbf{V} + W\mathbf{F}_\mathrm{m}\mathbf{F}_\mathrm{m}^T \tag{5.22}$$

where W and $\mathbf{V}$ are magnitude of the constant two-sided spectral densities for the white noises used in the LQG control design. The controller given in Eq. (5.10) has been shown to be effective in protecting structural systems from seismic loading (Dyke et al., 1996b).

5.2 Hysteresis control force loops by numerical simulations

To investigate the nature of the energy dissipation capabilities of acceleration feedback control strategies clearly, first, a one-story building model shown in Figure 5.1(a) is considered. Subsequently, the three-story model shown in Figure 5.1(b) is investigated to determine if the trends found in the one-story model are also seen in multi-DOFs structures. The three-story building model was previously investigated by Dyke et al. (1995, 1996a). Because the actuator is installed between the first floor and the ground, its displacement is equal to the displacement of the first floor of the structure relative to the ground. Here, x_i, $\dot{x}_i$, $\ddot{x}_{ai}$ and d_i represent relative displacement, relative velocity, absolute accelerations of ith floor, and inter-story drift between ith and $(i-1)$th floor (i.e., $x_i - x_{i-1}$), respectively. f is the force in the actuator installed between the ground and the first floor.

The models are subjected to 1940 El Centro NS and 1995 JMA Kobe NS earthquake records using numerical simulation. To satisfy scaling laws, the earthquakes must be reproduced at five times the recorded rate. The time histories of the employed earthquake records are shown in Figure 5.2.

To explore how the weighting matrices affect the natural frequency, the damping ratio, and the hysteresis loops produced by the LQG controller, various values of the weighting matrices $\mathbf{Q}$ and

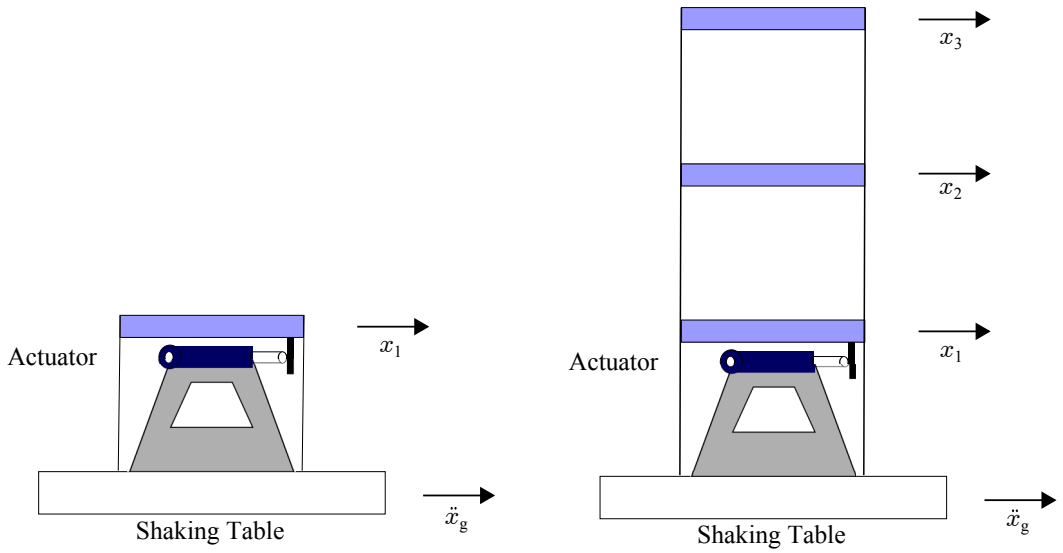

Figure 5.1: Schematic diagram; (a) One-story building model, (b) three-story building model

R in Eq. (5.9) are employed. The earthquake input energy is defined as (Chopra, 2007)

$$E_{\mathrm{i}} = -\int_0^t \dot{\mathbf{x}}^T \mathbf{M}_{\mathrm{s}} \mathbf{L}_{\mathrm{s}} \ddot{x}_g d\tau \tag{5.23}$$

and investigated for each case. The LQR controller is applied as well by assuming that all state vectors are measurable and compared with the analogous LQG controller.

5.2.1 One-story building model

For the one-story structure as shown in Figure 5.1(a), the parameters given in Eq. (5.1) are

$$\mathbf{M}_{\mathrm{s}} = M_{\mathrm{s}} = 98.3 \text{ (kg)}, \qquad \mathbf{C}_{\mathrm{s}} = C_{\mathrm{s}} = 125 \text{ (N·sec/m)}, \qquad \mathbf{K}_{\mathrm{s}} = K_{\mathrm{s}} = 5.16 \times 10^5 \text{ (N/m)},$$
$$\mathbf{f} = f, \qquad \mathbf{G}_{\mathrm{s}} = G_{\mathrm{s}} = -1, \qquad \mathbf{L}_{\mathrm{s}} = L_{\mathrm{s}} = 1. \tag{5.24}$$

The state vector $\mathbf{z}$ in Eqs. (5.2), (5.3), (5.4), and (5.5) is then

$$\mathbf{z} = \begin{bmatrix} x_1 & \dot{x}_1 \end{bmatrix}^T \tag{5.25}$$

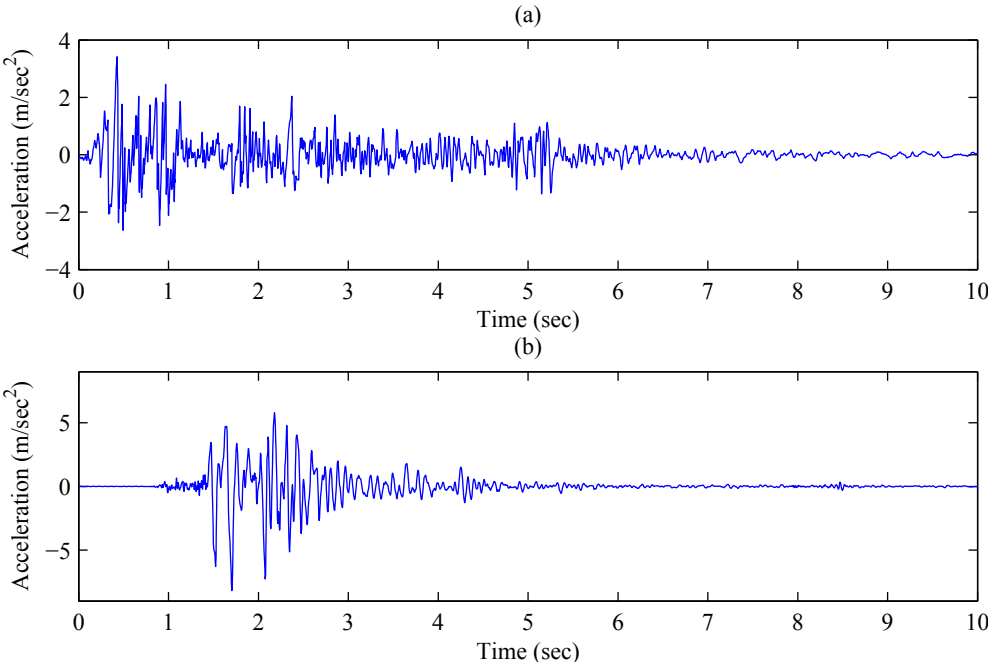

Figure 5.2: Earthquake records; (a) 1940 El Centro NS, (b) 1995 JMA Kobe NS

Also, the measurement vector $\mathbf{y}_\mathrm{m}$ in Eq. (5.3) and the evaluation vector $\mathbf{y}_\mathrm{e}$ in Eq. (6.4) are defined by

$$\mathbf{y}_\mathrm{m} = \begin{bmatrix} x_1 & \ddot{x}_\mathrm{a1} \end{bmatrix}^T \tag{5.26}$$

$$\mathbf{y}_\mathrm{e} = \begin{bmatrix} x_1 & \ddot{x}_\mathrm{a1} \end{bmatrix}^T \tag{5.27}$$

respectively. Therefore, in this case, the matrices $\mathbf{C}_\mathrm{m}$, $\mathbf{C}_\mathrm{e}$, $\mathbf{D}_\mathrm{m}$, $\mathbf{D}_\mathrm{e}$, $\mathbf{E}_\mathrm{m}$, and $\mathbf{E}_\mathrm{e}$ can be written as

$$\mathbf{C}_\mathrm{m} = \mathbf{C}_\mathrm{e} = \begin{bmatrix} 1 & 0 \\ -\frac{K_\mathrm{s}}{M_\mathrm{s}} & -\frac{C_\mathrm{s}}{M_\mathrm{s}} \end{bmatrix}, \qquad \mathbf{D}_\mathrm{m} = \mathbf{D}_\mathrm{e} = \begin{bmatrix} 0 \\ \frac{G_\mathrm{s}}{M_\mathrm{s}} \end{bmatrix}, \qquad \mathbf{F}_\mathrm{m} = \mathbf{F}_\mathrm{e} = \mathbf{0}_{2\times 1} \tag{5.28}$$

Hence, the weighting matrices $\mathbf{Q}$ and $\mathbf{R}$ in Eq. (5.9) should be a 2×2 matrix and a scalar, R, respectively. Here, the weighting matrix $\mathbf{Q}$ is set as follows: all of the elements of the displacement weighting matrix $\mathbf{Q}_\mathrm{d}$ are zero, except for $Q_{\mathrm{d}11} = 1$, and all of the elements of the acceleration weighting matrix $\mathbf{Q}_\mathrm{a}$ are zero, except for $\mathbf{Q}_{\mathrm{a}22} = 1$. We assume that power spectral densities W and $\mathbf{V}$ are 5×10^4 and $\mathbf{I}_{2\times 2}$, respectively. These values are determined by trial and error so that the LQG shows good performance compared to the LQR controller. Calculations to determine $\mathbf{K}$

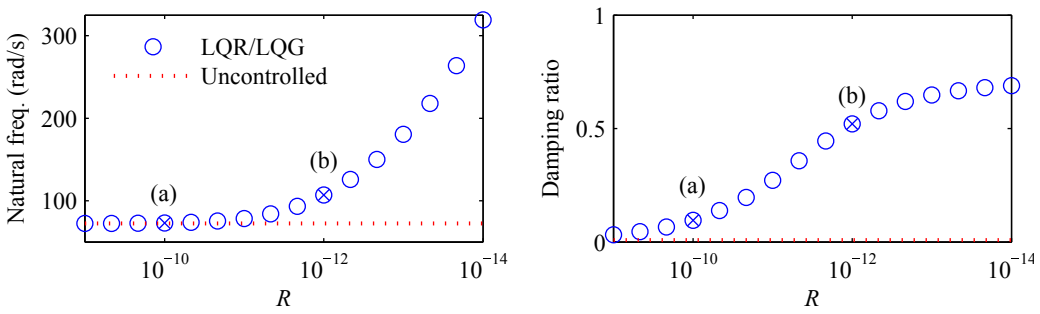

Figure 5.3: Natural frequency and damping ratio of the one-story building model for displacement weighting; (a) $\mathbf{Q} = \mathbf{Q}_{\mathrm{d}}$, $R = 10^{-10}$, (b) $\mathbf{Q} = \mathbf{Q}_{\mathrm{d}}$, $R = 10^{-12}$

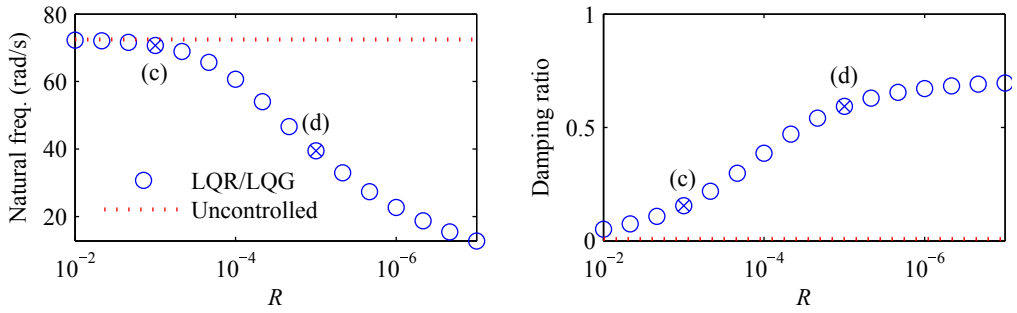

Figure 5.4: Natural frequency and damping ratio of the one-story building model for acceleration weighting; (c) $\mathbf{Q} = \mathbf{Q}_{\mathrm{a}}$, $R = 10^{-3}$, (d) $\mathbf{Q} = \mathbf{Q}_{\mathrm{a}}$, $R = 10^{-5}$

in Eq. (5.11) and $\mathbf{L}$ in Eq. (5.17) are performed using the control toolbox in MATLAB (2013).

Figures 5.3 and 5.4 show how natural frequencies and damping ratios are affected by changing the value of R in the case of both displacement and acceleration weightings, respectively. From the separation theorem, the poles (i.e., natural frequencies and damping ratios) obtained by the LQG are the sum of the poles from the LQR and the Kalman filter. From Figure 5.3, the actuator controlled by displacement weighted LQR and LQG results in the natural frequency of the building model increasing as the control authority increases (i.e., R decreases), which means that the controller added positive stiffness to the structure. In contrast, Figure 5.4 shows that acceleration weighting leads to smaller natural frequency as the control authority is increased (i.e., R decreases), which indicates that the controller adds a negative stiffness on the structure. Figures 5.3 and 5.4 also show that the damping ratios become larger as the control force increases in both cases.

Figures 5.5 and 5.6 show hysteresis loops of the actuator produced by the LQG and the LQR

Table 5.1: Peak values for the one-story model to 1940 El Centro NS; (a) $\mathbf{Q} = \mathbf{Q}_{\mathrm{d}}$, $R = 10^{-10}$, (b) $\mathbf{Q} = \mathbf{Q}_{\mathrm{d}}$, $R = 10^{-12}$, (c) $\mathbf{Q} = \mathbf{Q}_{\mathrm{a}}$, $R = 10^{-3}$, (d) $\mathbf{Q} = \mathbf{Q}_{\mathrm{a}}$, $R = 10^{-5}$

		(a)		(b)		(c)		(d)	
Parameter	Uncontrolled	LQG	LQR	LQG	LQR	LQG	LQR	LQG	LQR
x_1 (cm)	0.173	0.099	0.098	0.032	0.029	0.099	0.097	0.102	0.097
$\ddot{x}_{\mathrm{a1}}$ (m/s^2)	9.098	5.389	5.310	3.798	3.728	4.995	4.957	3.404	3.333
f (N)	N/A	93.3	93.7	274.1	261.4	152.5	152.6	422.6	408.3

Table 5.2: Peak values for the one-story model to 1995 JMA Kobe NS; (a) $\mathbf{Q} = \mathbf{Q}_{d}$, $R = 10^{-10}$, (b) $\mathbf{Q} = \mathbf{Q}_{d}$, $R = 10^{-12}$, (c) $\mathbf{Q} = \mathbf{Q}_{a}$, $R = 10^{-3}$, (d) $\mathbf{Q} = \mathbf{Q}_{a}$, $R = 10^{-5}$

		(a)		(b)		(c)		(d)	
Parameter	Uncontrolled	LQG	LQR	LQG	LQR	LQG	LQR	LQG	LQR
x_1 (cm)	0.641	0.332	0.327	0.078	0.070	0.291	0.285	0.352	0.336
$\ddot{x}_{\mathrm{a1}}$ (m/s^2)	33.674	17.819	17.687	8.885	8.758	14.758	14.599	8.977	8.796
f (N)	N/A	241.4	241.2	529.1	523.1	336.2	329.2	1404.8	1350.7

controllers when 1940 El Centro NS and 1995 JMA Kobe NS are input, respectively. Here, four cases are considered for the LQG and the LQR controllers: (a) $\mathbf{Q} = \mathbf{Q}_{\mathrm{d}}$, $R = 10^{-10}$ (displacement weighting with small control force); (b) $\mathbf{Q} = \mathbf{Q}_{\mathrm{d}}$, $R = 10^{-12}$ (displacement weighting with large control force): (c) $\mathbf{Q} = \mathbf{Q}_{\mathrm{a}}$, $R = 10^{-3}$ (acceleration weighting with small control force); and (d) $\mathbf{Q} = \mathbf{Q}_{\mathrm{a}}$, $R = 10^{-5}$ (acceleration weighting with large control force). Peak values of relative displacement, absolute acceleration, and actuator force are summarized in Tables 5.1 and 5.2. Plots of energy input to the structure by the earthquake, that is, Eq. (5.23), for the four cases are shown in Figures 5.7 and 5.8.

The results shown in Figures 5.3 and 5.4 are confirmed in Figures 5.5 and 5.6, where the hysteresis loops of the actuators controlled by the LQG and the LQR are seen to produce both positive and negative stiffness, depending on the weighting matrices employed. Moreover, the LQG and the LQR produced quite similar hysteresis loops, as well as earthquake input energy (see Figures 5.7 and 5.8), although the LQR controller showed slightly better performance. Finally, Tables 5.1 and 5.2 confirms that the displacement responses were reduced by the controller using displacement weighting, and the acceleration responses were reduced by the controllers using acceleration weighting.

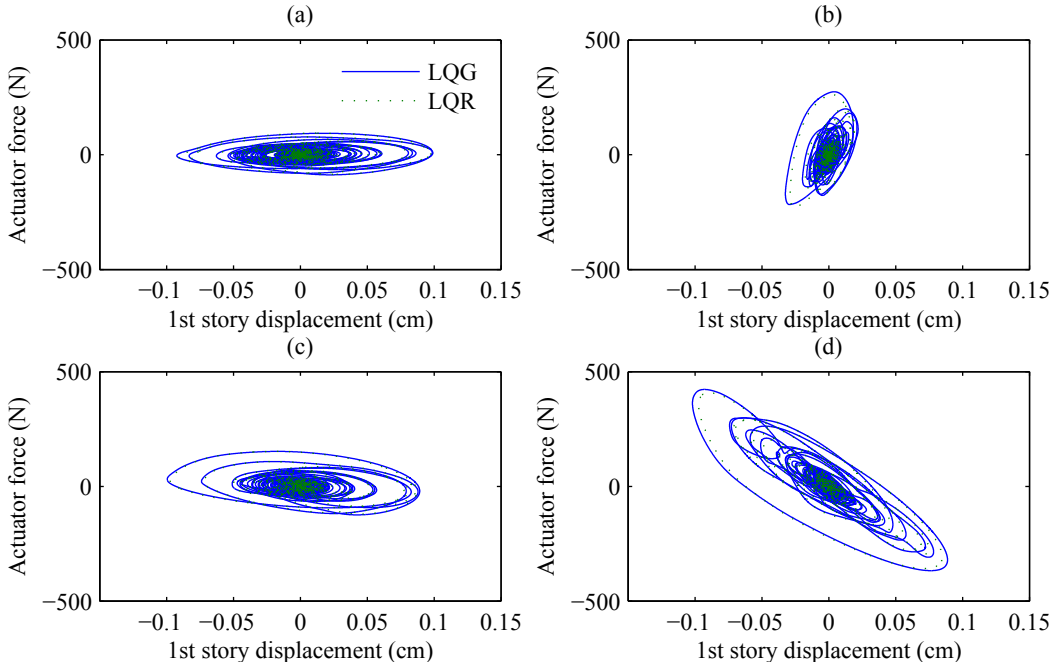

Figure 5.5: Hysteresis control force loops for the one-story model produced by LQR and LQG to 1940 El Centro NS; (a) $\mathbf{Q} = \mathbf{Q}_{\rm d}$, $R = 10^{-10}$, (b) $\mathbf{Q} = \mathbf{Q}_{\rm d}$, $R = 10^{-12}$, (c) $\mathbf{Q} = \mathbf{Q}_{\rm a}$, $R = 10^{-3}$, (d) $\mathbf{Q} = \mathbf{Q}_{\rm a}$, $R = 10^{-5}$

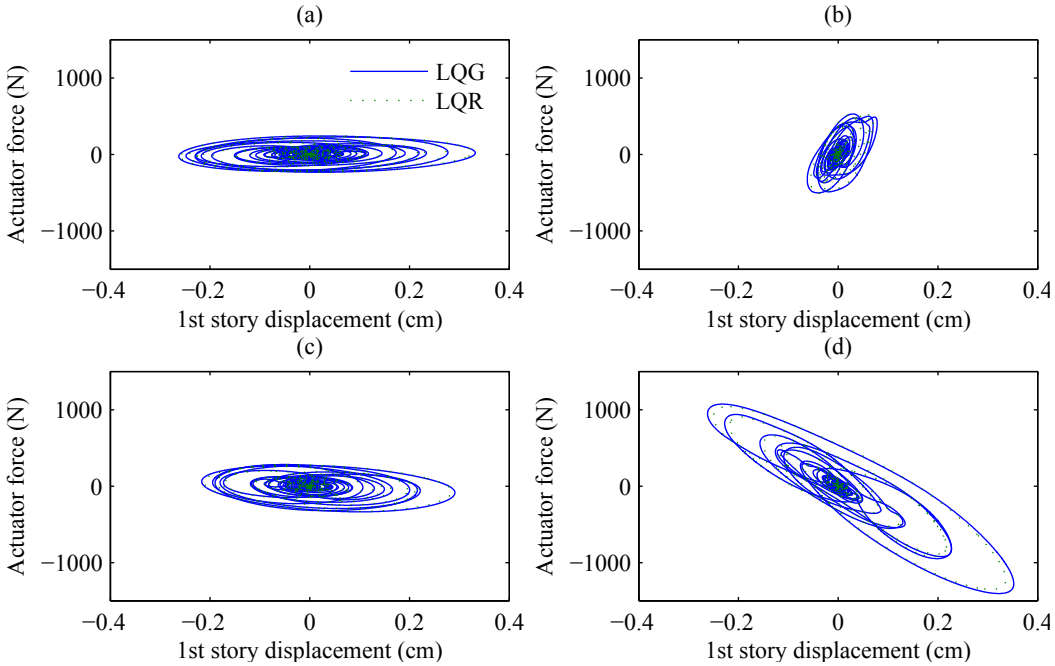

Figure 5.6: Hysteresis control force loops for the one-story model produced by LQR and LQG to 1995 Kobe NS; (a) $\mathbf{Q} = \mathbf{Q}_{\rm d}$, $R = 10^{-10}$, (b) $\mathbf{Q} = \mathbf{Q}_{\rm d}$, $R = 10^{-12}$, (c) $\mathbf{Q} = \mathbf{Q}_{\rm a}$, $R = 10^{-3}$, (d) $\mathbf{Q} = \mathbf{Q}_{\rm a}$, $R = 10^{-5}$

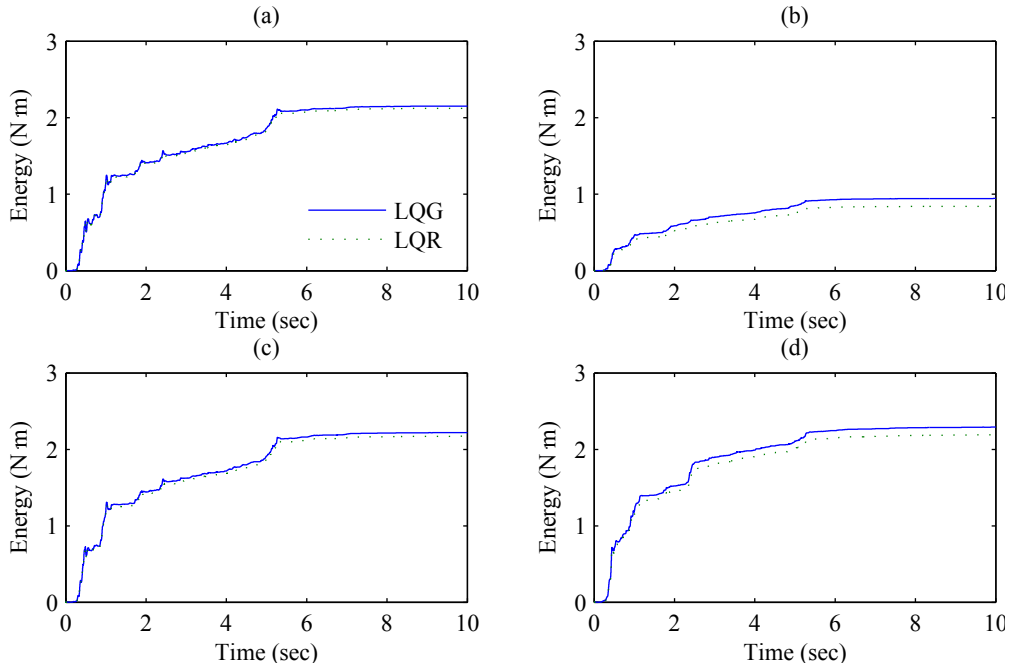

Figure 5.7: Earthquake input energy of a one-story model by LQG and LQR to 1940 El Centro NS; (a) $\mathbf{Q} = \mathbf{Q}_{\rm d}$, $R = 10^{-10}$, (b) $\mathbf{Q} = \mathbf{Q}_{\rm d}$, $R = 10^{-12}$, (c) $\mathbf{Q} = \mathbf{Q}_{\rm a}$, $R = 10^{-3}$, (d) $\mathbf{Q} = \mathbf{Q}_{\rm a}$, $R = 10^{-5}$

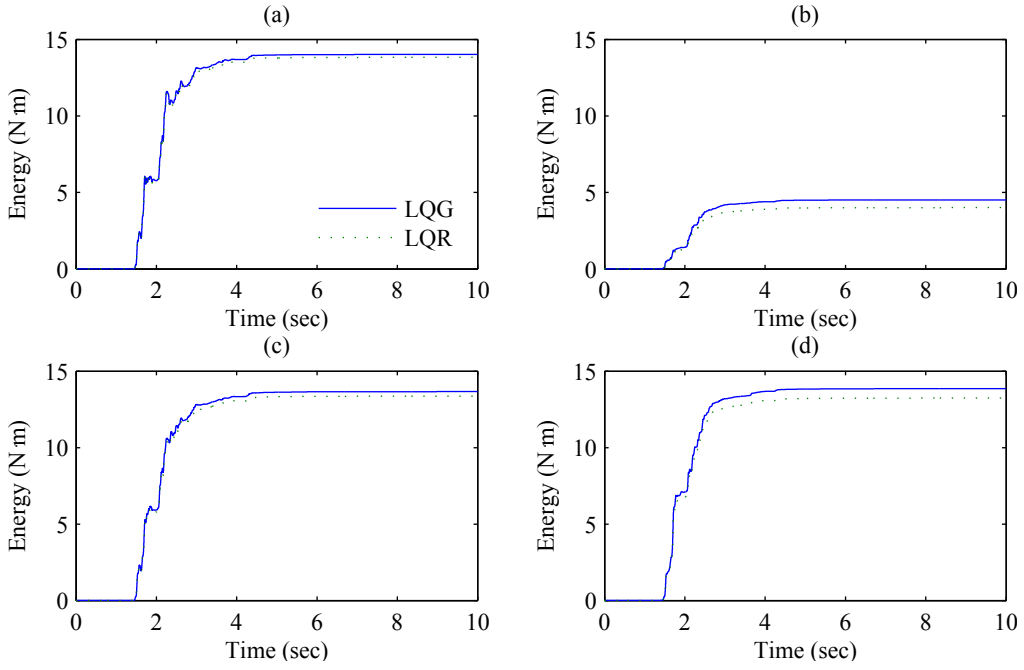

Figure 5.8: Earthquake input energy of a one-story model by LQG and LQR to 1995 JMA Kobe NS; (a) $\mathbf{Q} = \mathbf{Q}_{\rm d}$, $R = 10^{-10}$, (b) $\mathbf{Q} = \mathbf{Q}_{\rm d}$, $R = 10^{-12}$, (c) $\mathbf{Q} = \mathbf{Q}_{\rm a}$, $R = 10^{-3}$, (d) $\mathbf{Q} = \mathbf{Q}_{\rm a}$, $R = 10^{-5}$

The next section investigates active control of a three-story model to see if the trends found in the one-story controlled structure are also found in multi-DOF structures.

5.2.2 Three-story building model

For the three-story structure as shown in Figure 5.1(b), the parameters for the equation of motion given in Eq. (5.1) are

$$\begin{gathered}\mathbf{M}_{\mathrm{s}}=\begin{bmatrix}98.3 & 0 & 0\\ 0 & 98.3 & 0\\ 0 & 0 & 98.3\end{bmatrix}\ (\mathrm{kg}),\qquad \mathbf{C}_{\mathrm{s}}=\begin{bmatrix}175 & -50 & 0\\ -50 & 100 & -50\\ 0 & -50 & 50\end{bmatrix}\ (\mathrm{N{\cdot}sec/m}),\\ \mathbf{K}_{\mathrm{s}}=10^5\begin{bmatrix}12.0 & -6.84 & 0\\ -6.84 & 13.7 & -6.84\\ 0 & -6.84 & 6.84\end{bmatrix}\ (\mathrm{N/m}),\qquad \mathbf{f}=f,\qquad \mathbf{G}_{\mathrm{s}}=\begin{bmatrix}-1\\ 0\\ 0\end{bmatrix},\qquad \mathbf{L}_{\mathrm{s}}=\begin{bmatrix}1\\ 1\\ 1\end{bmatrix}\end{gathered}\tag{5.29}$$

The state vector $\mathbf{z}$ in Eqs. (5.2), (5.3), (5.4), and (5.5) is then

$$\mathbf{z}=\begin{bmatrix}x_1 & x_2 & x_3 & \dot{x}_1 & \dot{x}_2 & \dot{x}_3\end{bmatrix}^T\tag{5.30}$$

Also, the measurement vector $\mathbf{y}_{\mathrm{m}}$ in Eq. (5.3) and the evaluation vector $\mathbf{y}_{\mathrm{e}}$ in Eq. (5.4) are defined by

$$\mathbf{y}_{\mathrm{m}}=\begin{bmatrix}x_1 & \ddot{x}_{\mathrm{a}1} & \ddot{x}_{\mathrm{a}2} & \ddot{x}_{\mathrm{a}3}\end{bmatrix}^T\tag{5.31}$$

$$\mathbf{y}_{\mathrm{e}}=\begin{bmatrix}x_1 & d_2 & d_3 & \ddot{x}_{\mathrm{a}1} & \ddot{x}_{\mathrm{a}2} & \ddot{x}_{\mathrm{a}3}\end{bmatrix}^T\tag{5.32}$$

Therefore, the matrices $\mathbf{C}_\mathrm{m}$, $\mathbf{C}_\mathrm{e}$, $\mathbf{D}_\mathrm{m}$, $\mathbf{D}_\mathrm{e}$, $\mathbf{E}_\mathrm{m}$, and $\mathbf{E}_\mathrm{e}$ become

$$\mathbf{C}_\mathrm{m} = \begin{bmatrix} 1 & 0 & 0 & \mathbf{0}_{1\times 3} \\ -\mathbf{M}_\mathrm{s}^{-1}\mathbf{K}_\mathrm{s} & & & -\mathbf{M}_\mathrm{s}^{-1}\mathbf{C}_\mathrm{s} \end{bmatrix}, \qquad \mathbf{C}_\mathrm{e} = \begin{bmatrix} \mathbf{\Delta} & \mathbf{0}_{3\times 3} \\ -\mathbf{M}_\mathrm{s}^{-1}\mathbf{K}_\mathrm{s} & -\mathbf{M}_\mathrm{s}^{-1}\mathbf{C}_\mathrm{s} \end{bmatrix},$$

$$\mathbf{\Delta} = \begin{bmatrix} 1 & 0 & 0 \\ -1 & 1 & 0 \\ 0 & -1 & 1 \end{bmatrix}, \qquad \mathbf{D}_\mathrm{m} = \begin{bmatrix} 0 \\ \mathbf{M}_\mathrm{s}^{-1}\mathbf{G}_\mathrm{s} \end{bmatrix}, \qquad \mathbf{D}_\mathrm{e} = \begin{bmatrix} \mathbf{0}_{3\times 1} \\ \mathbf{M}_\mathrm{s}^{-1}\mathbf{G}_\mathrm{s} \end{bmatrix}, \tag{5.33}$$

$$\mathbf{F}_\mathrm{m} = \mathbf{0}_{4\times 1}, \qquad \mathbf{F}_\mathrm{e} = \mathbf{0}_{6\times 1}$$

Hence, the weighting matrices $\mathbf{Q}$ and $\mathbf{R}$ in Eq. (5.9) should be a 6×6 matrix and a scalar R, respectively. Here, two cases are considered. The first case weights the second and third inter-story drifts equally, whereas the weighting on the first floor relative displacement is taken as a control design parameter α; that is

$$\mathbf{Q}_\mathrm{d} = \mathrm{diag}\left(\begin{bmatrix} \alpha & 1 & 1 & 0 & 0 & 0 \end{bmatrix}\right) \tag{5.34}$$

The second case places equal weighting on the acceleration of each floor of the structure; that is,

$$\mathbf{Q}_\mathrm{a} = \mathrm{diag}(\begin{bmatrix} 0 & 0 & 0 & 1 & 1 & 1 \end{bmatrix}) \tag{5.35}$$

The power spectral densities of the disturbance W and the measurement noise vector $\mathbf{V}$ are chosen to be 5×10^4 and $\mathbf{I}_{4\times 4}$, respectively, so as to achieve comparable control performance with the LQR controller.

Figure 5.9 shows contours of the natural frequencies and damping ratios of first, second, and third modes for the displacement weighted LQR/LQG controllers as a function of R and α. The natural frequencies of the uncontrolled model for three modes are 34.2 rad/sec, 99.3 rad/sec, and 148.5 rad/sec, and noted in this figure by a heavier line weight. As can be seen here, the natural frequency of the first mode increases as a increases, regardless of the value of R. This result indicates that the controller can produce both positive and negative stiffness contributions to the first mode. Additionally, Fig. 5.9 shows that the natural frequencies of the second and third modes are not substantially affected by α, and that the damping ratio increases generally as the control force gets larger, as was the case of the one-story building model.

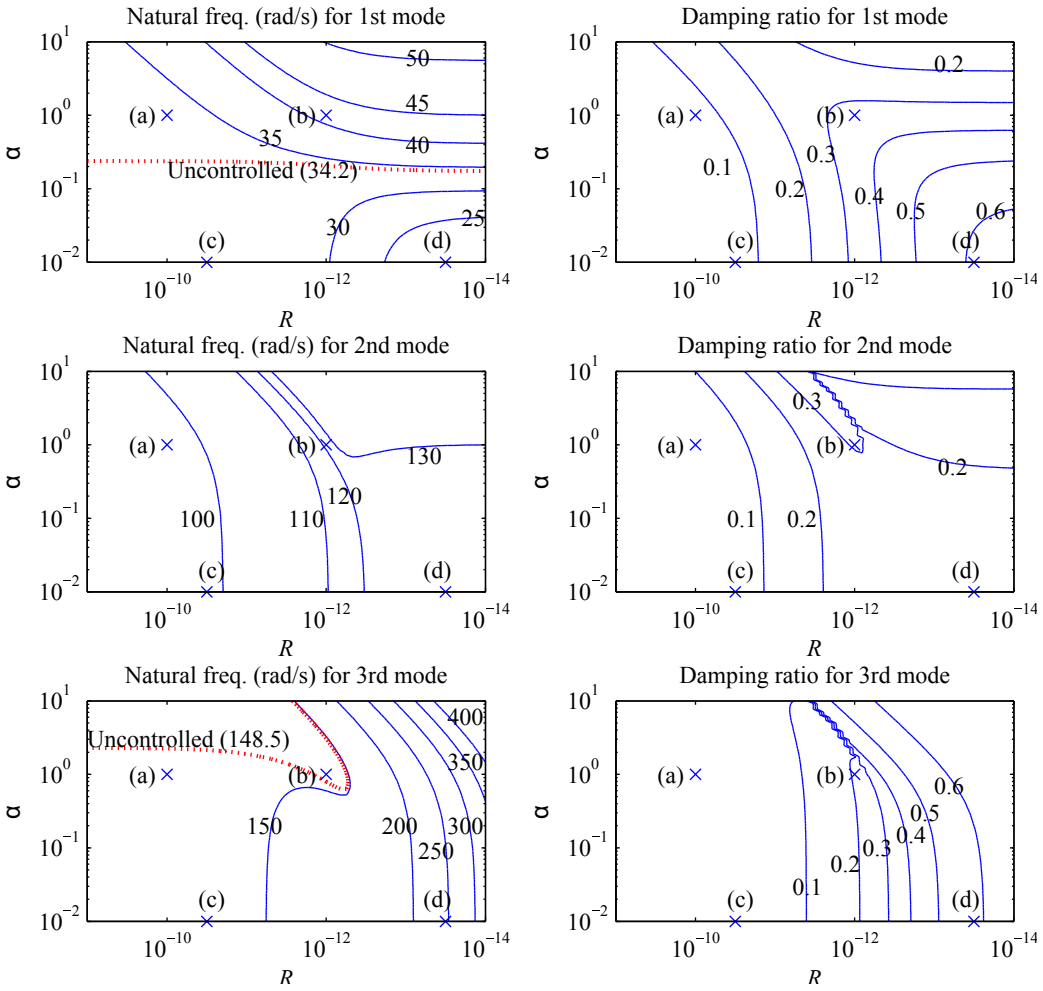

Figure 5.9: Natural frequency and damping ratio of the three-story building model for displacement weighting; (a) $\mathbf{Q} = \mathbf{Q}_{\mathrm{d}}(\alpha = 1)$, $R = 10^{-10}$, (b) $\mathbf{Q} = \mathbf{Q}_{\mathrm{d}}(\alpha = 1)$, $R = 10^{-12}$, (c) $\mathbf{Q} = \mathbf{Q}_{\mathrm{d}}(\alpha = 0.01)$, $R = 10^{-10.5}$, (d) $\mathbf{Q} = \mathbf{Q}_{\mathrm{d}}(\alpha = 0.01)$, $R = 10^{-13.5}$

Figure 5.10 shows the natural frequencies and damping ratios of the first, second, and third modes as a function of R for acceleration weighting. For this case, the natural frequencies of all modes decrease as the control force increases (i.e., R decreases); additionally, the damping ratio of the first mode increases as the control force is increased, which is again similar to the one-story model.

Six specific cases are considered for more investigation: (a) $\mathbf{Q} = \mathbf{Q}_{\mathrm{d}}(\alpha = 1)$, $R = 10^{-10}$ (equal inter-story displacement weighting, with small control force); (b) $\mathbf{Q} = \mathbf{Q}_{\mathrm{d}}(\alpha = 1)$, $R = 10^{-12}$ (equal inter-story displacement weighting, with large control force); (c) $\mathbf{Q} = \mathbf{Q}_{\mathrm{d}}(\alpha = 0.01)$, $R = 10^{-10.5}$ (inter-story displacement weighting mainly on the second and third stories, with small control

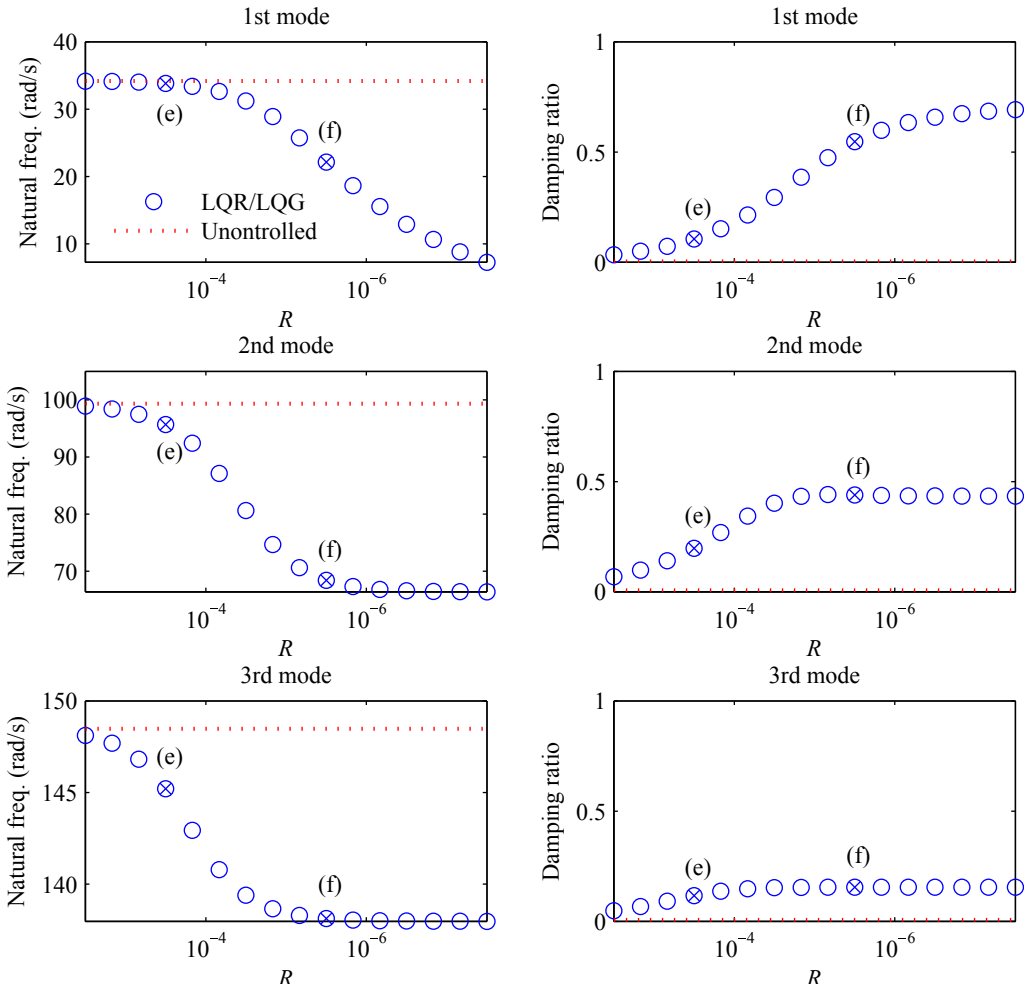

Figure 5.10: Natural frequency and damping ratio of the three-story building model for acceleration weighting; (c) $\mathbf{Q} = \mathbf{Q}_{\mathrm{a}}$, $R = 10^{-3.5}$, (d) $\mathbf{Q} = \mathbf{Q}_{\mathrm{a}}$, $R = 10^{-5.5}$

force); (d) $\mathbf{Q} = \mathbf{Q}_{\mathrm{d}}(\alpha = 0.01)$, $R = 10^{-13.5}$ (inter-story displacement weighting mainly on the second and third stories, with large control force); (e) $\mathbf{Q} = \mathbf{Q}_{\mathrm{a}}$, $R = 10^{-3.5}$ (equal acceleration weighting, with small control force); and (f) $\mathbf{Q} = \mathbf{Q}_{\mathrm{a}}$, $R = 10^{-5.5}$ (equal acceleration weighting, with large control force). These controllers are marked with an x in Figs. 5.9 and 5.10. Figure 5.9 shows that controller (a) produces positive stiffness in all modes, controller (b) produces positive stiffness in the first and second modes and negative stiffness in third mode, and controllers (c), and (d) produce negative stiffness in first mode and positive stiffness in second and third modes. Figure 5.10 shows that controllers (e) and (f) produce negative stiffness in all three modes.

The hysteresis loops (i.e., control force versus displacement) for these six cases are shown in

Figs. 5.11 and 5.12 for the structure subjected by the NS components of the 1940 El Centro and the 1995 JMA Kobe earthquakes. The dominance of the first mode in the response is seen in Figs. 5.11 and 5.12, that is, controllers (b) and (d) produce positive and negative stiffness, respectively. We can also see that controller (f) has negative stiffness as in the case of one-story building model. Thus, the LQR/LQG can produce both positive and negative stiffness, depending on the control weightings chosen. Moreover, the LQR and LQG hysteresis loops and earthquake input energies are nearly identical.

Peak values of relative displacement, inter-story drift, and absolute acceleration for each floor, along with actuator force, are summarized in Tables 5.3 and 5.4. When the control force is small (i.e., controllers (a), (c), and (e)), the controller has little impact on the responses. However, when the control force is large, the nature of the controllers is clearer; here, controllers (d) and (f) reduce absolute acceleration for each floor more than controller (b). Again, the LQG controller has comparable performance to its LQR counterpart.

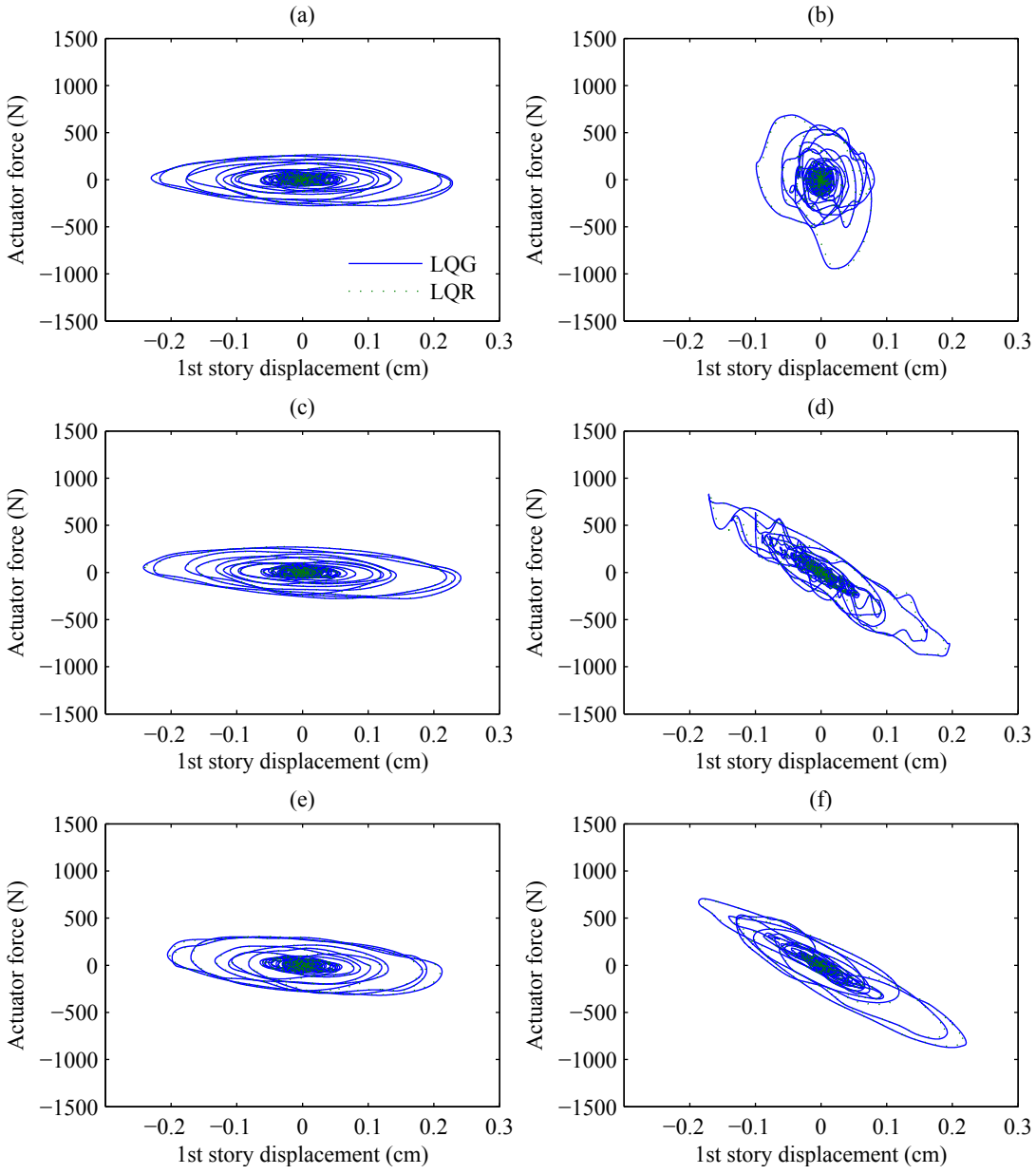

Figure 5.11: Hysteresis control force loops of the three-story model produced by LQR and LQG to 1940 El Centro NS; (a) $\mathbf{Q} = \mathbf{Q}_{\rm d}(\alpha = 1)$, $R = 10^{-10}$, (b) $\mathbf{Q} = \mathbf{Q}_{\rm d}(\alpha = 1)$, $R = 10^{-12}$, (c) $\mathbf{Q} = \mathbf{Q}_{\rm d}(\alpha = 0.01)$, $R = 10^{-10.5}$, (d) $\mathbf{Q} = \mathbf{Q}_{\rm d}(\alpha = 0.01)$, $R = 10^{-13.5}$, (e) $\mathbf{Q} = \mathbf{Q}_{\rm a}$, $R = 10^{-3.5}$, (f) $\mathbf{Q} = \mathbf{Q}_{\rm a}$, $R = 10^{-5.5}$

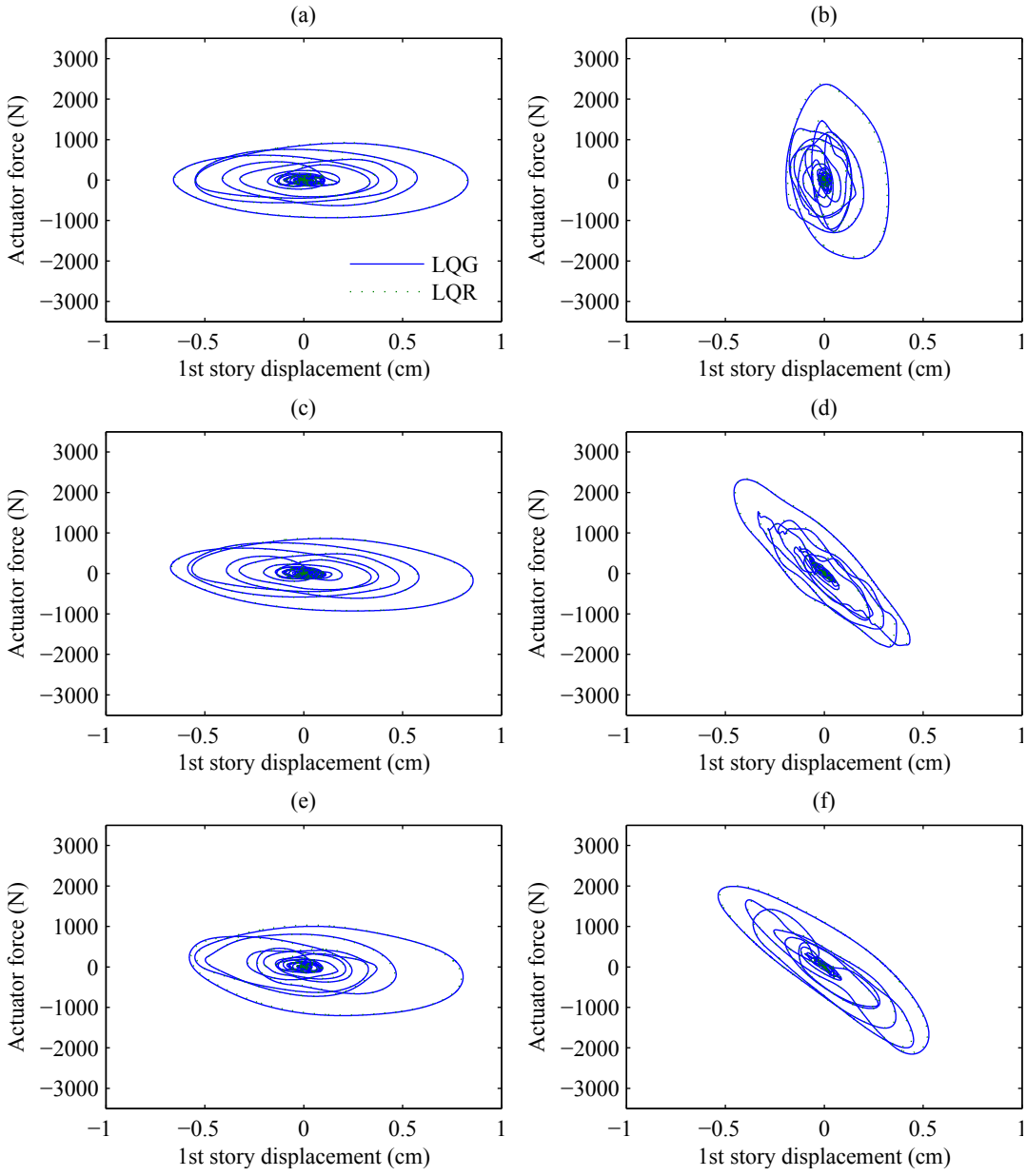

Figure 5.12: Hysteresis control force loops of the three-story model produced by LQR and LQG to 1995 JMA Kobe NS; (a) $\mathbf{Q} = \mathbf{Q}_{\rm d}(\alpha = 1)$, $R = 10^{-10}$, (b) $\mathbf{Q} = \mathbf{Q}_{\rm d}(\alpha = 1)$, $R = 10^{-12}$, (c) $\mathbf{Q} = \mathbf{Q}_{\rm d}(\alpha = 0.01)$, $R = 10^{-10.5}$, (d) $\mathbf{Q} = \mathbf{Q}_{\rm d}(\alpha = 0.01)$, $R = 10^{-13.5}$, (e) $\mathbf{Q} = \mathbf{Q}_{\rm a}$, $R = 10^{-3.5}$, (f) $\mathbf{Q} = \mathbf{Q}_{\rm a}$, $R = 10^{-5.5}$

Table 5.3: Peak values for the three-story model to 1940 El Centro NS; (a) $\mathbf{Q} = \mathbf{Q}_{\mathrm{d}}(\alpha = 1)$, $R = 10^{-10}$, (b) $\mathbf{Q} = \mathbf{Q}_{\mathrm{d}}(\alpha = 1)$, $R = 10^{-12}$, (c) $\mathbf{Q} = \mathbf{Q}_{\mathrm{d}}(\alpha = 0.01)$, $R = 10^{-10.5}$, (d) $\mathbf{Q} = \mathbf{Q}_{\mathrm{d}}(\alpha = 0.01)$, $R = 10^{-13.5}$, (e) $\mathbf{Q} = \mathbf{Q}_{\mathrm{a}}$, $R = 10^{-3.5}$, (f) $\mathbf{Q} = \mathbf{Q}_{\mathrm{a}}$, $R = 10^{-5.5}$

		(a)		(b)		(c)		(d)		(e)		(f)	
Parameter	Uncontrolled	LQG	LQR	LQG	LQR	LQG	LQR	LQG	LQR	LQG	LQR	LQG	LQR
x_1 (cm)	0.541	0.230	0.228	0.099	0.096	0.240	0.242	0.196	0.192	0.212	0.210	0.221	0.216
x_2 (cm)	0.826	0.365	0.362	0.162	0.157	0.375	0.377	0.220	0.215	0.332	0.327	0.258	0.253
x_3 (cm)	0.964	0.458	0.454	0.249	0.242	0.461	0.465	0.237	0.231	0.401	0.396	0.277	0.272
d_2 (cm)	0.320	0.158	0.157	0.131	0.127	0.152	0.154	0.041	0.041	0.129	0.127	0.056	0.056
d_3 (cm)	0.202	0.099	0.097	0.087	0.085	0.093	0.095	0.031	0.031	0.077	0.075	0.039	0.038
$\ddot{x}_{\mathrm{a}1}$ (m/s^2)	8.664	4.684	4.563	4.069	3.928	4.179	4.285	2.690	2.653	3.402	3.358	1.601	1.583
$\ddot{x}_{\mathrm{a}2}$ (m/s^2)	10.450	4.905	4.819	4.239	4.075	4.615	4.691	1.533	1.514	4.107	4.034	1.664	1.642
$\ddot{x}_{\mathrm{a}3}$ (m/s^2)	14.061	6.879	6.782	6.084	5.938	6.484	6.578	2.167	2.136	5.351	5.240	2.686	2.647
f (N)		276.6	275.5	944.0	946.9	277.2	278.7	887.9	872.4	318.2	312.7	874.4	859.3

Table 5.4: Peak values for the three-story model to 1995 JMA Kobe NS; (a) $\mathbf{Q} = \mathbf{Q}_{\mathrm{d}}(\alpha = 1)$, $R = 10^{-10}$, (b) $\mathbf{Q} = \mathbf{Q}_{\mathrm{d}}(\alpha = 1)$, $R = 10^{-12}$, (c) $\mathbf{Q} = \mathbf{Q}_{\mathrm{d}}(\alpha = 0.01)$, $R = 10^{-10.5}$, (d) $\mathbf{Q} = \mathbf{Q}_{\mathrm{d}}(\alpha = 0.01)$, $R = 10^{-13.5}$, (e) $\mathbf{Q} = \mathbf{Q}_{\mathrm{a}}$, $R = 10^{-3.5}$, (f) $\mathbf{Q} = \mathbf{Q}_{\mathrm{a}}$, $R = 10^{-5.5}$

		(a)		(b)		(c)		(d)		(e)		(f)	
Parameter	Uncontrolled	LQG	LQR	LQG	LQR	LQG	LQR	LQG	LQR	LQG	LQR	LQG	LQR
x_1 (cm)	1.490	0.831	0.827	0.326	0.318	0.857	0.827	0.456	0.408	0.806	0.797	0.537	0.528
x_2 (cm)	2.372	1.351	1.343	0.583	0.564	1.367	1.321	0.527	0.517	1.281	1.265	0.674	0.662
x_3 (cm)	2.883	1.665	1.653	0.786	0.762	1.671	1.617	0.584	0.608	1.560	1.539	0.767	0.752
d_2 (cm)	0.895	0.537	0.532	0.372	0.364	0.524	0.510	0.141	0.230	0.490	0.483	0.205	0.202
d_3 (cm)	0.529	0.315	0.312	0.206	0.203	0.306	0.298	0.089	0.140	0.282	0.278	0.122	0.120
$\ddot{x}_{\mathrm{a}1}$ (m/s^2)	23.349	11.521	11.283	8.812	8.521	10.558	10.189	4.619	5.702	8.753	8.485	3.865	3.815
$\ddot{x}_{\mathrm{a}2}$ (m/s^2)	27.983	15.960	15.782	11.951	11.673	15.554	15.141	4.122	7.089	14.617	14.386	5.790	5.716
$\ddot{x}_{\mathrm{a}3}$ (m/s^2)	36.830	21.911	21.710	14.345	14.091	21.294	20.719	6.185	9.750	19.616	19.327	8.480	8.365
f (N)		932.0	924.8	2367.2	2386.8	926.9	975.4	2322.7	2308.0	1204.2	1189.8	2154.3	2119.9

The plots of earthquake energy input to the structure as given by Eq. (5.23) are shown in Figures 5.13 and 5.14 for cases (a)–(h). For both earthquakes, controller (b) shows the best performance. However, considering the peak actuator forces given in Tables 5.3 and 5.4, controllers producing negative stiffness (i.e., controllers (d) and (h)) are more effective at limiting the input earthquake energy than the controllers controllers (b) and (f).

5.3 Summary

This chapter investigated the nature of the hysteric behavior of the control forces produced by the widely employed LQG-based acceleration feedback control strategy. Numerical simulation studies carried out on one-story and three-story buildings with active bracing show that the LQG-based algorithms are quite versatile and can produce controllers with a variety of behaviors depending upon the control objectives chosen. Additionally, the numerical results demonstrated that the presented LQG-based acceleration feedback control had performance comparable to the LQR in the presented SDOF and 3DOF building models.

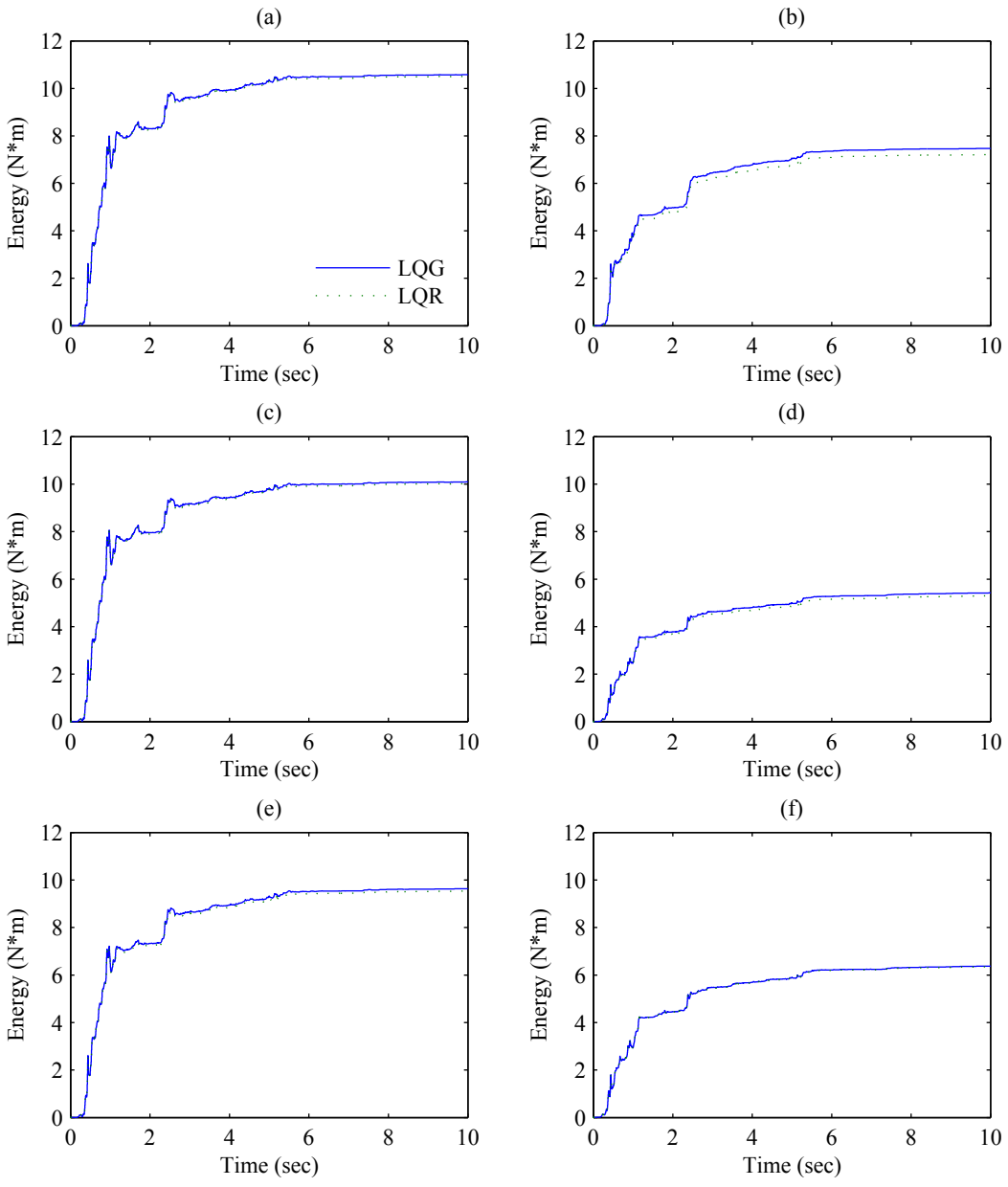

Figure 5.13: Earthquake input energy of the three-story model by LQG and LQR to 1940 El Centro NS; (a) $\mathbf{Q} = \mathbf{Q}_{\rm d}(\alpha = 1)$, $R = 10^{-10}$, (b) $\mathbf{Q} = \mathbf{Q}_{\rm d}(\alpha = 1)$, $R = 10^{-12}$, (c) $\mathbf{Q} = \mathbf{Q}_{\rm d}(\alpha = 0.01)$, $R = 10^{-10.5}$, (d) $\mathbf{Q} = \mathbf{Q}_{\rm d}(\alpha = 0.01)$, $R = 10^{-13.5}$, (e) $\mathbf{Q} = \mathbf{Q}_{\rm a}$, $R = 10^{-3.5}$, (f) $\mathbf{Q} = \mathbf{Q}_{\rm a}$, $R = 10^{-5.5}$

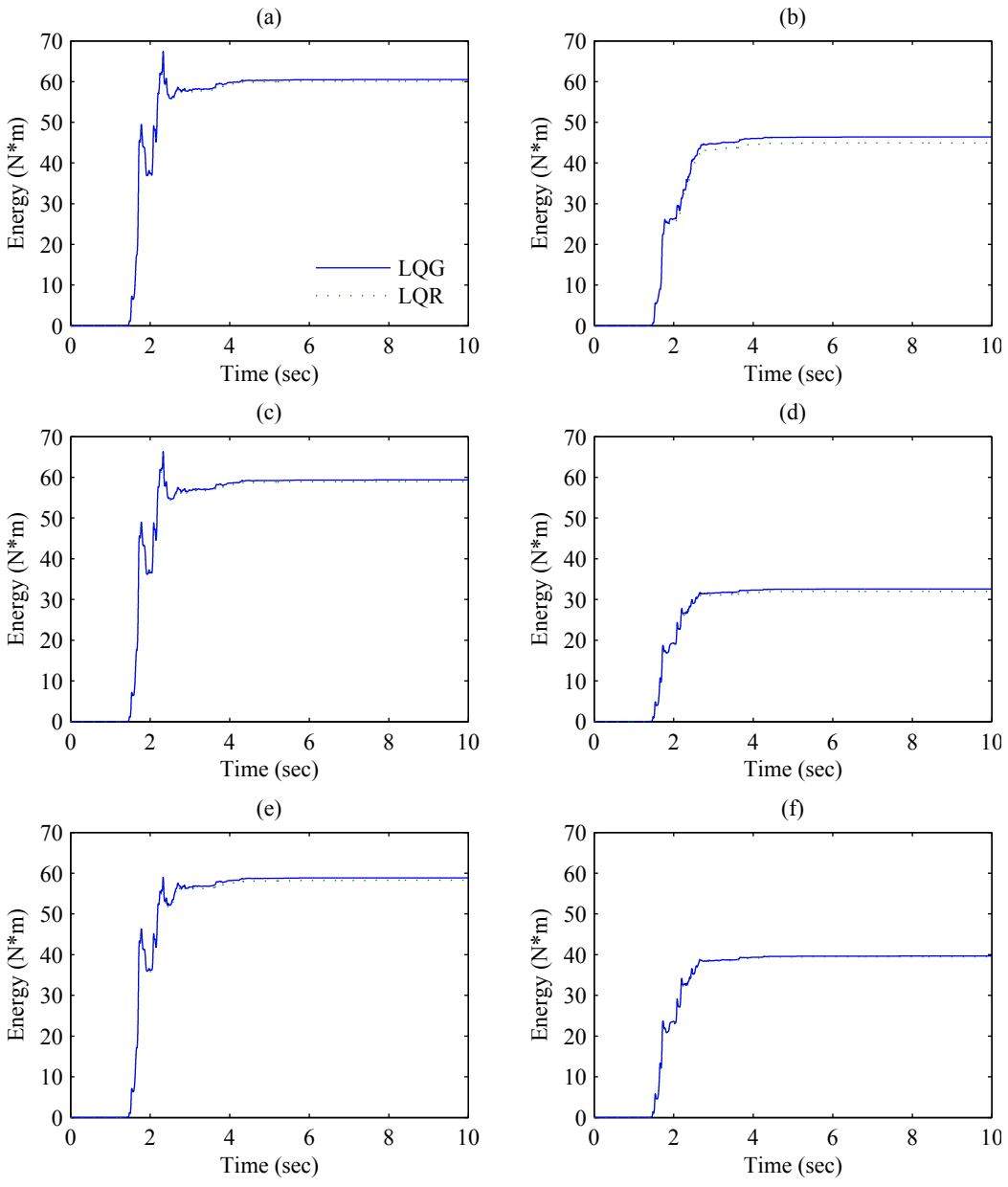

Figure 5.14: Earthquake input energy of the three-story model by LQG and LQR to 1995 JMA Kobe NS;(a) $\mathbf{Q} = \mathbf{Q}_{\mathrm{d}}(\alpha = 1)$, $R = 10^{-10}$, (b) $\mathbf{Q} = \mathbf{Q}_{\mathrm{d}}(\alpha = 1)$, $R = 10^{-12}$, (c) $\mathbf{Q} = \mathbf{Q}_{\mathrm{d}}(\alpha = 0.01)$, $R = 10^{-10.5}$, (d) $\mathbf{Q} = \mathbf{Q}_{\mathrm{d}}(\alpha = 0.01)$, $R = 10^{-13.5}$, (e) $\mathbf{Q} = \mathbf{Q}_{\mathrm{a}}$, $R = 10^{-3.5}$, (f) $\mathbf{Q} = \mathbf{Q}_{\mathrm{a}}$, $R = 10^{-5.5}$

Chapter 6

Semi-active Control Algorithms

In this chapter, new model-free algorithms realizing versatile hysteresis loops are proposed. As an example of semi-active control devices, MR dampers, which are one of the widely accepted, are employed. First, the formulation of the problem is provided, including the equation of motion and the associated state-space representation. Then, the algorithms for the proposed controllers are described. Through numerical simulation of a scaled three-story building, the hysteresis loops produced by the proposed algorithms are investigated. In parallel, the hysteresis loops produced by the widely employed LQG-based clipped-optimal control and Lyapunov stability-based control are introduced and compared. Subsequently, control performance obtained from numerical studies are presented. Conclusions obtained from this study then follow.

6.1 Problem formulation

Consider a structural system, excited by a one-dimensional earthquake loading, with an equation of motion given by

$$\mathbf{M}_{\mathrm{s}}\ddot{\mathbf{x}} + \mathbf{C}_{\mathrm{s}}\dot{\mathbf{x}} + \mathbf{K}_{\mathrm{s}}\mathbf{x} = \mathbf{G}_{\mathrm{s}}\mathbf{f} - \mathbf{M}_{\mathrm{s}}\mathbf{L}_{\mathrm{s}}\ddot{x}_g \tag{6.1}$$

where $\mathbf{f}$ is the vector of control forces, $\ddot{x}_g$ is the ground acceleration, $\mathbf{M}_{\mathrm{s}}$, $\mathbf{C}_{\mathrm{s}}$, and $\mathbf{K}_{\mathrm{s}}$ are the mass, linear damping and stiffness matrices of the structure, respectively, and $\mathbf{G}_{\mathrm{s}}$ and $\mathbf{L}_{\mathrm{s}}$ are the influence coefficient vectors of the control force and structural mass, respectively. If so, $\mathbf{x}$ is the displacement vector, which is composed of the displacement of each floor relative to the ground. An over dot represents the time derivative.

The state-space representation of the equation of motion can be written as

$$\dot{\mathbf{z}} = \mathbf{A}\mathbf{z} + \mathbf{B}\mathbf{f} + \mathbf{E}\ddot{x}_g \tag{6.2}$$

$$\mathbf{y}_{\mathrm{m}} = \mathbf{C}_{\mathrm{m}}\mathbf{z} + \mathbf{D}_{\mathrm{m}}\mathbf{f} + \mathbf{F}_{\mathrm{m}}\ddot{x}_g + \mathbf{v} \tag{6.3}$$

$$\mathbf{y}_{\mathrm{e}} = \mathbf{C}_{\mathrm{e}}\mathbf{z} + \mathbf{D}_{\mathrm{e}}\mathbf{f} + \mathbf{F}_{\mathrm{e}}\ddot{x}_g \tag{6.4}$$

where $\mathbf{z}$ is the state vector of the story displacements and velocities relative to the base; that is,

$$\mathbf{z} = \begin{bmatrix} \mathbf{x}^T & \dot{\mathbf{x}}^T \end{bmatrix}^T \tag{6.5}$$

$\mathbf{y}_{\mathrm{m}}$ is the vector corresponding to the measured outputs, $\mathbf{v}$ is an observation noise vector, $\mathbf{y}_{\mathrm{e}}$ is the vector corresponding to the regulated outputs that are used for evaluation of the system. The matrices $\mathbf{A}$, $\mathbf{B}$, and $\mathbf{E}$ are given as

$$\mathbf{A} = \begin{bmatrix} \mathbf{0} & \mathbf{I} \\ -\mathbf{M}_{\mathrm{s}}^{-1}\mathbf{K}_{\mathrm{s}} & -\mathbf{M}_{\mathrm{s}}^{-1}\mathbf{C}_{\mathrm{s}} \end{bmatrix}, \quad \mathbf{B} = \begin{bmatrix} \mathbf{0} \\ -\mathbf{M}_{\mathrm{s}}^{-1}\mathbf{G}_{\mathrm{s}} \end{bmatrix}, \quad \mathbf{E} = \begin{bmatrix} \mathbf{0} \\ -\mathbf{L}_{\mathrm{s}}^{-1} \end{bmatrix} \tag{6.6}$$

and $\mathbf{C}_{\mathrm{m}}$, $\mathbf{C}_{\mathrm{e}}$, $\mathbf{D}_{\mathrm{m}}$, $\mathbf{D}_{\mathrm{e}}$, $\mathbf{F}_{\mathrm{m}}$, and $\mathbf{F}_{\mathrm{e}}$ are appropriately chosen matrices corresponding to the associated output vectors.

The vector of control force is defined as

$$\mathbf{f} = \begin{bmatrix} f_{\mathrm{MR},1} & f_{\mathrm{MR},2} & \cdots & f_{\mathrm{MR,n}} \end{bmatrix}^T \tag{6.7}$$

where $f_{\mathrm{MR},j}, j = 1, 2, \cdots n$ is the jth measured MR damper output force.

6.2 LQG-based clipped-optimal control

The LQG based clipped-optimal control method for MR dampers (Dyke et al., 1996c,d; Spencer et al., 1997) is explained briefly. By reconsidering Eq. (6.2), the cost function of the LQG control can be written as

$$J = \lim_{t\to\infty} \frac{1}{t} \mathrm{E}\left[\int_0^t \left(\mathbf{y}_{\mathrm{e}}^T \mathbf{Q} \mathbf{y}_{\mathrm{e}} + \mathbf{f}_{\mathrm{c}}^T \mathbf{R} \mathbf{f}_{\mathrm{c}} \right) dt \right] \tag{6.8}$$

where $\mathbf{Q}$ and $\mathbf{R}$ are the weighting parameters; $\mathbf{f}_{\mathrm{c}}$ is a control force vector defined as

$$\mathbf{f}_c = \begin{bmatrix} f_{\mathrm{c},1} & f_{\mathrm{c},2} & \cdots & f_{\mathrm{c},n} \end{bmatrix}^T \tag{6.9}$$

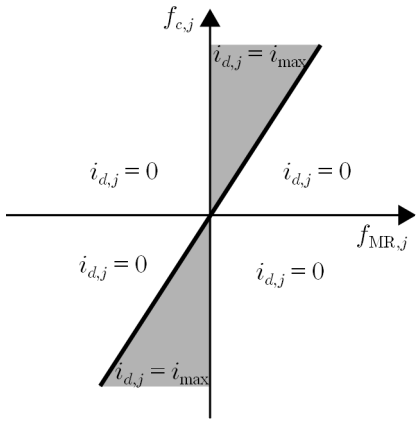

Figure 6.1: Graphical representation of clipped-optimal control algorithm

where $f_{c,j}, j = 1, 2, \cdots n$ is the jth calculated control force. E[$\cdot$] means the expected value of the quantity in brackets and t represents the time. By minimizing Eq. (6.8), the control force is a function of the structural states. In the LQG control, the Kalman filter estimates (Dyke et al., 1996c) the state based on the measured responses such that

$$\dot{\hat{\mathbf{z}}} = \mathbf{A}\hat{\mathbf{z}} + \mathbf{B}\mathbf{f}_{\mathrm{c}} + \mathbf{L}\left(\mathbf{y}_{\mathrm{m}} - \mathbf{C}_{\mathrm{m}}\hat{\mathbf{z}} - \mathbf{D}_{\mathrm{m}}\mathbf{f}_{\mathrm{c}} - \mathbf{F}_{\mathrm{m}}\ddot{x}_g\right) \tag{6.10}$$

$$\mathbf{f}_{\mathrm{c}} = -\mathbf{K}_{\mathrm{c}}\hat{\mathbf{z}} \tag{6.11}$$

where $\mathbf{L}$ is the Kalman gain; $\mathbf{K}_{\mathrm{c}}$ is the optimal control gain found by minimizing Eq. (6.8); and $\hat{\mathbf{z}}$ is the estimated state by the Kalman filter. The clipped-optimal control algorithms are used to convert the optimal control force of Eq. (6.11) to a desired command current for the MR damper. The desired command current is given by

$$i_{\mathrm{d},j} = i_{\max} H\left\{\left(f_{\mathrm{c},j} - f_{\mathrm{MR},j}\right) f_{\mathrm{MR},j}\right\} \tag{6.12}$$

where H$\{\cdot\}$ is the Heaviside function, $i_{\mathrm{d},j}$ is the desired input current to the jth MR damper; $i_{\max}$ is the maximum input current, $f_{\mathrm{c},j}$ is the jth optimal control force generated by Eq. (6.11) and $f_{\mathrm{MR},j}$ is the actual force generated by the jth MR damper. The clipped-optimal controller logic is illustrated in Figure 6.1.

6.3 Lyapunov stability-based control

Leitmann (1994) applied Lyapunov's direct method for the design of a semi-active controller. In this approach, a Lyapunov function is defined as (Khalil, 2002)

$$V(\mathbf{z}) = \frac{1}{2}\|\mathbf{z}\|_p^2 \tag{6.13}$$

where $\|\mathbf{z}\|_p$ is p-norm of the state $\mathbf{z}$ defined by

$$\|\mathbf{z}\|_p = \left[\mathbf{z}^T\mathbf{P}\mathbf{z}\right]^{1/2} \tag{6.14}$$

and $\mathbf{P}$ is real, symmetric, positive definite matrix. In the case of linear system, to ensure $\dot{V}$ is negative, the matrix $\mathbf{P}$ is found by solving the Lyapunov equation

$$\mathbf{A}^T\mathbf{P} + \mathbf{P}\mathbf{A} = -\mathbf{Q}_p \tag{6.15}$$

for a given positive semidefinite matrix $\mathbf{Q}_p$. Then, the derivative of the Lyapunov function for a solution of Eq. (6.2) is

$$\dot{V} = -\frac{1}{2}\mathbf{z}^T\mathbf{Q}_p\mathbf{z} + \mathbf{z}^T\mathbf{P}\mathbf{B}\mathbf{f} + \mathbf{z}^T\mathbf{P}\mathbf{E}\ddot{x}_g \tag{6.16}$$

The only term that can be directly affected by a change in the control current is the middle term $\mathbf{z}^T\mathbf{P}\mathbf{B}\mathbf{f}$ that contains the force vector $\mathbf{f}$. Thus, the input current to the jth MR damper which will minimize $\dot{V}$ is

$$i_{\mathrm{d},j} = i_{\max}H((-\mathbf{z}^T)\mathbf{P}\mathbf{B}_j f_{\mathrm{MR},j}) \tag{6.17}$$

where $H(\cdot)$ is Heaviside step function; $f_{\mathrm{MR},j}$ is the measured force produced by the jth MR damper; and $\mathbf{B}_j$ is the jth column of the $\mathbf{B}$ matrix in Eq. (6.2). To implement this algorithm, the estimated state by the Kalman filter, $\hat{\mathbf{z}}$, can be used instead of $\mathbf{z}$.

6.4 Model-free algorithms for semi-active control

In this section, new simple algorithms for use with MR dampers which do not require the structure model are introduced. Two model-free algorithms which can produce positive and pseudo-negative stiffness hysteresis loops are proposed herein. Let d_j, $\dot{d}_j$, and $\ddot{d}_{a,j}$ be the displacement, velocity, and absolute acceleration of the piston of the jth MR damper. Figure 6.2 (a) and (b) depict the schematic illustrations of displacement-force hysteresis loops for the cases of $i_{d,j} = i_{\max}$ and $i_{d,j} = 0$, respectively.

6.4.1 Proposed simple algorithm 1

The first proposed algorithm controls the desired input current based on the sign of the product of the displacement and velocity of the MR damper. As shown in Figure 6.2(c), to produce pseudo-negative stiffness, the desired input current is maximum when the direction of the displacement of the MR damper is different from that of the velocity and 0 when the displacement and velocity of the MR damper have the same direction. Thus, the input current determined by

$$i_{d,j} = i_{\max} H(-d_j \dot{d}_j) \tag{6.18}$$

can yield pseudo-negative stiffness by the MR damper.

Positive stiffness can be realized by changing the sign in Eq. (6.18); i.e.,

$$i_{d,j} = i_{\max} H(d_j \dot{d}_j) \tag{6.19}$$

In Eq. (6.19), $i_{\max}$ input is applied when the directions of displacement and velocity are the same, otherwise it is 0. This is shown in Figure 6.2(d) schematically. To implement this algorithm, only sensors to measure the displacement and velocity of the devices are needed. In this dissertation, the algorithms given by Eqs. (6.18) and (6.19) are named simple controller 1N and simple controller 1P, respectively.

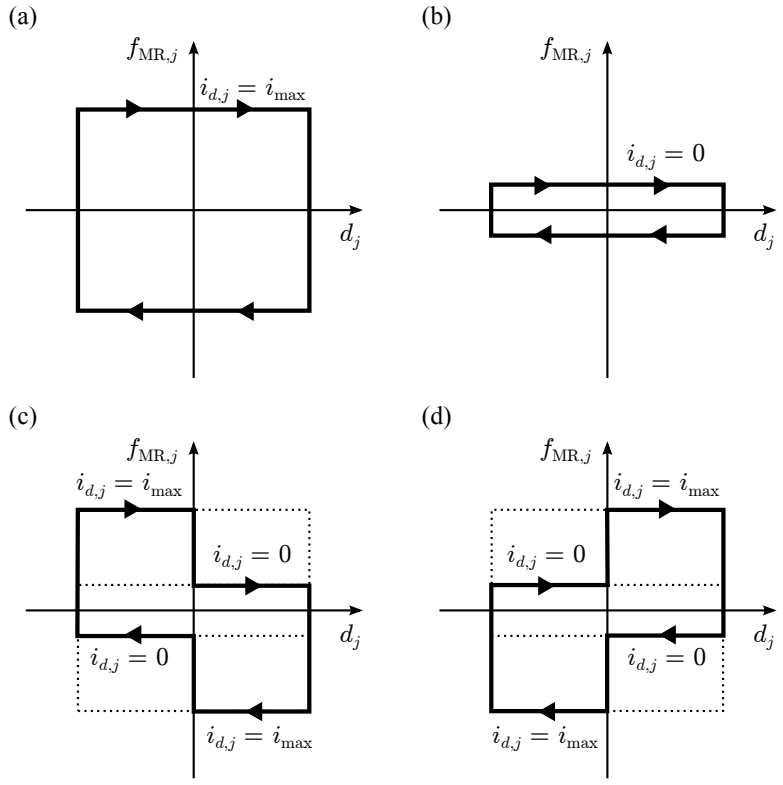

Figure 6.2: Schematic illustration of MR damper force; (a) $i_{d,j} = i_{\max}$, (b) $i_{d,j} = 0$, (c) Pseudo-negative stiffness, (d) Positive stiffness

6.4.2 Proposed simple algorithm 2

Another algorithm is obtained by measuring the displacement and the output force of the MR damper. Pseudo-negative stiffness can be obtained when the desired input current is controlled as

$$i_{d,j} = i_{\max} H(d_j f_{\mathrm{MR},j}) \tag{6.20}$$

as shown in Figure 6.2(c). In Eq. (6.20), the input current is the maximum when the displacement and output MR damper force have the same direction; otherwise it is 0.

As shown in Figure 6.2(d), positive stiffness can be produced by controlling the input current by

$$i_{d,j} = i_{\max} H(-d_j f_{\mathrm{MR},j}) \tag{6.21}$$

In Eq. (6.20), the input current is maximum when the direction of the displacement and output

MR damper force are different; otherwise it is 0.

6.5 Numerical simulation of the three-story building model

To investigate the nature of the energy dissipation capabilities of the semi-active controllers described in the previous section through numerical studies, a building and MR damper model are presented in this section. Also, the two LQG-based clipped-optimal controllers, i.e., acceleration and displacement weighting, and the Lyapunov stability-based controller are designed.

6.5.1 Building model

The building model used in this study is a scaled three-story building model as shown in Figure 6.3 schematically. As can be seen, one MR damper is installed between the ground and the first floor. This model was previously investigated by Dyke et al. (1995, 1996a) and in Section 5.2.2. The parameter values for this model is summarized as

$$\mathbf{M}_\mathrm{s} = \begin{bmatrix} 98.3 & 0 & 0 \\ 0 & 98.3 & 0 \\ 0 & 0 & 98.3 \end{bmatrix} \text{(kg)}, \qquad \mathbf{C}_\mathrm{s} = \begin{bmatrix} 175 & -50 & 0 \\ -50 & 100 & -50 \\ 0 & -50 & 50 \end{bmatrix} \text{(N·sec/m)},$$

$$\mathbf{K}_\mathrm{s} = 10^5 \begin{bmatrix} 12.0 & -6.84 & 0 \\ -6.84 & 13.7 & -6.84 \\ 0 & -6.84 & 6.84 \end{bmatrix} \text{(N/m)}, \qquad \mathbf{f} = f_\mathrm{MR}, \qquad \mathbf{G}_\mathrm{s} = \begin{bmatrix} -1 \\ 0 \\ 0 \end{bmatrix}, \qquad \mathbf{L}_\mathrm{s} = \begin{bmatrix} 1 \\ 1 \\ 1 \end{bmatrix} \tag{6.22}$$

The state vector $\mathbf{z}$ in Eqs. (6.2), (6.3), (6.4), (6.5) is then

$$\mathbf{z} = \begin{bmatrix} x_1 & x_2 & x_3 & \dot{x}_1 & \dot{x}_2 & \dot{x}_3 \end{bmatrix}^T \tag{6.23}$$

In this study, assume that only the first floor displacement and velocity, and the absolute accelerations of each floor are measured, since collecting interstory displacements and velocities is not practical in the real world. Then, the measurement vector $\mathbf{y}_m$ in Eq. (6.3) is given by

$$\mathbf{y}_\mathrm{m} = \begin{bmatrix} x_1 & \dot{x}_1 & \ddot{x}_{\mathrm{a},1} & \ddot{x}_{\mathrm{a},2} & \ddot{x}_{\mathrm{a},3} \end{bmatrix}^T \tag{6.24}$$

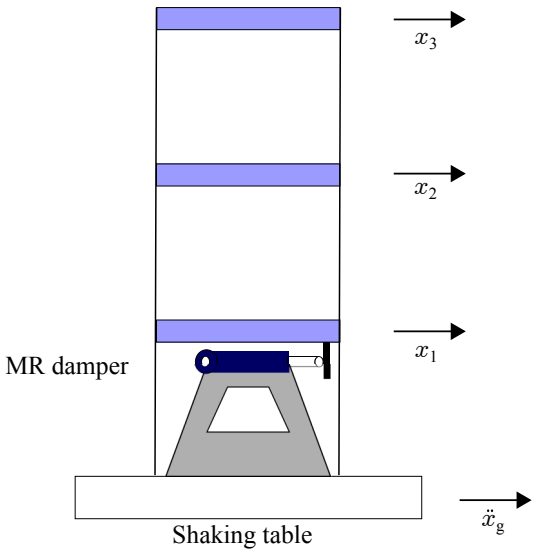

Figure 6.3: Three-story building model wtih a MR damper

and the evaluation vector $\mathbf{y}_e$ in Eq. (6.4) are defined by

$$\mathbf{y}_{\mathrm{e}} = \begin{bmatrix} x_1 & x_2 & x_3 & \ddot{x}_{\mathrm{a},1} & \ddot{x}_{\mathrm{a},2} & \ddot{x}_{\mathrm{a},3} \end{bmatrix}^T \tag{6.25}$$

where x_j, $\dot{x}_j$, and $\ddot{x}_j$ represent relative displacement, relative velocity, and absolute acceleration of the jth floor, respectively. Therefore, the matrices $\mathbf{C}_{\mathrm{m}}$, $\mathbf{C}_{\mathrm{e}}$, $\mathbf{D}_{\mathrm{m}}$, $\mathbf{D}_{\mathrm{e}}$, $\mathbf{E}_{\mathrm{m}}$, and $\mathbf{E}_{\mathrm{e}}$ become

$$\mathbf{C}_{\mathrm{m}} = \begin{bmatrix} 1 & 0 & 0 & \mathbf{0}_{1\times 3} \\ 0 & 1 & 0 & \mathbf{0}_{1\times 3} \\ -\mathbf{M}_{\mathrm{s}}^{-1}\mathbf{K}_{\mathrm{s}} & & & -\mathbf{M}_{\mathrm{s}}^{-1}\mathbf{C}_{\mathrm{s}} \end{bmatrix}, \quad \mathbf{C}_{\mathrm{e}} = \begin{bmatrix} \mathbf{I}_{3\times 3} & \mathbf{0}_{3\times 3} \\ -\mathbf{M}_{\mathrm{s}}^{-1}\mathbf{K}_{\mathrm{s}} & -\mathbf{M}_{\mathrm{s}}^{-1}\mathbf{C}_{\mathrm{s}} \end{bmatrix},$$

$$\mathbf{D}_{\mathrm{m}} = \begin{bmatrix} 0 \\ 0 \\ \mathbf{M}_{\mathrm{s}}^{-1}\mathbf{G}_{\mathrm{s}} \end{bmatrix}, \quad \mathbf{D}_{\mathrm{e}} = \begin{bmatrix} \mathbf{0}_{3\times 1} \\ \mathbf{M}_{\mathrm{s}}^{-1}\mathbf{G}_{\mathrm{s}} \end{bmatrix}, \quad \mathbf{F}_{\mathrm{m}} = \mathbf{0}_{5\times 1}, \quad \mathbf{F}_{\mathrm{e}} = \mathbf{0}_{6\times 1} \tag{6.26}$$

where $\mathbf{I}$ is an identity matrix. Since the MR damper is installed between the ground and the first floor in this model, the displacement, velocity, and absolute acceleration of the piston of the MR damper are defined as

$$d = x_1, \quad \dot{d} = \dot{x}_1 \tag{6.27}$$

6.5.2 Controller design

The two LQG-based controllers and the Lyapunov stability-based controller are designed here. However, the proposed simple controllers do not need to be designed. The parameter values to design the controllers are as follows:

LQG-based controller with acceleration weighting

The parameter values in Eq. (6.8) are determined as

$$\mathbf{Q} = \text{diag}\begin{bmatrix} 0 & 0 & 0 & 0 & 0 & 1 \end{bmatrix} \tag{6.28}$$

$$\mathbf{R} = 10^{-5} \tag{6.29}$$

Further, to design the Kalman filter, the power spectral densities of the disturbance W and the measurement noise vector $\mathbf{V}$ are chosen to be 50 and $\mathbf{I}_{5\times5}$, respectively,

LQG-based controller with inter-story drift weighting

The parameter values in Eq. (6.8) are determined as

$$\mathbf{Q} = \begin{bmatrix} 0 & 0 & 0 & 0 & 0 & 0 \\ 0 & 1 & -1 & 0 & 0 & 0 \\ 0 & -1 & 1 & 0 & 0 & 0 \\ 0 & 0 & 0 & 0 & 0 & 0 \\ 0 & 0 & 0 & 0 & 0 & 0 \\ 0 & 0 & 0 & 0 & 0 & 0 \end{bmatrix} \tag{6.30}$$

$$\mathbf{R} = 10^{-12} \tag{6.31}$$

The Kalman filter is designed by using the same values as the case of acceleration weighted controller.

LQG-based controller with relative displacement weighting

The parameter values in Eq. (6.8) are determined as

$$\mathbf{Q} = \text{diag}\begin{bmatrix} 0 & 0 & 1 & 0 & 0 & 0 \end{bmatrix} \tag{6.32}$$

$$\mathbf{R} = 10^{-12} \tag{6.33}$$

The Kalman filter is designed by using the same values as the case of acceleration weighted controller.

Lyapunov stability-based controller

The matrix $\mathbf{P}$ in Eq. (6.15) used here is given by

$$\mathbf{P} = \begin{bmatrix} 6114.959 & 4020.990 & 1347.485 & 1.097 & 1.925 & 1.374 \\ 4020.990 & 6479.310 & 5037.158 & -1.394 & -1.067 & -0.741 \\ 1347.485 & 5037.158 & 10171.078 & 0.298 & -0.029 & -0.029 \\ 1.097 & -1.394 & 0.298 & 2.189 & 2.961 & 3.155 \\ 1.925 & -1.067 & -0.029 & 2.961 & 4.616 & 5.340 \\ 1.374 & -0.741 & -0.029 & 3.155 & 5.340 & 6.802 \end{bmatrix} \tag{6.34}$$

This is calculated by the lyap command within MATLAB (2013) using a positive definite matrix $\mathbf{Q}$. $\mathbf{Q}$ is determined by $\mathbf{T}^T\mathbf{T}$, where $\mathbf{T}$ is created by rand command within MATLAB (2013).

6.6 Results

In this section, hysteresis force-displacement loops and seismic performance obtained from the semi-actively controlled MR damper are shown. The three story building model is subjected to five earthquake records using numerical simulation. The earthquakes used in this study are El Centro (1994, Northridge Earthquake, El Centro record, fault-parallel), Ji-ji (1999, station TCU 068, North-South component), Kobe (1995, JMA station, East-West component), Newhall (1994, Northridge Earthquake, Newhall county, fault-parallel), and Sylmar (1994, Northridge Earthquake,

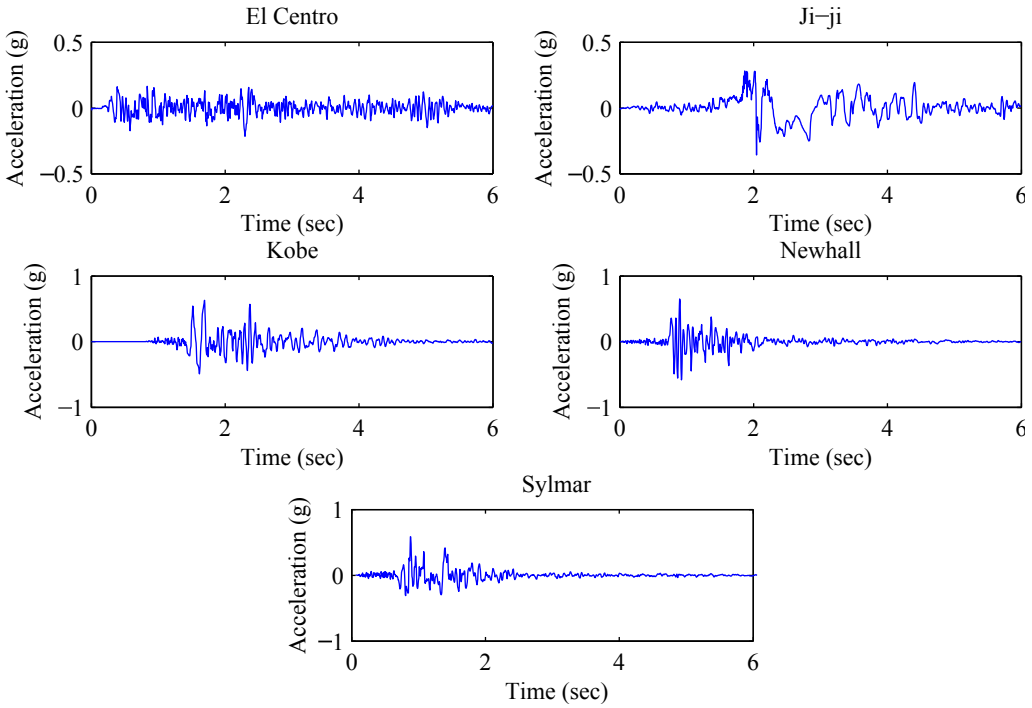

Figure 6.4: Scaled earthquake records

Sylmar station, fault-parallel) (Narasimhan et al., 2008). To satisfy scaling laws, the earthquakes must be reproduced at five times the recorded rate. The time histories of the employed earthquake records are shown in Figure 6.4.

Figures 6.5 through 6.13 depict hysteresis loops produced by the passive-off mode, the passive-on mode, the LQG-based clipped-optimal control with acceleration weighting, the LQG-based clipped-optimal control with displacement weighting, the Lyapunov stability-based control, the simple control 1N, the simple control 1P, the simple control 2N, and the simple control 2P, respectively, when subjected to the five scaled earthquake records. As can be seen, for the five earthquake records, pseudo-negative stiffness is obtained from the LQG-based clipped-optimal control with acceleration weighting, the Lyapunov stability-based control, the simple control 1N, and the simple control 2N, while, positive stiffness is found in the LQG-based clipped-optimal control with displacement weighting, the simple control 1P, and the simple control 2P. These results show that the proposed algorithms can produce various types of hysteresis control force loops as expected.

Tables 6.1 through 6.5 summarize the peak and RMS values of response relative displacements and absolute accelerations of each floor for the semi-active controllers including the LQG-based

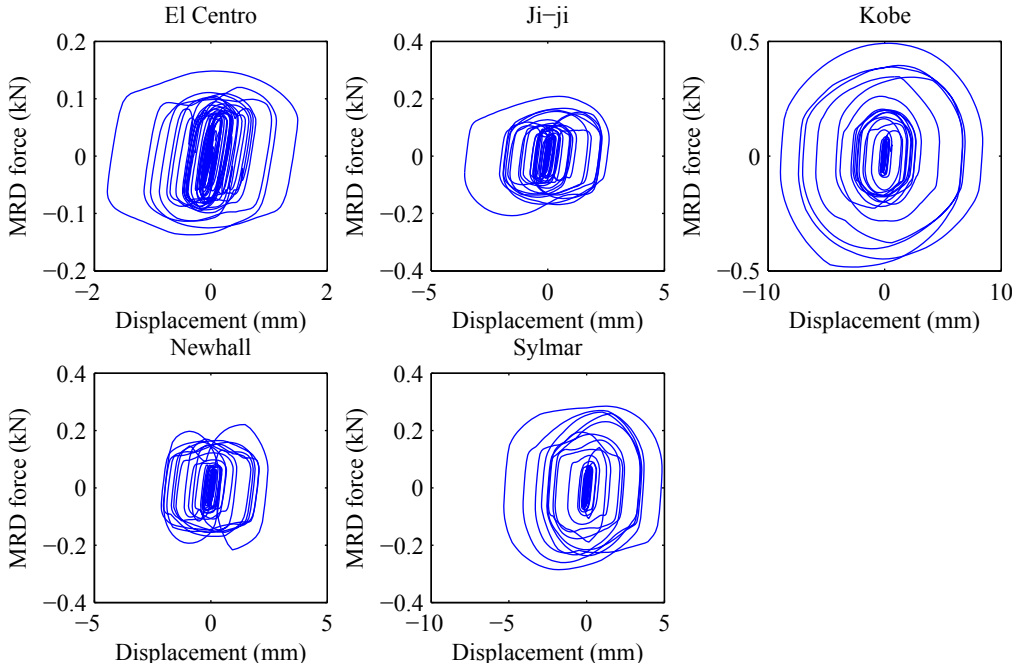

Figure 6.5: Hysteresis loops produced by the passive-off control

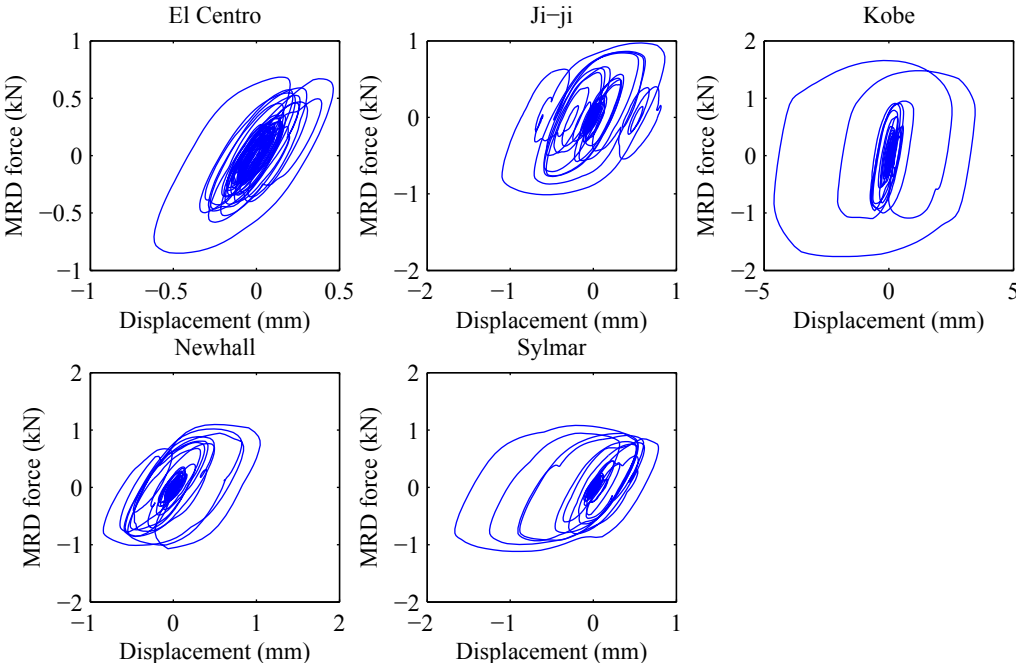

Figure 6.6: Hysteresis loops produced by the passive-on control

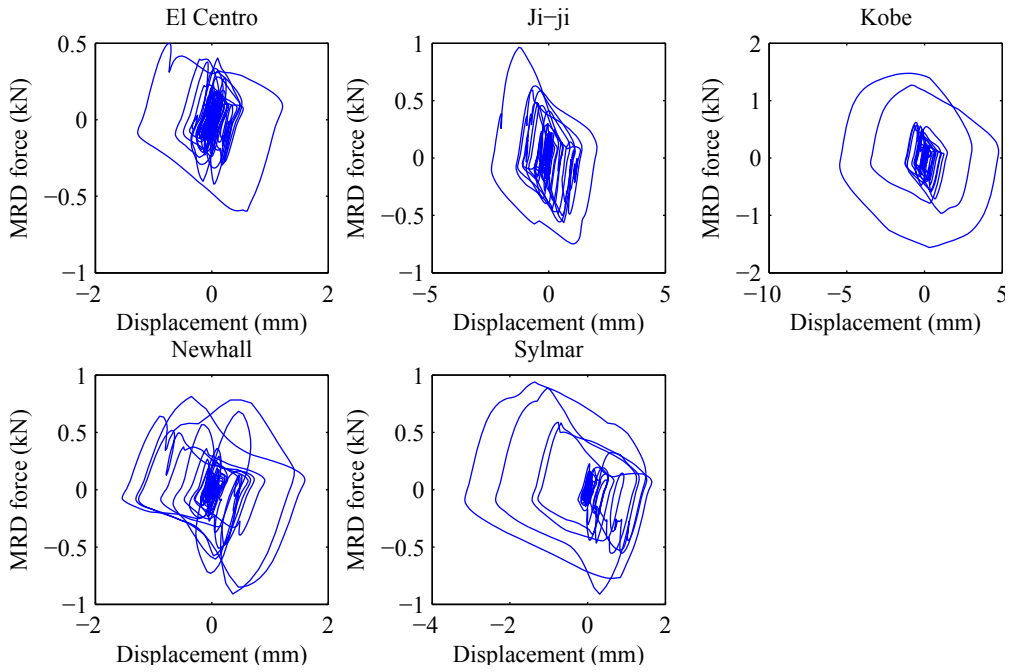

Figure 6.7: Hysteresis loops produced by the LQG-based clipped-optimal control with acceleration weighting

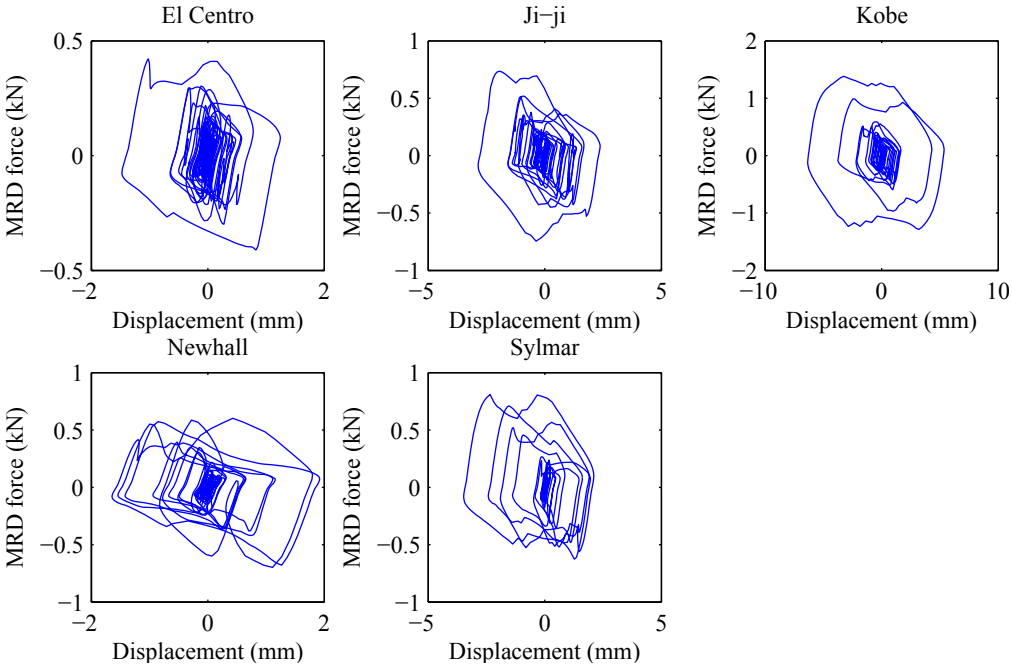

Figure 6.8: Hysteresis loops produced by the LQG-based clipped-optimal control with inter-story drift weighting

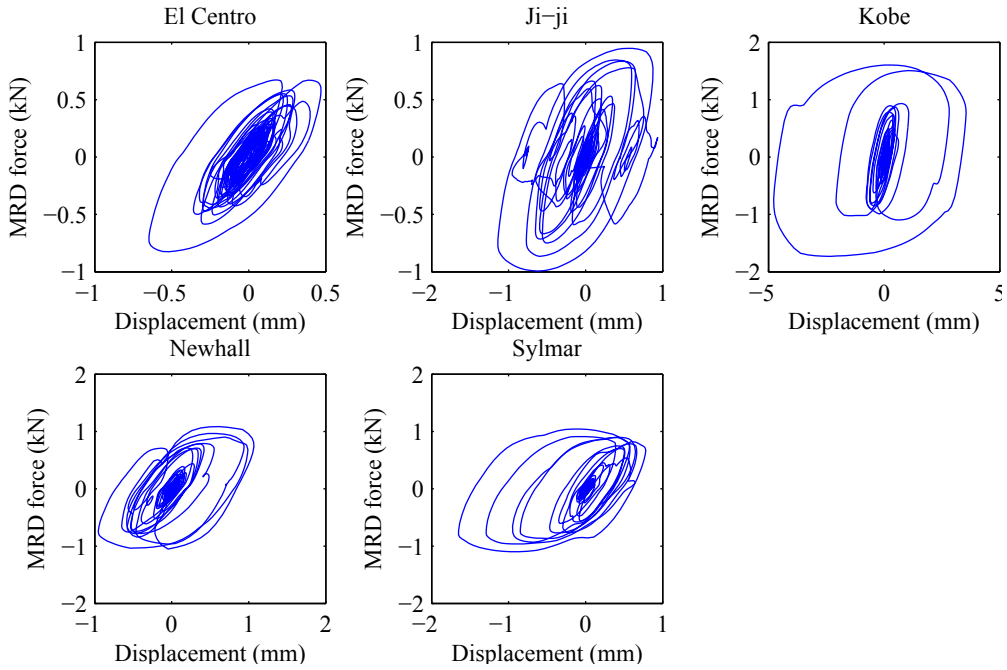

Figure 6.9: Hysteresis loops produced by the LQG-based clipped-optimal control with relative displacement weighting

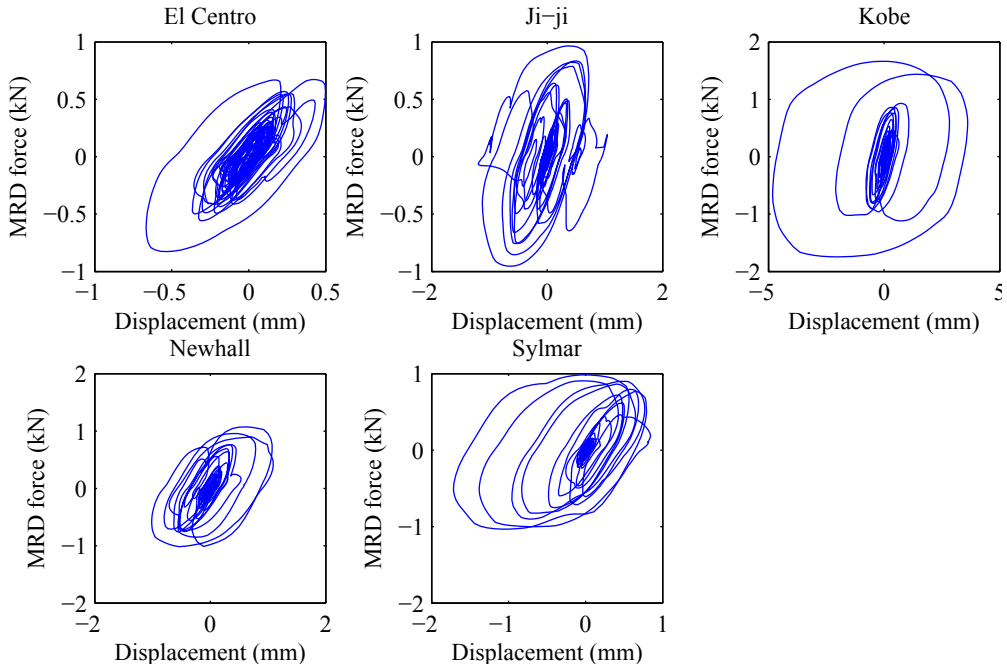

Figure 6.10: Hysteresis loops produced by the Lyapunov stability-based control

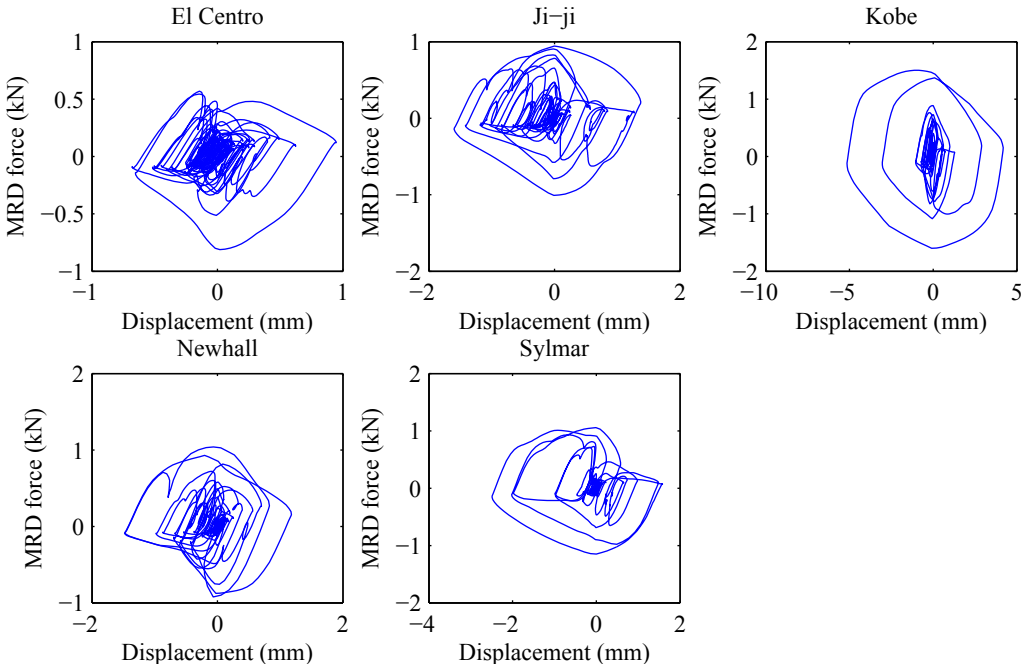

Figure 6.11: Hysteresis loops produced by the simple control 1N by Eq. (6.18)

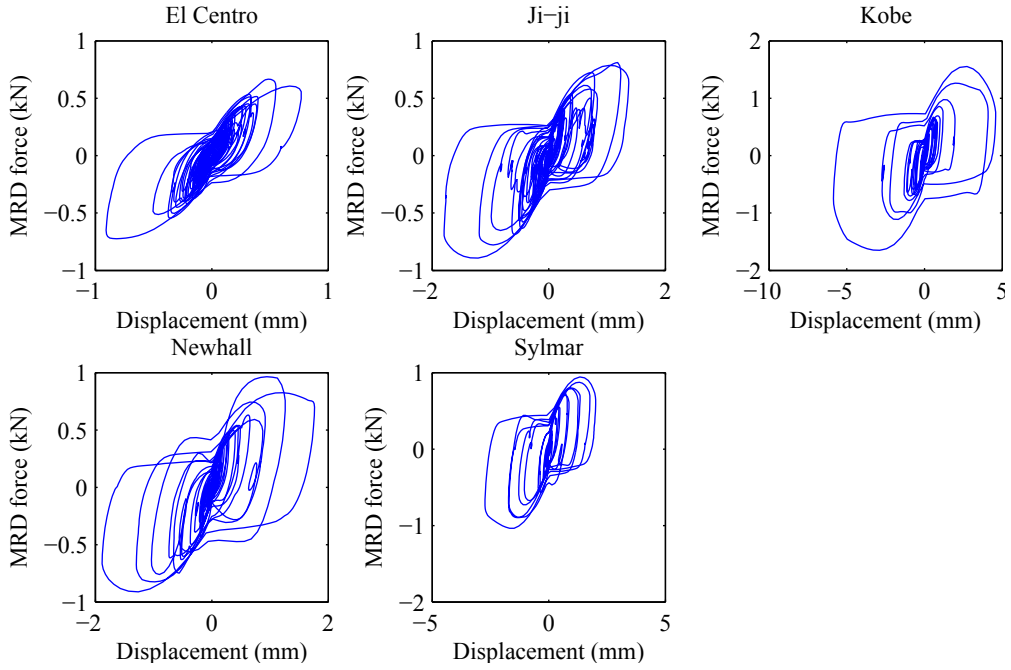

Figure 6.12: Hysteresis loops produced by the simple control 1P by Eq. (6.19)

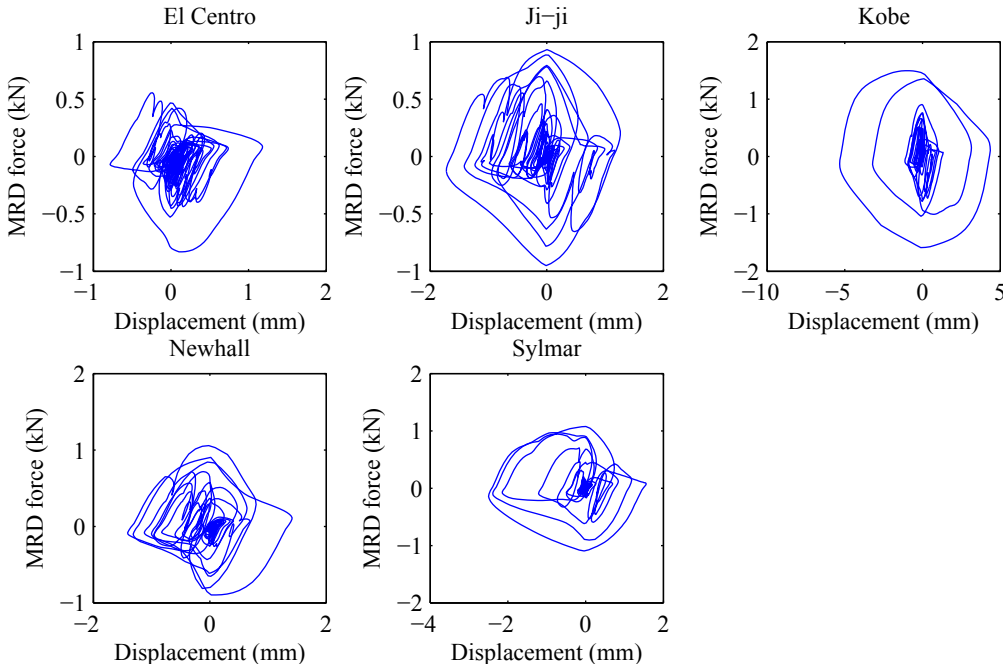

Figure 6.13: Hysteresis loops produced by the simple control 2N by Eq. (6.20)

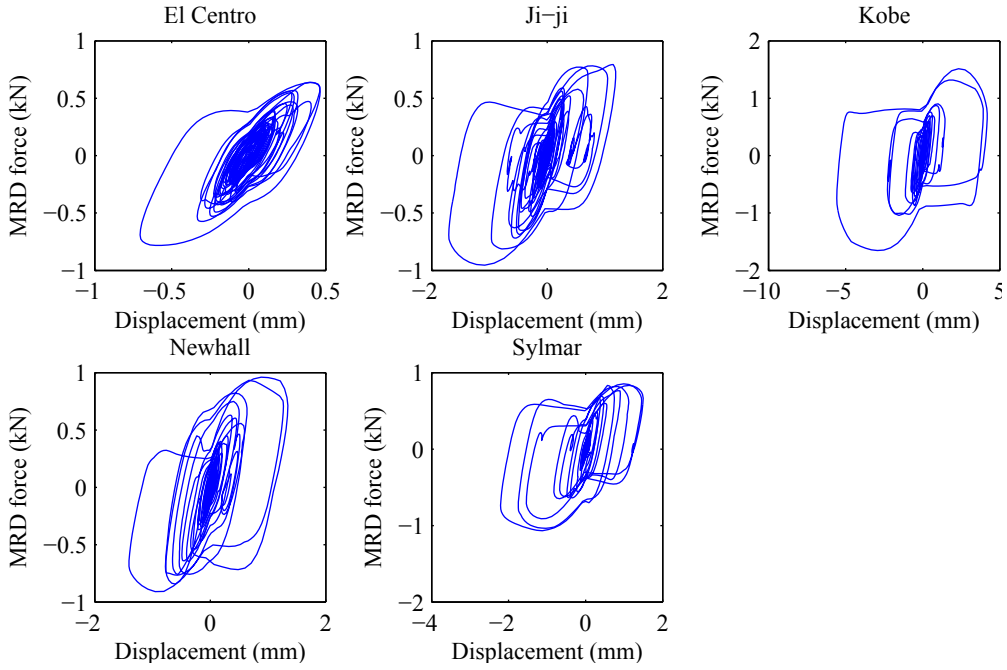

Figure 6.14: Hysteresis loops produced by the simple control 2P by Eq. (6.21)

clipped-optimal control with acceleration weighting, the LQG-based clipped-optimal control with displacement weighting, the Lyapunov stability-based control, the simple control 1N, the simple control 1P, the simple control 2N, the simple control 2N. In addition to these semi-active controllers, uncontrolled (i.e., no MR damper), passive-off (the input current to the MR damper is 0), and passive-on (the input current to the MR damper is 2.0 A) cases are included in these tables for comparisons. Figures 6.15 and 6.16 compare the ratios to the uncontrolled case of the peak and RMS relative displacements of the third floor for each controller. The RMS value of n data $\{p_1, p_2, \cdots p_n\}$ is defined as

$$p_{\text{RMS}} = \sqrt{\frac{\sum_{k=1}^{n} p_k^2}{n}} \tag{6.35}$$

The comparisons of the absolute acceleration of the third floor can be found in Figures 6.17 and 6.18. As can be seen in these tables and figures, in general, the semi-active controllers producing pseudo-negative stiffness, i.e., the LQG-based clipped-optimal control with acceleration weighting, the simple control 1N, and the simple control 2N show better performance in reducing both response displacements and accelerations, although some exceptions can be found. In particular, negative stiffness is effective at reducing response acceleration. Evaluating the results given in the tables and figures, the proposed two algorithms producing pseudo-negative stiffness, i.e., the simple control 1N and the simple control 2N show performance comparable to the LQG-based clipped-optimal controller, or even better results for some cases.

Table 6.1: Comparisons of peak and RMS values to El Centro earthquake

		Displacement (mm)			Acceleration (g)			Force (N)
	Controller	x_1	x_2	x_3	$x_{a,1}$	$x_{a,2}$	$x_{a,3}$	f_{MR}
Peak	Uncontrolled	3.372	5.199	6.073	5.242	6.660	7.498	N/A
	Passive-off	1.775	2.821	3.459	2.759	3.870	4.453	148.2
	Passive-on	0.616	1.831	2.492	2.673	4.303	4.753	850.1
	LQG w/ A.	1.272	1.946	2.481	3.569	5.213	4.925	597.1
	LQG w/ I.D.	1.474	2.338	2.758	3.300	5.528	4.651	421.3
	LQG w/ R.D.	0.647	1.858	2.493	2.766	4.723	4.834	823.8
	Laypunov	0.666	1.874	2.533	2.998	4.870	4.829	826.9
	Simple control 1N	0.947	1.634	2.315	4.324	4.371	5.497	811.2
	Simple control 1P	0.907	2.224	2.840	4.840	5.842	5.677	723.8
	Simple control 2N	1.181	1.843	2.380	3.526	4.368	5.390	830.2
	Simple control 2P	0.705	1.928	2.513	2.904	4.617	4.807	782.4
RMS	Uncontrolled	1.375	2.177	2.618	1.835	2.571	3.141	N/A
	Passive-off	0.367	0.604	0.739	0.715	0.840	1.043	58.4
	Passive-on	0.124	0.474	0.690	0.626	1.196	1.583	225.8
	LQG w/ A.	0.213	0.388	0.503	0.828	0.999	1.078	128.7
	LQG w/ I.D.	0.251	0.424	0.531	0.807	0.890	0.983	103.0
	LQG w/ R.D.	0.132	0.473	0.683	0.679	1.239	1.572	217.8
	Laypunov	0.136	0.459	0.656	0.735	1.301	1.542	206.9
	Simple control 1N	0.181	0.384	0.523	0.761	1.019	1.177	166.2
	Simple control 1P	0.173	0.489	0.681	0.796	1.260	1.493	189.5
	Simple control 2N	0.222	0.411	0.544	0.784	1.026	1.169	168.5
	Simple control 2P	0.136	0.482	0.692	0.666	1.211	1.562	216.2

Table 6.2: Comparisons of peak and RMS values to Ji-ji earthquake

		Displacement (mm)			Acceleration (g)			Force (N)
	Controller	x_1	x_2	x_3	$x_{a,1}$	$x_{a,2}$	$x_{a,3}$	f_{MR}
Peak	Uncontrolled	5.010	7.957	9.593	6.913	9.449	12.070	N/A
	Passive-off	3.562	5.552	6.588	6.505	7.220	8.316	208.2
	Passive-on	1.099	2.473	3.228	4.736	6.308	6.327	1011.5
	LQG w/ A.	2.459	3.594	4.479	7.064	6.033	6.868	964.7
	LQG w/ I.D.	2.861	4.448	5.594	5.635	7.302	7.986	744.7
	LQG w/ R.D.	1.139	2.514	3.290	4.742	5.841	5.906	992.4
	Laypunov	1.191	2.389	3.201	4.478	6.241	5.776	964.8
	Simple control 1N	1.598	2.348	2.896	5.470	6.334	6.536	1008.7
	Simple control 1P	1.795	3.583	4.700	6.626	7.957	8.679	893.2
	Simple control 2N	1.722	2.490	2.880	5.608	5.668	6.841	951.5
	Simple control 2P	1.703	3.347	4.247	6.703	7.858	7.803	953.6
RMS	Uncontrolled	2.149	3.397	4.077	2.733	3.984	4.784	N/A
	Passive-off	0.838	1.328	1.594	1.287	1.629	1.926	78.2
	Passive-on	0.301	0.713	0.971	0.918	1.472	1.910	298.8
	LQG w/ A.	0.584	0.876	1.050	1.259	1.325	1.532	200.5
	LQG w/ I.D.	0.664	1.005	1.197	1.333	1.380	1.588	162.6
	LQG w/ R.D.	0.328	0.728	0.978	0.961	1.446	1.859	282.4
	Laypunov	0.340	0.724	0.966	0.968	1.450	1.822	279.4
	Simple control 1N	0.470	0.755	0.943	1.055	1.353	1.577	269.0
	Simple control 1P	0.408	0.845	1.099	1.283	1.657	1.955	241.5
	Simple control 2N	0.474	0.767	0.958	1.061	1.370	1.608	263.5
	Simple control 2P	0.369	0.778	1.022	1.152	1.588	1.888	252.0

Table 6.3: Comparisons of peak and RMS values to Kobe earthquake

		Displacement (mm)			Acceleration (g)			Force (kN)
	Controller	x_1	x_2	x_3	$x_{a,1}$	$x_{a,2}$	$x_{a,3}$	f_{MR}
Peak	Uncontrolled	13.289	21.227	25.658	19.278	24.467	30.858	N/A
	Passive-off	8.941	14.422	17.527	11.006	17.177	21.651	491.7
	Passive-on	4.601	8.292	9.940	8.940	17.000	14.907	1759.7
	LQG w/ A.	5.457	8.539	10.283	10.705	12.402	16.162	1561.2
	LQG w/ I.D.	6.342	10.031	11.791	9.740	15.317	13.711	1383.0
	LQG w/ R.D.	4.772	8.595	10.373	8.751	17.131	14.913	1729.0
	Laypunov	4.822	8.729	10.603	7.665	16.147	14.806	1745.0
	Simple control 1N	5.142	8.208	9.944	9.493	11.684	14.969	1599.9
	Simple control 1P	5.859	10.573	13.414	14.243	20.075	22.324	1650.4
	Simple control 2N	5.335	8.490	10.306	9.760	11.754	15.859	1588.3
	Simple control 2P	5.567	9.970	12.413	13.586	20.337	20.696	1654.7
RMS	Uncontrolled	6.930	10.994	13.215	8.173	12.852	15.473	N/A
	Passive-off	2.117	3.376	4.069	2.660	4.010	4.884	137.3
	Passive-on	0.580	1.154	1.523	1.312	2.152	2.818	392.7
	LQG w/ A.	0.749	1.212	1.498	1.539	1.941	2.363	285.4
	LQG w/ I.D.	0.971	1.519	1.840	1.718	2.063	2.537	251.6
	LQG w/ R.D.	0.603	1.199	1.574	1.299	2.182	2.839	381.6
	Laypunov	0.618	1.210	1.582	1.291	2.177	2.815	373.5
	Simple control 1N	0.682	1.146	1.442	1.332	1.900	2.365	324.0
	Simple control 1P	0.913	1.634	2.054	2.123	2.669	3.265	307.7
	Simple control 2N	0.717	1.199	1.501	1.358	1.948	2.419	320.1
	Simple control 2P	0.813	1.463	1.852	1.916	2.489	3.057	326.6

Table 6.4: Comparisons of peak and RMS values to Newhall earthquake

		Displacement (mm)			Acceleration (g)			Force (kN)
	Controller	x_1	x_2	x_3	$x_{a,1}$	$x_{a,2}$	$x_{a,3}$	f_{MR}
Peak	Uncontrolled	3.702	4.797	6.494	13.663	8.932	13.959	N/A
	Passive-off	2.453	3.830	4.402	8.550	7.348	8.462	220.9
	Passive-on	1.045	2.611	3.682	8.398	11.303	13.866	1095.4
	LQG w/ A.	1.598	2.600	3.136	8.615	9.984	10.241	909.4
	LQG w/ I.D.	1.923	2.936	3.309	7.003	9.140	8.650	699.4
	LQG w/ R.D.	1.067	2.817	3.930	8.204	10.190	13.629	1081.6
	Laypunov	1.091	2.860	4.035	8.638	10.036	12.868	1071.8
	Simple control 1N	1.482	2.463	2.978	9.429	9.073	10.700	1039.0
	Simple control 1P	1.882	3.845	4.844	7.691	9.526	10.568	963.6
	Simple control 2N	1.414	2.363	3.134	7.501	8.655	10.361	1057.2
	Simple control 2P	1.405	3.169	4.102	8.055	10.014	12.218	959.4
RMS	Uncontrolled	1.276	1.930	2.340	4.230	2.642	4.216	N/A
	Passive-off	0.604	0.974	1.188	1.296	1.314	1.729	69.8
	Passive-on	0.196	0.620	0.886	1.036	1.693	2.072	284.7
	LQG w/ A.	0.307	0.518	0.658	1.169	1.374	1.453	168.4
	LQG w/ I.D.	0.376	0.607	0.749	1.084	1.172	1.326	132.2
	LQG w/ R.D.	0.214	0.626	0.886	1.057	1.640	2.024	273.9
	Laypunov	0.223	0.613	0.857	1.079	1.654	1.962	256.2
	Simple control 1N	0.278	0.523	0.693	1.117	1.450	1.586	216.1
	Simple control 1P	0.345	0.746	0.990	1.211	1.574	1.923	221.1
	Simple control 2N	0.299	0.540	0.709	1.103	1.338	1.547	211.2
	Simple control 2P	0.252	0.635	0.875	1.137	1.584	1.908	243.7

Table 6.5: Comparisons of peak and RMS values to Sylmar earthquake

		Displacement (mm)			Acceleration (g)			Force (kN)
	Controller	x_1	x_2	x_3	$x_{a,1}$	$x_{a,2}$	$x_{a,3}$	f_{MR}
Peak	Uncontrolled	8.128	12.445	14.470	12.816	16.097	17.079	N/A
	Passive-off	5.325	8.371	9.948	7.535	10.549	11.145	285.5
	Passive-on	1.668	3.761	5.521	5.958	8.338	13.856	1118.9
	LQG w/ A.	3.161	4.708	5.163	6.996	8.952	9.658	939.0
	LQG w/ I.D.	3.481	5.339	6.239	6.620	9.448	8.188	809.8
	LQG w/ R.D.	1.651	3.737	5.485	5.645	8.347	13.772	1097.9
	Laypunov	1.715	3.758	5.420	5.731	7.791	13.179	1032.9
	Simple control 1N	2.492	3.759	4.534	7.114	6.662	10.658	1148.9
	Simple control 1P	2.736	5.325	6.920	8.897	10.091	11.747	1037.4
	Simple control 2N	2.496	3.698	4.805	6.812	6.957	10.157	1095.8
	Simple control 2P	2.207	4.415	5.535	7.769	9.689	13.067	1068.5
RMS	Uncontrolled	3.750	5.948	7.151	4.662	6.979	8.475	N/A
	Passive-off	1.180	1.891	2.285	1.577	2.284	2.822	93.9
	Passive-on	0.240	0.688	0.975	0.894	1.593	2.132	298.6
	LQG w/ A.	0.479	0.736	0.901	1.170	1.220	1.494	185.7
	LQG w/ I.D.	0.562	0.880	1.069	1.097	1.251	1.532	155.8
	LQG w/ R.D.	0.248	0.690	0.973	0.866	1.532	2.082	288.6
	Laypunov	0.266	0.693	0.965	0.877	1.462	2.004	275.0
	Simple control 1N	0.404	0.682	0.875	1.048	1.317	1.655	244.3
	Simple control 1P	0.485	0.938	1.209	1.412	1.764	2.163	220.8
	Simple control 2N	0.418	0.706	0.901	1.025	1.328	1.652	235.2
	Simple control 2P	0.377	0.800	1.064	1.248	1.742	2.120	251.2

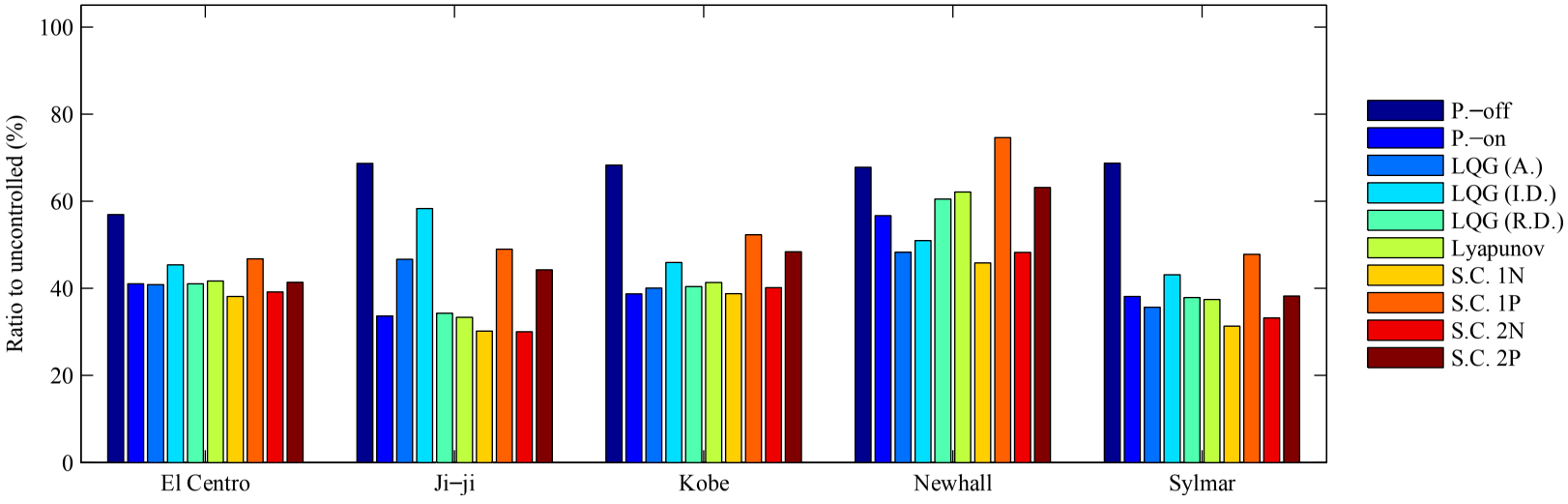

Figure 6.15: Comparisons of the peak response displacements of 3rd floor

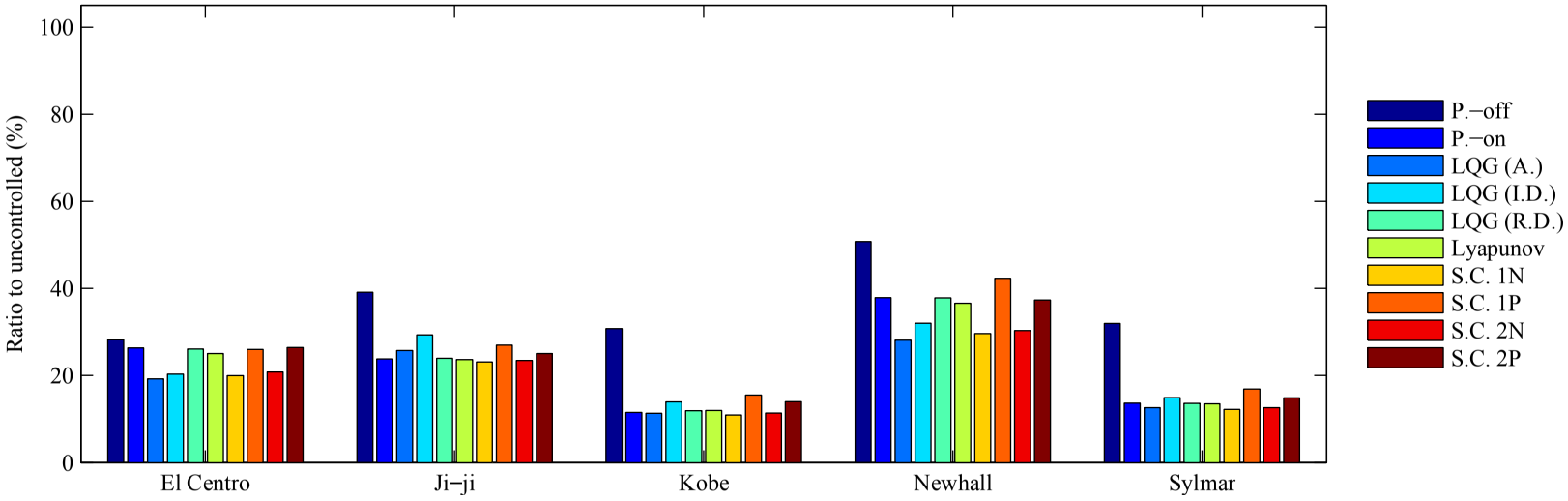

Figure 6.16: Comparisons of the RMS response displacements of 3rd floor

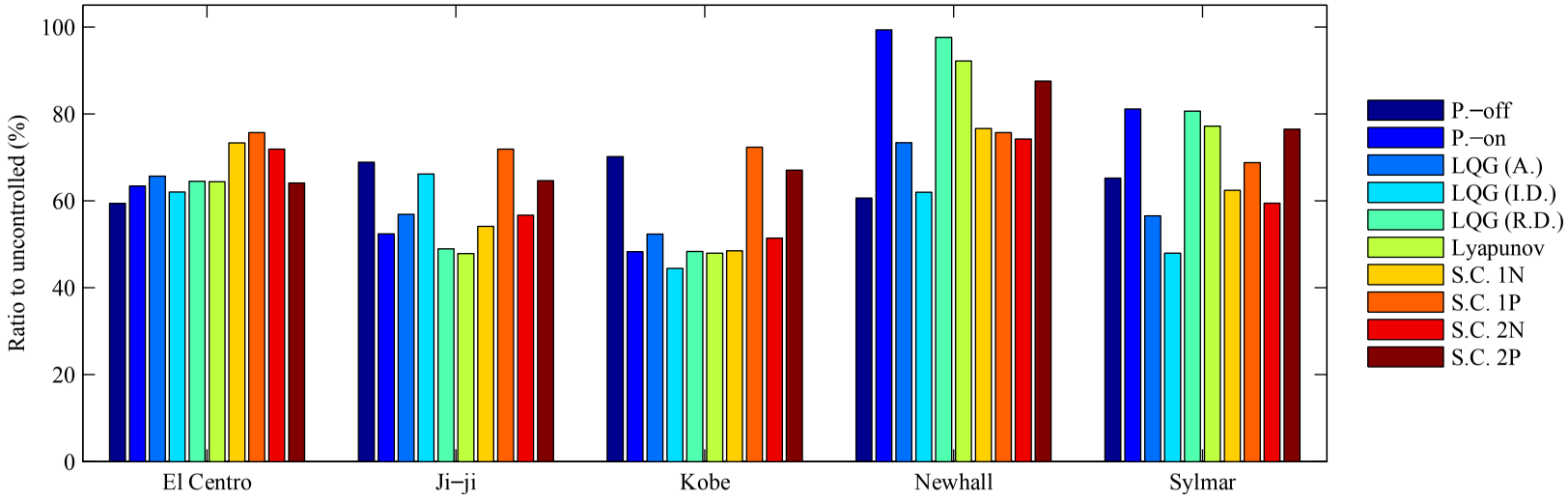

Figure 6.17: Comparisons of the peak response accelerations of 3rd floor

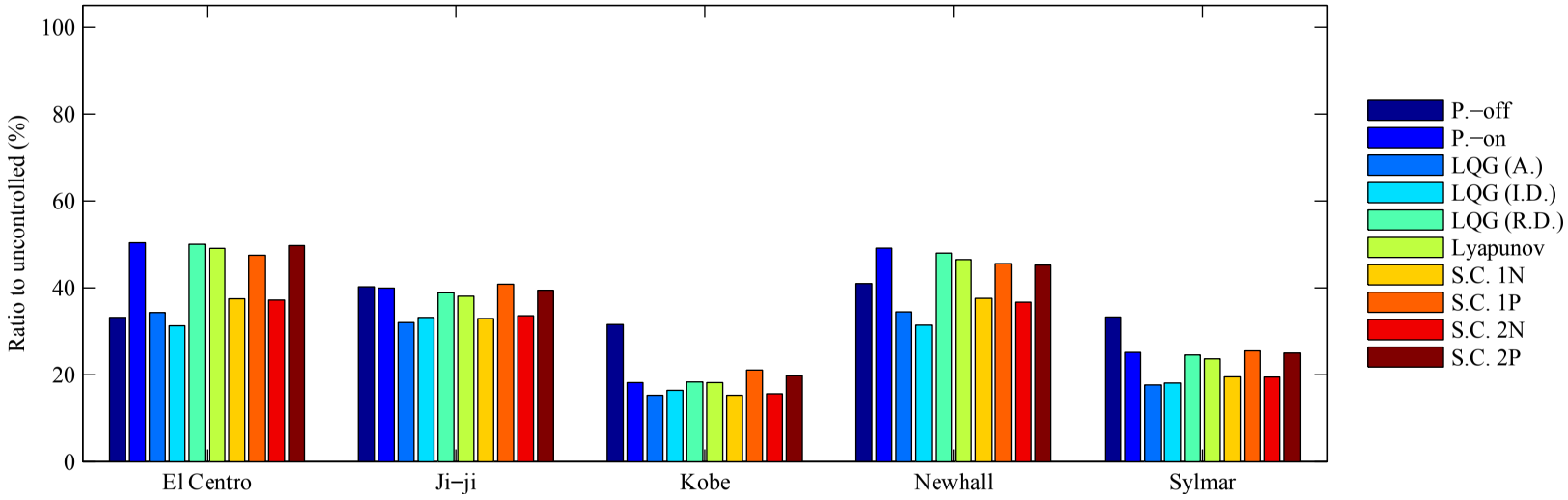

Figure 6.18: Comparisons of the RMS response accelerations of 3rd floor

Figure 6.19 shows the earthquake input energies into the building model for three semi-active controllers producing pseudo-negative stiffness, i.e., the LQG-based clipped-optimal control with acceleration weighting, the simple control 1N, and the simple control 2N. The earthquake input energy E_{i} is defined as (Chopra, 2007)

$$E_{\mathrm{i}} = -\int_0^t \dot{\mathbf{x}}^T \mathbf{M}_{\mathrm{s}} \mathbf{L}_{\mathrm{s}} \ddot{x}_g d\tau \tag{6.36}$$

As can be seen in the figure, the simple controls 1N and 2N can reduce input earthquake energy more than the LQG-based clipped-optimal control applied to El Centro, Ji-ji, and Kobe earthquake records. Even for Newhall and Sylmar records, the energy absorption capabilities of the proposed two simple controllers are comparable to the LQG-based clipped-optimal control case.

6.7 Summary

This chapter proposed two new model-free semi-active control algorithms for controllable dampers. One of the algorithms needs only the directions of the displacement and the velocity of the damper to decide the property of the damper. The other needs the directions of only the displacement and the output force of the damper. Thus, the structure model and a number of sensors are not required to implement the proposed algorithms. Moreover, this research showed that the proposed controllers can produce versatile hysteresis control force loops through numerical simulations on the scaled three-story building model with a MR damper. Also, the effectiveness of hysteresis loops having negative stiffness was verified. Additionally, the numerical results showed that the proposed two algorithms producing pseudo-negative stiffness had performance comparable to the LQG-based clipped-optimal controllers, which need the accurate structure model and more sensors.

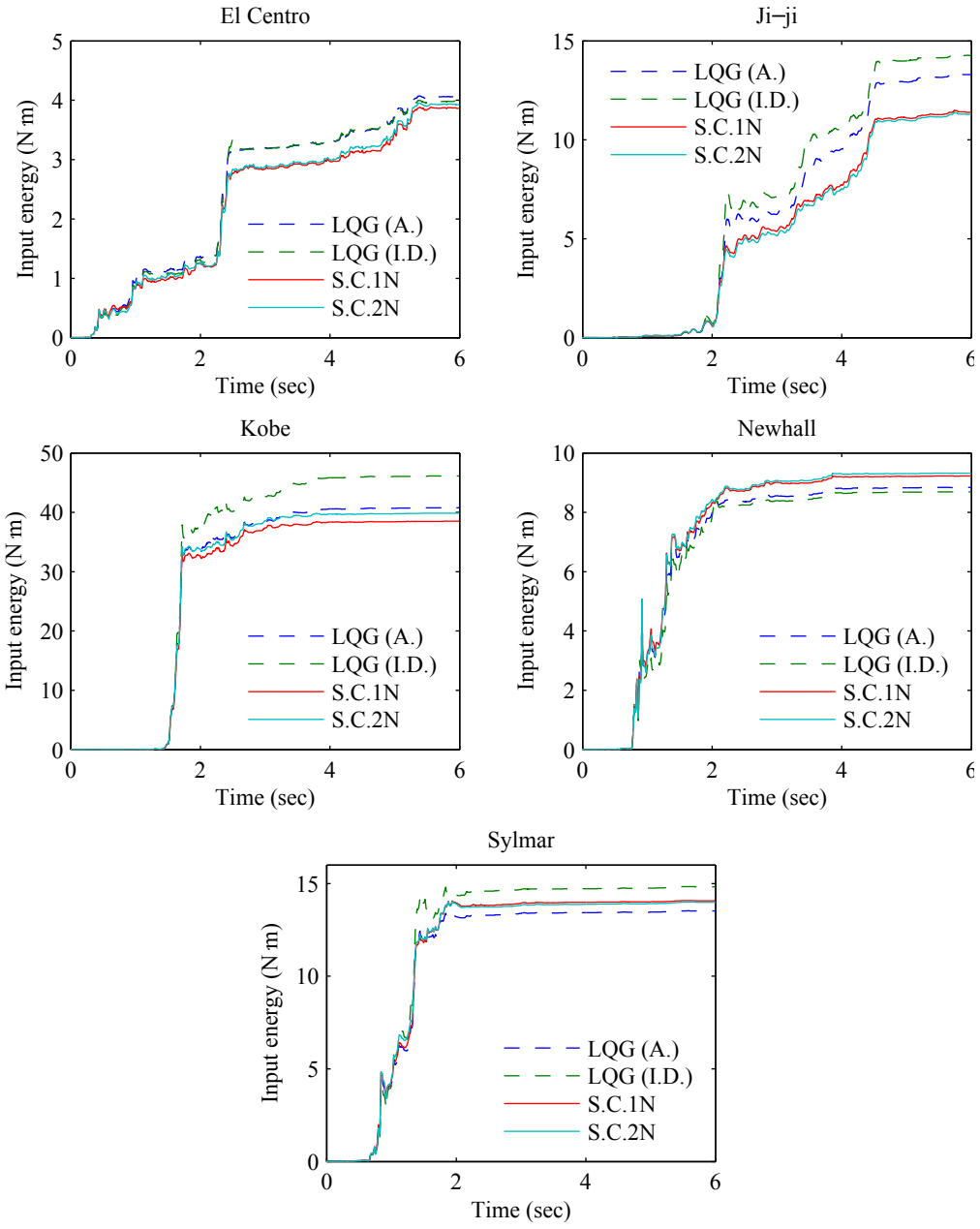

Figure 6.19: Comparisons of earthquake input energy

Chapter 7

RTHS for Semi-active Control on a MDOF structure

To show the effectiveness of semi-active control strategies, experimental verification is necessary. However, due to the limitation of cost and facilities, it is not practical to carry out shaking table testing for full-scale structures. To provide experimental verification, RTHS is an alternative method where the semi-active control devices can be experimentally tested, while the remaining components in the structural system are simultaneously tested through numerical simulation.

Time delays/lags are critical issues in RTHS, so introducing compensation for them is essential. However, RTHS becomes more challenging for MDOF structures because MDOF structures include significant contributions at different frequencies which can not be compensated by assuming a constant time delay. The focus of this chapter is to show the accuracy of the model-based compensator for RTHS on a MDOF structure using a smart outrigger damping system.

Smart outrigger damping systems have been proposed as a novel energy dissipation system to protect high-rise buildings from severe earthquakes and strong winds. In these damping systems, devices such as MR dampers are installed vertically between the outrigger and perimeter columns to achieve large and adaptable energy dissipation. In this chapter, to complement the high performance shown in previous theoretical studies, this control approach is experimentally verified as well.

7.1 Smart outrigger damping system

In this section, the models for both the high-rise building and the MR damper are presented. Also, the semi-active control algorithm selected for the system is illustrated. In RTHS, a physical MR damper is used, while in numerical simulation, the MR damper model created in Section 4.1 is used.

7.1.1 Problem formulation

Smart outrigger damping systems are an attractive method to achieve sufficient displacement for damping devices on high-rise buildings. According to Yang et al. (2004a), a high-rise building can be modeled as a cantilevered beam in which the structural deformations are derived from the behavior of the core. For a high-rise building with outrigger damping, the control devices (e.g., viscous dampers or MR dampers) are located between the outrigger walls and the perimeter columns. Assuming that the perimeter columns are axially very stiff and that the outrigger behaves as a rigid body, then the high-rise building with damped outriggers can be modeled as shown in Figure 7.1. As can be seen, the forces from the control devices result in moments being applied to the core through the rigid outrigger. In essence, the damped outrigger acts as a point rotational damping device. The moment applied to the core by the outrigger system f_{m} can be written as

$$f_{\mathrm{m}} = n_{\mathrm{d}} o_{\mathrm{e}} f \tag{7.1}$$

where f is the force from a single control device; n_{d} is the number of control devices; o_{e} is the distance from the control devices to the center of the core (see Figure 7.1). The equation of motion

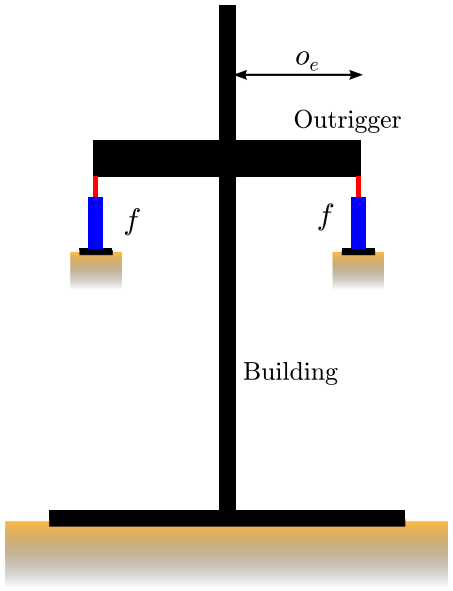

Figure 7.1: Mechanism of outrigger systems

can be written as

$$\mathbf{M}\ddot{\mathbf{u}} + \mathbf{C}\dot{\mathbf{u}} + \mathbf{K}\mathbf{u} = \mathbf{\Lambda} f_{\mathrm{m}} - \mathbf{M}\mathbf{\Gamma}\ddot{x}_g \tag{7.2}$$

where $\mathbf{M}$, $\mathbf{C}$, $\mathbf{K}$ are the structural mass, damping, stiffness matrices, respectively; $\mathbf{u}$ is the structural deformation vector; $\mathbf{\Lambda}$ is an influence vector that applies the damper restoring force to the appropriate rotational degrees of freedom (DOF); $\mathbf{\Gamma}$ is a vector with entries equal to unity for translational DOFs and zero for others; and $\ddot{x}_g$ is the ground acceleration. The state-space form of Eq. (7.2) is given by

$$\dot{\mathbf{x}} = \mathbf{A}\mathbf{x} + \mathbf{B} f_{\mathrm{m}} + \mathbf{E}\ddot{x}_g \tag{7.3}$$

$$\mathbf{y} = \mathbf{C}_y\mathbf{x} + \mathbf{D}_y f_{\mathrm{m}} + \mathbf{F}_y\ddot{x}_g + \mathbf{v} \tag{7.4}$$

$$\mathbf{z} = \mathbf{C}_z\mathbf{x} + \mathbf{D}_z f_{\mathrm{m}} + \mathbf{F}_z\ddot{x}_g \tag{7.5}$$

where $\mathbf{y}$ presents the measured structural responses including the relative displacements, the relative velocities, and the absolute floor accelerations; $\mathbf{v}$ is the measurement noise; and $\mathbf{z}$ corresponds to the regulated structural responses. $\mathbf{A}$, $\mathbf{B}$, $\mathbf{C}_y$, $\mathbf{C}_z$, $\mathbf{D}_y$, $\mathbf{D}_z$, $\mathbf{E}$, $\mathbf{F}_y$, and $\mathbf{F}_z$ are appropriately chosen matrices corresponding to the associated state-space equations.

7.1.2 Building model

The building used in this study is the St. Francis Shangri-La Place in the Philippines (Willford et al., 2008; Infanti et al., 2008; Chang et al., 2013). This 60-story building has a height of 210 m and has 12 perimeter columns which are 20 m from the building centerline. The concrete core is assumed to be 12 m $\times$ 12 m with 0.5 m thickness. The total mass of the building is 30,000 tons and the outrigger system installed consists of 16 viscous dampers, 8 of which control the response in each of the two orthogonal directions.

To create the model for evaluation, a vertical cantilever beam model based on the Bernoulli-Euler beam theory is applied. A finite element model is developed so that every story has one translational and one rotational degree of freedoms. Therefore, the total number of degrees-of-freedom should be 120 (60 in translation and 60 in rotation). Hence, the reduced structural

deformation vector up to mth mode, $\mathbf{u}_{\text{red},m}$, can be represented by

$$\mathbf{u}_{\text{red},m}(t) = \sum_{i=1}^{m} \phi_i q_i(t) = \mathbf{\Phi}_m \mathbf{q}_m(t) \tag{7.6}$$

where

$$\mathbf{\Phi}_m = \begin{bmatrix} \phi_1 & \phi_2 & \cdots & \phi_m \end{bmatrix} \tag{7.7}$$

is the mode shape matrix up to the mth mode and

$$\mathbf{q}_m = \begin{bmatrix} q_1 & q_2 & \cdots & q_m \end{bmatrix} \tag{7.8}$$

is the modal coordinate vector up to the mth mode. In this study, $m = 10$ for the evaluation model (i.e., to perform the response calculations) and $m = 5$ for the control design model (i.e., to design the semi-active controllers). The first 10 natural frequencies are 0.18 Hz, 1.15 Hz, 3.14 Hz, 6.00 Hz, 9.61 Hz, 13.84 Hz, 18.56 Hz, 23.66 Hz, 29.06 Hz, and 34.66 Hz, respectively. Damping of 2 % is assumed in each mode.

The 42nd floor is selected as the optimal location of the outrigger and dampers in this study based on the numerical study of Chang et al. (2013). In this study, to assume that the MR dampers installed on the opposite sides behave anti-symmetrically, the displacement of the MR dampers are calculated only from the rotation of the 42nd floor; i.e. the horizontal translation effect to the displacement of the MR dampers is ignored. The magnitudes of the transfer functions for the reduced building model from input earthquake acceleration to the displacement and acceleration of the damper are shown in Figure 7.2. As can be seen, high-frequency content due to high-mode responses affects the acceleration significantly.

Note that the estimated damping after the MR dampers are installed to the 42nd floor are, from the first mode, 4.74 %, 4.77 %, 2.00 %, 3.72 %, 4.03 %, 2.05 %, 3.32 %, 4.09 %, 2.17 %, and 2.89 %, respectively. These values are calculated by assuming viscous dampers which have the same level damping as the passive on mode MR dampers.

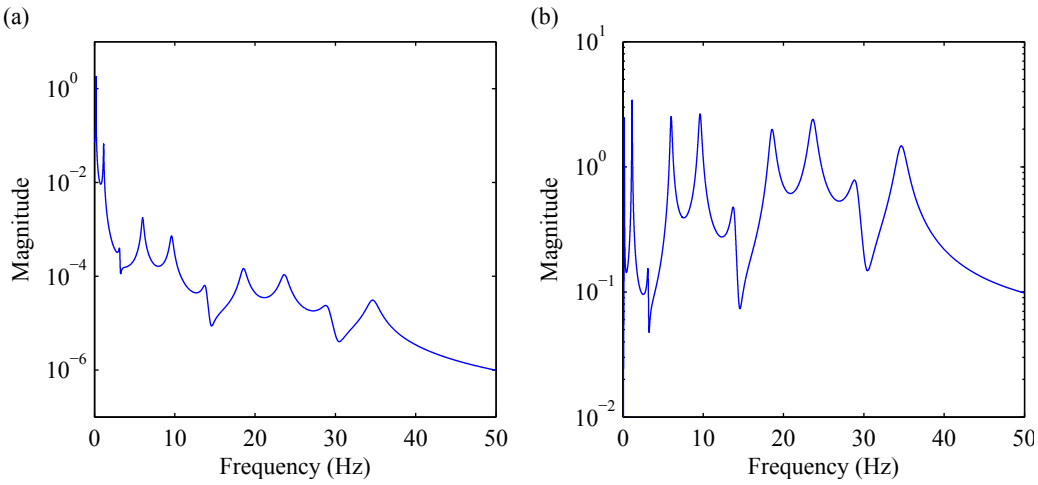

Figure 7.2: Transfer functions from input acceleration to the damper; (a) Displacement, (b) Acceleration

7.1.3 Semi-active control designs

To facilitate semi-active control using MR dampers, control methods that translate the required control force into an input current command are typically used. Dyke et al. (1996c) proposed a LQG-based clipped-optimal control method which had been experimentally verified using MR dampers and will be selected for this study. In this control method, the outrigger system employs the LQG/H_2 control algorithm to calculate the optimal control force. By reconsidering Eq. (7.5), the cost function of the LQG/H_2 control can be written by

$$J = \lim_{t\to\infty} \frac{1}{t} \mathrm{E}\left[\int_0^t \left(\mathbf{z}^T \mathbf{Q}\mathbf{z} + R{f_{m,c}}^2\right) dt\right] \tag{7.9}$$

where $\mathbf{Q}$ and R are the weighting parameters, $f_{m,c}$ is a control moment, E[·] means the expected value of the quantity in brackets and t represents the time. By minimizing Eq. (7.9), the control force is a function of the structural states. In the LQG/H_2 control, the Kalman filter estimates (Nagarajaiah and Narasimhan, 2006) the state based on the measured responses such that

$$\dot{\hat{\mathbf{x}}} = \mathbf{A}\hat{\mathbf{x}} + \mathbf{B}f_{\mathrm{m,c}} + \mathbf{L}\left(\mathbf{y} - \mathbf{C}_y\hat{\mathbf{x}} - \mathbf{D}_y f_{\mathrm{m,c}}\right) \tag{7.10}$$

$$f_{\mathrm{m,c}} = -\mathbf{K}_c\hat{\mathbf{x}} \tag{7.11}$$

where $\mathbf{L}$ is the Kalman gain, $\mathbf{K}_c$ is the optimal control gain found by minimizing Eq. (7.9), and $\hat{\mathbf{x}}$ is the estimated state by the Kalman filter. The clipped-optimal control algorithms are used to convert the optimal control force of Eq. (7.11) to a command voltage for the MR damper. The desired input is given by

$$i_{\mathrm{d}} = V_{\max} \mathrm{H}\left\{\left(f_{\mathrm{m,c}} - f_{\mathrm{m,MR}}\right) f_{\mathrm{m,MR}}\right\} \tag{7.12}$$

where $\mathrm{H}\{\cdot\}$ is the Heaviside function, i_{d} is the input voltage to a MR damper; $V_{\max}$ is the maximum input voltage, $f_{\mathrm{m,c}}$ is the desired optimal control moment generated by Eq. (7.11) and $f_{m,\mathrm{MR}}$ is the actual damping moment generated by the MR damper force and Eq. (7.1). The clipped-optimal controller logic is illustrated in Figure 6.1.

Four LQG-based clipped-optimal control strategies are created through different LQG designs and evaluated in this study. Controller #1 focuses on minimizing the relative translational displacements to the ground at the 10th, 20th, 30th, 40th, 50th, and 60th floors in Eq. (7.9), while controller #2 focuses on minimizing the translational absolute floor accelerations at the same locations. In addition, controllers #3 and #4 minimize the rotational displacements and accelerations at the same locations, respectively. For the Kalman filter in Eqs. (7.10) and (7.11), this study assumes that the absolute translational floor accelerations at the 10th, 20th, 30th, 40th, 50th, and 60th floors are available to estimate the required force. The maximum input current $i_{\max}$ in the clipped-optimal control is 2.0 A based on the MR damper specifications.

7.2 Results

To investigate the seismic performance of the smart outrigger system, the results obtained from RTHS and numerical simulations are shown. The influence of magnitude and time delay errors on the results of RTHS is presented. In this section, two earthquake records are considered: (1) the north-south component of the El Centro earthquake in Imperial Valley, CA in 1940 and (2) the north-south component of the Kobe earthquake in Hyogo-ken Nanbu in 1995 (Yoshida and Dyke, 2004).

In this research, an assumption is made that required capacity of the MR damper to the target building can be achieved in both simulation and RTHS as follows: The output force of the MR

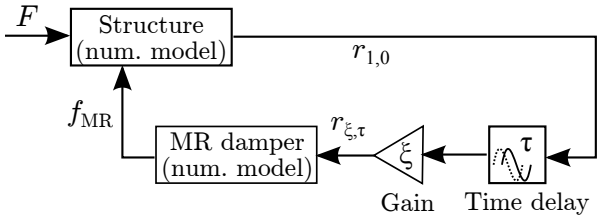

Figure 7.3: Schematic block diagram to investigate the RTHS error

damper is multiplied by 2500 and the displacement of the MR damper is scaled such that 1 inch (25.4 mm) in the MR damper corresponds to 0.1 m in the model of the outrigger damping system. The peak ground accelerations (PGAs) of input records are normalized to 0.3 g, and 0.5 g for the El Centro earthquake and 0.3 g, 0.5 g, and 0.7 g for the Kobe earthquake. The parameters $\mathbf{Q}$ and R of each semi-active controller are determined based on the simulation results of 0.3 g El Centro case by trial and error. These values are selected such that the maximum stroke of the physical MR damper is not exceeded. All numerical simulations are performed in SIMULINK (2013). For RTHS, models are created in SIMULINK (2013) and implemented in the DSP using MATLAB (2013)'s Real-Time Workshop.

7.2.1 Influence of magnitude and time delay errors on RTHS

First, the need for accurate actuator control is illustrated by investigating the effects due to magnitude and time delay errors in simulation, as shown in Figure 7.3. The magnitude and time delay provide quantitative means to simulate the effects of uncompensated actuator dynamics. In Figure 7.3, $r_{\xi,\tau}$ is the input signal to the MR damper, which is affected by a gain ξ and time delay τ (msec). Therefore, $r_{1,0}$ represents the case without any modeled actuator dynamics, i.e., the desired signal. The MR damper model developed in the previous section is used here. The input voltage into the MR damper model is set at 2.0 A (passive-on). For external forces F, El Centro and Kobe earthquakes with PGAs of 0.3 g are input.

Figure 7.4 shows the RMS errors when the gain and time delay are changed. The RMS errors are calculated by

$$\text{RMS error } (\%) = \sqrt{\frac{\sum_{k=1}^{n}(r_{\xi,\tau,k} - r_{1,0,k})^2}{\sum_{k=1}^{n}(r_{1,0,k})^2}} \times 100 \tag{7.13}$$

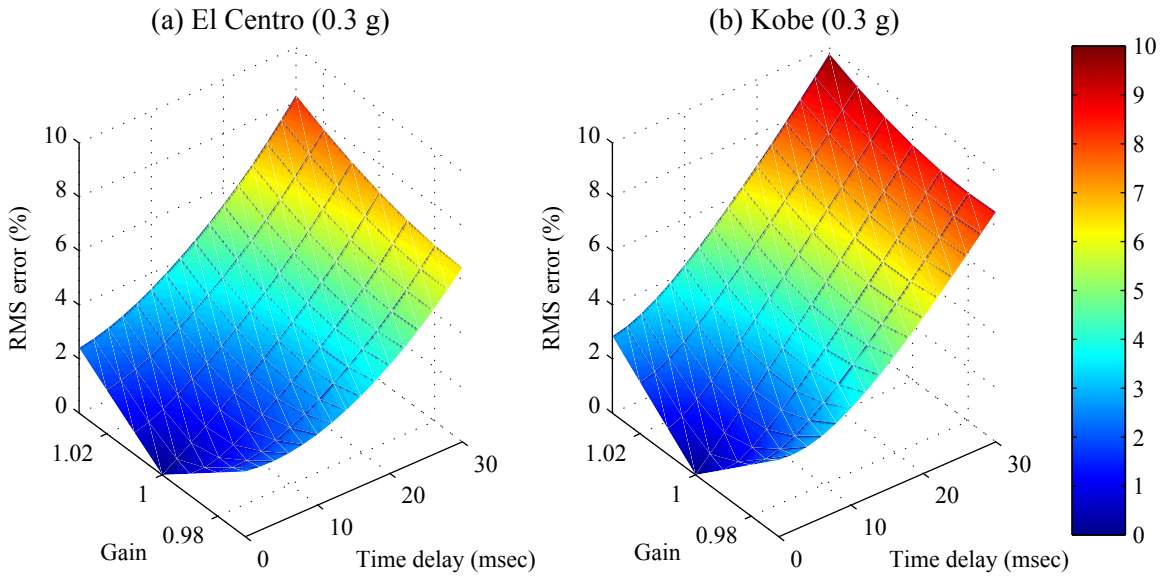

Figure 7.4: RMS errors generated by gain and time delay errors; (a) El Centro (0.3 g), (b) Kobe (0.3 g)

where n is the number of the data points, and $r_{\xi,\tau,k}$ is the kth data point of $r_{\xi,\tau}$. As can be observed, magnitude and time delay errors considerably detract from accuracy of RTHS, where the servo-hydraulic system would be the cause of such errors. The Kobe earthquake contains higher frequency content than El Centro, leading to larger error in the presence of time delay. The necessity of the feedforward controller to improve actuator displacement tracking is demonstrated through this parametric numerical study.

To confirm the performance of the model-based feedforward controller during RTHS for the MDOF structure, RMS errors between desired displacements and measured displacements from the LVDT are calculated in the same way as Eq. (7.13) for each case. The results are summarized in Table 7.1. To minimize the influence of transducer noise at low signal-to-noise ratios, only data during the strong motion portion of the RTHS is considered for error calculations (i.e., 3 sec to 35 sec for El Centro and 6 sec to 13 sec for Kobe). Table 7.1 shows that as inputs become larger, the ratios of errors to the inputs get smaller.

The time histories of desired displacements, compensated commands, and measured displacements for passive on cases are compared in Figure 7.5. This figure shows that the feedforward controller makes the compensated commands lead the desired displacements by more than 20

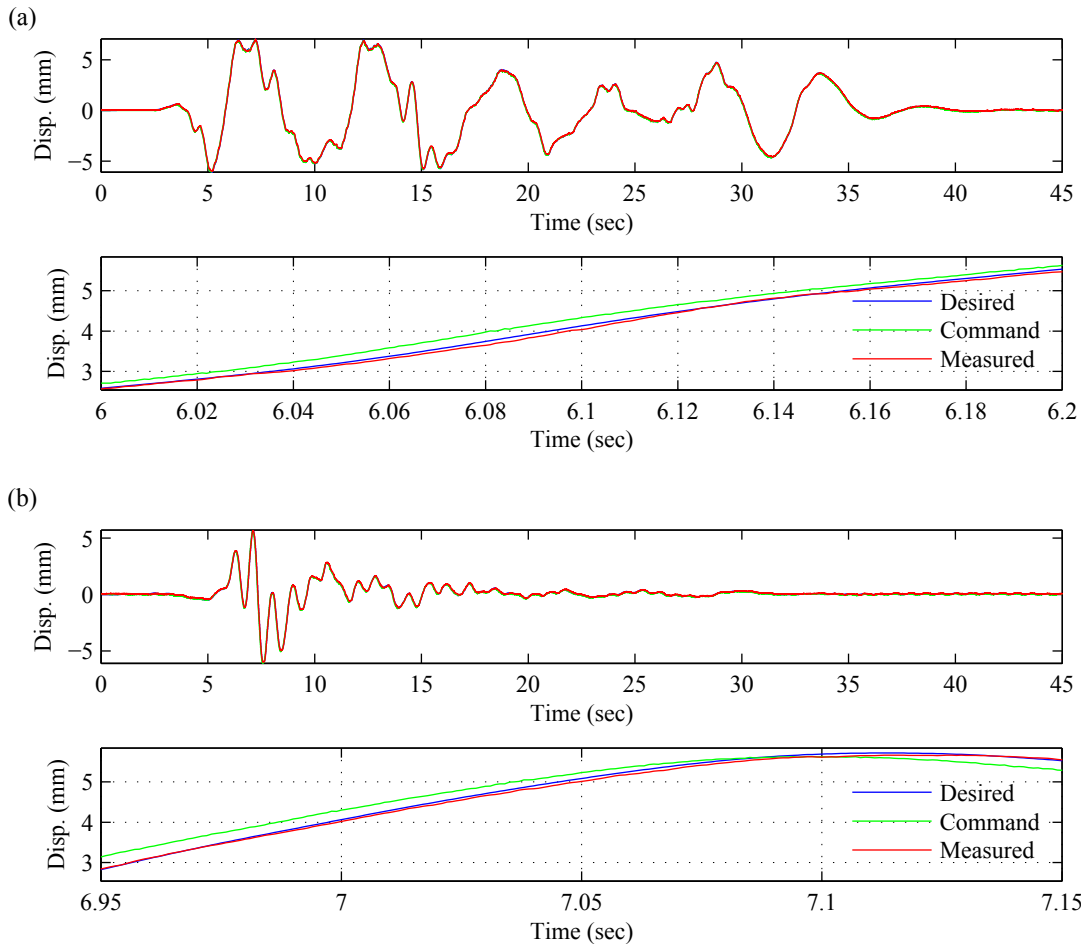

Figure 7.5: Comparisons between measured and command displacements for passive-on case; (a) El Centro (0.3 g), (b) Kobe (0.3 g)

msec. Also, the power spectral densities of command inputs are plotted in Figure 7.6 to investigate the influence of high-frequency commands to the servo-hydraulic system due to high-mode responses. As can be seen, peaks appear around natural frequency of each mode even in the high-frequency range. Also, this figure shows that Kobe cases need a more effective compensator in the high-frequency range for RTHS than El Centro cases.

7.2.2 Experimental assessment

For structural control performance evaluation, the structural control design is primarily aimed at reducing relative displacements and base shear forces, which are the major indicators of the performance of a structure. In addition to the semi-active control strategies, the outrigger damping

Table 7.1: RMS errors for each test (%)

Input	Passive	LQG #1	LQG #2	LQG #3	LQG #4
El Centro (0.3 g)	1.945	2.196	2.333	2.097	2.009
El Centro (0.5 g)	1.418	1.263	1.342	1.323	1.282
Kobe (0.3 g)	2.423	3.358	2.848	2.646	2.965
Kobe (0.5 g)	1.244	1.846	1.517	1.314	1.569
Kobe (0.7 g)	0.929	1.323	1.057	1.022	1.102

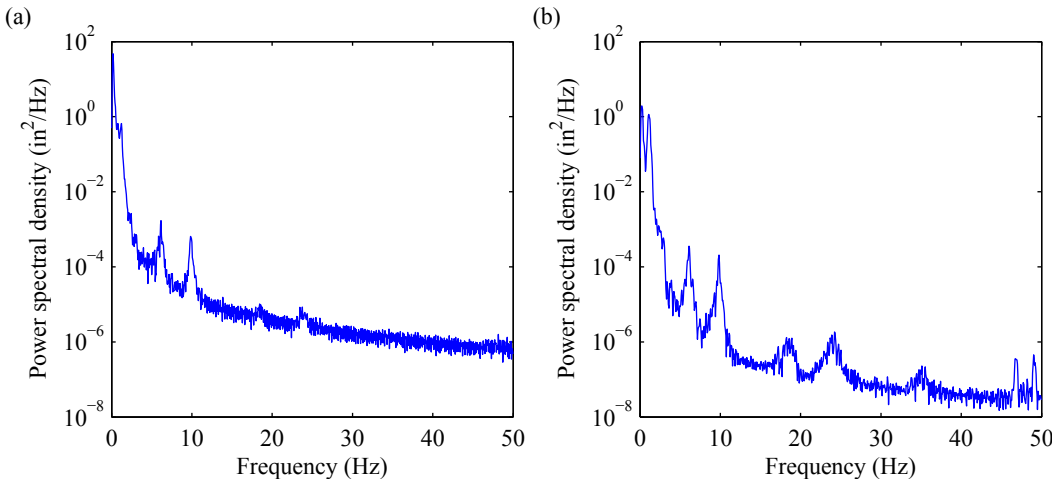

Figure 7.6: Power spectral densities of command inputs for passive-on cases; (a) El Centro (0.3 g), (b) Kobe (0.3 g)

system with passive-on mode (i.e., constant current) MR dampers and the performance of the uncontrolled (bare) building are also considered.

The time histories of the MR damper forces, the relationships between the displacements and the forces, and between the velocities and forces subjected to El Ceontro and Kobe earthquakes whose PGAs are scaled to 0.3 g are depicted in Figures 7.7 through 7.24. Figures 7.7 through 7.11 and Figures 7.16 through 7.20 compares the MR damper forces obtained from numerical simulation and RTHS produced by the passive-on, the LQG-based clipped-optimal controllers #1, #2, #3, and #4. These figures show that the proposed MR damper model created by the phenomenological model simulates the physical MR damper very well in both passive and semi-active cases. However, slight discrepancies can be observed. These differences between the simulation and the experimental results demonstrate the need for RTHS to assess the performance of advanced damping systems.

It should be noted that the expected properties of the hysteresis loops can not be found in any LQG-based clipped optimal controllers.

For comparison, the numerical simulation results of the MR damper forces produced by the proposed simple controllers are shown in Figures 7.12 through 7.15 and Figures 7.21 through 7.24. Contrary to the cases of the LQG-based clipped-optimal controllers, pseudo-negative stiffness is obtained from the simple control 1N and 2N while positive stiffness arises from the simple control 1P and 2P, as expected.

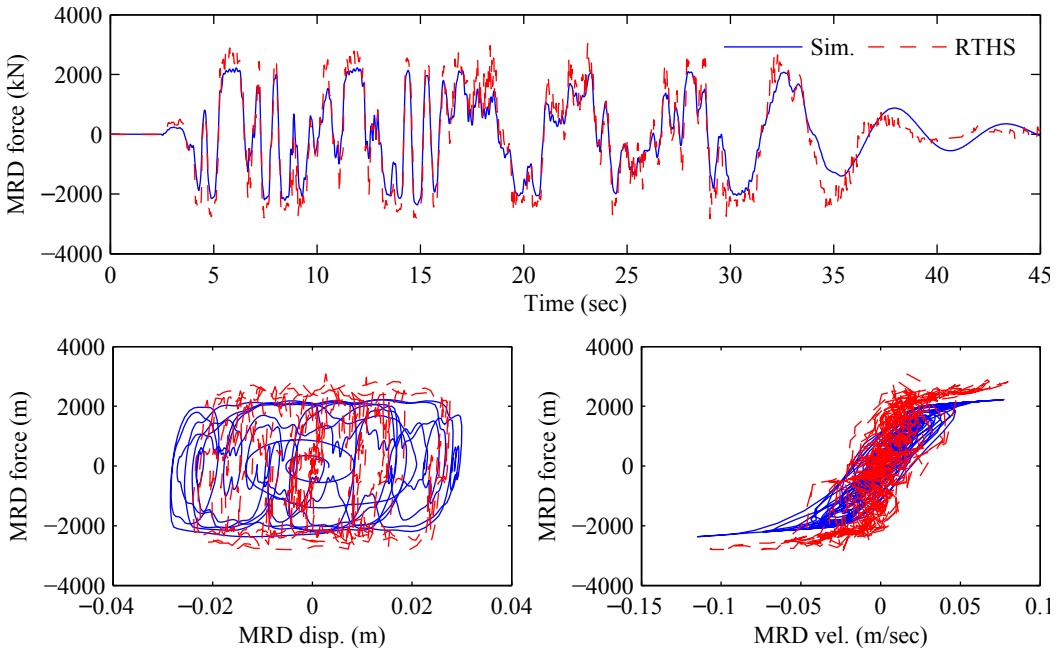

Figure 7.7: MR damper force by the passive-on control to El Centro of 0.3 g PGA

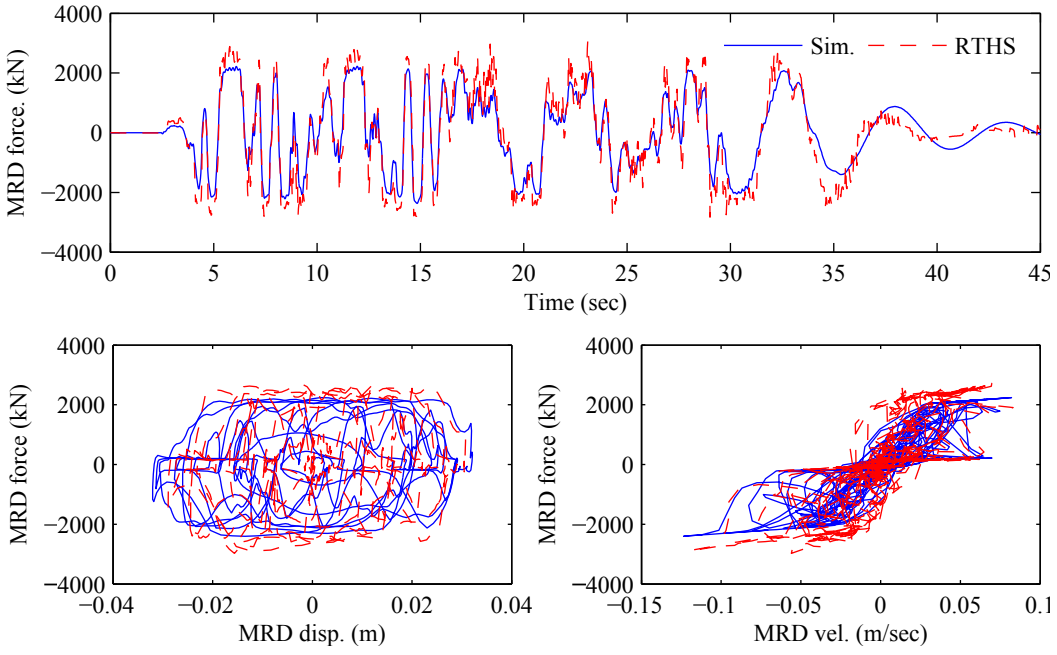

Figure 7.8: MR damper force by the semi-active control #1 to El Centro of 0.3 g PGA

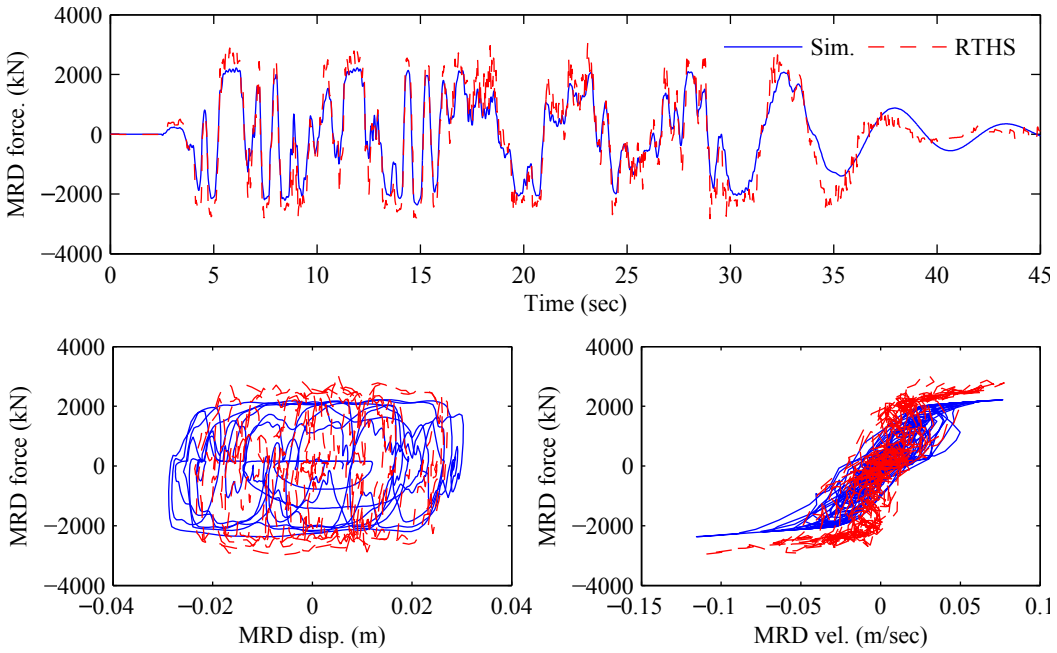

Figure 7.9: MR damper force by the semi-active control #2 to El Centro of 0.3 g PGA

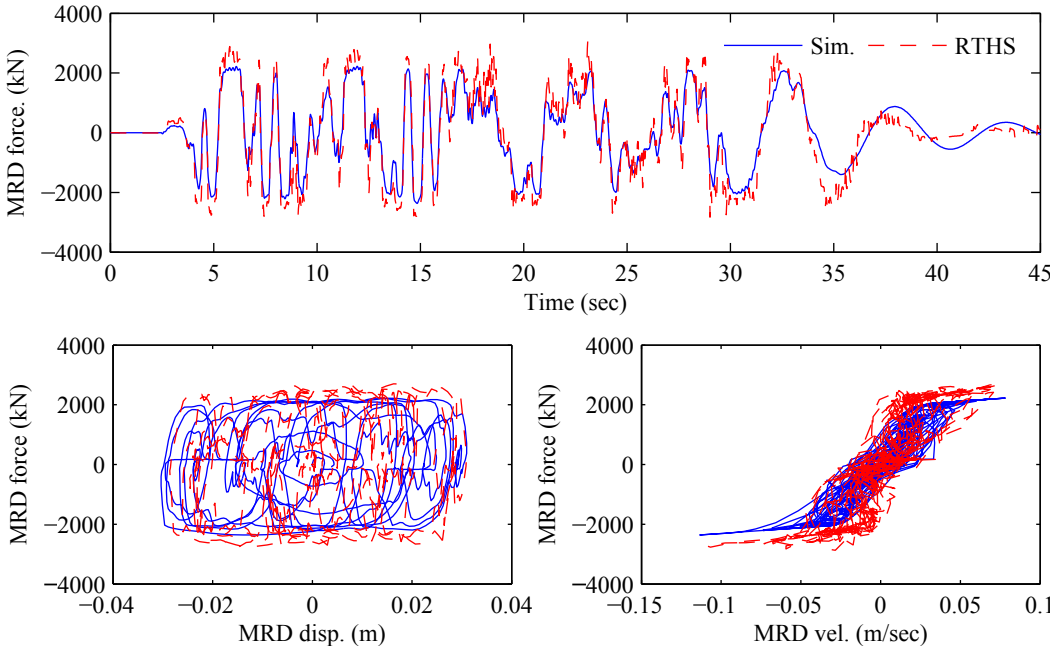

Figure 7.10: MR damper force by the semi-active control #3 to El Centro of 0.3 g PGA

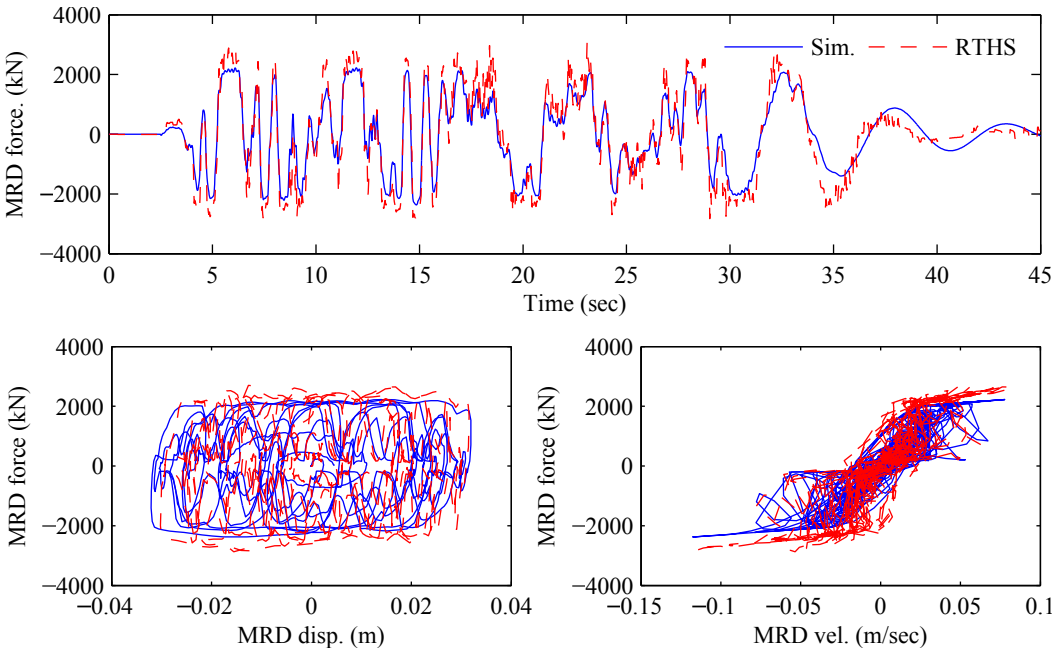

Figure 7.11: MR damper force by the semi-active control #4 to El Centro of 0.3 g PGA

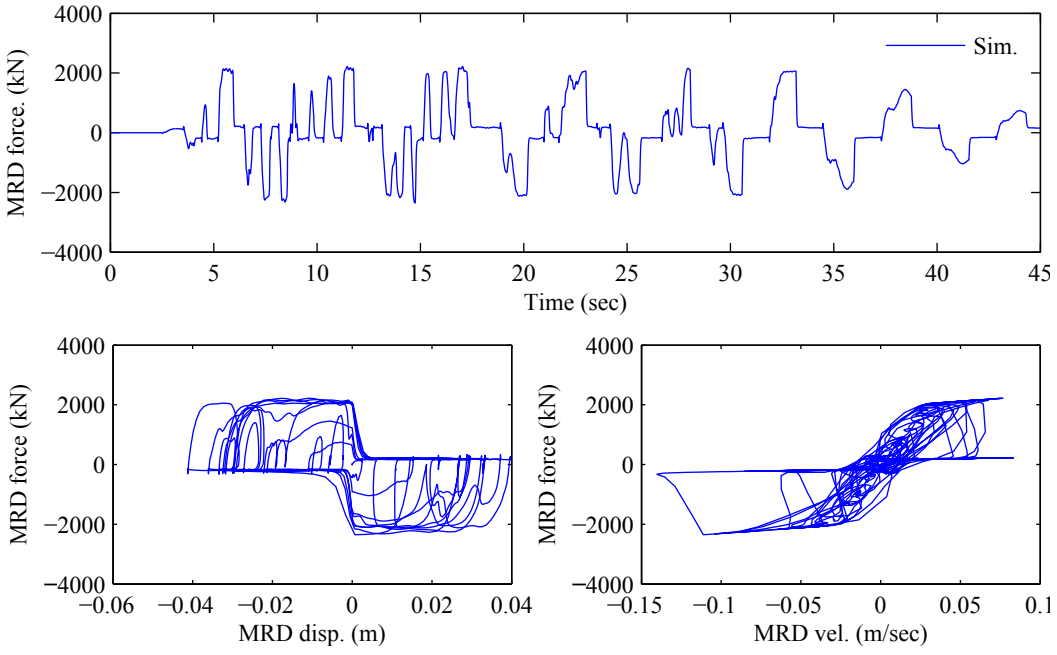

Figure 7.12: MR damper force by the simple control 1N to El Centro of 0.3 g PGA

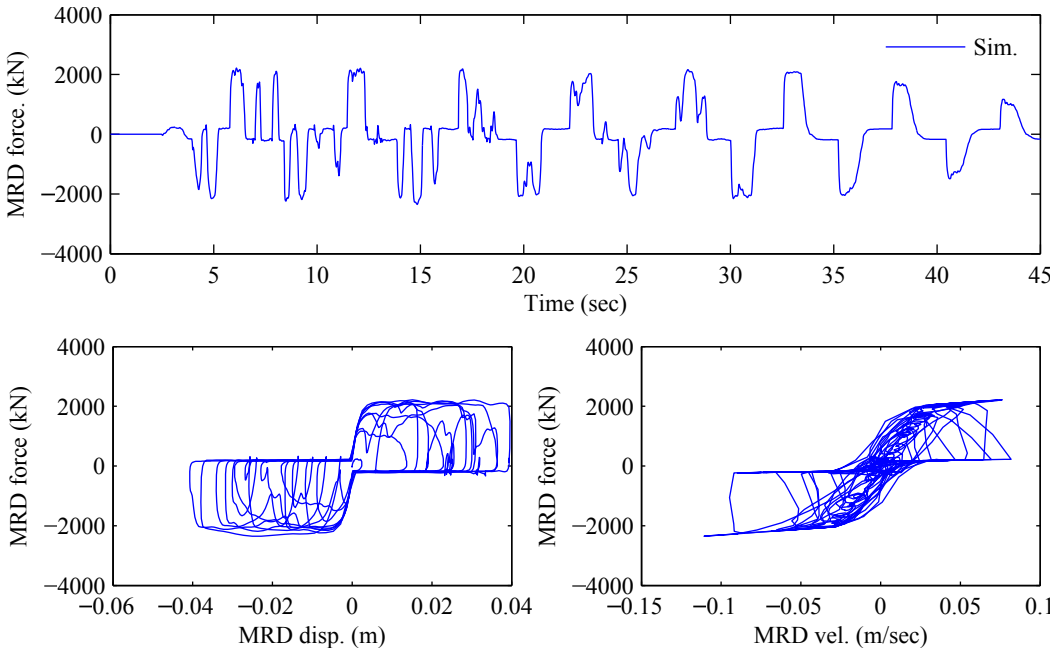

Figure 7.13: MR damper force by the simple control 1P to El Centro of 0.3 g PGA

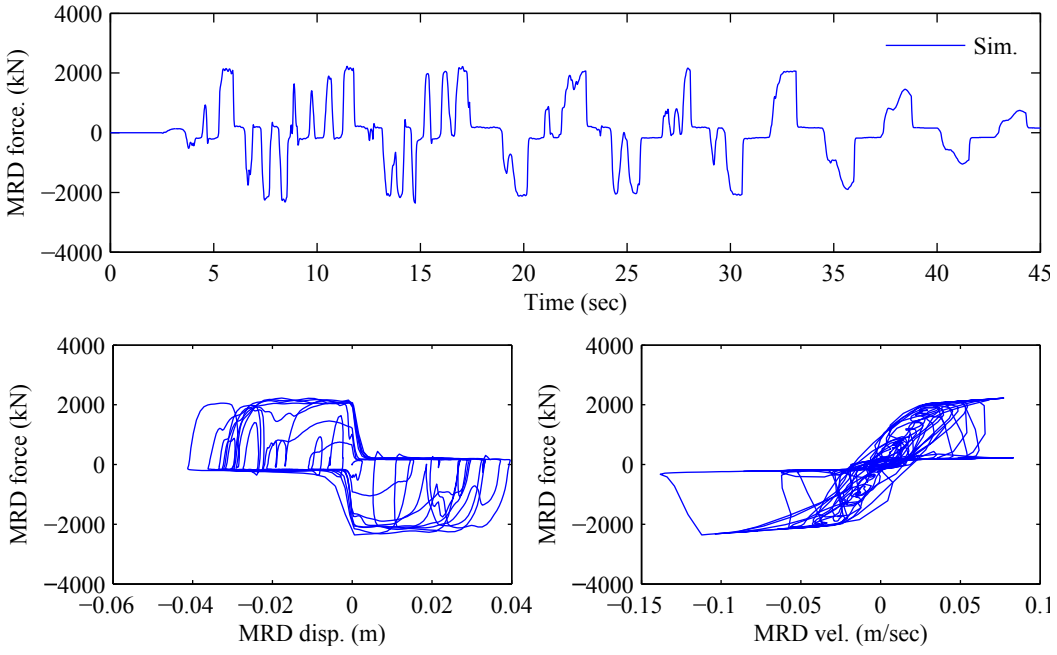

Figure 7.14: MR damper force by the simple control 2N to El Centro of 0.3 g PGA

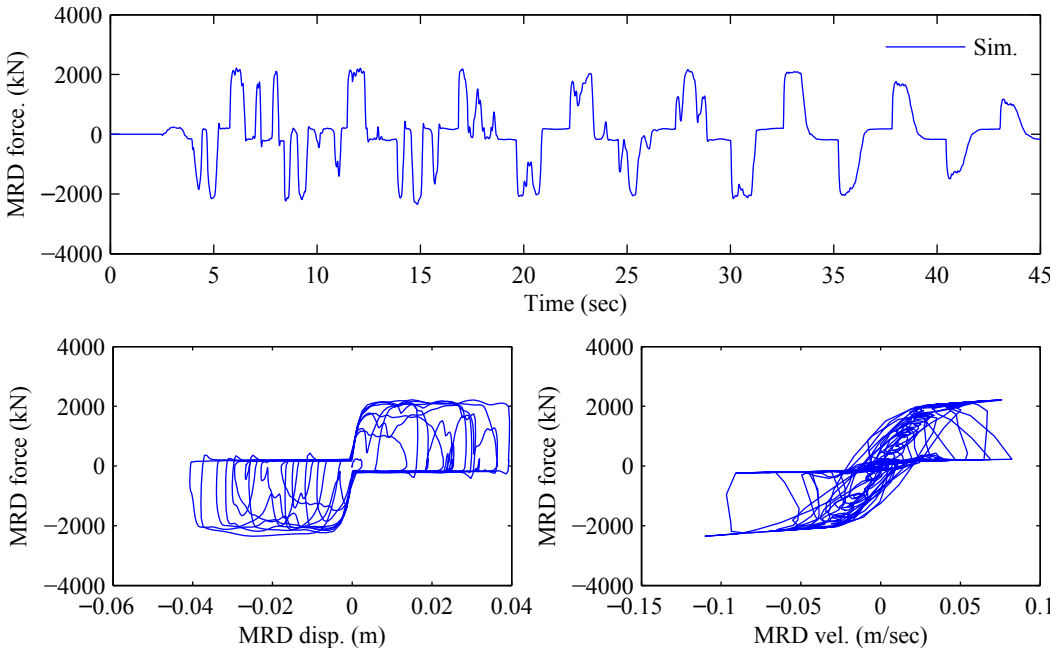

Figure 7.15: MR damper force by the simple control 2P to El Centro of 0.3 g PGA

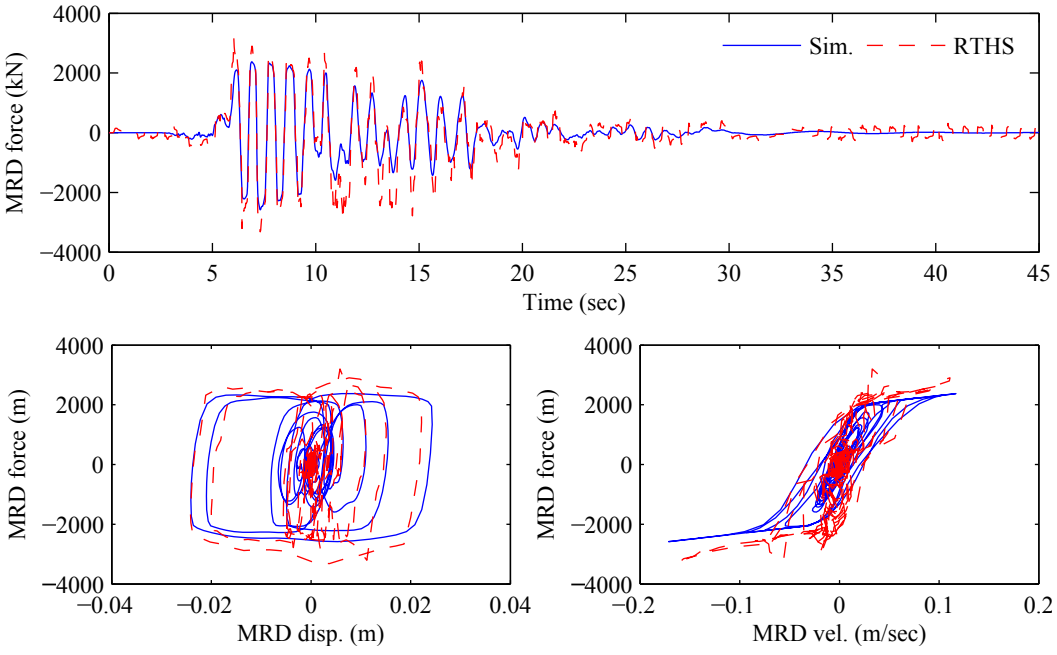

Figure 7.16: MR damper force by the passive-on control to Kobe of 0.3 g PGA

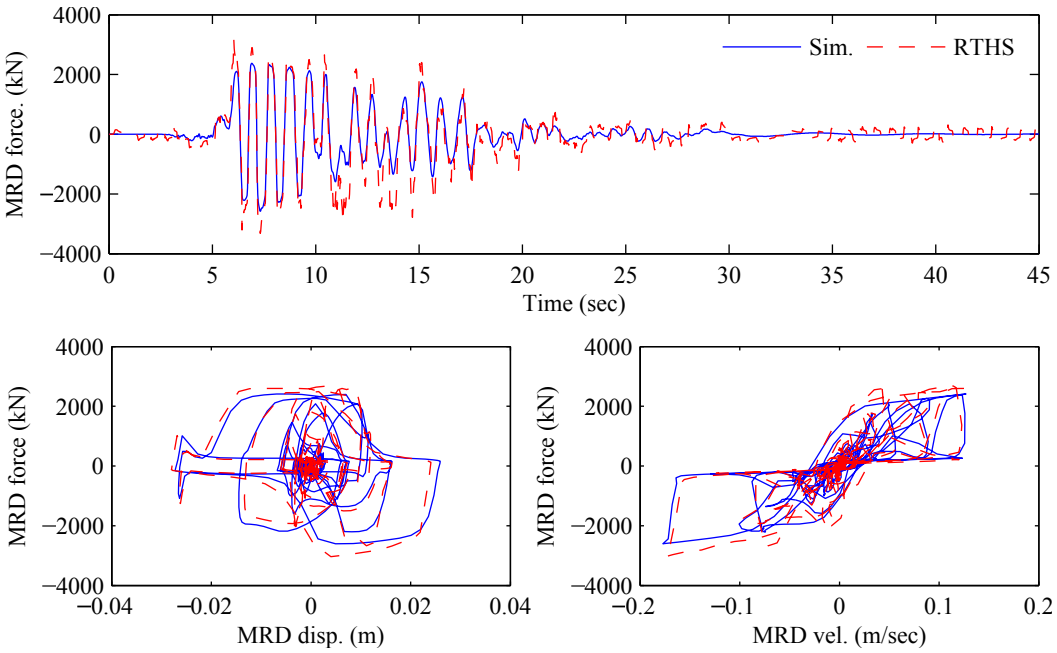

Figure 7.17: MR damper force by the semi-active control #1 to Kobe of 0.3 g PGA

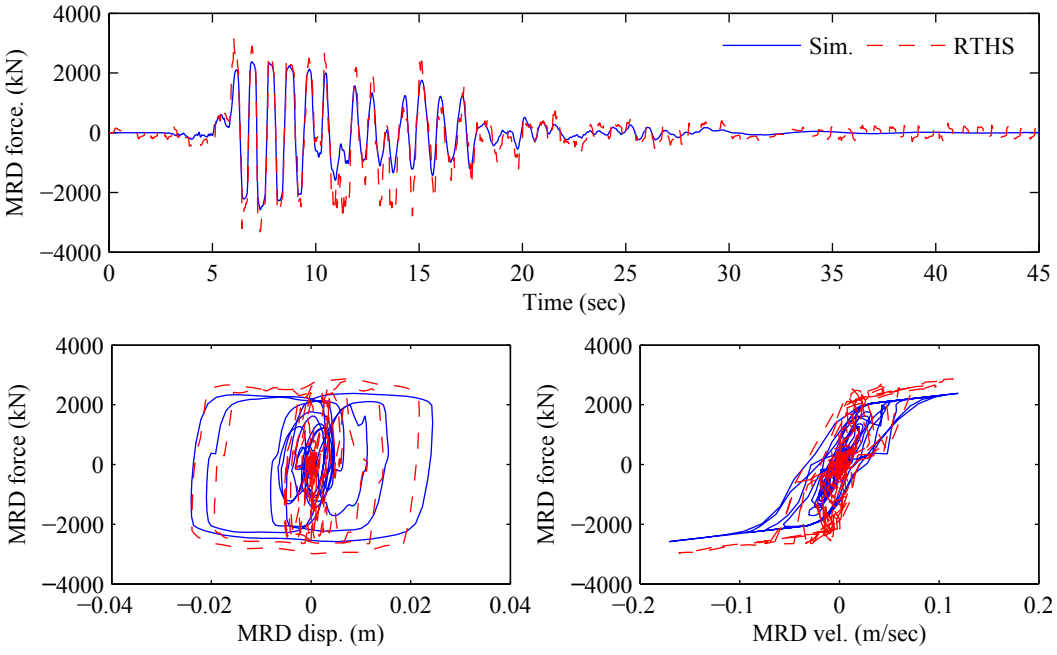

Figure 7.18: MR damper force by the semi-active control #2 to Kobe of 0.3 g PGA

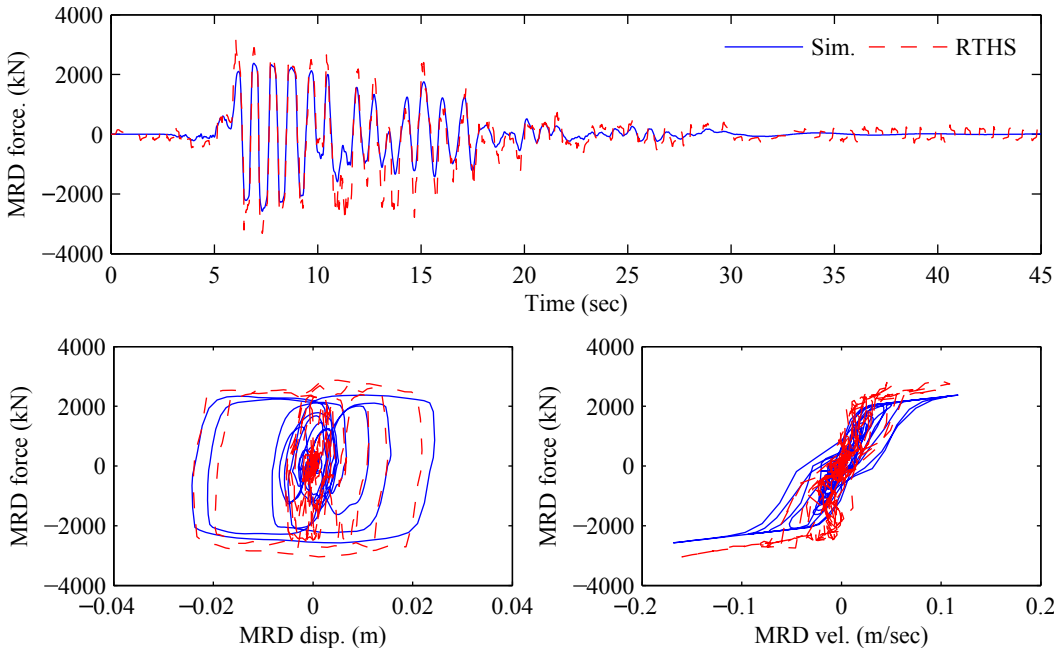

Figure 7.19: MR damper force by the semi-active control #3 to Kobe of 0.3 g PGA

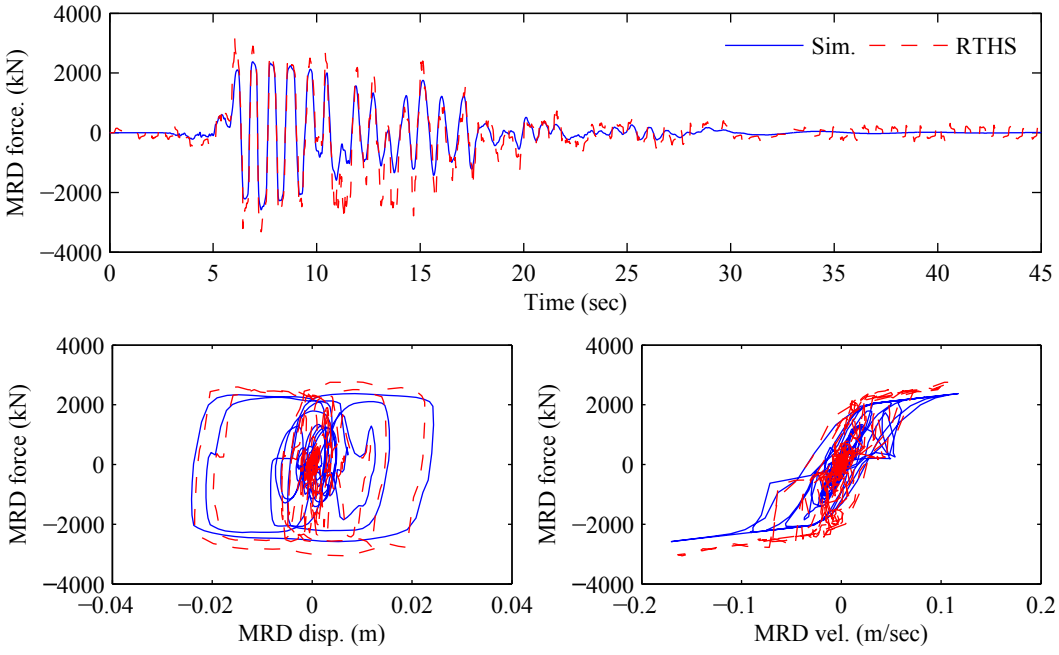

Figure 7.20: MR damper force by the semi-active control #4 to Kobe of 0.3 g PGA

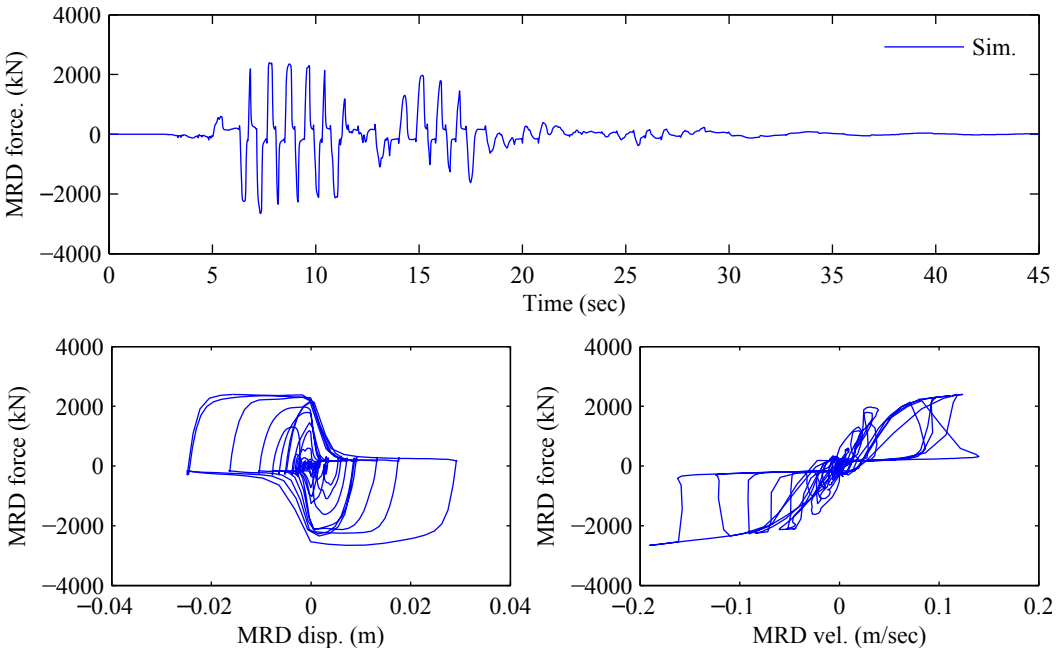

Figure 7.21: MR damper force by the simple control 1N to Kobe of 0.3 g PGA

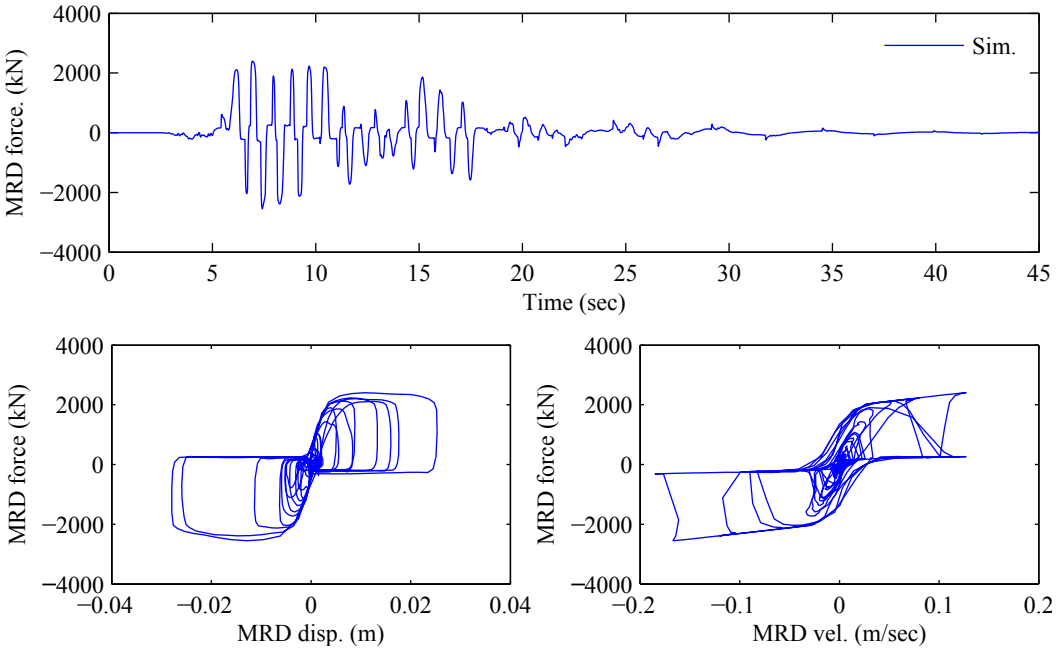

Figure 7.22: MR damper force by the the simple control 1P to Kobe of 0.3 g PGA

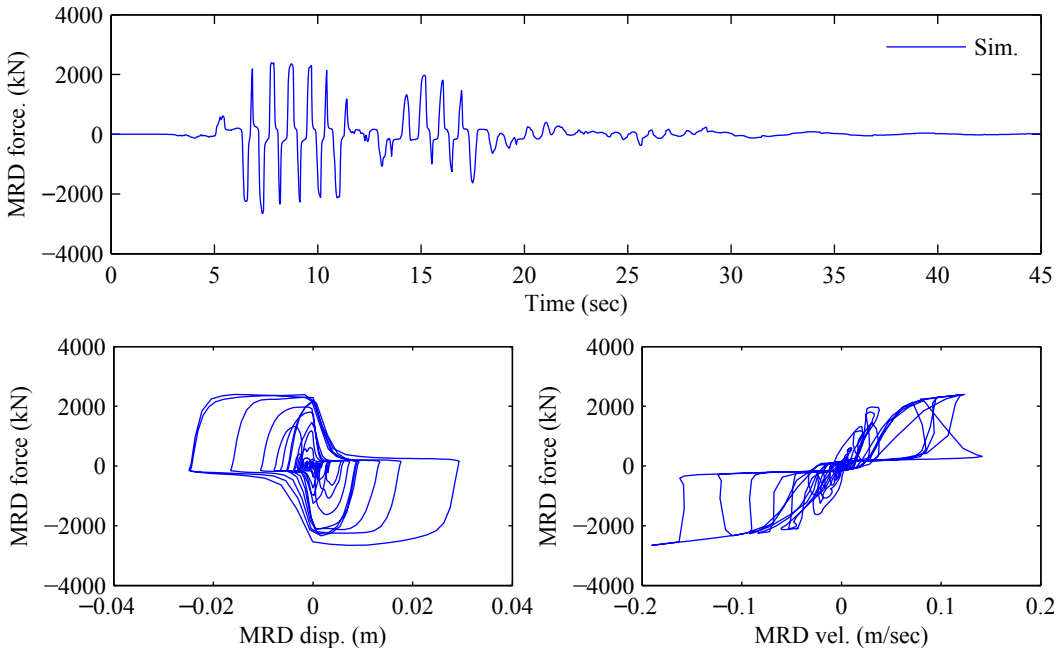

Figure 7.23: MR damper force by the simple control 2N to Kobe of 0.3 g PGA

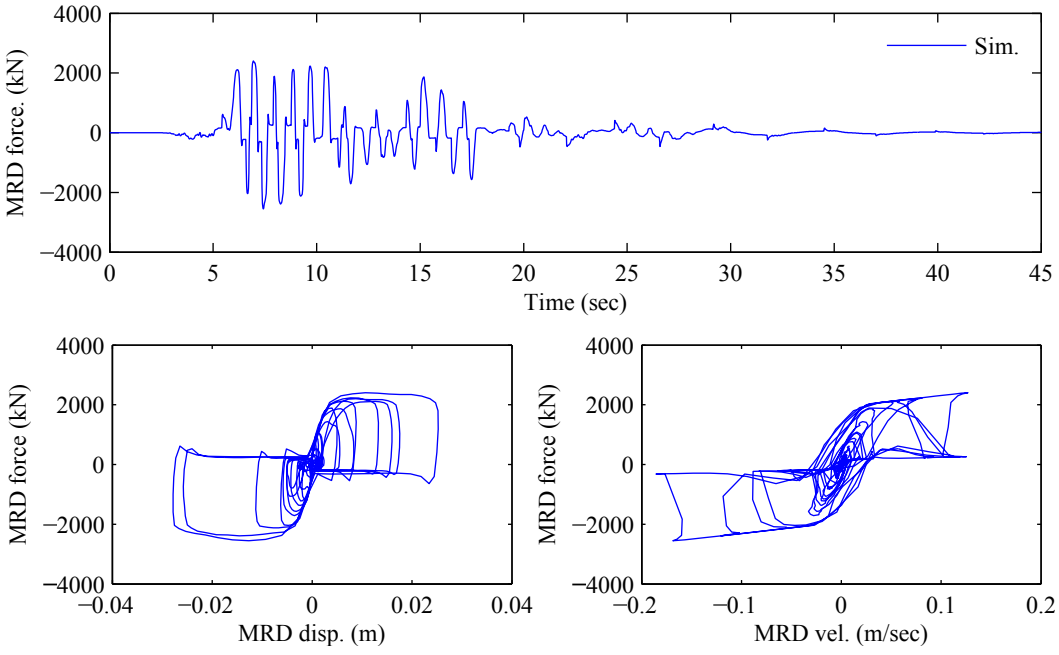

Figure 7.24: MR damper force by the the simple control 2P to Kobe of 0.3 g PGA

Table 7.2: Displacements to 0.3 g PGA El Centro earthquake

	Controller	20th		40th		60th	
		Sim.	RTHS	Sim.	RTHS	Sim.	RTHS
Peak (m)	Bare	0.195		0.644		1.174	
	Passive-on	0.090	0.083	0.268	0.240	0.470	0.410
	LQG-based C.O. #1	0.099	0.089	0.278	0.264	0.501	0.477
	LQG-based C.O. #2	0.090	0.081	0.268	0.236	0.469	0.409
	LQG-based C.O. #3	0.093	0.090	0.274	0.268	0.481	0.471
	LQG-based C.O. #4	0.099	0.094	0.282	0.276	0.498	0.485
	Simple control 1N	0.112		0.335		0.605	
	Simple control 1P	0.109		0.352		0.641	
	Simple control 2N	0.112		0.335		0.605	
	Simple control 2P	0.109		0.352		0.641	
RMS ($\times 10^{-3}$ m)	Bare	2.061		6.754		12.369	
	Passove-on	0.776	0.606	2.521	1.944	4.625	3.558
	LQG-based C.O. #1	0.847	0.716	2.720	2.271	4.976	4.145
	LQG-based C.O. #2	0.790	0.609	2.564	1.949	4.698	3.563
	LQG-based C.O. #3	0.830	0.728	2.695	2.340	4.932	4.260
	LQG-based C.O. #4	0.874	0.785	2.849	2.552	5.227	4.682
	Simple control 1N	1.048		3.454		6.388	
	Simple control 1P	1.116		3.601		6.540	
	Simple control 2N	1.049		3.456		6.392	
	Simple control 2P	1.115		3.597		6.534	

In Tables 7.2 through 7.6, the peak and RMS displacements relative to the ground at 20th, 40th, and 60th floors for the passive-on mode MR dampers, the four LQG-based clipped-control cases, and the four proposed simple controllers are compared with the case of bare (uncontrolled) buildings. Scaled El Centro earthquakes whose PGAs are 0.3 g and 0.5 g and scaled Kobe earthquakes whose PGAs are 0.3 g, 0.5 g, and 0.7 g are used as input excitations here. The values for passive-on mode and LQG-based clipped-optimal control cases are obtained from numerical simulation and RTHS , while, the values for bare and proposed simple control cases are calculated from numerical simulation alone. As can be seen, MR dampers controlled both passively and semi-actively work well to reduce response in both peak and RMS displacements subjected to both El Centro and Kobe earthquakes. Especially, for El Centro cases, huge reductions can be found. The smaller reduction for Kobe cases might be because the LQG-based clipped-optimal controller parameters were designed based on the El Centro input. Simulations and RTHSs have good agreement in both peak and RMS displacements for both earthquake inputs. Also, unfortunately, the simple

Table 7.3: Displacements to 0.5 g PGA El Centro earthquake

	Controller	20th		40th		60th	
		Sim.	RTHS	Sim.	RTHS	Sim.	RTHS
Peak (m)	Bare	0.325		1.074		1.957	
	Passive-on	0.183	0.171	0.523	0.497	0.934	0.880
	LQG-based C.O. #1	0.190	0.180	0.555	0.509	1.004	0.916
	LQG-based C.O. #2	0.183	0.168	0.518	0.493	0.926	0.870
	LQG-based C.O. #3	0.191	0.183	0.567	0.523	1.034	0.955
	LQG-based C.O. #4	0.194	0.188	0.566	0.524	1.024	0.934
	Simple control 1N	0.211		0.657		1.217	
	Simple control 1P	0.230		0.728		1.315	
	Simple control 2N	0.211		0.658		1.218	
	Simple control 2P	0.230		0.728		1.315	
RMS ($\times 10^{-3}$ m)	Bare	3.435		11.257		20.617	
	Passive-on	1.630	1.454	5.316	4.719	9.749	8.641
	LQG-based C.O. #1	1.735	1.535	5.611	4.936	10.267	9.021
	LQG-based C.O. #2	1.648	1.415	5.363	4.583	9.825	8.391
	LQG-based C.O. #3	1.791	1.667	5.839	5.421	10.683	9.903
	LQG-based C.O. #4	1.793	1.669	5.861	5.452	10.751	10.002
	Simple control 1N	2.180		7.186		13.248	
	Simple control 1P	2.297		7.456		13.578	
	Simple control 2N	2.181		7.189		13.253	
	Simple control 2P	2.297		7.457		13.581	

controllers cannot reduce the displacements as much as the LQG-base clipped-optimal controllers.

For the base shear forces, Figures 7.25 through 7.29 compares the control performance among the passive-on mode MR dampers and semi-active control strategies in the smart outrigger system. In these figures, all values are normalized based on the base shear of the bare (uncontrolled) building case. Though simulations, in general, show slightly larger base shears than RTHS in the both peak and RMS senses, these differences are quite small. This might be due to the the difference of the MR damper force between the numerical model and the physical specimen. And another reason is the acceleration sensitivity to the high-frequency components, as well as non-ideal experimental conditions such as high-frequency noise. As can be observed, LQG-based clipped-optimal controllers #2 and #3 perform the best in both peak and RMS senses, however compared to the passive-on mode cases, significant improvement cannot be achieved for both earthquakes. Also, sufficient reduction of base shear force cannot be found in all the proposed simple controllers.

Table 7.4: Displacements to 0.3 g PGA Kobe earthquake

	Controller	20th		40th		60th	
		Sim.	RTHS	Sim.	RTHS	Sim.	RTHS
Peak (m)	Bare	0.114		0.160		0.308	
	Passive-on	0.082	0.080	0.131	0.132	0.243	0.243
	LQG-based C.O. #1	0.099	0.099	0.140	0.148	0.270	0.273
	LQG-based C.O. #2	0.082	0.078	0.131	0.128	0.242	0.236
	LQG-based C.O. #3	0.083	0.079	0.132	0.133	0.245	0.242
	LQG-based C.O. #4	0.083	0.078	0.131	0.126	0.246	0.236
	Simple control 1N	0.090		0.151		0.249	
	Simple control 1P	0.101		0.148		0.287	
	Simple control 2N	0.090		0.151		0.249	
	Simple control 2P	0.101		0.148		0.286	
RMS ($\times 10^{-3}$ m)	Bare	0.429		0.686		1.362	
	Passive-on	0.248	0.237	0.501	0.515	0.975	0.987
	LQG-based C.O. #1	0.309	0.304	0.524	0.529	1.038	1.038
	LQG-based C.O. #2	0.249	0.230	0.499	0.490	0.972	0.944
	LQG-based C.O. #3	0.251	0.236	0.506	0.514	0.984	0.981
	LQG-based C.O. #4	0.252	0.234	0.519	0.501	1.008	0.966
	Simple control 1N	0.307		0.538		1.076	
	Simple control 1P	0.308		0.597		1.146	
	Simple control 2N	0.307		0.539		1.077	
	Simple control 2P	0.307		0.596		1.144	

7.3 Summary

This study shows that MR dampers can be employed effectively in outrigger damping systems using passive-on mode and semi-active controllers. The MR damper's restoring force can be simulated quite well by the proposed MR damper model for the two earthquake records; however, differences are still present. In particular, discrepancies between simulations and RTHSs were found in the base shear. Moreover, the physical specimen contains no modeling errors, while it is subject to experimental error such as magnitude and time delay. The numerical model provides a good verification tool for RTHS, however is subject to numerical errors, is only valid within the range of behavior for which the model is calibrated, and cannot fully represent the complex specimen behavior. Thus, the importance of combining RTHS with numerical simulation to ensure accurate results is demonstrated.

The effectiveness of semi-active control applied to the outrigger damping system of a high-

Table 7.5: Displacements to 0.5 g PGA Kobe earthquake

	Controller	20th		40th		60th	
		Sim.	RTHS	Sim.	RTHS	Sim.	RTHS
Peak (m)	Bare	0.190		0.266		0.514	
	Passive-on	0.155	0.152	0.227	0.230	0.442	0.436
	LQG-based C.O. #1	0.170	0.172	0.237	0.247	0.464	0.470
	LQG-based C.O. #2	0.154	0.151	0.227	0.226	0.435	0.424
	LQG-based C.O. #3	0.155	0.153	0.228	0.235	0.439	0.440
	LQG-based C.O. #4	0.155	0.153	0.227	0.230	0.442	0.441
	Simple control 1N	0.162		0.253		0.440	
	Simple control 1P	0.175		0.250		0.494	
	Simple control 2N	0.162		0.253		0.440	
	Simple control 2P	0.175		0.249		0.492	
RMS ($\times 10^{-3}$ m)	Bare	0.715		1.143		2.270	
	Passive-on	0.478	0.461	0.905	0.911	1.770	1.770
	LQG-based C.O. #1	0.546	0.544	0.899	0.910	1.788	1.797
	LQG-based C.O. #2	0.476	0.450	0.887	0.854	1.739	1.667
	LQG-based C.O. #3	0.478	0.466	0.902	0.936	1.765	1.805
	LQG-based C.O. #4	0.482	0.467	0.917	0.917	1.790	1.780
	Simple control 1N	0.556		0.938		1.877	
	Simple control 1P	0.562		1.024		1.984	
	Simple control 2N	0.556		0.937		1.877	
	Simple control 2P	0.560		1.022		1.980	

rise building is also shown for scaled El Centro and Kobe earthquakes. In both simulation and RTHS, LQG-based clipped-optimal controller (e.g., controller #2 which minimizes the translational floor accelerations and #3 which minimizes rotational displacements) provided the best control performance considering both relative displacements and base shear. However, the passive-on mode and LQG-based clipped-optimal cases gave similar results, especially in base shear. Also, to improve the reliability of the smart outrigger damping system for high-rise buildings, different earthquakes should be considered as well as wind excitation.

The following general conclusions can be drawn with regard to the RTHS framework employed in this research: a) RTHS worked when all modes of the structure were lightly damped, demonstrating the robustness of the actuator controller without the need for adding numerical damping; b) the actuator control strategy used in this study demonstrated stable and accurate results in MDOF structural systems; c) RTHS can be employed for validation of structural control algorithms; d) RTHS provides an effective means for assessing the system performance of rate-dependent compo-

Table 7.6: Displacements to 0.7 g PGA Kobe earthquake

	Controller	20th		40th		60th	
		Sim.	RTHS	Sim.	RTHS	Sim.	RTHS
Peak (m)	Bare	0.265		0.373		0.719	
	Passive-on	0.226	0.228	0.325	0.334	0.634	0.645
	LQG-based C.O. #1	0.243	0.247	0.335	0.348	0.661	0.671
	LQG-based C.O. #2	0.225	0.224	0.325	0.326	0.629	0.625
	LQG-based C.O. #3	0.226	0.229	0.327	0.338	0.634	0.648
	LQG-based C.O. #4	0.226	0.227	0.326	0.332	0.638	0.646
	Simple control 1N	0.234		0.355		0.633	
	Simple control 1P	0.250		0.350		0.699	
	Simple control 2N	0.234		0.355		0.633	
	Simple control 2P	0.250		0.350		0.698	
RMS ($\times 10^{-3}$ m)	Bare	1.001		1.601		3.179	
	Passive-on	0.715	0.711	1.293	1.331	2.541	2.595
	LQG-based C.O. #1	0.793	0.792	1.290	1.301	2.570	2.579
	LQG-based C.O. #2	0.717	0.693	1.286	1.253	2.530	2.459
	LQG-based C.O. #3	0.715	0.716	1.286	1.350	2.528	2.624
	LQG-based C.O. #4	0.722	0.712	1.313	1.329	2.575	2.591
	Simple control 1N	0.807		1.318		2.648	
	Simple control 1P	0.824		1.470		2.857	
	Simple control 2N	0.808		1.318		2.647	
	Simple control 2P	0.823		1.468		2.853	

nents in complex structures.

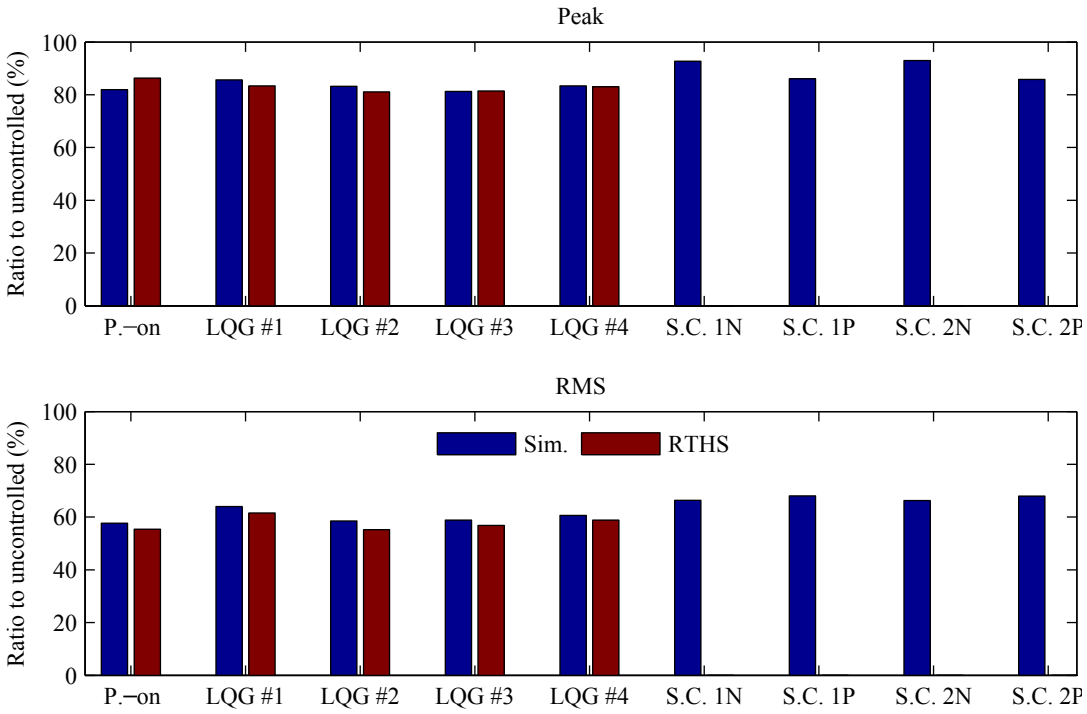

Figure 7.25: Base shear to 0.3 g PGA El Centro earthquake

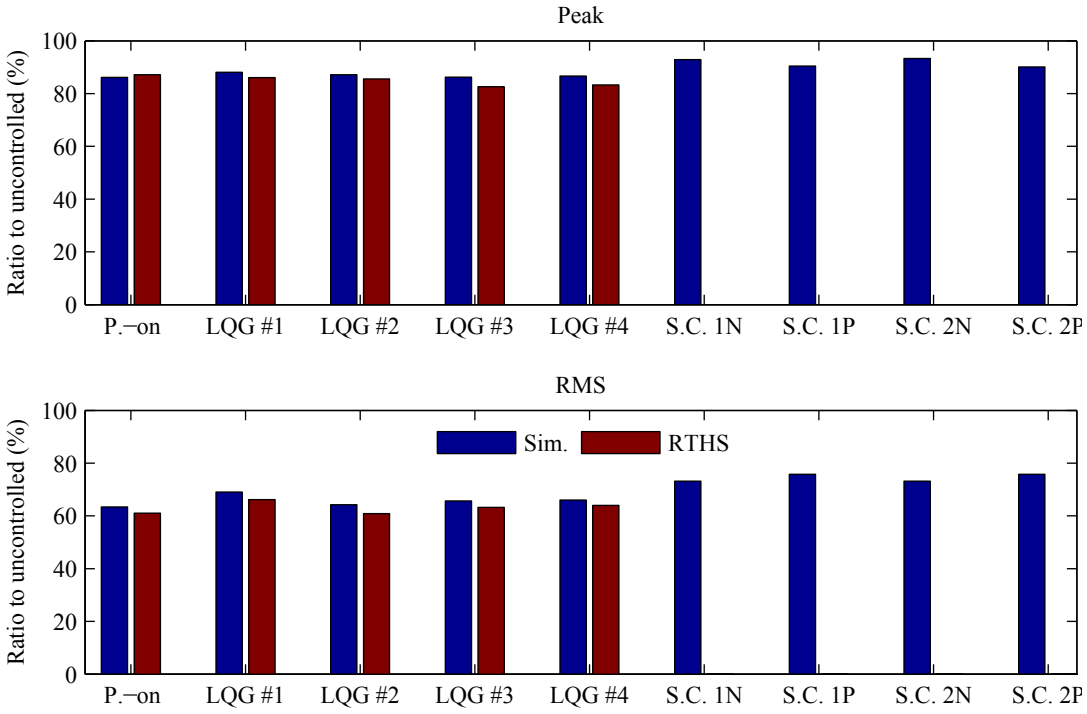

Figure 7.26: Base shear to 0.5 g PGA El Centro earthquake

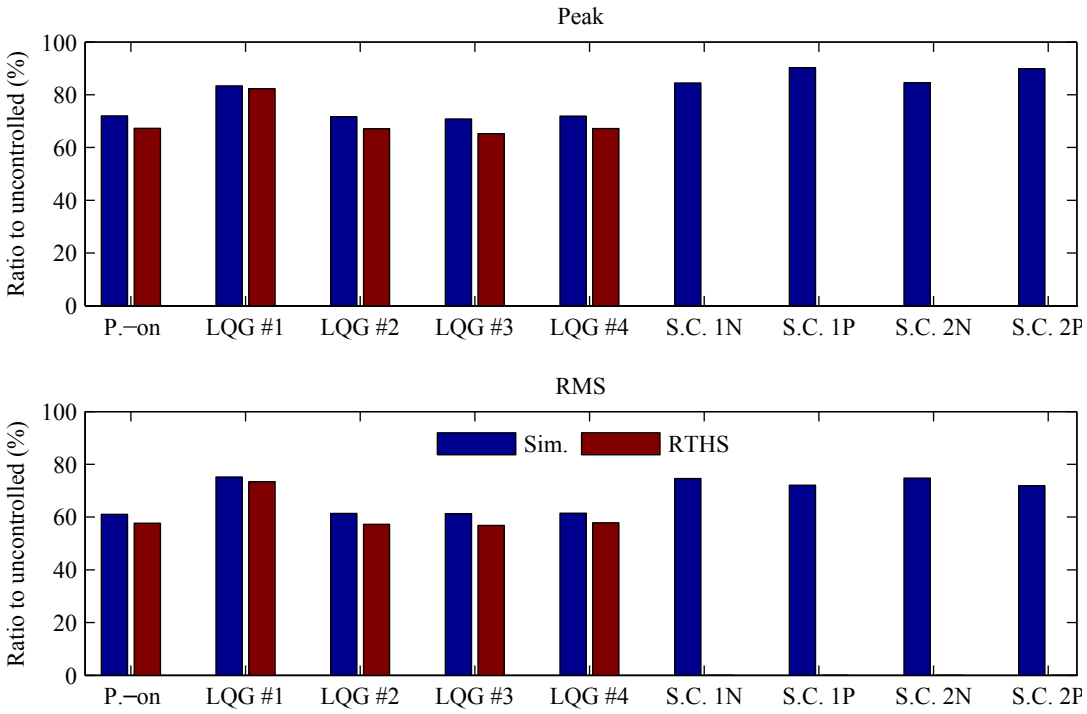

Figure 7.27: Base shear to 0.3 g PGA Kobe earthquake

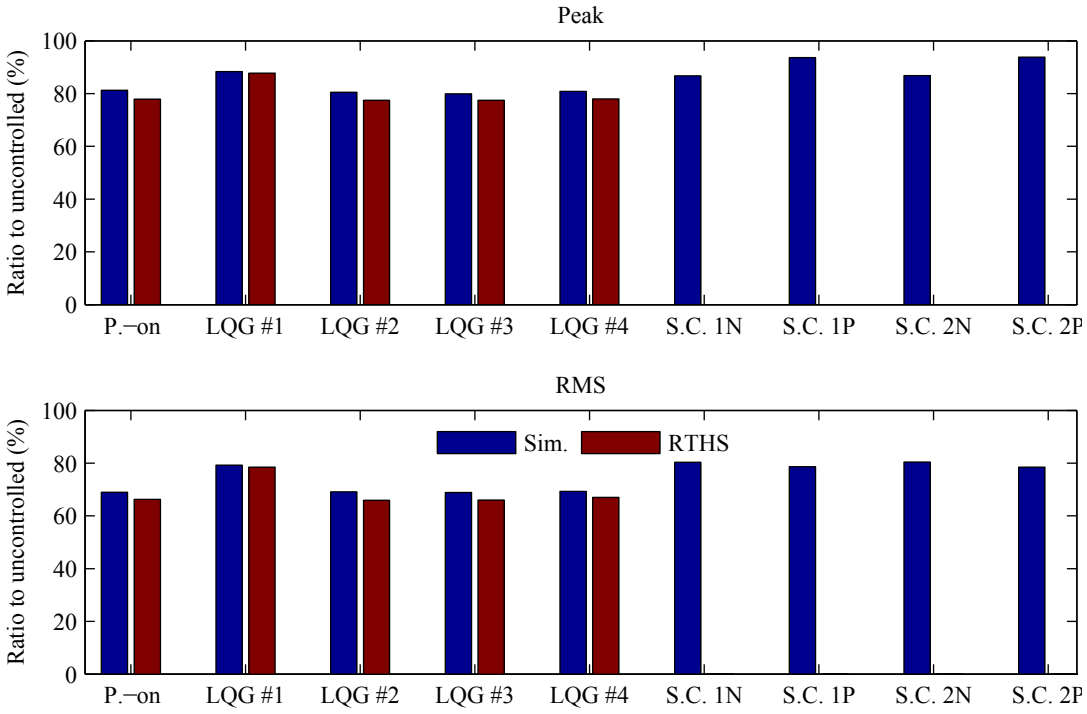

Figure 7.28: Base shear to 0.5 g PGA Kobe earthquake

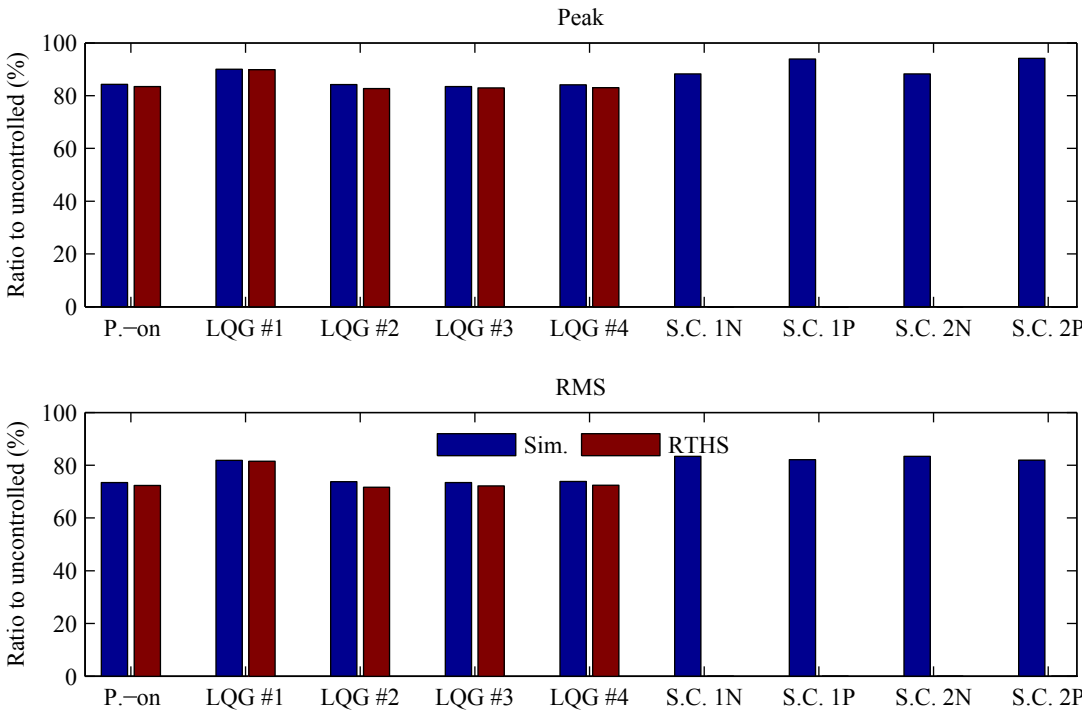

Figure 7.29: Base shear to 0.7 g PGA Kobe earthquake

Chapter 8

Verification of Smart Base Isolation Systems

Traditional passive base isolation systems provide an effective means to mitigate the responses of seismically-excited structures. A challenge for these systems can be found in accommodating the large base displacements during severe earthquakes. Recently, active base isolation systems, combining actively controlled actuators with passive isolation bearings, have been shown experimentally to produce reduced base displacements, while maintaining similar responses of the superstructure obtained by the passive base isolation systems. The active control devices employed in hybrid isolation systems are typically driven by an external power source, which may not be available during severe seismic events. Another class of isolation systems is smart base isolation, in which semi-active control devices are employed in place of their active counterparts. This control strategy has been proven to be effective against a wide range of seismic excitation, yet limited efforts to experimentally validate smart base isolation systems have been seen. In this study, the focus is to experimentally investigate and verify a smart base isolation system employing a MR damper through RTHS.

In this chapter, the MR damper is physically tested, while the isolated building is concurrently simulated numerically. A model-based compensation strategy is employed to carry out high-precision RTHS. Performance of the semi-active control strategies is evaluated using RTHS, and the efficacy of a smart base isolation system is demonstrated. This smart base isolation system is found to reduce base displacements and floor accelerations in a manner comparable with the active isolation system, without the need for large external power sources.

Figure 8.1: Photograph of the six-story base-isolated building model

8.1 Base-isolated building model: Problem formulation

In this section, the base-isolated building model considered in this study is presented. In RTHS, the MR damper is physically implemented, while the building model is numerically simulated.

Consider the base-isolated six-story scale-building model shown in Figure 8.1, which was developed at the Smart Structures Technology Laboratory (SSTL), University of Illinois at Urbana-Champaign (`http://sstl.cee.illinois.edu/`). The building is comprised of 45 inch $\times$ 28 inch $\times$ 1 inch steel plates for floors each weighing 360 lbs. Each floor consists of six 100 ksi steel columns to support the plates. The isolation bearings used in this system are ball-and-cone type bearings from WorkSafe Technologies (Valencia, CA, USA). More details regarding this building can be found in Chang and Spencer (2012).

In this research, only the strong direction is considered, with a single MR damper located at the isolation layer as shown in Figure 8.2. The stiffness associated with the columns on each floor are obtained from system identification as 7287 lbf/inch, 4018 lbf/inch, 5475 lbf/inch, 5475 lbf/inch, 2803 lbf/inch, and 1546 lbf/inch, respectively, starting from the lowest floor. The stiffness associated with the isolation bearings is as 264 lbf/inch. The unisolated modes for the superstructure are assumed to have 2 % of critical damping. Once mounted on the isolation bearing, the damping

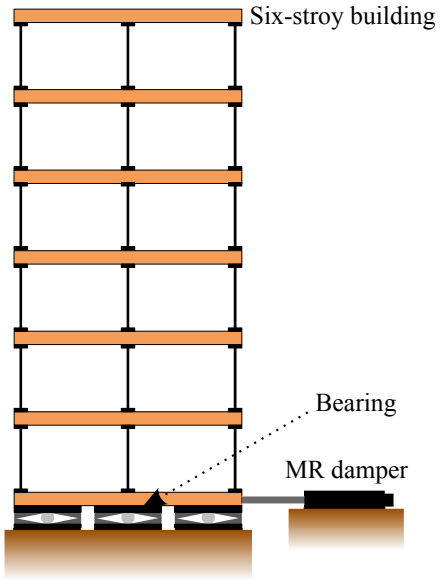

Figure 8.2: Schematic illustration of analysis model

of each mode of the isolated building becomes 5.806 %, 2.023 %, 1.789 %, 1.920 %, 1.964 %, 2.088 %, and 2.092 %, respectively. The natural frequencies of the isolated building are 0.966 Hz, 4.681 Hz, 8.038 Hz, 11.778 Hz, 16.015 Hz, 21.063 Hz, and 22.940 Hz.

The equation of motion of the building model can be written as

$$\mathbf{M}_\mathrm{b}\ddot{\mathbf{u}}_\mathrm{b} + \mathbf{C}_\mathrm{b}\dot{\mathbf{u}}_\mathrm{b} + \mathbf{K}_\mathrm{b}\mathbf{u}_\mathrm{b} = \mathbf{\Lambda}_\mathrm{b} f_\mathrm{MR} - \mathbf{M}_\mathrm{b}\mathbf{\Gamma}_\mathrm{b}\ddot{x}_g \tag{8.1}$$

where $\mathbf{M}_\mathrm{b}$, $\mathbf{C}_\mathrm{b}$, $\mathbf{K}_\mathrm{b}$ are the structural mass, damping, stiffness matrices, respectively; f_MR is the control force produced by the MR damper; $\mathbf{u}_\mathrm{b}$ is the structural deformation vector; $\mathbf{\Lambda}_\mathrm{b}$ and $\mathbf{\Gamma}_\mathrm{b}$ are the influence coefficient vectors of the MR damper and inertial forces, respectively, and $\ddot{x}_g$ is the ground acceleration.

Defining the state as

$$\mathbf{x}_\mathrm{p} = \begin{bmatrix} \mathbf{u}_\mathrm{b}^\mathrm{T} & \dot{\mathbf{u}}_\mathrm{b}^\mathrm{T} \end{bmatrix}^\mathrm{T}, \tag{8.2}$$

the state-space form of Eq. (8.1) is given by

$$\dot{\mathbf{x}}_\mathrm{p} = \mathbf{A}_\mathrm{p}\mathbf{x}_\mathrm{p} + \mathbf{B}_\mathrm{p} f_\mathrm{MR} + \mathbf{E}_\mathrm{p}\ddot{x}_g \tag{8.3}$$

$$\mathbf{y}_{\mathrm{p}} = \mathbf{C}_{\mathrm{yp}}\mathbf{x}_{\mathrm{p}} + \mathbf{D}_{\mathrm{yp}}f_{\mathrm{MR}} + \mathbf{F}_{\mathrm{yp}}\ddot{x}_g + \mathbf{v}_{\mathrm{p}} \tag{8.4}$$

$$\mathbf{z}_{\mathrm{p}} = \mathbf{C}_{\mathrm{zp}}\mathbf{x}_{\mathrm{p}} + \mathbf{D}_{\mathrm{zp}}f_{\mathrm{MR}} + \mathbf{F}_{\mathrm{zp}}\ddot{x}_g \tag{8.5}$$

where $\mathbf{y}_{\mathrm{p}}$ presents the measured structural responses; $\mathbf{v}_{\mathrm{p}}$ is the measurement noise; $\mathbf{z}_{\mathrm{p}}$ corresponds to the regulated structural responses. $\mathbf{A}_{\mathrm{p}}$, $\mathbf{B}_{\mathrm{p}}$, $\mathbf{C}_{\mathrm{yp}}$, $\mathbf{C}_{\mathrm{zp}}$, $\mathbf{D}_{\mathrm{yp}}$, $\mathbf{D}_{\mathrm{zp}}$, $\mathbf{E}_{\mathrm{p}}$, $\mathbf{F}_{\mathrm{yp}}$, and $\mathbf{F}_{\mathrm{zp}}$ are appropriately chosen matrices corresponding to the associated state-space equations.

8.2 Results

In this section, the hysteresis force-displacement loops and seismic performance obtained from numerical studies and RTHS are shown. For the RTHS, the small-scale MR damper shown in Figure 4.1 is used, and for the numerical simulation, the MR damper model created in Section 4.1 is used. To adjust the capacity of the MR damper to the target building, the displacement of the MR damper is scaled such that 1 inch in the physical MR damper corresponds to 10 inches in the numerical model of the smart base-isolated building. The output force of the MR damper is not scaled (i.e., 1 lbf in the physical system is 1 lbf in the numerical model).

8.2.1 Numerical simulation

The results obtained from numerical simulation are shown here. The earthquakes used in this study are El Centro (1994, Northridge Earthquake, El Centro record, fault-parallel), Ji-ji (1999, station TCU 068, North-South component), Kobe (1995, JMA station, East-West component), Newhall (1994, Northridge Earthquake, Newhall county, fault-parallel), and Sylmar (1994, Northridge Earthquake, Sylmar station, fault-parallel) (Narasimhan et al., 2008). The PGAs of these earthquakes are scaled to 0.2 g and 0.5 g.

To compare the performance of a variety of semi-active controllers, three LQG-based clipped-optimal controllers are designed and the simple algorithms proposed in Section 6.4 are applied as well. The three LQG-based clipped-optimal controllers including acceleration weighting, inter-story drift weighting, and relative displacement weighting are designed. For the Kalman filter in Eqs. (7.10) and (7.11), this study assumes that the absolute floor accelerations at the base and 1st through 6th floors are available to estimate the required force. In addition to these two

semi-active controllers, three passive systems are also considered: (i) an uncontrolled passive base-isolated building, (ii) a base-isolated building with an MR damper in passive-off mode (i.e., the input current is 0), and (iii) a base-isolated building with an MR damper in passive-on mode (i.e., the input current is 2.0 A). For the uncontrolled passive base isolation case, simulation studies are carried out.

Figures 8.3 to 8.9 show the hystetetic force-displacement loops obtained from the semi-active controllers to 0.2 g PGA earthquakes. As expected, pseudo-negative stiffness can be found by the LQG-based clipped-optimal control with acceleration weighting, the LQG-based clipped-optimal control with inter-story drift weighting, the simple control 1N, and the simple control 2N while, the LQG-based clipped-optimal control with relative displacement weighting, the simple control 1P, and the simple control 2P produced positive stiffness. The hysteresis loops subjected to 0.5 g PGA earthquakes are depicted in Figures 8.10 to 8.16. As can be seen in Figures 8.10 and 8.11, clear pseudo-negative stiffness cannot be found in the hysteresis loops produced by the LQG-based clipped optimal controllers with acceleration weighting and inter-story drift weighting, while the other controllers still show the expected properties.

The responses of the base displacement and the absolute accelerations of the base through 6th floor are summarized in Tables 8.1 through 8.5. Figures 8.17 through 8.28 compare the ratios of the peak and RMS responses based on the uncontrolled case (i.e., the passive base isolation). As can be seen, generally, the controllers producing pseudo-negative stiffness shows better performance than the positive stiffness controllers. However, the proposed simple algorithms cannot show comparable performance with the LQG-based clipped optimal controllers, especially in the response accelerations of the upper floor. These results show that it is difficult for the proposed simple algorithms to control complicated structures.

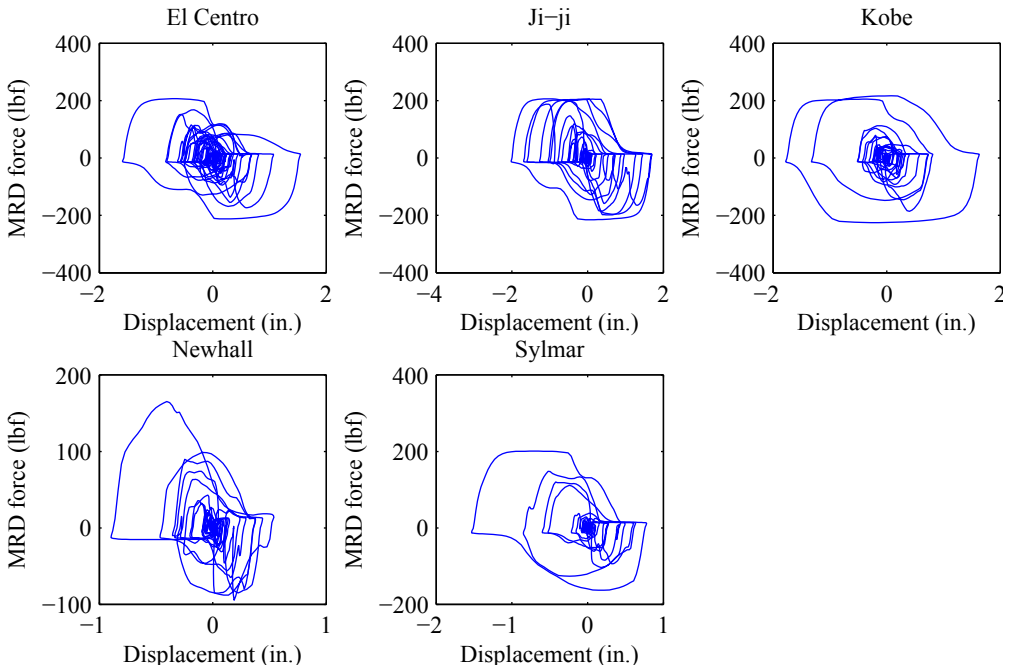

Figure 8.3: Hysteresis loops produced by the LQG-based clipped-optimal control with acceleration weighting to 0.2 g PGA earthquakes

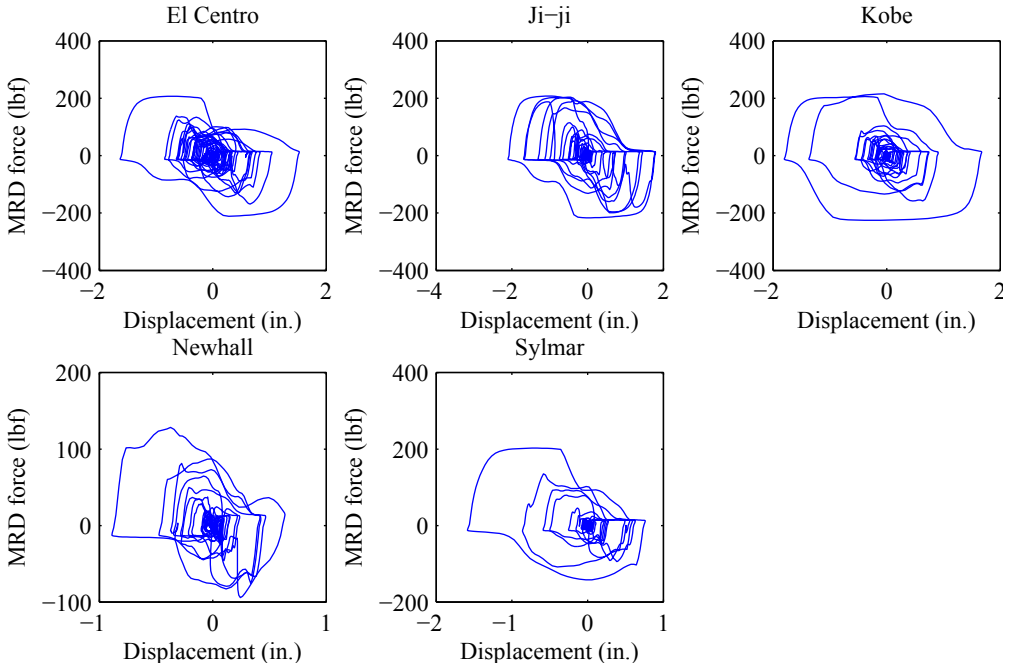

Figure 8.4: Hysteresis loops produced by the LQG-based clipped-optimal control with inter-story drift weighting

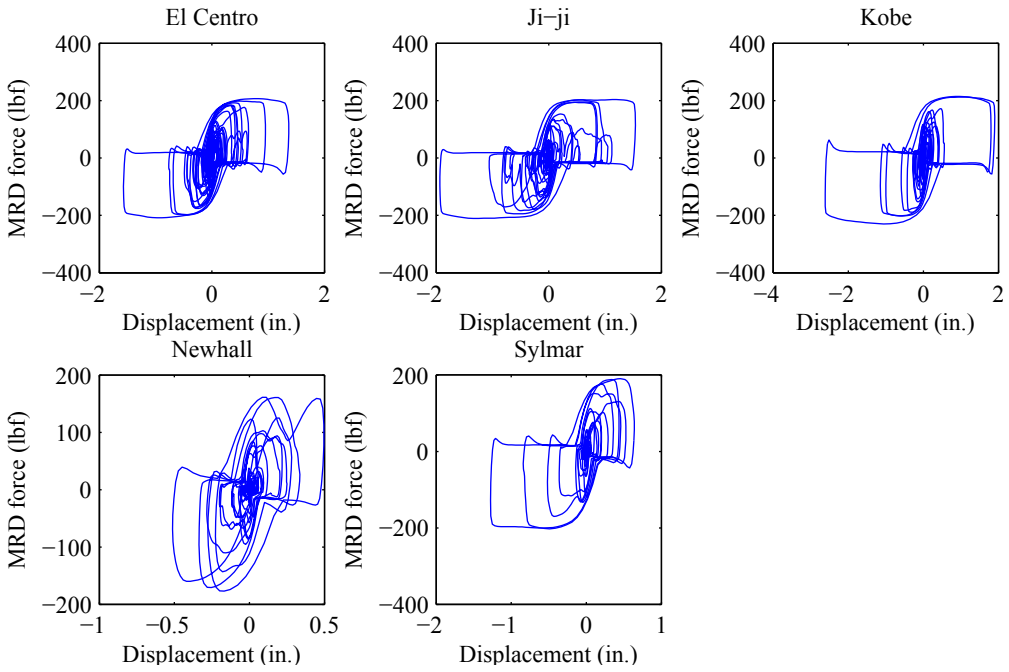

Figure 8.5: Hysteresis loops produced by the LQG-based clipped-optimal control with relative displacement weighting to 0.2 g PGA earthquakes

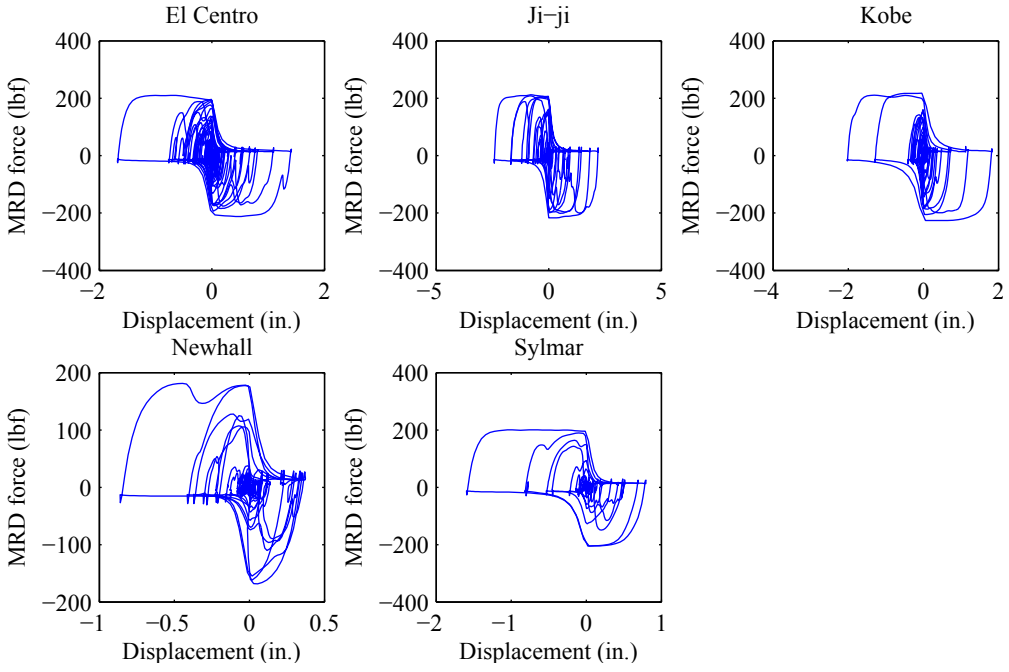

Figure 8.6: Hysteresis loops produced by the simple control 1N by Eq. (6.18) to 0.2 g PGA earthquakes

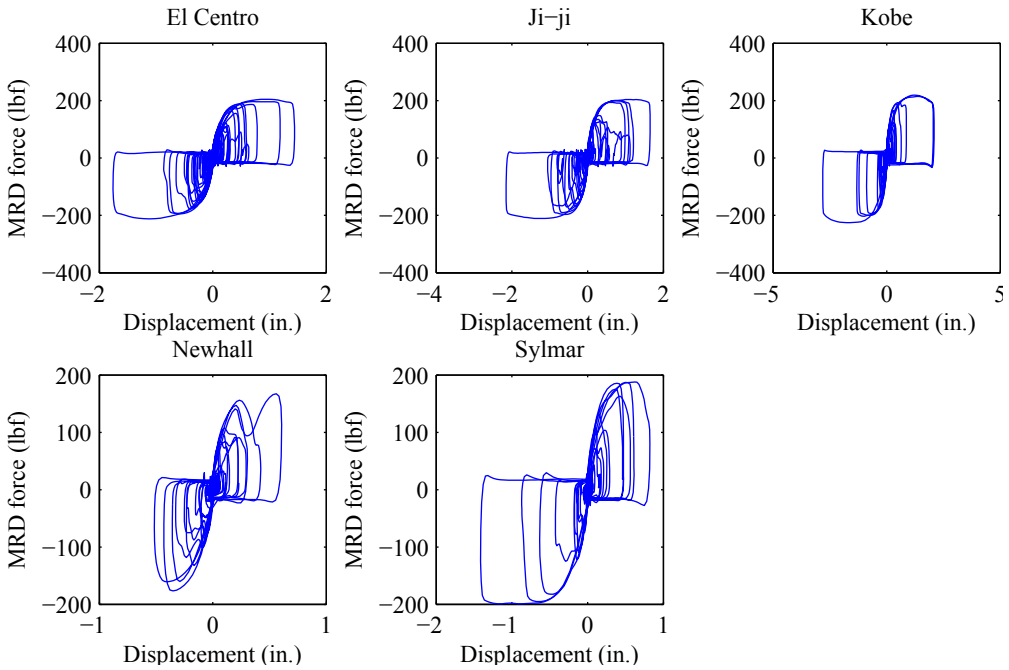

Figure 8.7: Hysteresis loops produced by the simple control 1P by Eq. (6.19) to 0.2 g PGA earthquakes

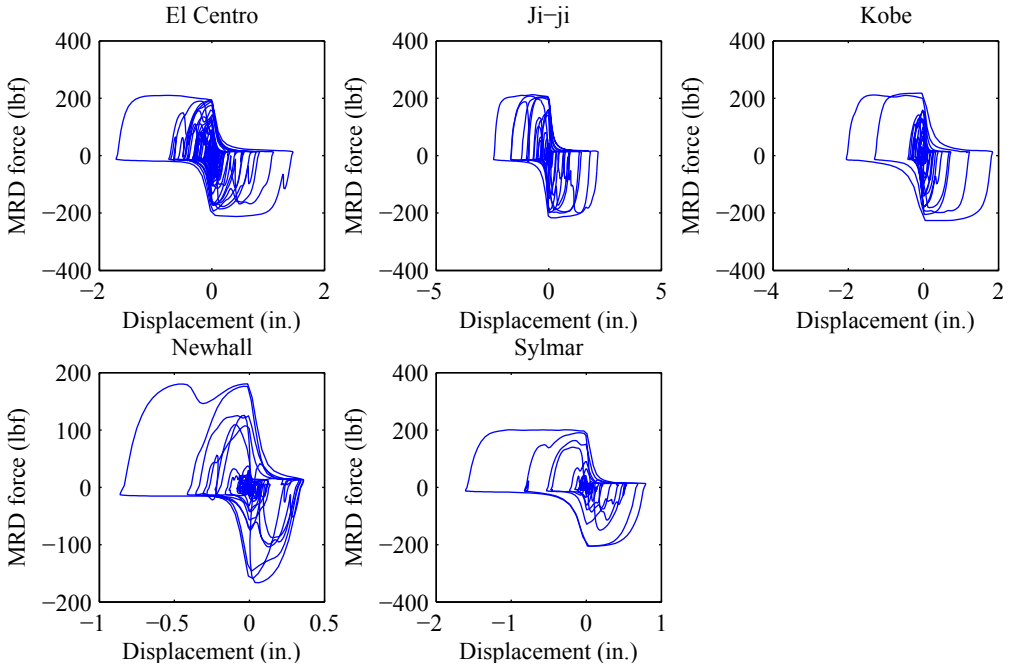

Figure 8.8: Hysteresis loops produced by the simple control 2N by Eq. (6.20) to 0.2 g PGA earthquakes

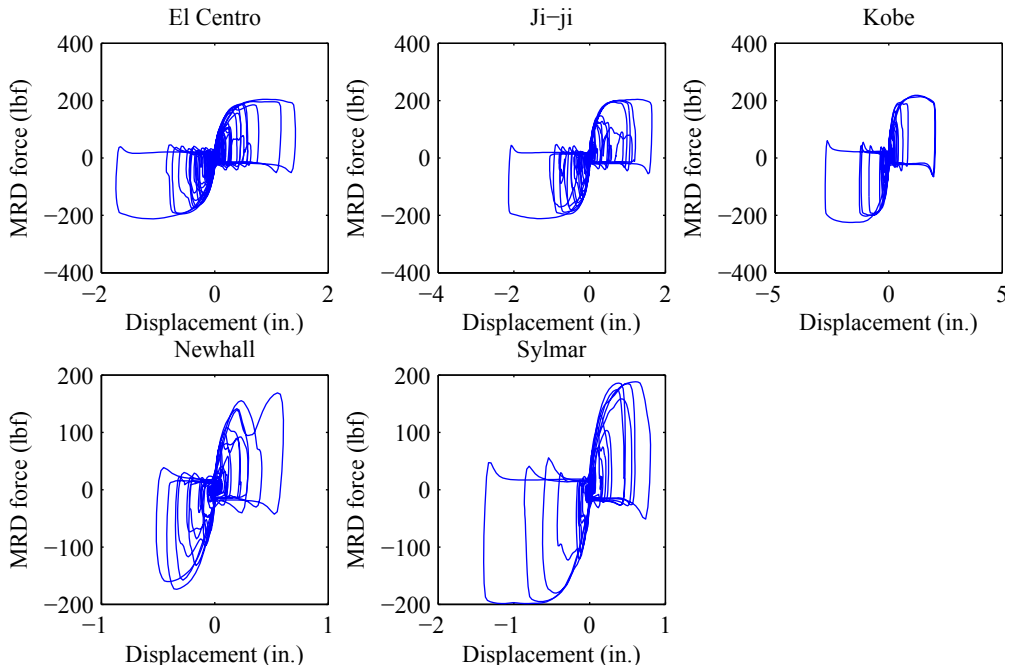

Figure 8.9: Hysteresis loops produced by the simple control 2P by Eq. (6.21) to 0.2 g PGA earthquakes

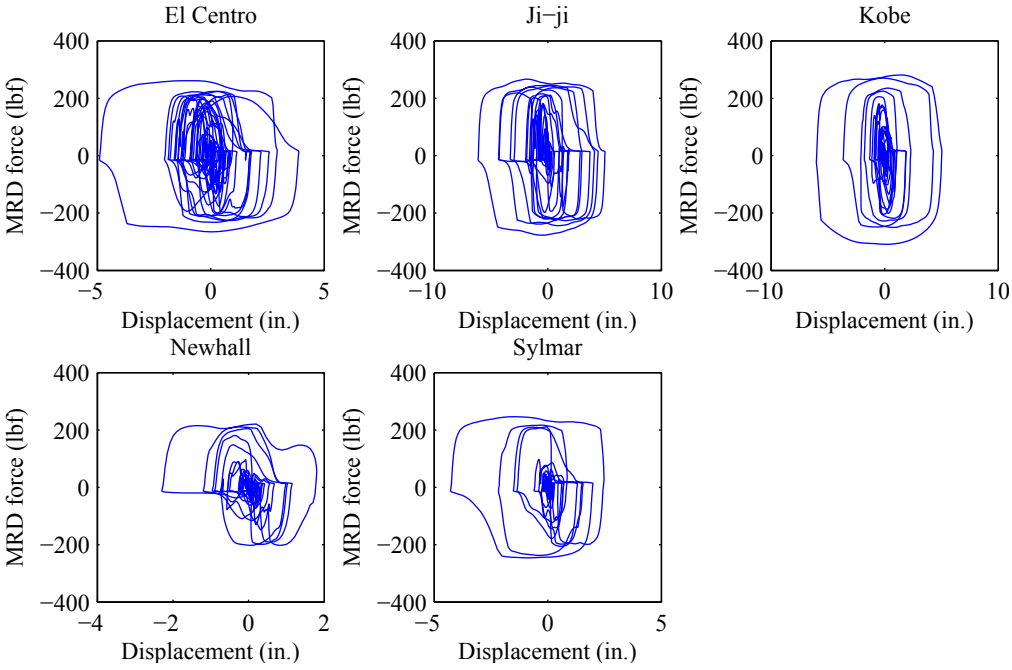

Figure 8.10: Hysteresis loops produced by the LQG-based clipped-optimal control with acceleration weighting to 0.5 g PGA earthquakes

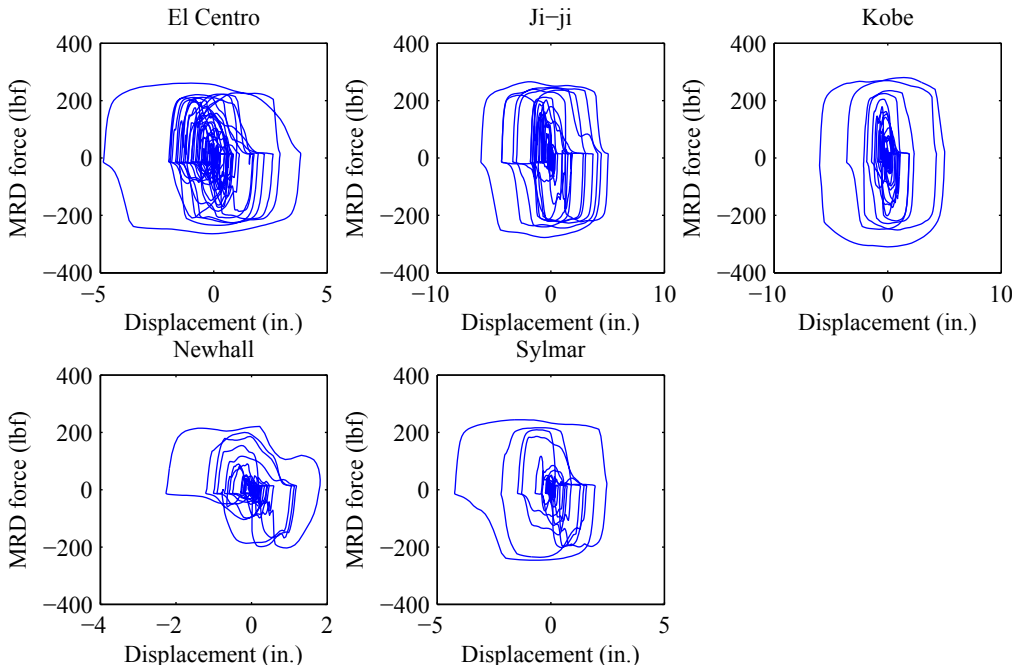

Figure 8.11: Hysteresis loops produced by the LQG-based clipped-optimal control with inter-story drift weighting

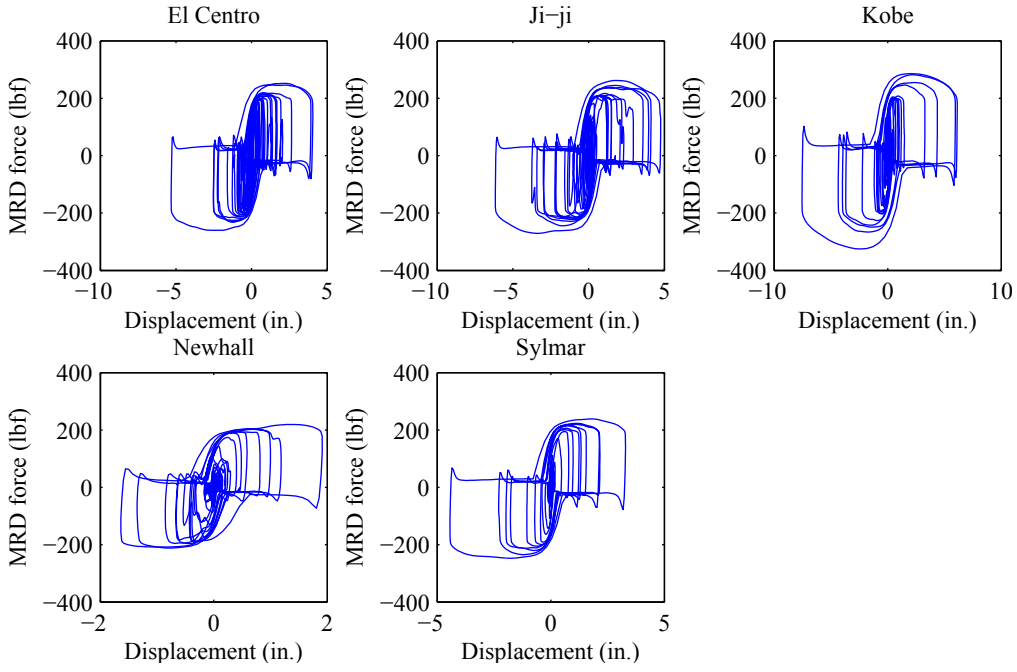

Figure 8.12: Hysteresis loops produced by the LQG-based clipped-optimal control with relative displacement weighting to 0.5 g PGA earthquakes

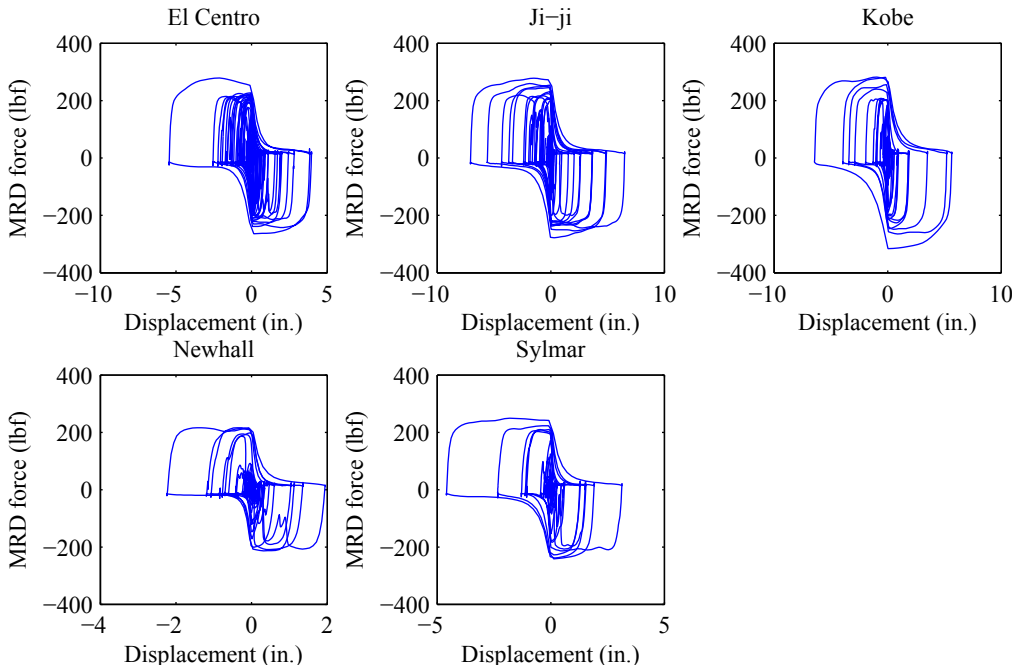

Figure 8.13: Hysteresis loops produced by the simple control 1N by Eq. (6.18) to 0.5 g PGA earthquakes

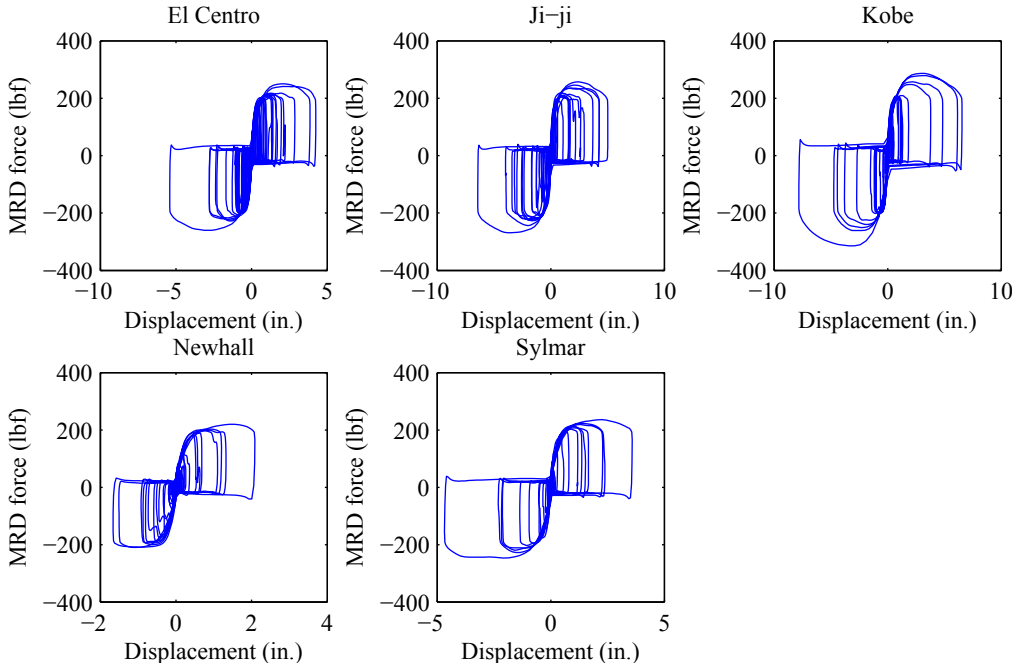

Figure 8.14: Hysteresis loops produced by the simple control 1P by Eq. (6.19) to 0.5 g PGA earthquakes

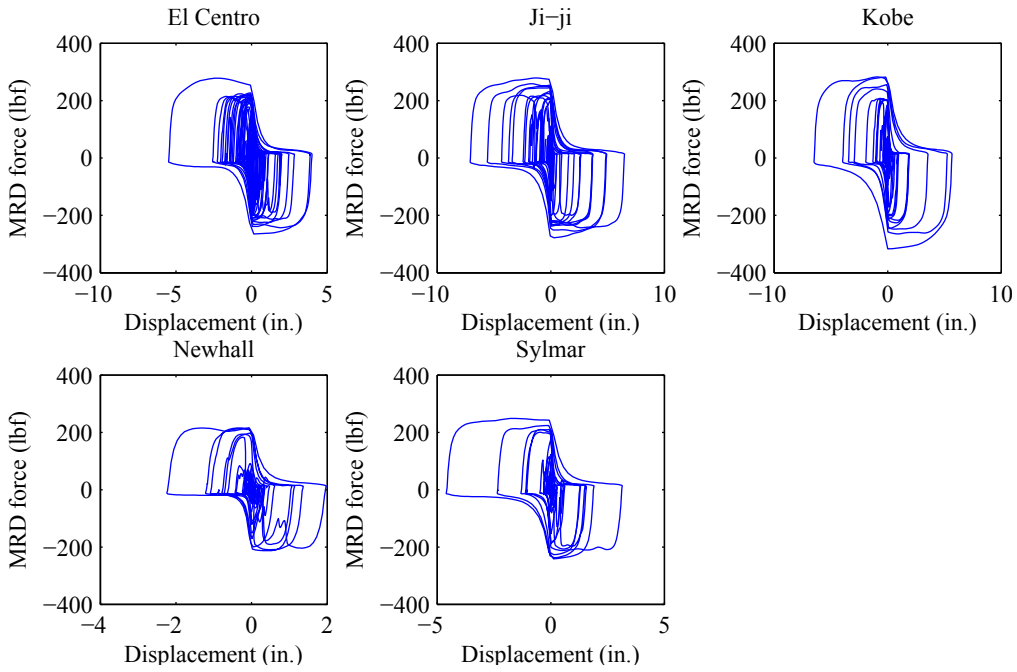

Figure 8.15: Hysteresis loops produced by the simple control 2N by Eq. (6.20) to 0.5 g PGA earthquakes

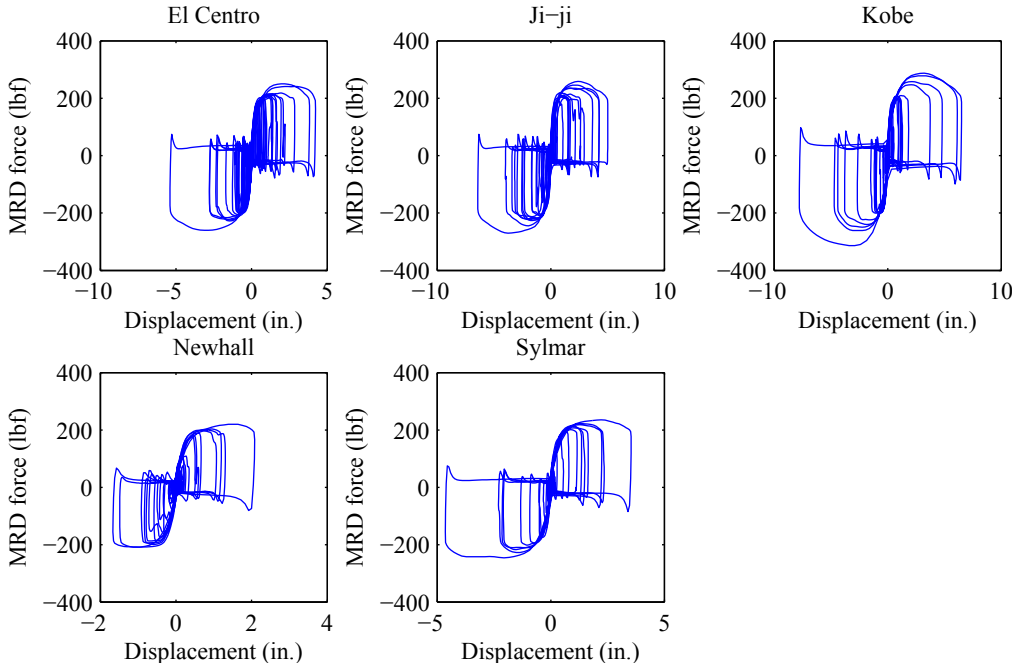

Figure 8.16: Hysteresis loops produced by the simple control 2P by Eq. (6.21) to 0.5 g PGA earthquakes

Table 8.1: Peak and RMS values to the scaled El Centro earthquakes

		Controller	Disp. (in.)	Acceleration (g)						
			Base	Base	1	2	3	4	5	6
0.2 g PGA	Peak	Uncontrolled	2.616	0.293	0.298	0.298	0.291	0.282	0.292	0.337
		Passive-off	2.395	0.279	0.279	0.280	0.275	0.268	0.274	0.305
		Passive-on	1.218	0.266	0.274	0.272	0.233	0.219	0.256	0.395
		LQG w/ A.	1.592	0.234	0.237	0.221	0.197	0.207	0.224	0.286
		LQG w/ I.D.	1.632	0.216	0.217	0.211	0.187	0.207	0.231	0.260
		LQG w/ R.D.	1.570	0.321	0.355	0.350	0.379	0.338	0.415	0.558
		Simple control 1N	1.676	0.353	0.344	0.304	0.310	0.349	0.343	0.440
		Simple control 1P	1.758	0.417	0.347	0.483	0.468	0.400	0.457	0.555
		Simple control 2N	1.701	0.318	0.331	0.311	0.292	0.357	0.370	0.437
		Simple control 2P	1.742	0.427	0.378	0.478	0.474	0.384	0.468	0.570
	RMS	Uncontrolled	0.673	0.067	0.068	0.070	0.072	0.073	0.076	0.080
		Passive-off	0.561	0.058	0.059	0.060	0.062	0.063	0.065	0.070
		Passive-on	0.227	0.044	0.045	0.045	0.046	0.047	0.054	0.070
		LQG w/ A.	0.358	0.042	0.042	0.042	0.043	0.045	0.049	0.057
		LQG w/ I.D.	0.369	0.042	0.042	0.043	0.044	0.045	0.048	0.055
		LQG w/ R.D.	0.286	0.066	0.064	0.062	0.064	0.067	0.073	0.091
		Simple control 1N	0.340	0.079	0.074	0.070	0.068	0.073	0.081	0.102
		Simple control 1P	0.322	0.075	0.072	0.071	0.070	0.075	0.083	0.103
		Simple control 2N	0.343	0.075	0.069	0.062	0.062	0.067	0.075	0.101
		Simple control 2P	0.320	0.074	0.072	0.069	0.070	0.073	0.081	0.103
0.5 g PGA	Peak	Uncontrolled	6.539	0.732	0.745	0.744	0.728	0.705	0.729	0.843
		Passive-off	6.172	0.713	0.706	0.694	0.688	0.677	0.712	0.768
		Passive-on	4.671	0.771	0.771	0.741	0.701	0.694	0.829	0.930
		LQG w/ A.	4.906	0.679	0.697	0.675	0.609	0.676	0.679	0.756
		LQG w/ I.D.	4.863	0.650	0.687	0.674	0.577	0.651	0.666	0.727
		LQG w/ R.D.	5.323	0.904	0.941	0.861	0.855	0.829	0.910	1.049
		Simple control 1N	5.457	0.847	0.856	0.798	0.677	0.738	0.866	1.164
		Simple control 1P	5.415	0.851	0.865	0.879	0.941	0.883	0.911	1.046
		Simple control 2N	5.482	0.836	0.841	0.784	0.712	0.731	0.877	1.151
		Simple control 2P	5.391	0.876	0.848	0.902	0.938	0.898	0.980	1.099
	RMS	Uncontrolled	1.682	0.166	0.170	0.176	0.179	0.183	0.189	0.201
		Passive-off	1.518	0.152	0.155	0.160	0.164	0.167	0.173	0.182
		Passive-on	0.858	0.129	0.128	0.123	0.123	0.126	0.139	0.185
		LQG w/ A.	0.995	0.112	0.112	0.112	0.115	0.119	0.125	0.143
		LQG w/ I.D.	1.006	0.110	0.111	0.112	0.115	0.119	0.125	0.139
		LQG w/ R.D.	1.026	0.163	0.161	0.156	0.160	0.164	0.179	0.217
		Simple control 1N	1.134	0.156	0.151	0.141	0.144	0.152	0.158	0.203
		Simple control 1P	1.077	0.172	0.167	0.164	0.166	0.172	0.188	0.227
		Simple control 2N	1.138	0.153	0.147	0.138	0.141	0.148	0.156	0.199
		Simple control 2P	1.073	0.174	0.168	0.166	0.167	0.174	0.191	0.230

Table 8.2: Peak and RMS values to the scaled Ji-ji earthquakes

		Controller	Disp. (in.)	Acceleration (g)						
			Base	Base	1	2	3	4	5	6
0.2 g PGA	Peak	Uncontrolled	2.909	0.295	0.300	0.306	0.311	0.316	0.333	0.352
		Passive-off	2.848	0.301	0.305	0.298	0.317	0.332	0.344	0.374
		Passive-on	1.445	0.271	0.237	0.269	0.289	0.278	0.311	0.342
		LQG w/ A.	2.021	0.292	0.304	0.294	0.244	0.261	0.291	0.353
		LQG w/ I.D.	2.103	0.293	0.309	0.283	0.259	0.272	0.302	0.333
		LQG w/ R.D.	1.935	0.376	0.341	0.439	0.353	0.393	0.376	0.435
		Simple control 1N	2.427	0.414	0.406	0.423	0.413	0.397	0.449	0.486
		Simple control 1P	2.152	0.400	0.412	0.428	0.429	0.414	0.420	0.537
		Simple control 2N	2.451	0.430	0.406	0.414	0.383	0.393	0.404	0.474
		Simple control 2P	2.142	0.369	0.367	0.444	0.417	0.423	0.416	0.551
	RMS	Uncontrolled	1.016	0.099	0.102	0.106	0.108	0.110	0.112	0.114
		Passive-off	0.855	0.086	0.088	0.090	0.092	0.094	0.096	0.100
		Passive-on	0.393	0.052	0.053	0.054	0.055	0.057	0.058	0.062
		LQG w/ A.	0.585	0.060	0.060	0.060	0.062	0.063	0.066	0.072
		LQG w/ I.D.	0.602	0.061	0.061	0.062	0.063	0.064	0.066	0.072
		LQG w/ R.D.	0.431	0.068	0.068	0.070	0.069	0.072	0.074	0.083
		Simple control 1N	0.617	0.074	0.072	0.073	0.073	0.077	0.081	0.088
		Simple control 1P	0.460	0.074	0.074	0.074	0.076	0.077	0.080	0.091
		Simple control 2N	0.618	0.072	0.070	0.070	0.071	0.075	0.077	0.087
		Simple control 2P	0.459	0.073	0.073	0.073	0.074	0.076	0.079	0.091
0.5 g PGA	Peak	Uncontrolled	7.272	0.738	0.750	0.765	0.777	0.791	0.832	0.880
		Passive-off	7.182	0.714	0.743	0.736	0.772	0.814	0.838	0.931
		Passive-on	6.135	0.886	0.900	0.829	0.841	0.970	0.929	1.051
		LQG w/ A.	6.144	0.838	0.836	0.830	0.758	0.739	0.780	0.972
		LQG w/ I.D.	6.150	0.800	0.812	0.815	0.771	0.742	0.774	0.942
		LQG w/ R.D.	6.160	0.843	0.863	0.907	0.954	0.913	0.958	1.159
		Simple control 1N	7.083	1.010	0.843	0.976	0.906	0.976	0.979	0.938
		Simple control 1P	6.432	0.911	0.860	0.916	0.965	0.974	0.866	1.006
		Simple control 2N	7.103	0.931	0.849	0.984	0.908	0.970	0.972	1.011
		Simple control 2P	6.426	0.922	0.868	0.919	0.981	1.022	0.917	1.063
	RMS	Uncontrolled	2.540	0.249	0.255	0.264	0.270	0.274	0.280	0.286
		Passive-off	2.296	0.227	0.232	0.240	0.245	0.249	0.255	0.261
		Passive-on	1.362	0.159	0.160	0.160	0.164	0.167	0.172	0.188
		LQG w/ A.	1.571	0.163	0.164	0.166	0.170	0.172	0.177	0.189
		LQG w/ I.D.	1.580	0.163	0.164	0.167	0.170	0.172	0.177	0.188
		LQG w/ R.D.	1.446	0.192	0.190	0.191	0.194	0.197	0.211	0.232
		Simple control 1N	1.810	0.192	0.190	0.192	0.195	0.202	0.206	0.222
		Simple control 1P	1.517	0.197	0.196	0.199	0.203	0.205	0.221	0.235
		Simple control 2N	1.812	0.190	0.189	0.192	0.193	0.201	0.204	0.222
		Simple control 2P	1.514	0.199	0.196	0.199	0.204	0.206	0.225	0.238

Table 8.3: Peak and RMS values to the scaled Kobe earthquakes

		Controller	Disp. (in.)	Acceleration (g)						
			Base	Base	1	2	3	4	5	6
0.2 g PGA	Peak	Uncontrolled	3.275	0.320	0.331	0.344	0.351	0.355	0.361	0.372
		Passive-off	3.178	0.337	0.342	0.352	0.353	0.364	0.355	0.375
		Passive-on	1.875	0.291	0.283	0.255	0.283	0.321	0.381	0.397
		LQG w/ A.	1.778	0.215	0.245	0.269	0.247	0.236	0.264	0.303
		LQG w/ I.D.	1.802	0.253	0.257	0.262	0.249	0.281	0.260	0.287
		LQG w/ R.D.	2.615	0.366	0.442	0.434	0.407	0.395	0.529	0.546
		Simple control 1N	2.033	0.433	0.495	0.300	0.473	0.475	0.365	0.563
		Simple control 1P	2.814	0.489	0.463	0.482	0.501	0.617	0.514	0.678
		Simple control 2N	2.053	0.412	0.445	0.267	0.427	0.487	0.367	0.566
		Simple control 2P	2.793	0.518	0.434	0.516	0.553	0.612	0.510	0.685
	RMS	Uncontrolled	0.918	0.088	0.091	0.095	0.098	0.100	0.103	0.106
		Passive-off	0.731	0.071	0.073	0.077	0.079	0.081	0.083	0.086
		Passive-on	0.248	0.036	0.037	0.039	0.042	0.044	0.047	0.054
		LQG w/ A.	0.298	0.034	0.034	0.036	0.037	0.039	0.041	0.046
		LQG w/ I.D.	0.310	0.035	0.036	0.037	0.038	0.040	0.042	0.046
		LQG w/ R.D.	0.363	0.059	0.060	0.062	0.063	0.066	0.069	0.079
		Simple control 1N	0.322	0.062	0.059	0.052	0.060	0.062	0.063	0.075
		Simple control 1P	0.415	0.071	0.069	0.070	0.073	0.078	0.080	0.092
		Simple control 2N	0.325	0.059	0.055	0.048	0.055	0.059	0.062	0.075
		Simple control 2P	0.411	0.070	0.068	0.068	0.073	0.076	0.079	0.092
0.5 g PGA	Peak	Uncontrolled	8.187	0.799	0.826	0.861	0.878	0.889	0.902	0.929
		Passive-off	7.994	0.806	0.837	0.869	0.879	0.885	0.878	0.895
		Passive-on	6.407	0.860	0.817	0.810	0.879	1.007	1.031	1.104
		LQG w/ A.	6.009	0.741	0.866	0.765	0.820	0.842	0.915	0.955
		LQG w/ I.D.	5.995	0.744	0.877	0.775	0.841	0.866	0.944	0.959
		LQG w/ R.D.	7.549	0.953	1.104	1.141	1.048	1.079	1.120	1.155
		Simple control 1N	6.441	0.874	0.903	0.862	0.976	0.991	0.928	1.205
		Simple control 1P	7.814	1.088	1.021	1.153	1.091	1.133	1.162	1.333
		Simple control 2N	6.478	0.888	0.873	0.817	0.932	0.967	0.889	1.214
		Simple control 2P	7.774	1.112	1.031	1.160	1.056	1.176	1.170	1.319
	RMS	Uncontrolled	2.294	0.220	0.227	0.238	0.245	0.250	0.257	0.265
		Passive-off	1.990	0.191	0.198	0.207	0.213	0.218	0.225	0.231
		Passive-on	0.999	0.121	0.120	0.123	0.127	0.134	0.140	0.158
		LQG w/ A.	0.994	0.105	0.108	0.111	0.117	0.120	0.124	0.132
		LQG w/ I.D.	1.001	0.105	0.108	0.112	0.117	0.120	0.124	0.132
		LQG w/ R.D.	1.331	0.162	0.165	0.171	0.176	0.180	0.189	0.204
		Simple control 1N	1.189	0.144	0.140	0.134	0.144	0.149	0.154	0.179
		Simple control 1P	1.443	0.184	0.180	0.187	0.194	0.207	0.208	0.226
		Simple control 2N	1.197	0.142	0.139	0.132	0.142	0.147	0.153	0.179
		Simple control 2P	1.434	0.183	0.180	0.185	0.195	0.206	0.207	0.226

Table 8.4: Peak and RMS values to the scaled Newhall earthquakes

		Controller	Disp. (in.)	Acceleration (g)						
			Base	Base	1	2	3	4	5	6
0.2 g PGA	Peak	Uncontrolled	1.321	0.129	0.131	0.136	0.141	0.145	0.162	0.185
		Passive-off	1.066	0.115	0.111	0.114	0.122	0.128	0.148	0.173
		Passive-on	0.509	0.147	0.131	0.104	0.113	0.122	0.173	0.250
		LQG w/ A.	0.896	0.127	0.106	0.108	0.103	0.109	0.121	0.185
		LQG w/ I.D.	0.890	0.144	0.122	0.115	0.104	0.109	0.122	0.175
		LQG w/ R.D.	0.512	0.241	0.222	0.253	0.235	0.281	0.246	0.303
		Simple control 1N	0.861	0.232	0.178	0.200	0.215	0.252	0.219	0.302
		Simple control 1P	0.607	0.258	0.245	0.240	0.230	0.282	0.233	0.323
		Simple control 2N	0.861	0.198	0.182	0.202	0.208	0.220	0.189	0.255
		Simple control 2P	0.604	0.229	0.237	0.233	0.244	0.274	0.231	0.320
	RMS	Uncontrolled	0.285	0.028	0.028	0.030	0.030	0.031	0.032	0.034
		Passive-off	0.210	0.022	0.022	0.023	0.024	0.025	0.026	0.028
		Passive-on	0.079	0.018	0.018	0.019	0.021	0.023	0.027	0.033
		LQG w/ A.	0.140	0.019	0.019	0.018	0.019	0.021	0.023	0.028
		LQG w/ I.D.	0.145	0.019	0.019	0.019	0.020	0.021	0.023	0.027
		LQG w/ R.D.	0.092	0.031	0.030	0.029	0.030	0.033	0.035	0.043
		Simple control 1N	0.127	0.034	0.033	0.031	0.033	0.034	0.037	0.044
		Simple control 1P	0.108	0.038	0.037	0.037	0.037	0.039	0.042	0.051
		Simple control 2N	0.127	0.029	0.029	0.025	0.027	0.029	0.029	0.042
		Simple control 2P	0.107	0.037	0.036	0.035	0.035	0.037	0.040	0.050
0.5 g PGA	Peak	Uncontrolled	3.303	0.321	0.327	0.341	0.353	0.362	0.404	0.464
		Passive-off	2.815	0.272	0.278	0.308	0.312	0.329	0.385	0.423
		Passive-on	1.622	0.399	0.327	0.249	0.290	0.332	0.411	0.512
		LQG w/ A.	2.294	0.354	0.309	0.247	0.261	0.332	0.362	0.437
		LQG w/ I.D.	2.264	0.368	0.312	0.246	0.270	0.311	0.353	0.426
		LQG w/ R.D.	1.911	0.449	0.395	0.396	0.402	0.538	0.498	0.567
		Simple control 1N	2.239	0.396	0.432	0.276	0.348	0.375	0.315	0.474
		Simple control 1P	2.089	0.407	0.388	0.458	0.414	0.449	0.508	0.694
		Simple control 2N	2.238	0.417	0.408	0.309	0.376	0.366	0.359	0.472
		Simple control 2P	2.081	0.409	0.402	0.430	0.422	0.448	0.532	0.708
	RMS	Uncontrolled	0.713	0.069	0.071	0.074	0.076	0.078	0.081	0.084
		Passive-off	0.604	0.060	0.061	0.064	0.066	0.067	0.070	0.074
		Passive-on	0.260	0.047	0.047	0.046	0.050	0.053	0.058	0.072
		LQG w/ A.	0.374	0.044	0.044	0.044	0.046	0.049	0.053	0.062
		LQG w/ I.D.	0.380	0.044	0.044	0.044	0.046	0.049	0.053	0.061
		LQG w/ R.D.	0.317	0.072	0.067	0.073	0.070	0.079	0.085	0.095
		Simple control 1N	0.388	0.063	0.062	0.053	0.062	0.062	0.064	0.081
		Simple control 1P	0.361	0.080	0.076	0.077	0.077	0.076	0.094	0.109
		Simple control 2N	0.390	0.061	0.058	0.053	0.058	0.061	0.063	0.081
		Simple control 2P	0.357	0.078	0.075	0.074	0.076	0.076	0.091	0.108

Table 8.5: Peak and RMS values to the scaled sylmar earthquakes

		Controller	Disp. (in.)	Acceleration (g)						
			Base	Base	1	2	3	4	5	6
0.2 g PGA	Peak	Uncontrolled	1.633	0.155	0.159	0.167	0.175	0.181	0.192	0.217
		Passive-off	1.697	0.171	0.171	0.178	0.192	0.200	0.227	0.269
		Passive-on	1.033	0.219	0.212	0.180	0.190	0.192	0.203	0.246
		LQG w/ A.	1.531	0.191	0.162	0.176	0.197	0.197	0.220	0.240
		LQG w/ I.D.	1.589	0.195	0.193	0.189	0.186	0.197	0.225	0.208
		LQG w/ R.D.	1.277	0.389	0.318	0.325	0.318	0.297	0.330	0.459
		Simple control 1N	1.597	0.310	0.333	0.237	0.328	0.322	0.255	0.429
		Simple control 1P	1.414	0.343	0.341	0.403	0.320	0.336	0.388	0.541
		Simple control 2N	1.610	0.264	0.287	0.274	0.319	0.332	0.292	0.393
		Simple control 2P	1.400	0.338	0.358	0.340	0.337	0.312	0.385	0.544
	RMS	Uncontrolled	0.370	0.036	0.037	0.038	0.040	0.040	0.042	0.043
		Passive-off	0.327	0.033	0.034	0.035	0.036	0.037	0.039	0.041
		Passive-on	0.151	0.025	0.026	0.027	0.028	0.029	0.032	0.037
		LQG w/ A.	0.233	0.026	0.026	0.026	0.027	0.028	0.030	0.034
		LQG w/ I.D.	0.238	0.026	0.026	0.027	0.028	0.028	0.030	0.033
		LQG w/ R.D.	0.176	0.041	0.041	0.039	0.042	0.044	0.045	0.055
		Simple control 1N	0.233	0.040	0.039	0.037	0.039	0.038	0.045	0.050
		Simple control 1P	0.202	0.050	0.049	0.047	0.048	0.049	0.056	0.068
		Simple control 2N	0.234	0.037	0.035	0.036	0.034	0.037	0.042	0.049
		Simple control 2P	0.199	0.049	0.048	0.045	0.047	0.047	0.054	0.067
0.5 g PGA	Peak	Uncontrolled	4.082	0.387	0.397	0.418	0.436	0.453	0.480	0.543
		Passive-off	4.150	0.406	0.414	0.440	0.464	0.465	0.497	0.602
		Passive-on	3.883	0.512	0.513	0.524	0.520	0.526	0.583	0.605
		LQG w/ A.	4.281	0.538	0.523	0.528	0.525	0.532	0.497	0.631
		LQG w/ I.D.	4.234	0.471	0.493	0.520	0.521	0.534	0.500	0.557
		LQG w/ R.D.	4.439	0.674	0.637	0.744	0.704	0.724	0.711	0.852
		Simple control 1N	4.602	0.621	0.577	0.665	0.733	0.713	0.673	0.751
		Simple control 1P	4.679	0.778	0.812	0.832	0.755	0.691	0.802	0.928
		Simple control 2N	4.600	0.571	0.582	0.641	0.727	0.663	0.713	0.747
		Simple control 2P	4.646	0.811	0.785	0.769	0.719	0.773	0.777	0.962
	RMS	Uncontrolled	0.926	0.089	0.092	0.096	0.099	0.101	0.104	0.108
		Passive-off	0.859	0.084	0.087	0.090	0.093	0.095	0.098	0.103
		Passive-on	0.547	0.073	0.073	0.073	0.075	0.077	0.084	0.098
		LQG w/ A.	0.645	0.068	0.069	0.070	0.073	0.075	0.078	0.087
		LQG w/ I.D.	0.640	0.066	0.067	0.069	0.072	0.074	0.077	0.083
		LQG w/ R.D.	0.695	0.102	0.102	0.101	0.106	0.110	0.115	0.131
		Simple control 1N	0.704	0.096	0.089	0.084	0.093	0.098	0.104	0.116
		Simple control 1P	0.755	0.118	0.115	0.115	0.118	0.125	0.128	0.151
		Simple control 2N	0.704	0.093	0.086	0.081	0.089	0.094	0.101	0.115
		Simple control 2P	0.747	0.116	0.113	0.110	0.115	0.122	0.125	0.151

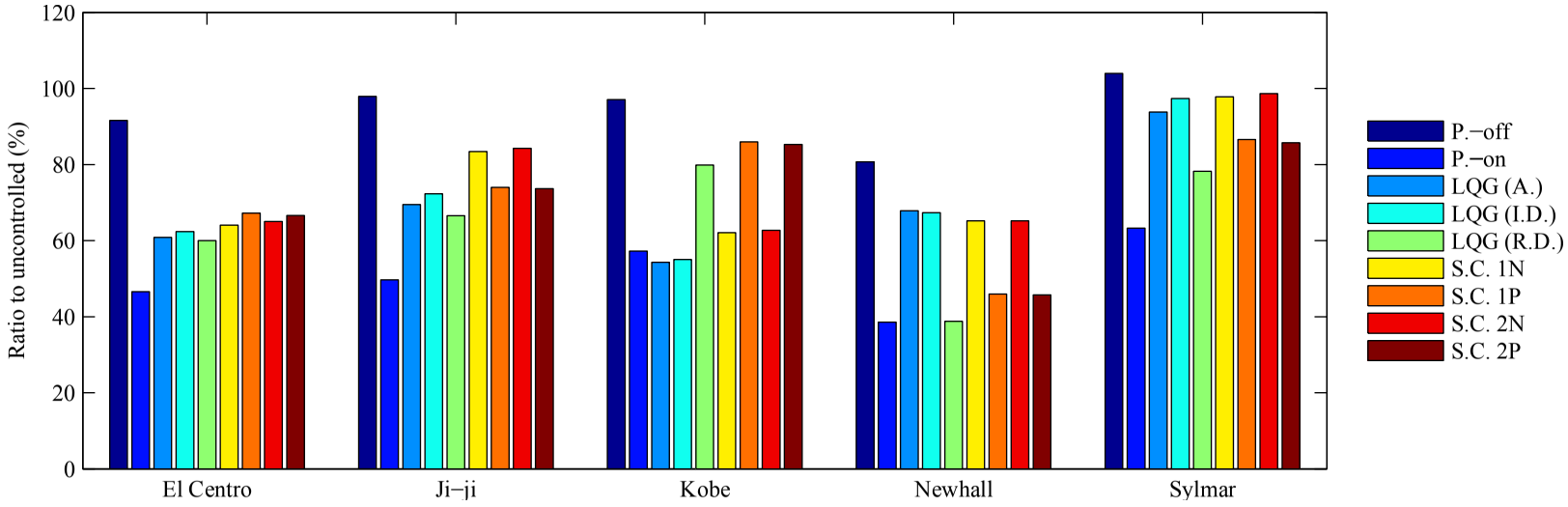

Figure 8.17: Comparisons of the peak response displacements of the base to 0.2 g PGA earthquakes

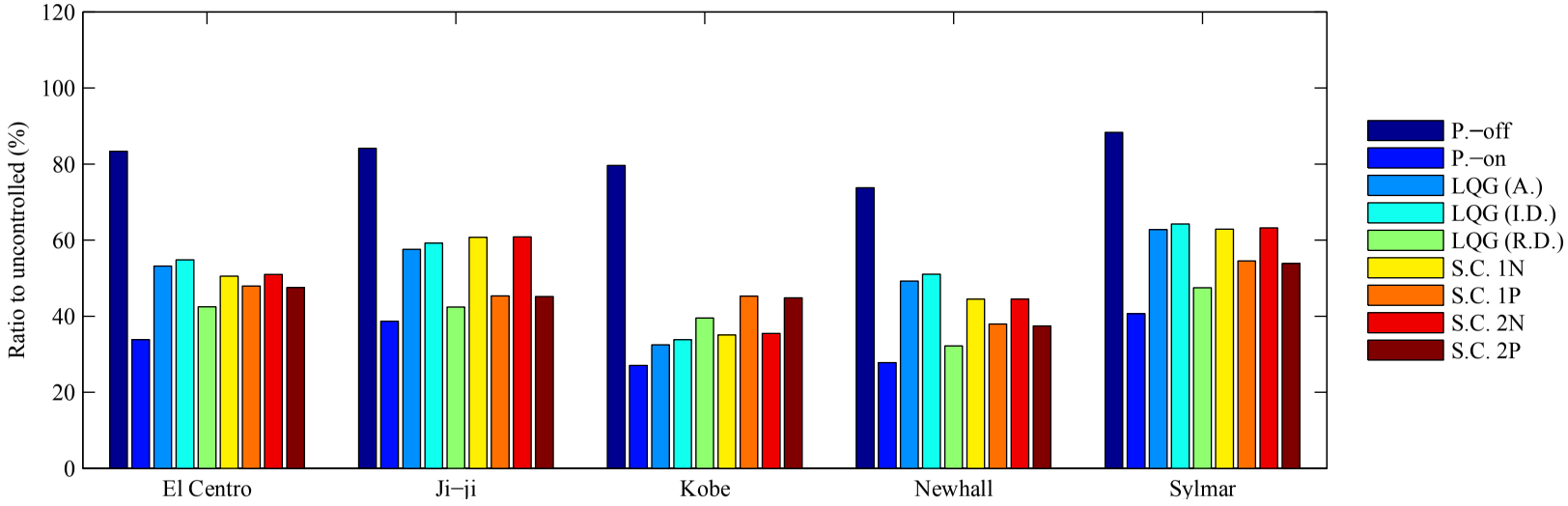

Figure 8.18: Comparisons of the RMS response displacements of the base to 0.2 g PGA earthquakes

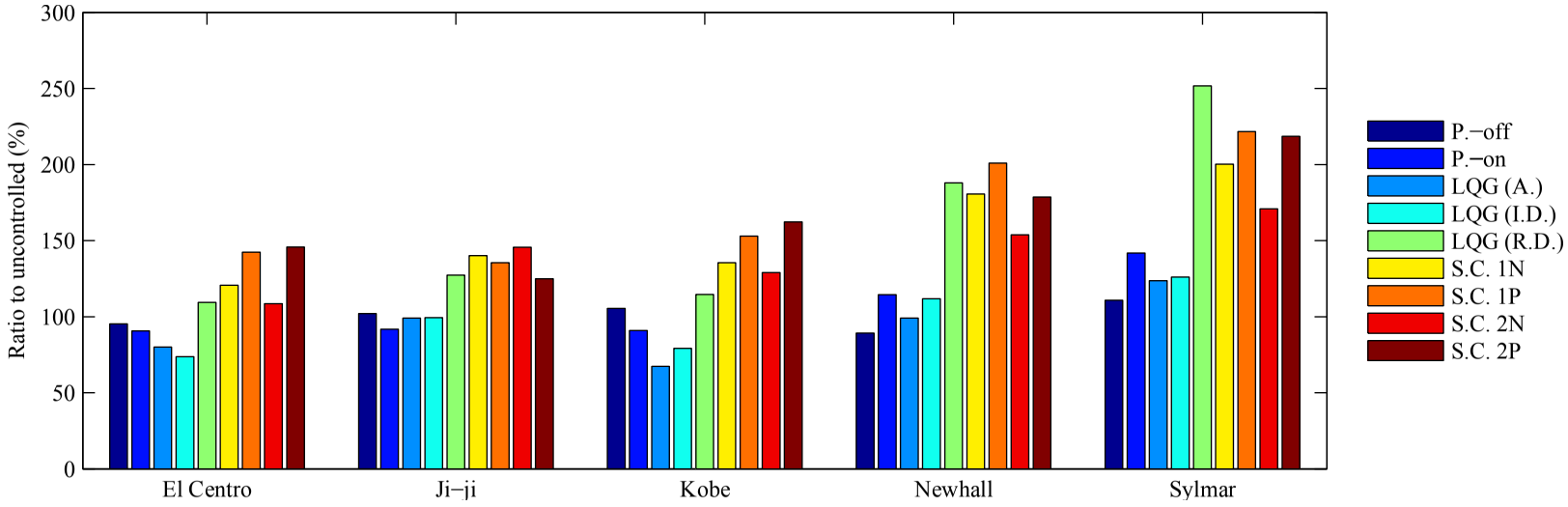

Figure 8.19: Comparisons of the peak response accelerations of the base to 0.2 g PGA earthquakes

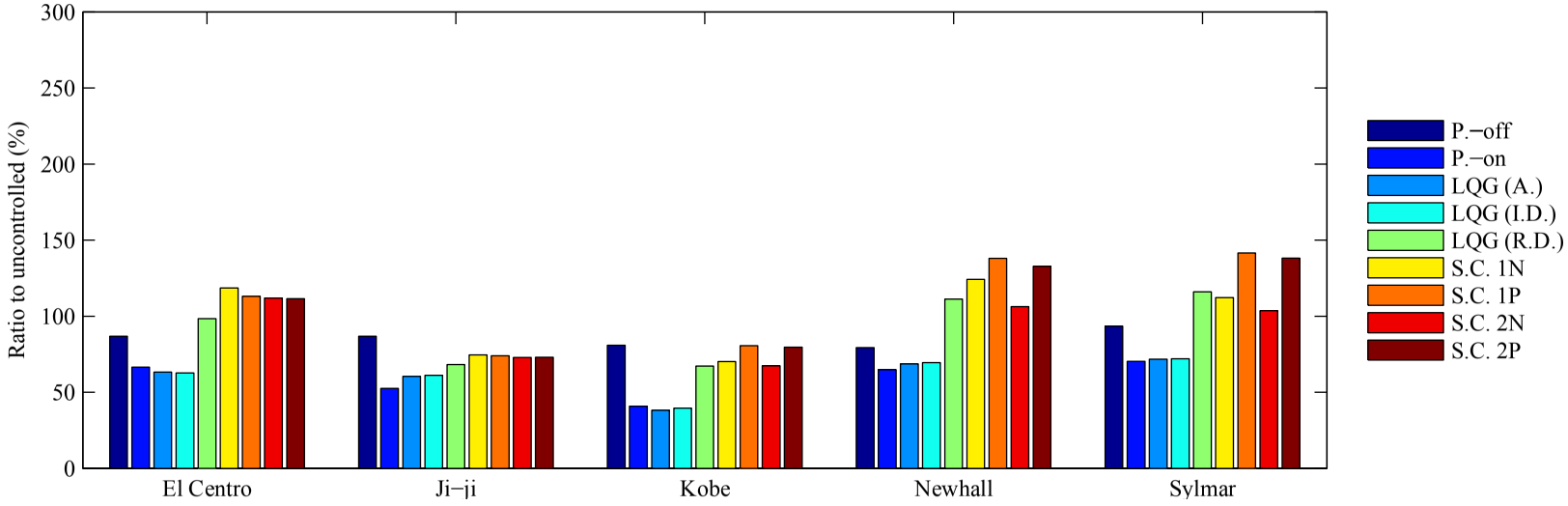

Figure 8.20: Comparisons of the RMS response accelerations of the base to 0.2 g PGA earthquakes

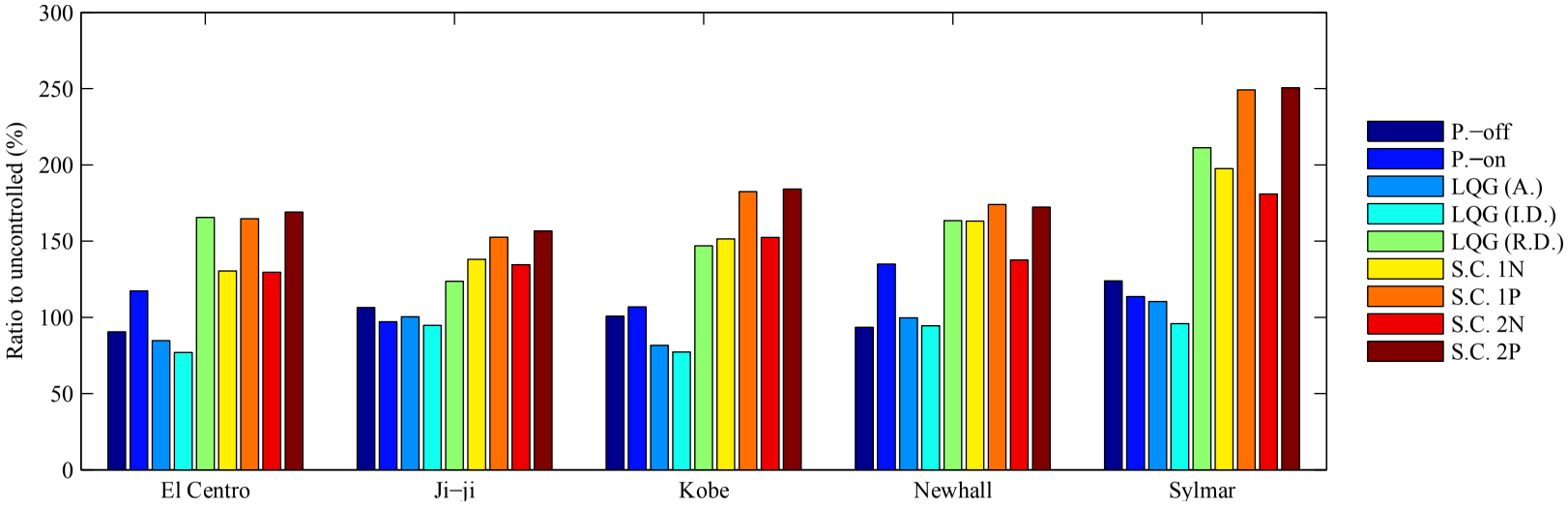

Figure 8.21: Comparisons of the peak response accelerations of the 6th floor to 0.2 g PGA earthquakes

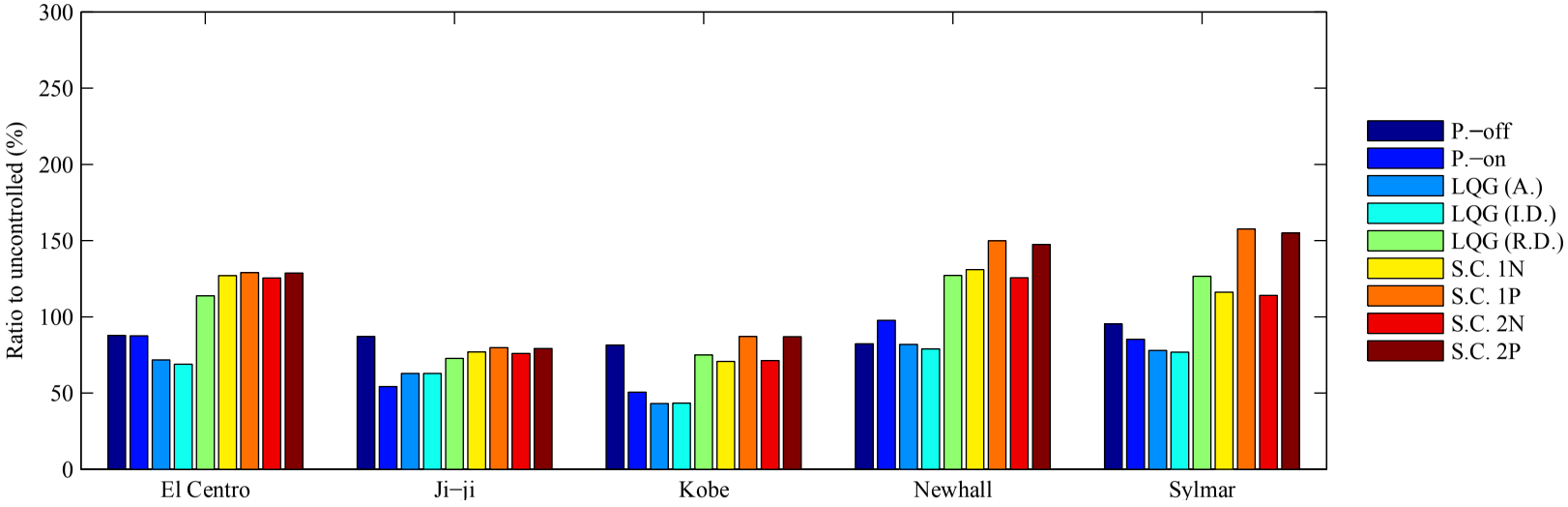

Figure 8.22: Comparisons of the RMS response accelerations of the 6th floor to 0.2 g PGA earthquakes

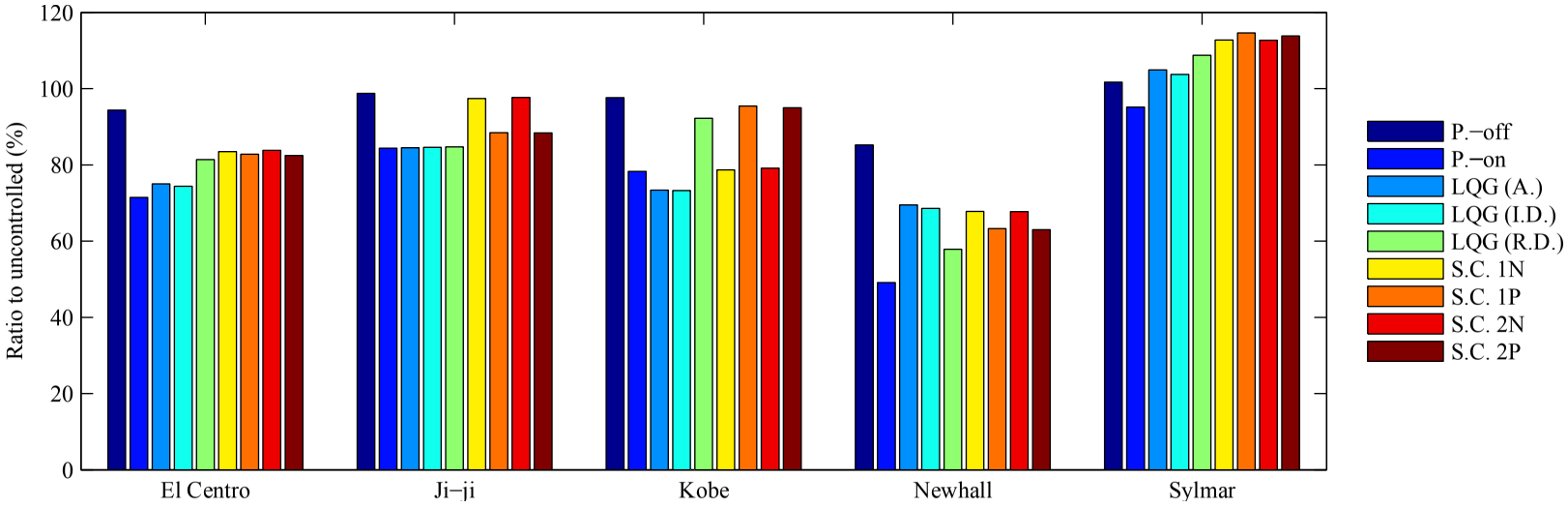

Figure 8.23: Comparisons of the peak response displacements of the base to 0.5 g PGA earthquakes

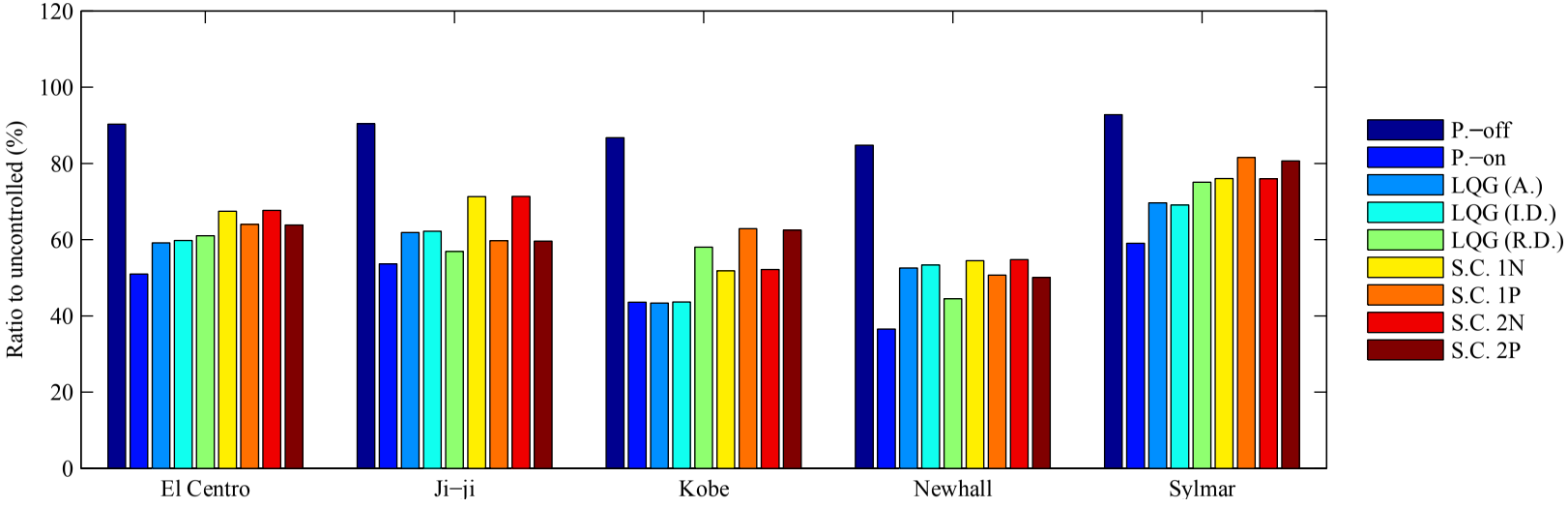

Figure 8.24: Comparisons of the RMS response displacements of the base to 0.5 g PGA earthquakes

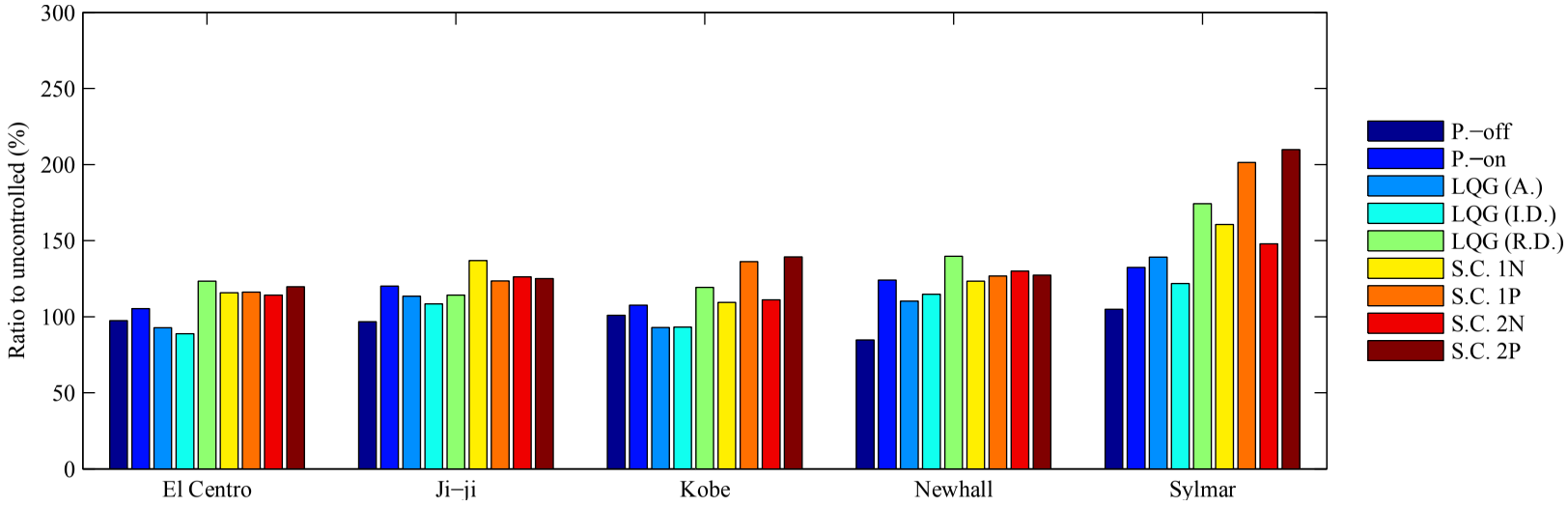

Figure 8.25: Comparisons of the peak response accelerations of the base to 0.5 g PGA earthquakes

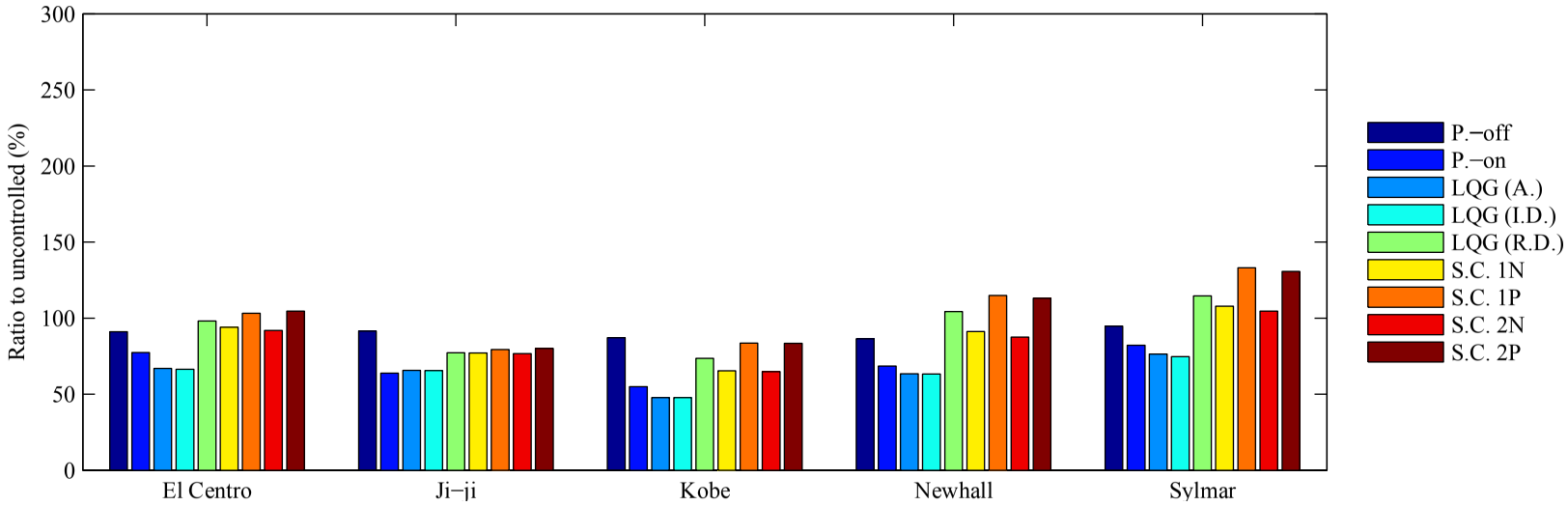

Figure 8.26: Comparisons of the RMS response accelerations of the base to 0.5 g PGA earthquakes

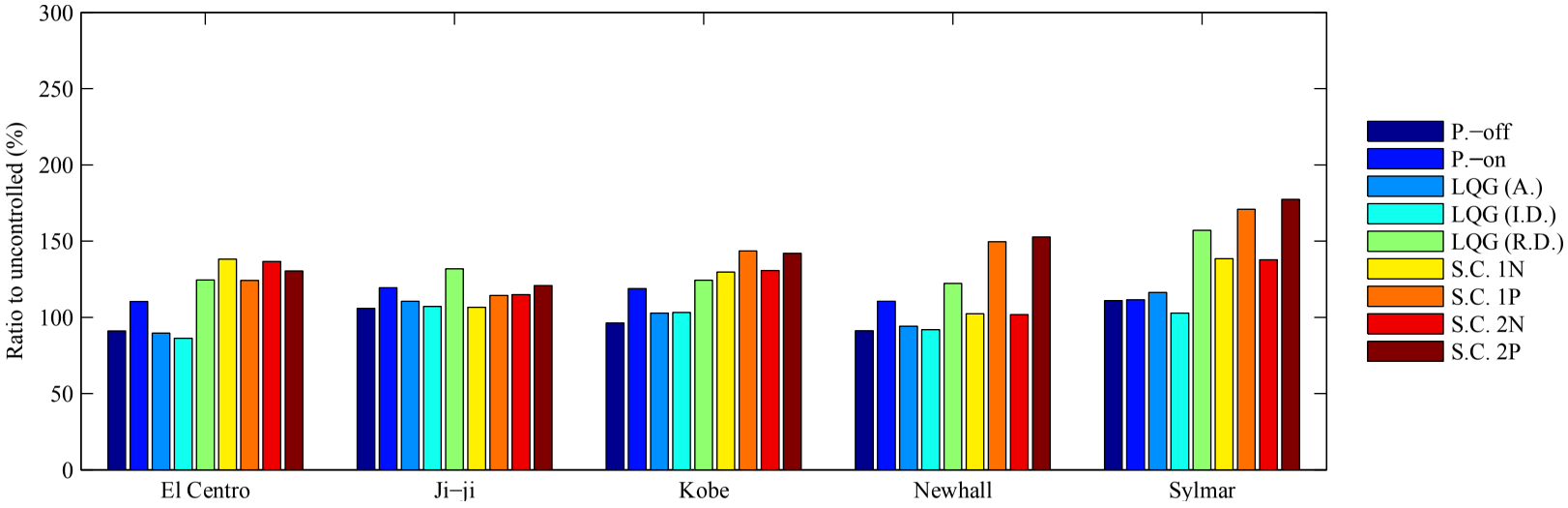

Figure 8.27: Comparisons of the peak response accelerations of the 6th floor to 0.5 g PGA earthquakes

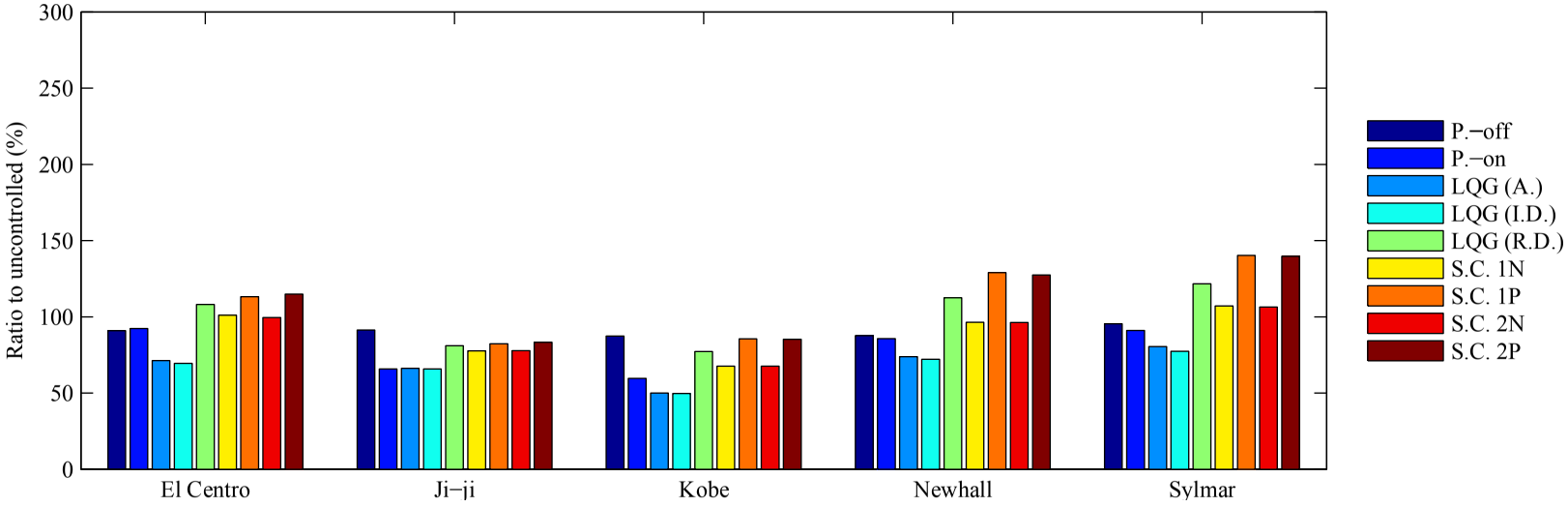

Figure 8.28: Comparisons of the RMS response accelerations of the 6th floor to 0.5 g PGA earthquakes

8.2.2 RTHS

The effectiveness of the smart base isolation system employing the MR damper is shown using RTHS. To compensate for time delays/lags, the feedforward-feedback compensator designed in Subsection 4.4.2 is employed. As input earthquakes, Kobe (1995, JMA station) and El Centro (1940, Imperial Valley) are considered. The Kobe record is scaled so that its peak ground acceleration (PGA) is 0.2 g and 0.5 g and the PGA of the El Centro record is scaled to 0.5 g.

The two semi-active control strategies, the LQG-based clipped-optimal control with acceleration weighting and the LQG-based clipped-optimal control with inter-story drift weighting, whose effectiveness were shown by the numerical simulations are applied. In addition to these two semi-active controllers, the passive-off mode and the passive-on mode cases are carried out.

The hystetetic force-displacement loops produced by the LQG-based clipped-optimal control with acceleration weighting and inter-story drift weighting subjected to the three scaled earthquakes are depicted in Figures 8.29, 8.30, and 8.31, respectively. These hysteresis loops produced by the physical MR damper agrees with the ones obtained by numerical simulation very well. As can be seen, the physical MR damper produces clear pseudo-negative stiffness to 0.2 g PGA Kobe earthquake, while for the amplified earthquakes to 0.5g PGA, distinct properties of pseudo-negative stiffness are gone.

Tables 8.6 through 8.8 summarize the peak and root mean square (RMS) values of the response base displacements relative to the ground and absolute accelerations at each floor for all cases. Figures 8.32 thorough 8.34 compare the normalized peak and RMS values based on the uncontrolled passive base isolation cases obtained from simulations. As can be seen in the tables and figures, the base isolation system with a passive-on mode or semi-actively controlled MR damper reduce both peak and RMS response and base displacement successfully compared to the uncontrolled passive base isolation and passive-off mode MR damper cases. In terms of response acceleration, the risk of increasing peak acceleration can be found when the MR damper in passive-on mode is applied. While the two semi-active controllers can reduce not only base displacement but also floor accelerations, the reductions in acceleration are not as large as in base displacement. Thus, considering both base displacement and floor accelerations, the two designed semi-active controllers show better response reduction performance than the three passive systems; the performance of

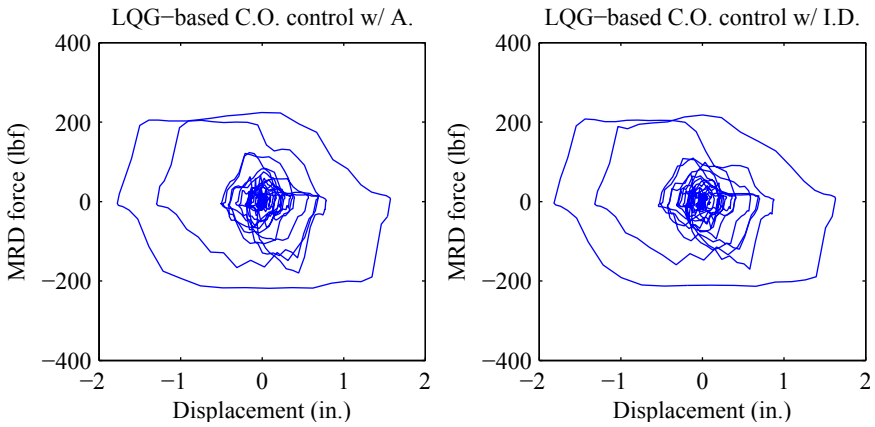

Figure 8.29: Hysteresis loops produced by the physical MR damper to 0.2 g PGA Kobe earthquake

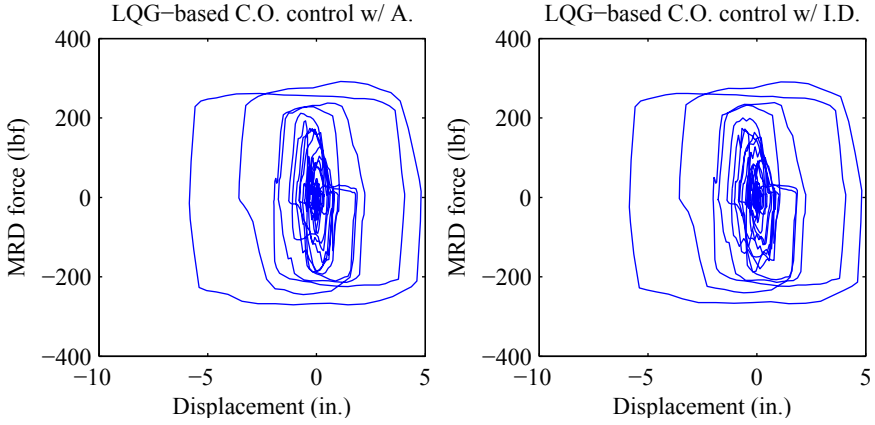

Figure 8.30: Hysteresis loops produced by the physical MR damper to 0.5 g PGA Kobe earthquake

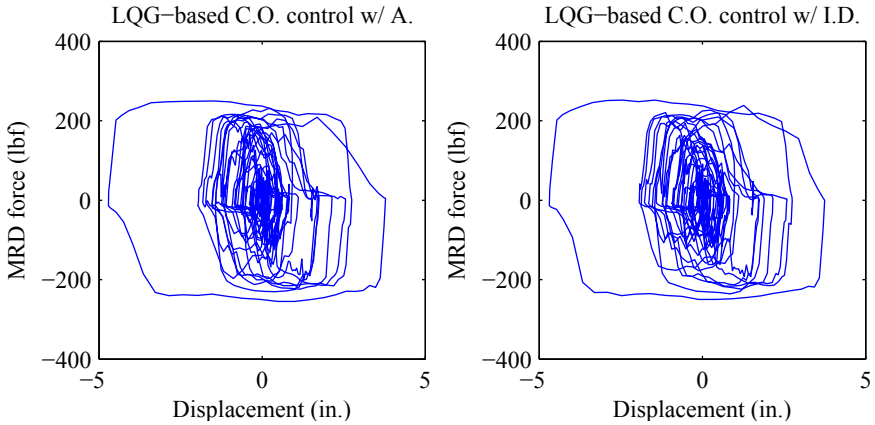

Figure 8.31: Hysteresis loops produced by the physical MR damper to 0.5 g PGA El Centro earthquake

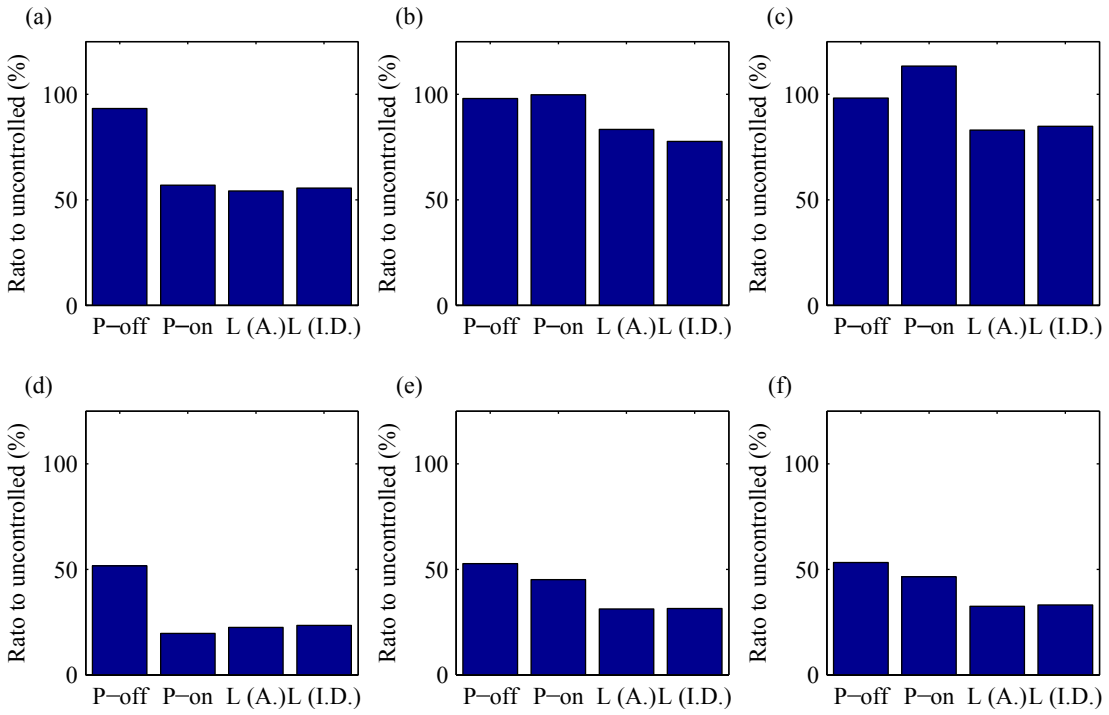

Figure 8.32: Reduction to 0.2 g Kobe earthquake; (a) Peak base displacement, (b) Peak base acceleration, (c) Peak 6th floor acceleration, (d) RMS base displacements, (e) RMS base acceleration, (f) RMS 6th floor acceleration

the two semi-active controllers are quite similar.

An active base isolation study employing the same base-isolated building model was conducted by Chang and Spencer (2012). The active control system was able to reduce the base displacement substantially, but this increased performance came at the expense of a small increase in floor accelerations. In contrast, the semi-active controllers show reductions in both floor accelerations, especially at higher floors, and base displacements. Considering that a semi-actively controlled system uses several orders of magnitude less power than the actively controlled system, the MR damper can be an attractive alternative for improved base isolation system performance.

8.3 Summary

This chapter employs numerical simulation and RTHS to investigate a class of isolation systems that use semi-active control devices (i.e., smart base isolation). A six-story building was considered. The isolation system consisted of linear, low-damping isolators, combined with a magnetorheological

Table 8.6: Comparisons of peak and RMS values to 0.2 g Kobe earthquake

		Disp. (in.)	Acceleration (g)						
		Base	Base	1	2	3	4	5	6
Peak	Isolation (Sim.)	3.275	0.320	0.331	0.344	0.351	0.355	0.361	0.372
	Passive-off	3.055	0.313	0.320	0.331	0.338	0.340	0.345	0.365
	Passive-on	1.865	0.319	0.312	0.330	0.348	0.357	0.349	0.421
	LQG w/ A.	1.775	0.266	0.226	0.271	0.294	0.246	0.256	0.309
	LQG w/ I.D.	1.818	0.248	0.242	0.289	0.326	0.262	0.249	0.315
RMS	Isolation (Sim.)	0.918	0.088	0.091	0.095	0.098	0.100	0.103	0.106
	Passive-off	0.621	0.061	0.063	0.066	0.067	0.069	0.071	0.074
	Passive-on	0.237	0.052	0.052	0.046	0.049	0.054	0.056	0.064
	LQG w/ A.	0.270	0.036	0.036	0.036	0.037	0.039	0.040	0.045
	LQG w/ I.D.	0.281	0.036	0.037	0.036	0.038	0.039	0.042	0.046

Table 8.7: Comparisons of peak and RMS values to 0.5 g Kobe earthquake

		Disp. (in.)	Acceleration (g)						
		Base	Base	1	2	3	4	5	6
Peak	Isolation (Sim.)	8.187	0.799	0.826	0.861	0.878	0.889	0.902	0.929
	Passive-off	7.724	0.775	0.799	0.831	0.849	0.854	0.858	0.892
	Passive-on	6.298	0.795	0.756	0.760	0.841	0.937	1.001	1.044
	LQG w/ A.	5.846	0.649	0.715	0.729	0.745	0.804	0.853	0.873
	LQG w/ I.D.	5.855	0.663	0.686	0.726	0.751	0.800	0.865	0.879
RMS	Isolation (Sim.)	2.294	0.220	0.227	0.238	0.245	0.250	0.257	0.265
	Passive-off	1.692	0.163	0.168	0.177	0.182	0.186	0.192	0.197
	Passive-on	0.892	0.112	0.114	0.114	0.119	0.124	0.129	0.144
	LQG w/ A.	0.888	0.094	0.097	0.100	0.104	0.108	0.112	0.119
	LQG w/ I.D.	0.897	0.095	0.097	0.101	0.104	0.108	0.112	0.119

Table 8.8: Comparisons of peak and RMS values to 0.5 g El Centro earthquake

		Disp. (in.)	Acceleration (g)						
		Base	Base	1	2	3	4	5	6
Peak	Isolation (Sim.)	6.539	0.732	0.745	0.744	0.728	0.705	0.729	0.843
	Passive-off	5.955	0.657	0.666	0.670	0.657	0.643	0.678	0.742
	Passive-on	4.467	0.643	0.685	0.675	0.662	0.603	0.672	0.835
	LQG w/ A.	4.713	0.613	0.593	0.594	0.574	0.637	0.629	0.678
	LQG w/ I.D.	4.692	0.582	0.586	0.585	0.570	0.617	0.632	0.632
RMS	Isolation (Sim.)	1.682	0.166	0.170	0.176	0.179	0.183	0.189	0.201
	Passive-off	1.322	0.131	0.134	0.139	0.143	0.145	0.150	0.156
	Passive-on	0.763	0.115	0.117	0.114	0.115	0.118	0.127	0.154
	LQG w/ A.	0.893	0.102	0.103	0.101	0.105	0.109	0.113	0.126
	LQG w/ I.D.	0.903	0.101	0.102	0.102	0.105	0.108	0.112	0.123

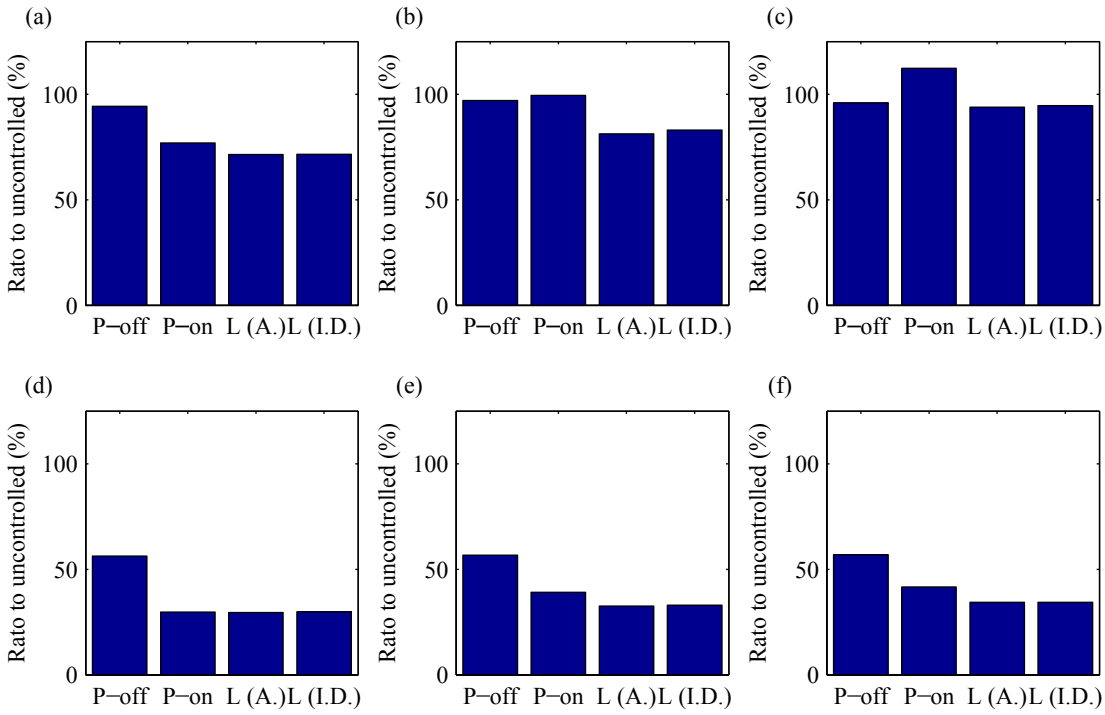

Figure 8.33: Reduction to 0.5 g Kobe earthquake; (a) Peak base displacement, (b) Peak base acceleration, (c) Peak 6th floor acceleration, (d) RMS base displacements, (e) RMS base acceleration, (f) RMS 6th floor acceleration

(MR) fluid damper. In RTHS, the smart isolated building was substructured, such that the building was modeled computationally, whereas the MR damper was tested physically. This smart base isolation system is found to reduce base displacements and floor accelerations better than the passive counterparts. Improvements were also demonstrated over the active isolation system, without the need for large external power sources.

The versatility of the hysteresis loops produced by the LQG-based clipped-optimal controllers and the proposed simple controllers was shown through numerical simulation and RTHS, as well. However, in seismic performance, the proposed simple controllers were not comparable to the LQG-based clipped-optimal controllers, especially in the upper floors.

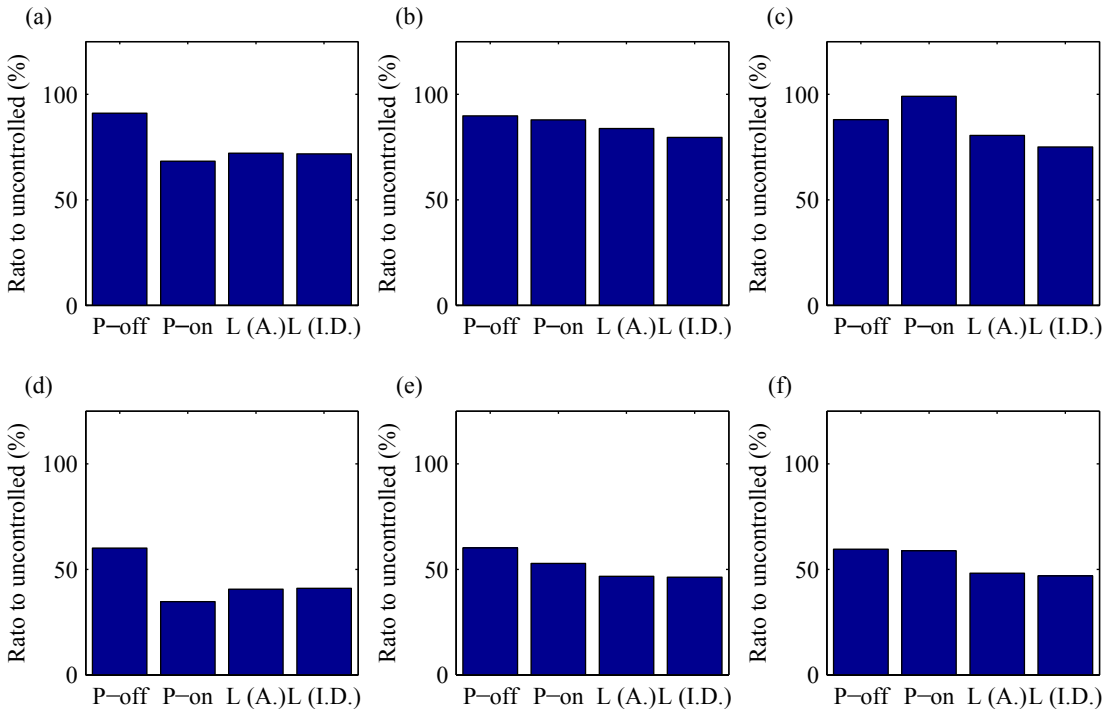

Figure 8.34: Reduction to 0.5 g El Centro earthquake; (a) Peak base displacement, (b) Peak base acceleration, (c) Peak 6th floor acceleration, (d) RMS base displacements, (e) RMS base acceleration, (f) RMS 6th floor acceleration

Chapter 9

Conclusions and Future Studies

9.1 Conclusions

In this dissertation, the possibility of semi-active control strategies have been explored, and their effectiveness has been verified experimentally for seismically excited buildings. The properties of the hysteretic force-displacement loops produced by semi-actively controlled MR dampers and their seismic performance were investigated.

A review of literature in the area of structural control technologies was first presented with a focus on outrigger damping systems and hybrid base-isolation systems. Literature related to real-time hybrid simulation was reviewed as well. Also, basic background on modern control theories which are necessary to design active and semi-active controllers was introduced, and the servo-hydraulic system model, the MR damper model, and the model-based compensators for RTHS were developed.

The nature of the hysteretic behavior of the active control forces produced by the widely employed LQG-based acceleration feedback control strategies was investigated, revealing the relationship between the properties of the control forces and the response. Numerical simulation studies carried out on one-story and three-story buildings with active bracing show that the LQG-based algorithms are quite versatile and can produce controllers with a variety of behaviors. The effectiveness of negative stiffness control force was shown through numerical studies. Additionally, the numerical results demonstrated that the presented LQG-based acceleration feedback control had performance comparable to the LQR in the presented SDOF and 3DOF building models.

Following the hysteretic behavior of the active control forces and the seismic responses, hysteresis loops produced by the semi-actively controlled MR damper were investigated. Two new model-free semi-active control algorithms for controllable dampers were proposed. One of the algo-

rithms needs only the directions of the displacement and the velocity of the damper to decide the input current to the damper. The other one needs the directions of only the displacement and the output force of the damper. Thus, the structure model and a number of sensors are not required to implement the proposed algorithms. Moreover, this research demonstrated that the proposed controllers can produce versatile hysteresis control force loops through numerical simulations on the scaled three-story building model with the MR damper. Also, the effectiveness of hysteresis loops having pseudo-negative stiffness was verified. Additionally, the numerical results showed that the proposed two algorithms producing pseudo-negative stiffness had performance comparable to the LQG-based clipped-optimal controllers, which need the accurate structure model and more sensors.

To show the effectiveness of the semi-active strategies on complicated structures experimentally, the efficacy of the model-based compensator for RTHS on a MDOF structure was verified through a high-rise building model with an outrigger damping system. Through this research, the following general conclusions were drawn: a) RTHS worked when all modes of the structure were lightly damped, demonstrating the robustness of the actuator controller without the need for adding numerical damping; b) the actuator control strategy used in this study demonstrated stable and accurate results in MDOF structural systems; c) RTHS can be employed for validation of structural control algorithms; d) RTHS provides an effective means for assessing the system performance of rate-dependent components in complex structures.

Also, this study showed that MR dampers can be employed effectively in outrigger damping systems using passive-on mode and semi-active controllers. The MR damper's restoring force can be simulated quite well by the proposed MR damper model for the two earthquake records; however, differences are still present. In particular, discrepancies between simulations and RTHSs were found in the base shear. Moreover, the physical specimen contains no modeling errors, while it is subject to experimental error such as magnitude and time delay. The numerical model provides a good verification tool for RTHS; however it is subject to numerical errors, is only valid within the range of behavior for which the model is calibrated, and cannot fully represent the complex specimen behavior. Thus, the importance of combining RTHS with numerical simulation to ensure accurate results was demonstrated.

A class of isolation systems that use semi-active control devices (i.e., smart base isolation) was investigated through numerical simulation and RTHS as well. In this study, a base-isolated six-story building was considered. The isolation system consisted of linear, low-damping isolators, combined with a MR damper. In RTHS, the smart isolated building was substructured, such that the building was modeled computationally, whereas the MR damper was tested physically. This smart base isolation system is found to reduce base displacements and floor accelerations better than the passive counterparts. Improvements were also demonstrated over the active isolation system, without the need for large external power sources.

On the base-isolated six-story building model, the versatility of the hysteresis loops produced by the LQG-based clipped-optimal controllers and the proposed simple controllers was shown through numerical simulation and RTHS, as well. However, in seismic performance, the proposed simple controllers were not comparable to the LQG-based clipped-optimal controllers, especially in the upper floors. This result implies that the proposed simple controllers are not suitable for complicated structures.

In conclusion, this dissertation provided the hysteresis behavior and the seismic performance of semi-active control strategies on buildings and showed the strong potential for practical use to mitigate seismic damage. However, some disappointing results were also observed.

9.2 Future studies

This dissertation investigated many aspects related to semi-active control strategies in building structures subjected to earthquake loadings. Some recommendations for future studies still exist, which will be detailed below.

- The effectiveness of the negative stiffness was shown in this dissertation. However, its seismic performance depended on excitation inputs to a large extent. Therefore, the magnitudes and dominant frequencies of the input earthquakes should be taken into account as well as the limitation of control devices.

- Generally, it is not easy to develop a mathematical model for nonlinear structures. Thus, the proposed simple semi-active control algorithms have an advantage when systems with strong

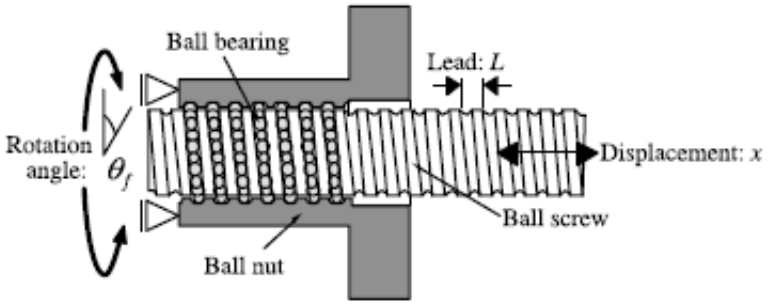

Figure 9.1: Mechanism of ball screw (Nakamura et al., 2013)

nonlinearity are considered because they does not require the model of the structure. The seismic performance and the hysteresis loops on nonlinear structures should be explored for future studies.

- Various types of inertial mass dampers, which can realize a large effective mass by rotatory inertia effect of a small mass, has been proposed (Ikago et al., 2012; Nakamura et al., 2013). In these inertial mass dampers, translational displacement is converted to rotational angle through the ball screw as illustrated in Figure 9.1. Due to inertia force, the natural frequency of the structure can be reduced, resulting in producing negative stiffness. The application of this device is an intriguing research topic.

- Semi-active control is promising, however, as shown in this dissertation, the advantage in reducing seismic responses cannot be found for some cases. While, active control needs large amount of external power source to impart control force to a structure, which is highly susceptible to destabilization and blackouts during earthquakes. To address this flaw, self-powered control has been proposed (Scruggs, 2004), in which energy harvesting technique is combined with active control. The mechanism of a self-powered control device is shown in Figure 9.2, schematically, where mechanical power is converted to electric power by an electric motor. Then this generated energy can be used to control the structure or stored for future events. Putting this technology to practical use is strongly desired.

- Recently, renewable energy has been getting attention all over the world. In addition to earthquake-induced vibration, energy harvesting techniques in tall buildings subjected to

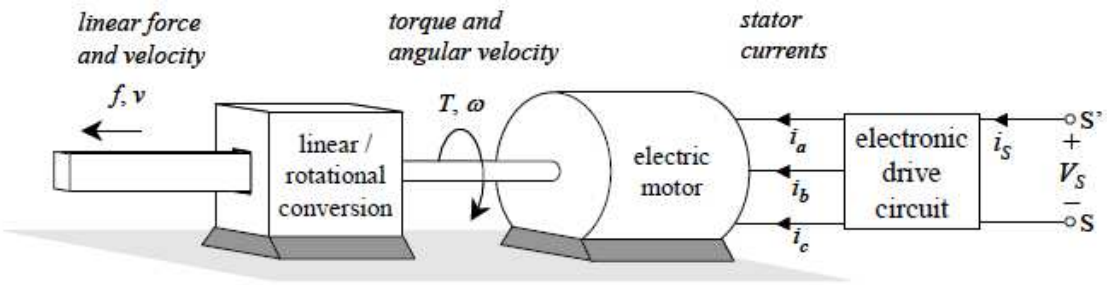

Figure 9.2: Mechanism of regenerative force actuation (Scruggs, 2004)

strong winds have been investigated by Ni et al. (2011); Tang and Zuo (2012). Ni et al. (2011) reported that a tuned mass damper (TMD) system with energy harvesting mechanism installed in the 76-story benchmark building (Samali et al., 2004) generated almost 100 kW by wind-excited vibration. Thus, the possibility of utilizing vibration energy in civil structures should be explored

- In both the inertial mass damper and the electric motor to generate power, translational displacement is converted to rotational angle by employing the same mechanism. Therefore, developing a device combining the electric motor with the inertial mass damper is considered feasible technology. Then, algorithms to minimize vibration responses and maximize power generation efficiency should be proposed. And, experimental verification is needed as well.

References

Abdel-Rohman, M. (1984). "Optimal control of tall buildings by appendages." *Journal of Structural Engineering*, 110(5), 937–947.

Abdel-Rohman, M. and Leipholz, H. (1983). "Active control of tall buildings." *Journal of Structural Engineering*, 109(3), 628–645.

Akbay, Z. and Aktan, H. (1990). "Intelligent energy dissipation devices." *Proceedings of the fourth U.S. National Conference on Earthquake Engineering*, Vol. 3, 427–435.

Akbay, Z. and Aktan, H. (1991). "Actively regulated friction slip devices." *Proceedings of the sixth Canadian Conference on Earthquake Engineering*, 363–374.

Berton, S. and Bolander, J. E. (2005). "Amplification system for supplemental damping devices in seismic applications." *Journal of Structural Engineering*, 131(6), 979–983.

Blakeborough, A., Williams, M. S., Darby, A., and Williams, D. M. (2001). "The development of real-time substructure testing." *Philosophical Transactions of the Royal Society A - Mathematical, Physical and Engineering Sciences*, 359, 1869.

Carlson, J. (1994). "The promise of controllable fluids." *Proceedings of Actuator 94*, 266–270.

Carlson, J., Catanzarite, D., and St. Clair, K. (1996). "Commercial magneto-rheological fluid devices." *International Journal of Modern Physics B*, 10(23 & 24), 2857–2865.

Carlson, J. and Spencer, Jr., B. F. (1996). "Magneto-rheological fluid dampers for semi-active seismic control." *Proceedings of the 3rd International Conference on Motion and Vibration Control*, 35–40.

Carlson, J. and Weiss, K. D. (1994). "A growing attraction to magnetic fluids." *Machine Design*, (August), 61–64.

Carrion, J. E. and Spencer, Jr., B. F. (2007). "Model-based strategies for real-time hybrid testing." *Report No. 6*, Department of Civil and Environmental Engineering, University of Illinois at Urbana-Champaign (Dec.).

Casciati, F., Faravelli, L., and Venini, P. (1993). *A Neural-Network Performance-Function Selection in Active Structural Control.* Dept. of Civil Engineering, School of Engineering, University of Southern California.

Chameau, J., Reed, D., and Yao, J. (1991). "Intelligent systems in civil engineering." *Proceedings of the International Fussy Systems Association*, Brussels, Belgium.

Chang, C.-M., Park, K.-S., Mullenix, A., and Spencer, Jr., B. F. (2008). "Semiactive control strategy for a phase ii smart base isolated benchmark building." *Structural Control and Health Monitoring*, 15(5), 673–696.

Chang, C. M. and Spencer, Jr., B. F. (2012). "Multi-axial active isolation for seismic protection of buildings." *Report No. 30*, Department of Civil and Environmental Engineering, University of Illinois at Urbana-Champaign (May).

Chang, C. M., Wang, Z., Spencer, Jr., B. F., and Chen, Z. (2013). "Semi-active damped outriggers for seismic protection of high-rise buildings." *Smart Structures and Systems*, 11(5), 435–451.

Chang, J. C. and Soong, T. T. (1980). "Structural control using active tuned mass dampers." *Journal of the Engineering Mechanics Division*, 106(6), 1091–1098.

Charles, J. (2006). "Application of damping in high-rise buildings." M.S. thesis, M.I.T., M.I.T.

Chopra, A. (2007). *Dynamics of Structures: Theory and Applications to Earthquake Engineering*. Pearson/Prentice Hall.

Constantinou, M. C., Symans, M. D., Tsopelas, P., and Taylor, D. P. (1993). "Fluid viscous dampers in applications of seismic energy dissipation and seismic isolation." *Proceedings of ATC 17-1 seminar on seismic isolation, passive energy dissipation, and active control*, 581–592.

Constantinou, M. C., Tsopelas, P., Hammel, W., and Sigaher, A. N. (2001). "Toggle-brace-damper seismic energy dissipation systems." *Journal of Structural Engineering*, 127(2), 105–112.

Darby, A. P., Blakeborough, A., and Williams, M. S. (2001). "Improved control algorithm for real-time substructure testing." *Earthquake Engineering & Structural Dynamics*, 30(3), 431–448.

Den Hartog, J. (1956). *Mechanical Vibrations*. Read Books.

Dyke, S. J., Spencer, Jr., B. F., Quast, P., Kaspari, D. C., and Sain, M. K. (1996a). "Implementation of an active mass driver using acceleration feedback control." *Computer-Aided Civil and Infrastructure Engineering*, 11(5), 305–323.

Dyke, S. J., Spencer, Jr., B. F., Quast, P., and Sain, M. K. (1995). "Role of control-structure interaction in protective system design." *Journal of Engineering Mechanics*, 121(2), 322–338.

Dyke, S. J., Spencer, Jr., B. F., Quast, P., Sain, M. K., Kaspari, Jr., D. C., and Soong, T. T. (1996b). "Acceleration feedback control of mdof structures." *Journal of Engineering Mechanics*, 122(9), 907–918.

Dyke, S. J., Spencer, Jr., B. F., Sain, M. K., and Carlson, J. D. (1996c). "Modeling and control of magnetorheological dampers for seismic response reduction." *Smart Materials and Structures*, 5(5), 565–575.

Dyke, S. J., Spencer, Jr., B. F., Sain, M. K., and Carlson, J. D. (1996d). "A new semi-active control device for seismic response reduction." *Proceedings of the 11th ASCE Engineering Mechanics Specialty Conference*, 886–889.

Ehrgott, R. and Masri, S. (1994). "Structural control applications of an electrorheological device." *Proceedings of the International Workshop on Structural Control*, Dept. of Civil Engineering, School of Engineering, University of Southern California, 115–129. USC publication No. CE-9311.

Feng, M. (1993). "Application of hybrid sliding isolation system to buildings." *Journal of Engineering Mechanics*, 119(10), 2090–2108.

Feng, Q. and Shinozuka, M. (1990). "Use of a variable damper for hybrid control of bridge response under earthquake." *Proceedings of the U.S. National Workshop on Structural Control Research*, Dept. of Civil Engineering, School of Engineering, University of Southern California, 107–112. USC publication No. CE-9013.

Fur, L., Yang, H., and Ankireddi, S. (1996). "Vibration control of tall buildings under seismic and wind loads." *Journal of Structural Engineering*, 122(8), 948–957.

Furuta, H., Okanan, H., Kaneyoshi, M., and Tanaka, H. (1994). "Application of genetic algorithms to self-tuning of fuzzy active control for structural vibration." *Proceedings of the first World Conference on Structural Control*, WP1:3–12.

Gattulli, V., Lin, R., and Soong, T. (1994). "Nonlinear control laws for enhancement of structural control effectiveness." *Proceedings of 5th U.S. National Conference for Earthquake Engineering*, Chicago, IL, 971–980.

Gavin, H., Hose, Y., and Hanson, R. (1994a). "Design and control of electrorheological dampers." *Proceedings of the 1st World Conference on Structural Control*, Pasadena, CA, WP3:83–92.

Gavin, H., Ortiz, D., and Hanson, R. (1994b). "Testing and modeling of a prototype er damper for seismic structural response control." *Proceedings of the International Workshop on Structural Control*, Dept. of Civil Engineering, School of Engineering, University of Southern California, 166–180. USC publication No. CE-9311.

Gordaninejad, F., Ray, A., and Bindu, R. (1994). "Vibration control of structures using hybrid er/viscous dampers." *Proceedings of the 1st World Conference on Structural Control*, Pasadena, CA, TA2:41–49.

Hakuno, M., Shidawara, M., and Hara, T. (1969). "Dynamic destructive test of a cantilever beam controlled by an analog-computer." *Journal of JSCE*, 171, 1–9 (in Japanese).

Haroun, M., Pires, J., and Won, A. (1994). "Active orifice control in hybrid liquid dampers." *Proceedings of the 1st World Conference on Structural Control*, Pasadena, CA, FA1:69–78.

Horiuchi, T., Nakagawa, M., Sugano, M., and Konno, T. (1996). "Development of a real-time hybrid experimental system with actuator delay compensation." *Proceedings of the 11th World Conference of Earthquake Engineering.* No. 660.

Housner, G., Bergman, L., Caughey, T., Chassiakos, A., Claus, R., Masri, S., Skelton, R., Soong, T., Spencer, Jr., B., and Yao, J. (1997). "Structural control: Past, present, and future." *Journal of Engineering Mechanics*, 123(9), 897–971.

Iemura, H., Igarashi, A., Pradono, M. H., and Kalantari, A. (2006). "Negative stiffness friction damping for seismically isolated structures." *Structural Control and Health Monitoring*, 13(2-3), 775–791.

Iemura, H., Igarashi, A., Toyooka, A., and Higuchi, M.and Kouchiyama, O. (2010). "Theoretical, numerical and experimental verification of negative stiffness dampers." *Proceedings of the 5th World Conference on Structural Control and Monitoring*, Tokyo, Japan.

Iemura, H., Igarashi, A., Toyooka, A., Kouchiyama, O., and Higuchi, M. (2008). "Seismic response control with innovative negative stiffness dampers." *Proceedings of the 14th World Conference on Structural Control and Monitoring*, Beijing, China.

Iemura, H. and Pradono, M. H. (2002). "Passive and semi-active seismic response control of a cable-stayed bridge." *Journal of Structural Control*, 9(3), 189–204.

Iemura, H. and Pradono, M. H. (2005). "Simple algorithm for semi-active seismic response control of cable-stayed bridges." *Earthquake Engineering & Structural Dynamics*, 34(4-5), 409–423.

Iemura, H. and Pradono, M. H. (2009). "Advances in the development of pseudo-negative-stiffness dampers for seismic response control." *Structural Control and Health Monitoring*, 16(7-8), 784–799.

Ikago, K., Saito, K., and Inoue, N. (2012). "Seismic control of single-degree-of-freedom structure using tuned viscous mass damper." *Earthquake Engineering & Structural Dynamics*, 41(3), 453–474.

Ikhouane, F., Rabeh, A., and Giri, F. (1997). "Transient performance analysis in robust nonlinear adaptive control." *Systems & Control Letters*, 31(1), 21 – 31.

Inaudy, J. and Kelly, J. (1990). "Active isolation." *Proceedings of the U.S. National Workshop on Structural Control Research*, Los Angeles, CA, 125–130.

Infanti, S., Robinson, J., and Smith, R. (2008). "Viscous dampers for high-rise buildings.

Jansen, L. and Dyke, S. (2000). "Semiactive control strategies for mr dampers: Comparative study." *Journal of Engineering Mechanics*, 126(8), 795–803.

Kalman, R. E. (1960). "A new approach to linear filtering and prediction problems." *Journal of Basic Engineering*, 82(1), 35–45.

Kalman, R. E. and Bucy, R. S. (1961). "New results in linear filtering and prediction theory." *Journal of Basic Engineering*, 83(1), 95–108.

Kamagata, S. and Kobori, T. (1994). "Autonomous adaptive control of active variable stiffness system for seismic ground motion." *Proceedings of the First World Conference on Structural Control*, Pasadena, CA, TA4:33–42.

Kannan, S., Uras, H. M., and Aktan, H. M. (1995). "Active control of building seismic response by energy dissipation." *Earthquake Engineering & Structural Dynamics*, 24(5), 747–759.

Kareem, A., Kijewski, T., and Y., T. (1999). "Mitigation of motion of tall buildings with recent applications." *Wind and Structures*, 2(3), 201–251.

Karimi, H. R., Zapateiro, M., and Luo, N. (2009). "Vibration control of base-isolated structures using mixed h2/h output-feedback control." *Proceedings of the Institution of Mechanical Engineers, Part I: Journal of Systems and Control Engineering*, 223(6), 809–820.

Karnopp, D., Crosby, M. J., and Harwood, R. A. (1974). "Vibration control using semi-active force generators." *Journal of Engineering for Industry*, 96(2), 619–626.

Kelly, J. (1997). *Earthquake-resistant design with rubber*. Springer.

Kelly, J. M., Leitmann, G., and Soldatos, A. G. (1987). "Robust control of base-isolated structures under earthquake excitation." *Journal of Optimization Theory and Applications*, 53, 159–180.

Khalil, H. (2002). *Nonlinear Systems*. Prentice Hall PTR.

Kim, S. B., Spencer, J. B. F., and Yun, C.-B. (2005). "Frequency domain identification of multi-input, multi-output systems considering physical relationships between measured variables." *Journal of Engineering Mechanics*, 131(5), 461–472.

Kobori, T. (1990). "Technology development and forecast of dynamical intelligent building (d.i.b)." *Journal of Intelligent Material systems and structures*, 1(4), 391–407.

Kobori, T. (1996). "Future direction on research and development of seismic-response-controlled structures." *Computer-Aided Civil and Infrastructure Engineering*, 11(5), 297–304.

Lee-Glauser, G., Ahmadi, G., and Horta, L. (1997). "Integrated passive/active vibration absorber for multistory buildings." *Journal of Structural Engineering*, 123(4), 499–504.

Leitmann, G. (1994). "Semiactive control for vibration attenuation." *Journal of Intelligent Material Systems and Structures*, 5(6), 841–846.

Liberzon, D. (2012). *Calculus of Variations and Optimal Control Theory: A Concise Introduction*. Princeton University Press.

Lin, P. Y., Roschke, P. N., and Loh, C. H. (2007). "Hybrid base-isolation with magnetorheological damper and fuzzy control." *Structural Control and Health Monitoring*, 14(3), 384–405.

Loh, C.-H. and Chao, C.-H. (1996). "Effectiveness of active tuned mass damper and seismic isolation on vibration control of multi-storey building." *Journal of Sound and Vibration*, 193(4), 773 – 792.

Loh, C.-H. and Ma, M.-J. (1996). "Control of seismically excited building structures using variable damper systems." *Engineering Structures*, 18(4), 279 – 287.

Lou, J. Y. K., Lutes, L. D., and Li, J. J. (1994). "Active tuned liquid damper for structural control." *Proceedings of the 1st World Conference on Structural Control*, Pasadena, CA, TP1:70–79.

Luo, N., Rodellar, J., la Sen, M., and Vehi, J. (2000). "Output feedback sliding mode control of base isolated structures." *Journal of the Franklin Institute*, 337(5), 555 – 577.

Luo, N., Rodellar, J., Villamizar, R., and Vehi, J. (2003). "Robust control law for a friction-based semiactive controller of a two-span bridge." *Proc. SPIE*.

Luo, N., Villamizar, R., and Vehi, J. (2004). "Quantitative feedback theory (qft): application to structural control." *Proceedings of China-Japan-US Symposium on Health Monitoring and Control of Structures*, Dailan, China.

Luo, N., Villamizar, R., Vehi, J., and Dyke, S. (2006). "Semiactive backstepping control for vibration attenuation in structures equipped with magnetorheological actuators." *Computer Aided Control System Design, 2006 IEEE International Conference on Control Applications, 2006 IEEE International Symposium on Intelligent Control, 2006 IEEE*, 1091 –1096 (oct.).

Makris, N. (1997). "Rigidityplasticityviscosity: Can electrorheological dampers protect base-isolated structures from near-source ground motions?." *Earthquake Engineering & Structural Dynamics*, 26(5), 571–591.

Makris, N., Burton, S., Hill, D., and Jordan, M. (1996). "Analysis and design of er damper for seismic protection of structures." *Journal of Engineering Mechanics*, 122(10), 1003–1011.

Makris, N., Hill, D., Burton, S., and Jordan, M. (1995). "Electrorheological fluid damper for seismic protection of structures." 184–194.

MATLAB (2013). The Math Works, Inc., Natick, MA.

McClamroch, N. and Gavin, H. (1995). "Closed loop structural control using electrorheological dampers." *American Control Conference, 1995. Proceedings of the*, Vol. 6, 4173–4177 (jun).

McClamroch, N., Oritz, D., Gavin, H., and Hanson, R. (1994). "Electrorheological dampers and semi-active structural control." *Decision and Control, 1994., Proceedings of the 33rd IEEE Conference on*, Vol. 1, 97–102.

Merritt, H. (1967). *Hydraulic Control Systems*. Wiley.

Moon, S., Bergman, L., and Voulgaris, P. (2003). "Sliding mode control of cable-stayed bridge subjected to seismic excitation." *Journal of Engineering Mechanics*, 129(1), 71–78.

Nagarajaiah, S. and Narasimhan, S. (2006). "Smart base-isolated benchmark building. part ii: phase i sample controllers for linear isolation systems." *Structural Control and Health Monitoring*, 13(2-3), 589–604.

Nagarajaiah, S. and Narasimhan, S. (2007). "Seismic control of smart base isolated buildings with new semiactive variable damper." *Earthquake Engineering & Structural Dynamics*, 36(6), 729–749.

Nagarajaiah, S., Reinhorn, A., Constantinou, M., Taylor, D., and Pasala, D. (2010). "Adaptive negative stiffness: A new structural modification approach for seismic protection." *Proceedings of the 5th World Conference on Structural Control and Monitoring*, Tokyo, Japan.

Nakamura, Y., Fukukita, A., Tamura, K., Yamazaki, I., Matsuoka, T., Hiramoto, K., and Sunakoda, K. (2013). "Seismic response control using electromagnetic inertial mass dampers." *Earthquake Engineering & Structural Dynamics*.

Nakashima, M., Kato, H., and Takaoka, E. (1992). "Development of real-time pseudo dynamic testing." *Earthquake Engineering & Structural Dynamics*, 21(1), 79–92.

Nakashima, M. and Masaoka, N. (1999). "Real-time on-line test for MDOF systems." *Earthquake Engineering & Structural Dynamics*, 28(4), 393–420.

Narasimhan, S., Nagarajaiah, S., and Johnson, E. A. (2008). "Smart base-isolated benchmark building part iv: Phase ii sample controllers for nonlinear isolation systems." *Structural Control and Health Monitoring*, 15(5), 657–672.

Ni, T., Zuo, L., and Kareem, A. (2011). "Assessment of energy potential and vibration mitigation of regenerative tuned mass dampers on wind excited tall buildings." *Proceedings of the 23rd Biennial Conference on Mechanical Vibration and Noise*, 333–342.

Nishimura, H. and Kojima, A. (1998). "Active vibration isolation control for a multi-degree-of-freedom structure with uncertain base dynamics." *JSME international journal. Series C, Mechanical systems, machine elements and manufacturing*, 41(1), 37 – 45.

Patten, W., Kuo, C., He, Q., Liu, L., and Sack, R. (1994a). "Seismic structural control via hydraulic semiactive vibration dampers (savd)." *Proceedings of the 1st World Conference on Structural Control*, Pasadena, CA, FA2:83–92.

Patten, W., Kuo, C., He, Q., Liu, L., and Sack, R. (1994b). "Suppression of vehicle-induced bridge vibration via hydraulic semiactive vibration dampers." *Proceedings of the 1st World Conference on Structural Control*, Pasadena, CA, FA1:30–38.

Phillips, B. M. and Spencer, Jr., B. F. (2012). "Model-based framework for real-time dynamic structural performance evaluation." *Report No. 31*, Department of Civil and Environmental Engineering, University of Illinois at Urbana-Champaign (Aug.).

Pu, J. and Kelly, J. (1991). "Active control and seismic isolation." *Journal of Engineering Mechanics*, 117(10), 2221–2236.

Rabinow, J. (1948). "The magnetic fluid clutch." *American Institute of Electrical Engineers, Transactions of the*, 67(2), 1308 –1315.

Ramallo, J., Johnson, E., and Spencer, Jr., B. F. (2002). "smart base isolation systems." *Journal of Engineering Mechanics*, 128(10), 1088–1099.

Ramallo, J. C., Johnson, E. A., Spencer, Jr., B. F., and Sain, M. K. (1999). "Semi-active building base isolation." *American Control Conference, 1999. Proceedings of the 1999*, Vol. 1, 515–519 vol.1.

Reinhorn, A., Soong, T., Lin, R., Wang, Y., Fukuo, Y., Abe, H., and Nakai, M. (1989). "1:4 scale model studies of active tendon systems and active mass dampers for aseismic protection." *Report no.*, National Center for Earthquake Engineering Research, State University of New York at Buffalo, Buffalo, NY.

Reinhorn, A. M., Li, C., and Constantinou, M. C. (1995). "Experimental and analytical investigation of seismic retrofit of structures with supplemental damping : Part.1 - fluid viscous damping devices." *Report no.*, National Center for Earthquake Engineering Research, State University of New York at Buffalo, Buffalo, NY (Jan.).

Riley, M., Reinhorn, A., and Nagarajaiah, S. (1998). "Implementation issues and testing of a hybrid sliding isolation system." *Engineering Structures*, 20(3), 144 – 154.

Sahasrabudhe, S. and Nagarajaiah, S. (2005). "Effectiveness of variable stiffness systems in base-isolated bridges subjected to near-fault earthquakes: An experimental and analytical study." *Journal of Intelligent Material Systems and Structures*, 16(9), 743–756.

Samali, B., Kwok, K., Wood, G., and Yang, J. (2004). "Wind tunnel tests for wind-excited benchmark building." *Journal of Engineering Mechanics*, 130(4), 447–450.

Scruggs, J. T. (2004). "Structural control using regenerative force actuation networks." Ph.D. thesis, California Institute of Technology, Pasadena, CA.

Shook, D., Lin, P.-Y., Lin, T.-K., and Roschke, P. N. (2007). "A comparative study in the semi-active control of isolated structures." *Smart Materials and Structures*, 16(4), 1433–1446.

Shoureshi, R., Bell, M., and Wheeler, M. (1994). "Neural-based intelligent control of structures." *Proceedings of the 1st World Conference on Structural Control*, Pasadena, CA, FP4:3–11.

Sigaher, A. N. and Constantinou, M. C. (2003). "Scissor-jack-damper energy dissipation system." *Earthquake Spectra*, 19(1), 133–158.

SIMULINK (2013). The Math Works, Inc., Natick, MA.

Skelton, R. E. (1988). *Dynamic Systems Control*. John Wiley and Sons.

Smith, B. S. and Salim, I. (1981). "Parameter study of outrigger-braced tall building structures." *Journal of the Structural Division*, 107(10), 2001–2014.

Smith, R. J. and Willford, M. R. (2007). "The damped outrigger concept for tall buildings." *The Structural Design of Tall and Special Buildings*, 16(4), 501–517.

Soong, T. and Costantinou, C. (1995). *Passive and Active Structural Vibration Control in Civil Engineering*. CISM INTERNATIONAL CENTRE FOR MECHANICAL SCIENCES COURSES AND LECTURES. Springer Verlag.

Soong, T. T. and Reinhorn, A. M. (1993). "Case studies of active control and implementational issues." *Proceedings of ATC-17-1 Seminar of Seismic Isolation, Passive Energy Dissipation, and Active Control*, Vol. 2, 701–713.

Soong, T. T. and Skinner, G. T. (1981). "Experimental study of active structural control." *Journal of the Engineering Mechanics Division*, 107(6), 1057–1067.

Spencer, Jr., B. F., Dyke, S. J., Sain, M. K., and Carlson, J. D. (1997). "Phenomenological model for magnetorheological dampers." *Journal of Engineering Mechanics*, 123(3), 230–238.

Spencer, Jr., B. F., Johnson, E. A., and Ramallo, J. C. (2000). "Smart isolation for seismic control." *JSME international journal. Series C, Mechanical systems, machine elements and manufacturing*, 43(3), 704 – 711.

Spencer, Jr., B. F. and Nagarajaiah, S. (2003). "State of the art of structural control." *Journal of Structural Engineering*, 129(7), 845–856.

Spencer, Jr., B. F., Suhardjo, J., and Sain, M. (1994). "Frequency domain optimal control strategies for aseismic protection." *Journal of Engineering Mechanics*, 120(1), 135–158.

Stengel, R. (1986). *Stochastic optimal control: theory and application*. Wiley-Interscience publication. Wiley.

Stengel, R. (1994). *Optimal control and estimation*. Dover Publications.

Suhardjo, J., Spencer, Jr., B. F., and Kareem, A. (1992). "Frequency domain optimal control of windexcited buildings." *Journal of Engineering Mechanics*, 118(12), 2463–2481.

Sun, L. and Goto, Y. (1994). "Application of fuzzy theory to variable dampers for bridge vibration control." *Proceedings of the 1st World Conference on Structural Control*, Pasadena, CA, WP1:31–40.

Takanashi, K., Udagawa, K., Seki, M., Okada, T., and Tanaka, H. (1975). "Non-linear earthquake response analysis of structures by a computer-actuator on-line system : Part 1 detail of the system." *Transactions of Architectural Institute of Japan*, (229), 77–83.

Takanashi, K., Udagawa, K., Seki, M., and Tanaka, H. (1974). "Seismic failure analysis of structures by computer-pulsator on-line system." *Industrial research*, 26(11), 413–425 (in Japanese).

Tamura, K., Shiba, K., Inada, Y., and Wada, A. (1994). "Control gain scheduling of a hybrid mass damper system against wind response of tall buildings.." *Proceedings of the 1st World Conference on Structural Control*, FA2:13–22.

Tang, X. and Zuo, L. (2012). "Simultaneous energy harvesting and vibration control of structures with tuned mass dampers." *Journal of Intelligent Material Systems and Structures*, 23(18), 2117–2127.

Tanida, K., Koike, Y., Mutaguchi, K., and Uno, N. (1991). "Development of hybrid active-passive mass damper." *Active and Passive Damping*, 211, 21–26.

Taylor, D. P. (2003). "Semi-active control of full-scale structures using variable joint damper system.." *74th Shock & Vibration Symposium*, San Diego, CA.

Umekita, K., Kametani, M., and Miyake, N. (1995). "Development of super real-time controller which can perform analysis with measurement/control in real time." *Proceedings of the 5th Robot Symposium*, Robotics society of Japan, 55–58.

Villaverde, R. (1994). "Seismic control of structures with damped resonant appendages." *Proceedings of the 1st World Conference on Structural Control*, Vol. 1, WP4:113–122.

Viti, S., Cimellaro, G. P., and Reihhorn, A. M. (2006). "Retrofit of a hospital through strength reduction and enhanced damping." *Smart Structures and Systems*, 2(4), 339–355.

Wang, X. and Gordaninejad, F. (2002). "Lyapunov-based control of a bridge using magneto-rheological fluid dampers." *Journal of Intelligent Material Systems and Structures*, 13(7-8), 415–419.

Wang, Y. and Dyke, S. (2013). "Modal-based lqg for smart base isolation system design in seismic response control." *Structural Control and Health Monitoring*, 20(5), 753–768.

Wang, Z., Chang, C.-M., Spencer, Jr., B. F., and Chen, Z. (2010). "Controllable outrigger damping system for high rise building with MR dampers." Vol. 7647, SPIE, 76473Z.

Weber, F. and Boston, C. (2011). "Clipped viscous damping with negative stiffness for semi-active cable damping." *Smart Materials and Structures*, 20(4), 045007.

Wen, Y.-K. (1976). "Method for random vibration of hysteretic systems." *Journal of the Engineering Mechanics Division*, 102(2), 249–263.

Whittaker, A. S., Bertero, V. V., Thompson, C. L., and Alonso, L. I. (1991). "eismic testing of steel plate energy dissipation systems." *Earthquake Spectra*, 7(4), 563–604.

Willford, M., Smith, R., Scott, D., and Jackson, M. (2008). "Viscous dampers come of age." *Structure Magazine*, (6), 15–18.

Winslow, W. (1947). "Method and means for translating electrical impulses into mechanical force. U.S. Patent No. 2,417,850.

Winslow, W. M. (1949). "Induced fibration of suspensions." *Journal of Applied Physics*, 20(12), 1137 –1140.

Wongprasert, N. and Symans, M. (2005). "Experimental evaluation of adaptive elastomeric base-isolated structures using variable-orifice fluid dampers." *Journal of Structural Engineering*, 131(6), 867–877.

Wu, B., Shi, P., and Ou, J. (2013). "Seismic performance of structures incorporating magnetorheological dampers with pseudo-negative stiffness." *Structural Control and Health Monitoring*, 20(3), 405–421.

Yang, J., Agrawal, A., and Wu, J. (1994). "Sliding mode control for structures subjected to seismic loads." *Proceedings of the 1st World Conference on Structural Control*, Pasadena, CA, WA1:13–22.

Yang, J., Li, Z., and Liu, S. (1992). "Stable controllers for instantaneous optimal control." *Journal of Engineering Mechanics*, 118(8), 1612–1630.

Yang, J., Wu, J., Reinhorn, A., and Riley, M. (1996). "Control of sliding-isolated buildings using sliding-mode control." *Journal of Structural Engineering*, 122(2), 179–186.

Yang, J. N. (1975). "Application of optimal control theory to civil engineering structures." *Journal of the Engineering Mechanics Division*, 101(6), 819–838.

Yang, J. N., Agrawal, A. K., Samali, B., and Wu, J.-C. (2004a). "Benchmark problem for response control of wind-excited tall buildings." *Journal of Engineering Mechanics*, 130(4), 437–446.

Yang, J. N., Lin, S., and Jabbari, F. (2003). "H2-based control strategies for civil engineering structures." *Journal of Structural Control*, 10(3-4), 205–230.

Yang, J. N., Lin, S., and Jabbari, F. (2004b). "H-based control strategies for civil engineering structures." *Structural Control and Health Monitoring*, 11(3), 223–237.

Yang, J. N., Wu, J. C., Kawashima, K., and Unjoh, S. (1995). "Hybrid control of seismic-excited bridge structures." *Earthquake Engineering & Structural Dynamics*, 24(11), 1437–1451.

Yao, T. P. (1972). "Concept of structural control." *Journal of the Structural Division*, 98(7), 1567–1574.

Yoshida, O. and Dyke, S. J. (2004). "Seismic control of a nonlinear benchmark building using smart dampers." *Journal of Engineering Mechanics*, 130(4), 386–392.

Yoshioka, H., Ramallo, J., and Spencer, Jr., B. F. (2002). "Smart base isolation strategies employing magnetorheological dampers." *Journal of Engineering Mechanics*, 128(5), 540–551.

Zapateiro, M., Karimi, H. R., Luo, N., Phillips, B. M., and Spencer, Jr., B. F. (2009). "Semiactive backstepping control for vibration reduction in a structure with magnetorheological damper subject to seismic motions." *Journal of Intelligent Material Systems and Structures*, 20(17), 2037–2053.

Zapateiro, M., Luo, N., and Karimi, H. (2008). "QFT control for vibration reduction in structures equipped with MR dampers." *American Control Conference, 2008*, 5142 –5144 (june).

Zhao, J., French, C., Shield, C., and Posbergh, T. (2006). "Comparison of tests of a nonlinear structure using a shake table and the eft method." *Journal of Structural Engineering*, 132(9), 1473–1481.